Estudio experimental del efecto de la inyección de CO_2 en rocas: acoplamiento de procesos hidrodinámicos, mecánicos y geoquímicos

(Experimental study of effect of CO_2 injection on rocks: coupling hydrodynamic, mechanical and geochemical processes)

AUTHOR: JACOBO CANAL VILA

DOCTORAL THESIS/ 2016

DIRECTOR: Dr. JORDI DELGADO MARTÍN

PROGRAMA DE DOCTORADO EN INGENIERÍA CIVIL

UNIVERSIDADE DA CORUÑA

D. JORDI DELGADO MARTÍN, Catedrático de Universidad de la Universidade da Coruña en el Área de Ingeniería del Terreno

HACE CONSTAR QUE:

La memoria "ESTUDIO EXPERIMENTAL DEL EFECTO DE LA INYECCIÓN DE CO_2 EN ROCAS: ACOPLAMIENTO DE PROCESOS HIDRODINÁMICOS, MECÁNICOS Y GEOQUÍMICOS (*Experimental study of effect of CO_2 injection on rocks: coupling hydrodynamic, mechanical and geochemical processes*)" ha sido realizada por D. Jacobo Canal Vila, bajo mi dirección en el Departamento de Métodos Matemáticos y de Representación, y constituye la Tesis que presenta para optar al Grado de Doctor en Ingeniería Civil por la Universidade da Coruña.

A Coruña, 2 de septiembre de 2016

Fdo: Dr. Jordi Delgado Martín

Acknowledgments

The activities collected in this thesis has been funded by the Spanish foundation CIUDEN, and the European Regional Development Funds 2007/2013. OXYCFB300 is cofinanced by the EU Energy Programme for Recovery.

There are few words to describe how grateful I am for all the help that Jordi Delgado has given me during my PhD journey. His help and advice on every aspect of my research was simple great.

I really appreciate all the support, patient and guide from Mike Batzle who contributes me in such a way that he never can imagine. He opened his world to me and shown me that he was a number one as a scientist but even greater as a human being. I miss you Mike.

I am very grateful for all my mates, colleagues and friends at University of Coruña. Víctor, Ana, Himar, Javi and Álvaro, we shared great time together. I need to acknowledge all the effort that Cesar Añón did introducing me in the world of the MTS and sensors.

I thank the way the people for the Center of Rock Abuse treated me during my stay. It was such a great time with them. Azar, Saul, Mandy and the rest of the "abusers", hope to remember again with you that time.

I need to acknowledge to Juan, Xénia, Amanda and Javi the year together that we spent in Ponferrada. Without them it would be much difficult that experience

I am very grateful to people at Repsol, where the whole petrophysicist team was incredible. I particularly thank Tamrat Worku for giving me the opportunity. I´m very thankful to Jose Alvarellos because without his help this work wouldn't be the same. I thank Basim Shubber for his companion, friendship, advice and mentoring.

I greatly thank Paula and my family, because it is their support that kept the energy to finish this work.

RESUMO

Este traballo nace amparado na necesidade de buscar novas solución ó aumento de emisións de gases nocivos para o medio ambiente. O almacenamento xeolóxico de CO_2 é a etapa final do proceso de captura, transporte e almacenamento de CO_2, consistente en inxectar CO_2 nunha formación xeolóxica profunda. Dita inxección garda relación coa preocupación do papel que os gases de efecto invernadoiro poden ter sobre o clima.

O obxectivo fundamental radica en obter información sobre o comportamento hidromecánico e xeoquímico das rocas a través do seguimento simultáneo de parámetros relevantes (deformacións, variacións na permeabilidade, indicadores xeofísicos, etc.).

Considéranse os seguintes fitos:

a) Deseño, definición e posta en marcha do sistema experimental
b) Obtención de resultados
c) Interpretación cualitativa e cuantitativa dos resultados

O dispositivo experimental utilizado sobre o que se constrúe o ensaio de inxección é a cela triaxial, con pratos deseñados para a aplicación de presión de poro e propagación de ondas. Adicionalmente realizouse o estudo de análises de frecuencias de ondas P, S_1 e S_2, así como unha batería de ensaios xeomecánicos (triaxiais, compresión simple e tracción directa e indirecta) co obxectivo de caracterizar o material previamente a ser ensaiado.

RESUMEN

Este trabajo nace amparado en la necesidad de buscar soluciones al incremento de emisiones de gases nocivos para el medio ambiente. El almacenamiento geológico de CO_2 es la etapa final del proceso de captura, transporte y almacenamiento de CO_2, consistente en inyectar CO_2 en una formación geológica profunda. Dicha inyección guarda relación con la preocupación del papel que los gases de efecto invernadero pueden tener sobre el clima.

El objetivo fundamental radica en obtener información sobre el comportamiento hidromecánico y geoquímico de las rocas a través del seguimiento simultáneo de parámetros relevantes (deformaciones, variaciones en permeabilidad, indicadores geofísicos, etc.)

Se tienen en consideración los siguientes hitos:

a) Diseño, definición y puesta en marcha del sistema experimental.
b) Obtención de resultados.
c) Interpretación cualitativa y cuantitativa de los resultados

El dispositivo experimental utilizado sobre el que construye el ensayo de inyección es la celda triaxial, con platos diseñados para la aplicación de presión de poro y propagación de ondas. Adicionalmente se realizó el estudio de análisis frecuencias de ondas P, S_1 y S_2, así como una batería de ensayos geomecánicos (triaxiales, comprensión simple y tracción directa e indirecta) con el objetivo de caracterizar el material previamente a ser ensayado.

ABSTRACT

This research work has its origins on the need to find solutions to increased emissions of harmful gases to the environment. CO_2 storage is the final stage of capture, transport and storage of CO_2 process. This process involves the injection of CO_2 in deep geological formations. That injection is directly related to the concern that greenhouse gases would have on climate.

The main objective is obtaining information about hydromecanic and geochemical behaviour of rocks through the simultaneous monitoring of relevant parameters (deformation, permeability variations, geophysical indicators, etc.).

The following milestones are taken into consideration:

a) Design, definition and implementation of the experimental system.

b) Obtainment of results.

c) Qualitative and quantitative interpretation of results

The experimental device used on building the injection test is the triaxial cell, with plates designed for the application of pore pressure and wave propagation. Additionally a frequency analysis study for P, S_1 and S_2 waves was performed, as well as a set of geomechanical tests (triaxial, simple compression, direct and indirect traction). These tests were performed in order to characterize the material before being tested.

To my parents, Elena y Pablo

My grandparents,

Manuela, Flores y Claudino

And, last but not least, to Paula

Index

FIGURES INDEX

CHAPTER 2

CHAPTER 3

CHAPTER 4

CHAPTER 5

CHAPTER 6

ANNEX 1

CHARTS INDEX

CHAPTER 3

CHAPTER 4

CHAPTER 5

CHAPTER 6

CHAPTER 7

CHAPTER 1. INTRODUCTION

1.1 Motivation

Carbon dioxide is an odourless, colourless, non-flammable and slightly acidic gaseous compound. It consists of linear molecules made of one carbon atom bonded to two oxygen atoms (i.e. C = O = C). Its chemical formula is CO_2. Its solubility is limited in water at constant pressure and it is gaseous at ambient temperature and pressure. However, it can also be either a liquid, solid, or a supercritical fluid, depending on the prevailing conditions of pressure and temperature.

Carbon is a chemical element with atomic number 6 and symbol C. It is solid at room temperature. The main geochemical reservoir of carbon is the atmosphere and hydrosphere. The carbon cycle is divided into two parts: The biological and the geological cycles, although they are both combined in the so called biogeochemical carbon cycle.

The biological cycle refers to the exchange of CO_2 between living beings and the atmosphere. This cycle is relatively fast: the gas in the atmosphere is in a concentration of more than 0.03%.

The biogeochemical cycle regulates the transfer of carbon between the atmosphere and lithosphere. In this cycle, atmospheric CO_2 dissolves in water forming carbonic acid that attacks silicates of the rocks. Bicarbonate ions are the result of that process. These ions, which are dissolved in water, reach the sea, and they are assimilated by living organisms to form their tissues and skeletons. After their death, they are deposited and they experience a variety of

biogeochemical processes that may fix them to sediments or pushed back to the hydrosphere (i.e. aqueous organic or inorganic species plus dissolved gasses) or to the atmosphere (gasses). Within the geological cycle, carbon dioxide may be sent back to the atmosphere via volcanic eruptions following the melting of metamorphically-evolved sediments. This cycle is long lasting because geological mechanisms are involved.

In recent years, the complexity of the dynamics of climate change and its evolution has deeply influenced the development of new fields of knowledge and new technological approaches. The contribution of greenhouse gases to global warming continues to be a growing concern. Carbon dioxide is one of the most significant (although not the only one) greenhouse gas contributors and, according to current perception, the main cause of global warming. Atmospheric levels of CO_2 have increased significantly as a result of expanded use of fossil fuel for energy. This increase in concentrations in the Earth's atmosphere is enhancing the greenhouse effect, leading to changes in the climate. Although the nature, extent and timing of these changes are uncertain, it is expected an increase in global temperature of the Earth.

Experts agree that action is needed soon in order to reduce the amount of CO_2 entering the atmosphere. The main techniques that can be used to reduce such levels of CO_2 are:

- Reduce the consumption of energy services
- Increase the efficiency of energy conversion or utilization
- Switch to lower carbon content fuels, e.g. natural gas instead of coal
- Enhance the sinks for CO_2, e.g. forests, soils and the ocean, which draw-down CO_2 from the atmosphere
- Use energy sources with very low CO_2 emissions, such as renewable energy or nuclear energy
- Capture and store CO_2 from fossil fuel combustion.

Carbon capture and storage (CCS) is one of the promising technologies under development. It is one of the remedial measures that is explicitly mentioned in the Kyoto protocol. The aim of CCS is to separate the CO_2 produced in different processes to obtain a gas stream with a sufficiently high concentration of CO_2 to compress it and transport (through CO_2-ducts) to the point where it will be stored permanently…or at least, stored for a long-enough time to ensure a positive impact over the emission rates (c.f. tens of thousands of years). CCS is defined as a system of technologies that integrates three stages: 1) CO_2 capture; 2) CO_2 transport and 3) geological storage. Capturing CO_2 and storing it underground can be done with available technology but it has only recently been seriously considered as a potential method of reducing emissions. Its importance stems from the fact that, currently, about 85% of the world's commercial energy needs

are supplied by fossil fuels. A rapid change to non-fossil energy sources, even if possible, would result in large disruption to the energy supply infrastructure, with substantial consequences for the global economy. The technology of CO_2 capture and storage would enable the world to continue to use fossil fuels but with much reduced emissions of CO_2. In view of the many uncertainties about the course of climate change, further development of CO_2 capture and storage technologies is a prudent precautionary action.

Most of the electricity we consume comes from the energy extracted from fossil fuels. The main technologies used to generate power from them are natural gas combined cycles and pulverized coal-fired steam cycles. Nowadays, CO_2 capture is considered only feasible in spot locations with significantly large emissions. The emission rate justifies the ideal size of the facility. An example is the case of power plants, which currently account for about a third of global emissions of CO_2. To a lesser extent, are also refineries, petrochemical, gases processing plants and fertilizers, cement and steel and paper industries. This capture would prevent the CO_2 was sent to the atmosphere and thus help reduce climate change.

The present thesis was born at a time that the European Union and, by extension, in Spain, experienced a significant blossom of research projects and activities around CCS and, more specifically, the geological sequestration of CO_2. In our specific case, the working frame was established by the OXYCFB 300 (Compostilla) Project, that was

leaded by the consortium Fundación Ciudad de la Energía (CIUDEN), ENDESA and Foster Wheeler which was awarded with 180 million euros from EU government in December 2009 as part of European Recovery Programme frame. The works presented here were developed within the context of a contract agreement subscribed by the Fundación CIUDEN and the Laboratory of Rock Mechanics of the Civil Engineering School of the University of A Coruña and they are mainly focused in trying to answer some significant questions related with experimental (laboratory scale) CO_2-rich fluid-rock interaction either from the geochemical, hydrodynamic and geomechanical standpoints.

The work is presented in 8 chapters that cover different topics: From the construction of a new experimental system, passing through a comprehensive characterization survey of experimental materials to the execution of long-lasting experiments of increasing complexity involving coupled phenomena and observation techniques.

The materials used to perform the experiments were selected based on the feedback provided by the managers of the Fundación CIUDEN and they correspond to target reservoir lithologies associated with the CO_2 injection site of the OXYCFB 300 project (i.e. the Hontomín Test Site).

The works documented in each chapter by themselves constituted a significant execution challenge and, in some cases, only a portion of

the information available is presented. Whenever possible, the chapters are constructed around peer-reviewed publications, some of the published in SCI journals of the speciality.

1.2 Objectives

The main objectives of the present work can be summarized in two:

- To design, construct, test and operate a new experimental rig that allows performing core flooding experiments integrating devices from different speciality fields (rock mechanics, geochemistry, petro-geophysics) which are not conventional in most core flooding test. That is mandatory in order to analyse coupled processes.

-To perform experiments with an integrated approach where we can learn more how this processes interlinked between them and how we can monitor them (direct and indirect techniques).

1.3 Thesis organization

The thesis is arranged in 8 chapters corresponding the present introduction to Chapter 1.

Chapter 2 is devoted to make a short summary about the state of the art of some relevant fields connected with the work developed in this thesis.

We noted earlier that it was considered necessary to design and build a new experimental rig. The equipment was improved during this time and the complexity was increasing. Accordingly, Chapter 3 is dedicated to the description of the equipment characteristics and functionality. A number of questions related with sample preparation for this test is also shown on this chapter.

The first successful and comprehensive and comprehensive core flooding experiment is described on Chapter 4. This experiment, which developed at room temperature, was performed using a sandstone plug in which we injected a CO_2-saturated salty fluid under subcritical (CO_2) conditions. Here we monitored wave propagation velocities, axial strain as well as geochemical analysis of pore waters. We further analysed the results from the point of view of reactive transport modelling.) The experimental rig was in an early development stage for this experiment.

Chapter 5 presents a core flooding experiment performed with a vuggy limestone plug in which a succession of fluids (N_2, deionized water, brine, and CO_2-saturated brine) were injected. This experiment was performed also under subcritical conditions using a more developed rig.

Based on the results obtained in the previous tests (that stressed the necessity of an in depth characterization of experimental materials), Chapter 6 presents the results of a wide number of rock

mechanics and other characterization tests and analyses that were done in order to characterize a sandstone material that was further studied (see Chapter 7) in a new core flooding experiment. Thus, in the experiment reported in Chapter 7, deionized water and deionized water saturated with CO_2 was injected under supercritical CO_2 conditions while setting a constant flow rate condition along the whole experiment. This experimental condition was different to the previous ones (i.e. experiments of chapters 4 and 5 were done under constant pressure condition). In this case, in order to minimize the geochemical coupling, a quartz-rich rock (the same whose characterization is presented in Chapter 6) was selected.

Finally, the most significant conclusions and proposed future lines of research are summarized in Chapter 8.

CHAPTER 2. STATE OF THE ART

2.1 Introduction

It is well known that the injection of reactive fluids like CO_2 into geological formations within the context of operations for enhanced oil recovery (EOR) or carbon capture and storage (CCS) projects trigger a series of interlinked phenomena that affect the physical (or mechanical) and hydraulic properties of the reservoir, its seal or even the cementitious materials used in wellbores. Because water is always present in the porous space of these systems, the forced injection of CO_2 (either as gas, liquid or supercritical fluid) induces a significant acidification and the onset of reactive processes which are especially notorious when carbonate (limestone, dolostone, marls) or carbonate-bearing rocks (sandstone, shale…) are present. The co-injection of subordinated gasses accompanying CO_2 (typically as impurities: O_2, SO_2,…) might exacerbate this reactivity due to the oxidation of reduced mineral phases already present in the rocks or by promoting an enhanced acidity associated to S-bearing gasses. Among the geochemical processes typically described in CO_2-injection environments worth mentioning are (Pruess and Garcia 2002): a) the dissolution/precipitation of mineral phases; b) ion exchange phenomena; c) salt precipitation (i.e. desiccation) due to CO_2 flooding; d) mobilization of fines in connection with changes in the mineral surface properties; e) clay swelling. Each one of them, acting

independently or in a coupled way may have either positive or deleterious effects over the whole system performance.

On the other hand, petrophysics provides with invaluable tools with which to assess key rock properties and to elaborate integrated reservoir models. However, classical rock physic approaches do not take into account the major role of chemo-hydro-mechanical couplings which are crucial when dealing with reactive systems. In the recent past years a number of worldwide research teams (most of them within the realm of CCS projects) have started to fill this gap of knowledge by experimentally combining petrophysics (sonic velocities, electrical resistivity...) with rock mechanics (acoustic emission, strain measurement…), hydrodynamics (tracer injection, permeability assessment…) and geochemistry (flow-thru column tests, continuous monitoring of eluates…) under realistic in situ conditions.

In this chapter we provide a short summary of some of the results obtained in the field of coupled processes associated with CO_2 injection and we describe future lines of research based on a modular experimental platform able to work with different size plugs up to a maximum diameter of 100 mm.

2.2 Economic Context of the study

According to the 2007 report of the Intergovernmental Panel on Climate Change greenhouse gas (GHG) emissions and other human

activities play a key role in the current understanding of climate and global change. Since CO_2 is, among the GHG, the most relevant contributor (i.e. volume of emissions and impact over global warming: ~70% of the warming effect), significant efforts are being addressed in the technological and legal frameworks in order to reduce the anthropogenic emissions towards the atmosphere. As a direct consequence, following the signature of the Kyoto protocol, a global-based business based on the trade of CO_2 emissions has arisen and consolidated in the past years. From a more practical point of view, the economic penalties imposed to countries and companies delivering GHG to the atmosphere in excess of the intended target emissions represent a stimulating incentive for conducting applied research addressed at the development of new technologies for the reduction of man-due emissions.

The reduction in emissions can be achieved in different ways. The CCS approach stands for the carbon capture (i.e. the separation of CO_2 from accompanying gasses) and, following transport through CO_2-ducts, its storage in adequate geological formations. CCS can be a cost-efficient approach when the CO_2 sources (power and cement plants, steel mills, etc.) are concentrated in a reduced area. A key element of the CCS concept is the availability of adequate geological reservoirs whose main examples are onshore/offshore depleted oil or gas reservoirs or saline aquifers. Of no less importance, the development of enhanced oil recovery (EOR) projects or the injection of CO_2 in coal

beds for the recovery of methane (ECBM) also constitute realistic approaches with valuable economic turnovers, which is a cornerstone in the demonstration of the feasibility of the CCS concept at the industrial scale.

In the past years, R&D activities concerning CCS technologies in the countries of the European Union have been fostered by the adoption, in 2009, of the European Directive 2009/31/EC. The CCS Directive establishes a legal framework for the environmentally safe geological storage of CO_2 in the territory, exclusive economic zones and continental shelves of EU member states. In its fourth article states that the suitability of a geological formation for use as a storage site shall be determined through a characterization and assessment of the potential storage complex and surrounding area pursuant to a number of criteria including, among others, the behaviour of the geological formations of interest when submitted to the injection of pure or impure supercritical CO_2 ($scCO_2$) or CO_2-saturated solutions. In June, 2008, the European Council called on the Commission to bring forward a mechanism to incentivize Member State and private sector investments to ensure the construction and operation by 2015 of up to 12 CCS demonstration plants. By the end of 2009 the European Commission granted financial assistance to six CCS integral commercial demonstration projects which are expected to lead the work towards developing the necessary technical, economic and

regulatory framework to bring environmentally safe CCS to deployment with new fossil-fuel power plants.

Deep saline aquifers represent, by far, the most widely represented systems for CO_2 geosequestration. In the particular case of Spain, where conventional gas and oil fields are virtually non-existent, they represent the most realistic option for CCS. The EU GeoCapacity (2009) project determined that Spain has the highest onshore storage capacity of all European countries with a conservative estimate of 14,000 Mt in combined onshore and offshore deep saline reservoirs. In December 2010 Spain also became the first European country to transpose the CCS Directive 2009/31/EC. Most of the storage capacity is in deep saline aquifers of the main sedimentary basins (Douro, Ebro, Guadalquivir and Tagus basins). The Douro basin, in particular, is of interest as it has an extension of approximately 50,000 km^2 and is the largest Cenozoic basin on the Iberian Peninsula.

The OXYCFB 300 Compostilla project, funded by the European Energy Program for Recovery and partnered by a consortium of ENDESA (the largest Spanish electric utility), CIUDEN (on behalf of the Government of Spain), and Foster Wheeler (a global leader in energy generation technology) is currently characterizing in the north of Spain the Cretaceous Utrillas Formation, a deep clastic reservoir in the Douro basin. The project is also examining storage potential of a deep Triassic reservoir in the Ebro Basin. The study has investigated a number of

sites for commercial development and for the construction of a Technology Development Plant (TDP). Commercial operations were planned to start by 2015 with injection of ~1.1 Mt during ~30 years. Extensive data acquisition surveys for the commercial site and the TDP started in 2010, including the definition of baseline conditions.

The Compostilla project aimed to demonstrate the full CCS chain and within its framework, a research facility for the deep injection of CO_2 was commissioned in Hontomín (Burgos, N Spain). The geological setting beneath the Hontomín test storage site is a small, dome-shaped, structure (3x4 km) developed in a thick series of carbonated and detritic formations belonging to the Jurassic to lower Cretaceous cycles. CIUDEN identified two targets for CO_2 storage: Main and secondary reservoirs. The main reservoir is located between 1376 and 1502 m below the surface and corresponds to vuggy limestones and dissolution-collapse breccias of Hettangian-lower Sinemurian age. Its seal is constituted by a ~100 m thick package of marls alternating with limestones (Pliensbachian/Bajocian). The secondary reservoir is constituted by siliceous sandstone and conglomerate lenses, which are included in the red mudstones of the Purbeck facies (Malm/Berriasian). Its corresponding seal are the central and upper lutitic formations of the Purbeck and marls of the Wealden (upper Berriasian/lower Aptian) megasequence.

A CO_2 saturated brine is highly acidic and, therefore, aggressive with respect the rock (for instance, a carbonate reservoir) which, in a

simplified first approach, will dissolve increasing its permeability but also reducing its strength. However, depending on the minerals dissolved and the brine chemistry, other minerals may also precipitate (some of them carbonates) which effectively leads to the effective mineralization of CO_2. Eventually, after injection stops, the brine will tend to fill back the pore space, but a sizable amount of CO_2 will remain trapped by capillary forces as residual CO_2 bubbles. In summary, four basic trapping mechanisms are involved in the conventional concept of CO_2 geosequestration. Ranked according to their long term stability, these are (1) stratigraphic or tectonic trapping as a CO_2 phase; (2) water-dissolved CO_2; (3) capillary trapping; and (4) mineral trapping.

The urgency of storing large amounts of CO_2 in a relatively short amount of time has triggered a worldwide number of initiatives aimed at promoting a better scientific understanding, technological achievements, fostering social acceptance, and developing sounder national and transnational regulations. Hence, it is not surprising the large number of projects initiated along the last decade (Hokkaido, SACS, SACS2, CO2STORE, Sleipner, FRIO, CO2SINK, etc.). In this rush, Spain does not lag far behind although the economic restraints imposed by the present financial crisis have forced to redefine the scope and intensity of many initiatives. On a worldwide basis, numerous pilot projects have been developed in the past years. Among the most successful ones worth mentioning are the Sleipner (North Sea, Norway) and Weyburn (Canada) projects. Sleipner was successful

on demonstrating the storage concept by actually injecting of some 15 Mt of CO_2 and its vivid geophysical monitoring. However, the conditions at Sleipner are very favourable (high permeability, large surface area, previously existing infrastructure) and cannot be easily extrapolated elsewhere. However, the injection of CO_2 into geological formations within the context of EOR projects for the oil industry is a rather mature technology that has been successfully applied at the industrial scale (i.e. Weyburn, In Salah, K12-B, Lacq, PCOR Zama, Rangely, etc.).

The onshore injection of CO_2 into deep saline aquifers has been tested with different scales in a relatively small number of sites: Sleipner, Frio, Ketzin, MRCSP (R.E. Burger, East Bend, Gaylord), WESTCARB (Cholla & Rosetta) SEACARB (Escatawpa & Cranfiled), Nagaoka, MGSC Decatur, etc. Some of them deal with demonstration and injection technology issues while few of them have pay attention to more basic scientific/research purposes, which is a key aspect in order to bridge the gap existing between the laboratory and the field scales.

According to Bachu (2002), the main technological challenges that the scientific and industrial community must face in order to achieve a good level of confidence on the CO_2 storage concept include: 1) Determining the performance of the storage formation upon injection; 2) Ensuring that CO_2 injection will not damage the seal (either by geo-mechanical effects associated with pressure build up or by

geochemical interactions). Furthermore, it is important to 3) know the size of the injected plume of CO_2 –as this will determine the spatial extent over which the seal is needed- and its change with time according to natural and injection-induced flow and 4) evaluate the impact of potential leakage paths such as faults and abandoned wells. To meet these challenges, scientific developments are needed in the fields of geology, geophysics, hydrodynamics, geochemistry and geomechanics.

A good geological understanding is needed not only for determining the location of favourable aquifer-caprock systems. It is also needed for determining geometry and anisotropy of the structure and facies within the aquifer, as these will control migration paths, and will activate CO_2 dissolution by enhancing the contact area between the CO_2 bubble and the resident brine. It is also needed to understand tectonic activity, and the natural stress field, which affects the mechanical stability of the caprock. It is also crucial to understand the mineral assemblages present, which control dissolution-precipitation reactions and how these relate to migration pathways.

Geophysics is needed both for geological characterization and for monitoring CO_2 plume migration. In fact, the success of time lapse seismic reflection surveys at Sleipner has spurred a renewed interest on this technique. Compressional wave velocity is sensitive to the presence of CO_2 in water, especially at low saturation rates, which

makes seismic data potentially amenable to precisely locate the plume. Unfortunately, standard 3D seismic reflection is far too expensive for regular monitoring purposes. Therefore, affordable near real-time techniques need to be developed. Moreover, while seismic velocity is almost insensitive to saturations lower than 10%, electric conductivity becomes dramatically reduced by CO_2 invasion and its reduction is proportional to saturation. Geoelectrical methods should therefore be particularly useful with respect accounting, verification and safety assessment.

Geochemistry is required at several levels. The thermodynamics of CO_2 dissolution is essentially well known. However, the response of the storage and seal formations to the massive injection of pure or impure CO_2 and the flow of acidified brine still demands further investigations. Thus, the patterns of mineral dissolution are complex and strongly coupled to fluid flow. The ratio between injection flux and dissolution/precipitation will be capital to determine the evolution of porosity-permeability relationships: Caverns near the well or channels progressing through the rock (i.e. wormholes). The nature and extent of $scCO_2$ or CO_2-bearing fluid/rock interactions is an important concern when considering injectivity, containment and long-term safety of geological storage systems. Siliceous detritic formations are not expected to react massively with the injectate but the presence of lesser amounts of reactive minerals may play a significant role in their performance as geological storage. In fact, there is a wide body of

evidence showing that coupled chemo-mechanical processes associated to CO_2 injection in sandstone reservoirs can trigger deleterious effects in the transport properties of the storage system. Among them, worth mentioning are the compaction of the rock grain skeleton induced by the dissolution/collapse of cement phases, the migration of fines or mineral scaling. Finally, critical in the safety assessment of the reservoir system and its short to mid-term performance is the behaviour of cementitious phases.

A better understanding of the mechanical behaviour of the system is also required, provided that it controls the flow rates of CO_2 that can be actually injected in a reservoir. Injection will produce large increases in fluid pressures, what may compromise the mechanical stability of the system (Figure 2- 1). Strain and/or rock failure as well as fracture re-openings may free escape routes for buoyant CO_2 and/or favour destabilizing dissolution processes. The rheological behaviour of caprocks under the high stresses likely to occur at storage sites is not sufficiently understood to assess what will happen. Still, seismic observations should provide information about localization of brittle strain, thus improving mechanical characterization.

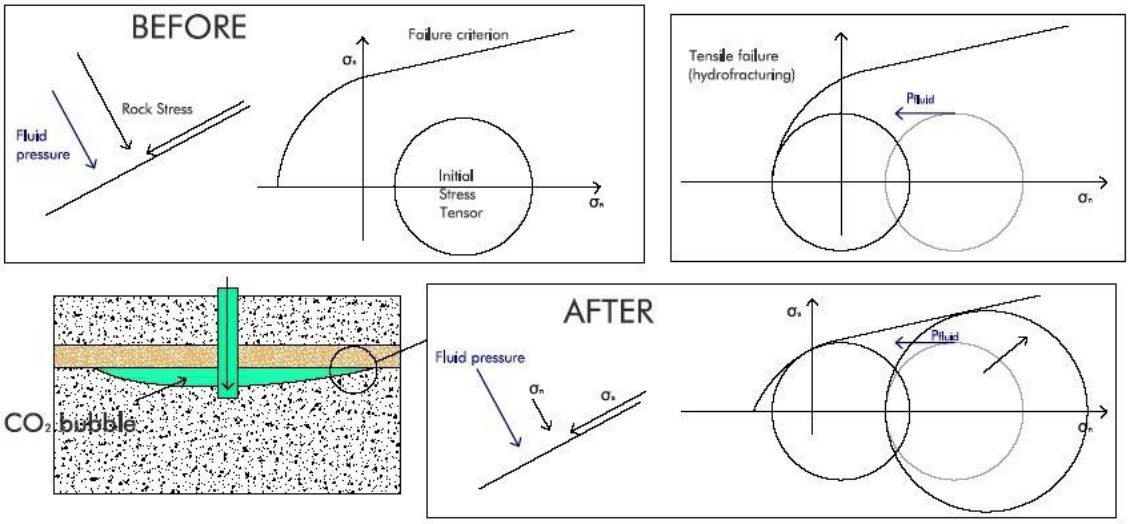

Figure 2- 1.Overpressure of fluid phases, caused by CO_2 injection, will reduce effective normal stresses and may compromise stability and/or sealing capacity of the caprock. Notice that failure mode (and hydraulic and geochemical feedbacks) is sensitive to both the initial stress tensor and to the rock strength. Source: The ISAAC Consortium.

2.3 Addressing Challenges

Challenging as some of the previous questions are, the main difficulties arise from their strongly coupled nature.

Probably, the first issue to try to understand is the behaviour of the host rock in front of the massive invasion of $scCO_2$ and the generation of acidified brine. A key question would be how dissolution and precipitation processes affect the hydraulic and mechanical properties of the host rock. The proposed host rocks are commonly carbonates and sandstones. To this respect, it is widely accepted the higher reactivity of carbonate rocks when submitted to the influence of acidic fluids, although more research is needed with respect the processes

governing the particular circumstances by which general or concentrated (i.e. wormholes) dissolution will take place in a carbonate rock. Therefore, the development of sound porosity/permeability relationships (known as poroperm) constitutes a major endeavour in carbonate systems. Similarly, poroperm relationships are not as straightforward at first glance in sandstones as it might appear. These rocks, although typically less reactive, are prone to large hydrodynamic changes associated to fines migration, fluid/clay mineral interactions and dissolution phenomena when this is concentrated in pore throats. None of the previous processes occur in a reservoir in the absence of stresses so that the hydro-chemo-mechanical couplings must be concomitant to the development of the explanatory paradigm.

The second frontier issue is to ensure the performance and chemical stability of the caprock, particularly when fissures or cracks are present. Recent works made with mudstones gives contradictory results. On one side, porosity increases progressively from the fracture wall towards the bulk rock as minerals dissolve, but the permeability of the matrix is not significantly affected because clay particles would form a continuous framework (Andreani et al. 2009). In contrast slow modification of the clay framework cohesion during the percolation of pulses of supercritical and enriched brine through a fracture in a marlstone (65% calcite) has also been observed (Noiriel et al. 2007).

This process produces a rearrangement of clay particles in the fracture gap and a progressive reduction in permeability.

Focusing our interest in reservoir rocks, it is worth to mention a number of recent scientific papers where different authors have addressed some of the coupled processes mentioned so far.

Kieffer et al. (1999) and Colón et al. (2004) have evaluated the reactive surface areas of Fontainebleau sandstone as a function of porosity, permeability, and bulk fluid flow rate at 80°C and far from equilibrium conditions using a solution with initial pH of 10.4. They observed a continuous permeability increment, independent of the increase of surface area (which is linked to mineral dissolution) probably due to the widening of connecting pore channels in pore throat locations in response to increasing pore fluid pressure. In their experiments the authors used loose sand grains (~200-250 mm diameter) introduced in a confining pressure jacket.

Heiland (2003) provides an excellent review of the published literature on laboratory testing of the stress dependence of rock-permeability.

Noiriel et al. (2005) have performed reactive flow-through experiments by injecting CO_2-saturated water (0.1 MPa) at room temperature in a porous limestone in order to identify the relationships between fluid chemistry, hydrodynamics and structural properties. Periodic imaging by X-ray microtomography allowed them

to observe the evolution of the micro-geometry of the core and fluid-rock interface in detail while its porosity and permeability increased due to dissolution. They identified several mechanisms involved in the rapid permeability increase observed. Early in the experiment, the permeability increase was related to concomitant particle dissolution and displacement while later on, permeability continued to rise due to solid-fluid interface smoothing and to pore connectivity increase. In their tests they employed a rock plug of 21 mm length and 9 mm diameter.

Le Guen et al. (2007) published an interesting study reporting several month-lasting experiments where low and high P_{CO2} (8 MPa) aqueous fluids where injected through rock samples (sandstone and limestone) under triaxial conditions with monitoring axial (25 MPa) and confining stresses (13 MPa), temperature (150 °C), pore pressure (13 MPa) and the composition of the fluid. The high P_{CO2} fluids induced an increase in strain rates of the limestones by up to a factor of 5, compared to the low P_{CO2} fluids. Injection of high P_{CO2} fluids into the sandstone resulted in deformation rates one order of magnitude smaller than for limestones. The creep-accelerating effect of high P_{CO2} fluids with respect to the limestones was mainly due to the acidification of the injected fluids, resulting in a significant increase in solubility and reaction kinetics of calcite. Compared to the limestones, the much weaker response of the sandstone was due to the much

lower solubility and reactivity of quartz in high P_{CO2} fluids. In their study they used cylindrical rock plugs of 48 mm length and 23 mm diameter.

Izgec et al. (2008) have conducted detailed combined X-ray tomography characterization with laboratory experiments at low pressure (P_{conf}=3 MPa) and temperatures ranging from 18 to 50 °C addressed to analyse permeability and porosity changes as well as relevant chemical reactions associated with the injection of CO_2 in homogeneous or vuggy carbonate formations. Their results show that either a permeability increase or decrease might be obtained depending on the properties of the studied rock, with particular emphasis in pore characteristics and distribution, brine composition and the physico-chemical conditions of the interaction. In their study they used epoxy coated core plugs of 107 mm long and 47.2 mm diameter (vertical arrangement) and 70 mm long and 38.1 mm diameter (horizontal arrangement).

Milsch et al. (2008) have investigated the relationship between hydraulic and electrical transport properties in sandstone-type rocks by measuring the pressure dependence of permeability and electrical conductivity. Their experiments were performed at a confining pressure of 50 MPa, pore pressure equal to 45 MPa and at a constant temperature of 40 °C. The fluid employed was a 0.1 m NaCl-brine. They conclude that none of the theoretical frameworks considered in their

study useful to relate these permeability and electric conductivity (equivalent channel concept, statistics and percolation, and interpretation of Hg porosimetry data) could adequately reproduce the respective transport property within experimental error margins. Conversely, they show that purely empirical permeability-conductivity relationships can always be adjusted to provide a reasonable description of the coupled k-σ dependence on effective pressure. The specimens used were cylindrical in shape having a length of ~ 40 mm and 30 mm diameter.

Wigand et al. (2008) have developed a long-lasting experiment (~1500 h) under situ conditions equivalent to that of a reservoir at 1500-2000 m depth (P_{conf} = 30 MPa; P_F = 15 MPa; T = 60 °C) focusing on the geochemical interactions between $scCO_2$, a red sandstone (representative of the Ketzin reservoir) and brine (1 m NaCl). The geochemical results of the experiment were modelled with PHREEQC. The core plug employed has 100 mm length and 50 mm diameter.

Luquot and Gouze (2009) have performed a series of reactive flow-through experiments with carbonated reservoir samples at 100 °C, 12 MPa confining pressure and a P_{CO2} ranging from 0.7 to 10 MPa. According to the authors, these conditions mimic mass transfers occurring near the injection well (where the brine is almost saturated with CO_2) and at increasing distances from it (where the fluid is less saturated with CO_2 and holds higher divalent cation concentrations

due rock dissolution along the fluid pathway). They conclude that all their dissolution experiments display power scaling between permeability and porosity with distinctly different scaling exponents characterizing the reactivity of the fluid percolating the sample, independently from the decrease with time of the reactive surface area. They show also that dissolution at moderate positive values of the Damkhöler number is efficient to increase permeability and promote a rapid spreading of the reaction front, while inducing minimal modification of the porosity in the vicinity of the CO_2 injection well. The cylindrical core plug used in the experiments had 18 mm length and 9 mm diameter.

Noiriel et al. (2009) have studied the dynamics of porosity and reactive surface area changes during porous limestone dissolution by CO_2-rich water at ~20 °C and low pressure. By observing key chemical elements relevant in the identification of a dissolution source (either sparite or micrite calcite crystals) the authors conclude that the reactive surface area changes in the micrite obeys to a parabolic law while in the case of sparite that increases at a much higher rate. They employed a silicon-jacketed cylindrical 15 mm length and 9 mm diameter porous rock plug.

Perrin and Benson (2010) present the results of CO_2/brine two-phase flow experiments in rocks at reservoir conditions (63 °C, 12.4 MPa). X-ray CT scanning was used to determine CO_2 saturation at a fine scale with a resolution of a few pore volumes and provide 3D porosity

and saturation maps that can be potentially used to correlate CO_2 saturations and rock properties. The study highlights the strong influence of sub-core scale heterogeneities on the spatial distribution of CO_2 at steady state and provides useful relative permeability data on a sample originated from the CO_2CRC-Otway project (Victoria, South-West Australia). The core plug employed had 83 mm length and 50.8 mm diameter.

Hangx et al. (2010) have performed uniaxial compaction experiments on granular aggregates of quartz and feldspar under both wet and dry conditions while changing grain size (25-75 mm), temperature ($20 \leq T \leq 100$ °C), P_{CO2} ($\sim 4 \times 10-5 \leq P_{CO2} \leq 10$ MPa), and effective stress ($20 \leq \sigma_{eff} \leq 100$ MPa) in order to determine their individual effect. Pore fluid pH was varied by the injection of CO_2 and by addition of acidic and alkaline additives. Wet samples showed instantaneous compaction upon application of load followed by a time-dependent creep. From the mechanical data and microstructures the authors concluded that the main compaction mechanism was inferred to be chemically enhanced microcracking in both quartz and feldspar, with subcritical crack growth (i.e., stress corrosion cracking) controlling deformation in the creep stage. The injection of CO_2 and the concomitant acidification of the pore fluid inhibited microcracking in both the quartz and feldspar samples. According to that, these authors infer that the injection of CO_2 into quartz- and plagioclase-bearing

sandstones will inhibit grain scale microcracking process and related geomechanical effects, such as reservoir compaction and surface subsidence, will be negligible compared with the poroelastic response. They employed loose quartz sand samples introduced in a sleeve of 20 mm diameter.

Xie et al. (2011) have investigated the chemical degradation effects on mechanical behaviour of a porous limestone. Hydrostatic and triaxial compression tests were performed (up to 60 MPa) over sound and chemically degraded samples (immersion in a 6 mol/L NH_4NO_3 solution for about one year) and the authors found that the chemical degradation induces the diminution of pore collapse limit stress, elastic modulus and material cohesion. The chemical degradation enhances the time-dependent deformation and can generate significant increase in permeability through the formation of wormhole networks. The laboratory tests were performed on cylindrical samples with 75 mm length and 37.5 mm diameter.

Gouze and Luquot (2011) have investigated the links between the dissolution mechanisms that control the porosity changes and the related changes of the reactive surface area and permeability combining flow-thru (using a brine-CO_2 fluid) experiments and X-ray microtomography. They show that shown that the increase of permeability observed is due to the decrease of the tortuosity for homogeneous dissolution, whereas it is due to the combination of tortuosity decrease and hydraulic radius increase for heterogeneous

dissolution. The cylindrical core plug used in the experiments had 18 mm length and 9 mm diameter.

Peysson et al. (2011) have experimentally investigated the alteration of permeability induced by drying of brine in porous media for different rocks and different brines in the context is the strong water desaturation expected in the vicinity of a wellbore due to CO_2 injection. The core plugs used had 93 mm length and 23 mm diameter.

Kummerow and Spangenberg (2011) have evaluated the impact of impure CO_2 on a possible CO_2 repository at a confining pressure of 15 MPa, 40 °C and a pore pressure of 7.5 MPa. In their work, during long-term exposure experiments with pure CO_2 no significant changes in the petrophysical properties (electrical resistivity, elastic wave velocity, and permeability) of the studied sample were observed. However, for the injection of SO_2-bearing CO_2 (1 vol %) these authors have observed significant and irreversible changes of all monitored physical parameters: First, a decrease of P wave velocity and an increase of electrical resistivity that points towards the dissolution of some components of the mineral skeleton. Second, a decrease in permeability suggesting the mobilization and redistribution of fines. The sample used in their tests was cylindrical and with 49.45 mm length and 47.6 mm diameter.

Newell and Carey (2012) have performed an interesting multiphase ($scCO_2$-brine) core flooding experiments that simulate a

leakage pathway along the cement/rock interface. They have constructed a composite core representative of an oil-well cement and siltstone separated by a simulated damage zone (defect) containing ground cement and siltstone was flooded with brine + $scCO_2$ at 10 MPa and 60 °C parallel to the defect. CO_2 injection resulted in a pH drop and carbonate-undersaturated conditions in the brine while a 5 mm thick carbonation front appeared extending into the cement, parallel to the damage zone without apparent dimensional changes. Cement carbonation does not appear to explain the permeability drop observed which is attributed by these authors to the migration and re-precipitation of alteration products derived from cement within the defect. The fabricated core plug used in the experiment had 51 mm length and 25.4 mm diameter.

Luquot et al. (2012) have investigated a chlorite/zeolite-rich sandstone from the Otway Basin (Australia) via a flow-through experiment setup to reproduce in situ temperature (95 °C) and confining pressure conditions (10 MPa) using a CO_2-saturated brine (6 MPa). They observe that, while porosity increases, permeability decreases by about one order of magnitude due to the precipitation of the kaolinite in the main flow paths. This explanation was also invoked by other authors (Shiraki and Dunn 2000) to explain the same phenomena in a different sandstone and different experimental conditions (P_{conf}=26.6 MPa, P_{pore}=16.6 MPa, T=80 °C). For these authors, the high reactivity of the studied sandstone makes this

reservoir a valuable target for CO_2 mineralization although its hydrodynamic behaviour may limit the injection rate and the spreading of the CO_2. The cylindrical core plugs used in the experiments had 18 mm length and 9 mm diameter.

The previous literature review, although non exhaustive, provides a valuable perspective about the state of the art concerning research on coupled processes (geochemistry, hydrodynamics, mechanics, geophysics) with different reservoir rock- types (sandstone, limestone, vuggy carbonates) or wellbore cements for temperatures and pressures relevant for CO_2 geosequestration and EOR projects. We observe a significant deal of effort considering chemo-hydrodynamic and mechanic-hydrodynamic couplings. In some of these studies some geophysical tools (sonic waves, electrical resistivity) are employed as a tool to better understand the chemical or mechanical processes triggering changes in the transport properties of the experimental materials. Many of them take advantage of microtomography for a better description of the results or even to track the evolution of the experimental materials as a function of time. It is also worth to mention that many of the most comprehensive studies have employed small size-samples, what limits the representativeness of the experimental results to a local scale.

Anyhow, both in the case of the reservoir or caprock systems the processes triggered by CO_2 flooding must be addressed from a

multidisciplinary approach and, although some technological issues still deserve especial attention, our present day experimental capabilities grant to tackle these multifaceted systems. This thesis represents a step forward in this line of work.

2.4 References

Andreani M, Luquot L, Gouze P, Godard M, Hoisé E, Gibert B. Experimental Study of Carbon Sequestration Reactions Controlled by the Percolation of CO_2-Rich Brine through Peridotites. Environ Sci Technol. 2009;43(4):1226–31.

Bachu S. Sequestration of CO_2 in geological media in response to climate change: road map for site selection using the transform of the geological space into the CO_2 phase space. 2002;43:87–102.

Colón CFJ, Oelkers EH, Schott J. Experimental investigation of the effect of dissolution on sandstone permeability, porosity, and reactive surface area1. Geochim Cosmochim Acta. 2004 Feb 15;68(4):805–17.

Gouze P, Luquot L. X-ray microtomography characterization of porosity, permeability and reactive surface changes during dissolution. J Contam Hydrol. Elsevier; 2011;120:45–55.

Le Guen Y, Renard F, Hellmann R, Brosse E, Collombet M, Tisserand D, et al. Enhanced deformation of limestone and sandstone in the presence of high fluids. J Geophys Res Solid Earth. Wiley Online Library; 2007;112(B5).

Hangx SJT, Spiers CJ, Peach CJ. Creep of simulated reservoir sands and coupled chemical-mechanical effects of CO_2 injection. J Geophys Res. 2010 Sep 14;115(B9):B09205.

Heiland J. Laboratory testing of coupled hydro-mechanical processes during rock deformation. Hydrogeol J. Springer; 2003;11(1):122–41.

Izgec O, Demiral B, Bertin H, Akin S. CO_2 injection into saline carbonate aquifer formations I: laboratory investigation. Transp Porous Media. Springer; 2008;72(1):1–24.

Kieffer B, Jové CF, Oelkers EH, Schott J. An experimental study of the reactive surface area of the Fontainebleau sandstone as a function of porosity, permeability, and fluid flow rate. Geochim Cosmochim Acta. 1999 Nov;63(21):3525–34.

Kummerow J, Spangenberg E. Experimental evaluation of the impact of the interactions of CO_2-SO_2, brine, and reservoir rock on petrophysical properties: A case study from the Ketzin test site, Germany. Geochemistry, Geophys Geosystems. Wiley Online Library; 2011;12(5).

Luquot L, Andreani M, Gouze P, Camps P. CO_2 percolation experiment through chlorite/zeolite-rich sandstone (Pretty Hill Formation – Otway Basin–Australia). Chem Geol. 2012;294–295:75–88.

Luquot L, Gouze P. Experimental determination of porosity and permeability changes induced by injection of CO_2 into carbonate rocks. Chem Geol. Elsevier; 2009;265(1):148–59.

Milsch H, Blöcher G, Engelmann S. The relationship between hydraulic and electrical transport properties in sandstones: An experimental evaluation of several scaling models. Earth Planet Sci Lett. Elsevier; 2008;275(3):355–63.

Newell DL, Carey JW. Experimental evaluation of wellbore integrity along the cement-rock boundary. Environ Sci Technol. ACS Publications; 2012;47(1):276–82.

Noiriel C, Bernard D, Gouze P, Thibault X. Hydraulic properties and microgeometry evolution accompanying limestone dissolution by acidic water. Oil gas Sci Technol. IFP; 2005;60(1):177–92.

Noiriel C, Gouze P, Madé B. Time-resolved 3D characterisation of flow and dissolution patterns in a single rough-walled fracture. In: Jir'i Krásný (Editor) JMS (Editor), editor. Groundw Fract rocks [Internet]. Taylor & Francis; 2007. p. 629–42.

Noiriel C, Luquot L, Madé B, Raimbault L, Gouze P, Van Der Lee J. Changes in reactive surface area during limestone dissolution: An experimental and modelling study. Chem Geol. Elsevier; 2009;265(1):160–70.

Perrin J-C, Benson S. An experimental study on the influence of sub-core scale heterogeneities on CO_2 distribution in reservoir rocks. Transp porous media. Springer; 2010;82(1):93–109.

Peysson Y, Bazin B, Magnier C, Kohler E, Youssef S. Permeability alteration due to salt precipitation driven by drying in the context of CO_2 injection. Energy Procedia. Elsevier; 2011;4:4387–94.

Pruess K, Garcia J. Multiphase flow dynamics during CO_2 disposal into saline aquifers. Environ Geol. Springer; 2002;42(2-3):282–95.

Shiraki R, Dunn TL. Experimental study on water–rock interactions during CO_2 flooding in the Tensleep Formation, Wyoming, USA. Appl Geochemistry. Elsevier; 2000;15(3):265–79.

Wigand M, Carey JW, Schütt H, Spangenberg E, Erzinger J. Geochemical effects of CO_2 sequestration in sandstones under simulated in situ conditions of deep saline aquifers. Appl Geochemistry. Elsevier; 2008;23(9):2735–45.

Xie SY, Shao JF, Xu WY. Influences of chemical degradation on mechanical behaviour of a limestone. Int J Rock Mech Min Sci. Elsevier; 2011;48(5):741–7.

CHAPTER 3. SAMPLES PREPARATION AND EXPERIMENTAL RIG DESIGN

3.1 Equipment sample preparation and testing

Characteristics of the equipment routinely used at the UDC laboratory are described in this chapter. The preparations of the rock samples as well as the setting up of the experimental device used to conduct the experiments described in the following chapters are also addressed.

3.1.1 Sample Preparation and Conditioning Equipment

Core and outcrop samples used in this research had different degrees of consistency preservation: in some cases, it was necessary to perform pre-conditioning operations in order to execute the tests. Rock cutting was performed with the aid of a CARAT P-3508 circular diamond saw blade (Figure 3- 1). This cutter guaranteed reasonably flat surfaces to provide a stable base for drilling operations.

Figure 3- 1. Sawing of vuggy limestone//Sawing of rock sample prior to core plug drilling.

Core plugs were cut with the aid of a Weka 32 drill associated with a DM 350 BC mast. The drill mast was firmly anchored to a heavy granite block (Figure 3- 2) to ensure stability during drilling operations, which is a critical element in the preparation of usable plug specimens that comply with the ISRM recommendations. In order to fix the rock to be drilled, a steel frame plus wood blocks proved successful in avoiding vibrations that could damage the drilled plugs. This provides a good cylindrical shape for the sample. Contrastingly, a more rigid system using steel fixings would transmit more vibration that would degrade the quality of the plug.

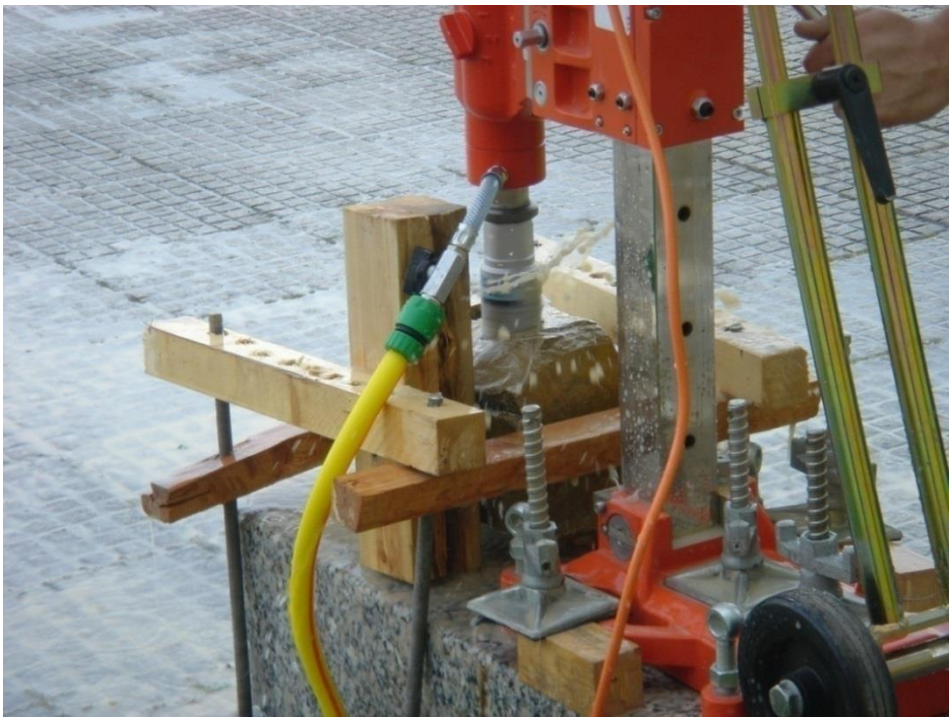

Figure 3- 2. Drill mast anchored to a heavy granite block. Wood blocks alleviate vibrations into the specimens.

Drilled plugs must be at high cilindricity with low roughness (i.e. perfect flat and parallel ends). However, top and bottom surfaces (perpendicular to the lateral face) had to be trimmed and grinded with the aid of S.A.E. Ibertest Ref. 210-103786 equipment (Figure 3- 3). This equipment allows the simultaneous grinding of several samples with different diameter while controlling variables like grinding speed, time, rate of advancement and flow of cooling fluid. Under normal conditions, grinding is finished within a few minutes. The grinding machine complies with the requirements of the UNE-EN 12390-1 for planarity.

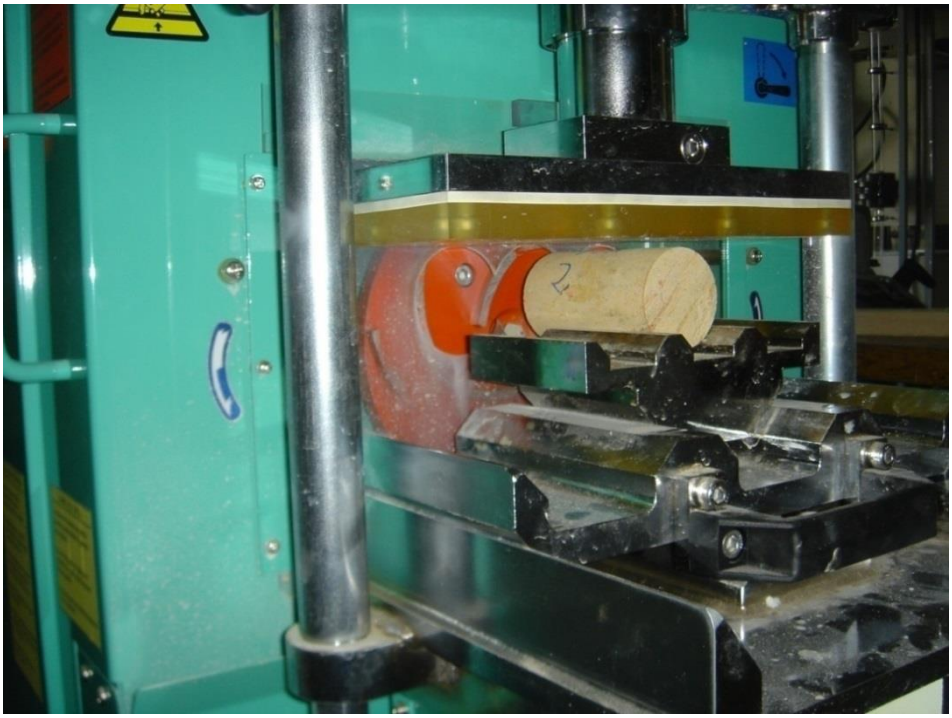

Figure 3- 3. Trimming and grinding machine used to ensure perfect cylindrical cut and parallel top and base surfaces of the core plugs.

The verification of the dimensional compliance of the specimens label was performed according to the standard (ASTM 4543) which sets that include:

- Slenderness (length: diameter ratio) should be between 2 and 2.5.
- It is desirable that the diameter of the cylinder is at least 10 times greater than the grain size of the rock. Accordingly, the studied rocks should have a diameter of 38 mm.
- Irregularities along the generatrix must not exceed 0.5 mm according to the procedures set forth below.

- Cylinder faces should be perpendicular to the generatrix of the cylinder and therefore mutually parallel. The tolerance limit is set to 25 μm.
- Each generatrix profile should not have a deviation over 25 μm on the best fit by a straight line (flatness condition).
- The maximum angular difference between one side and the opposite cylinder should not be greater than 0.25°, for frames with fulcrum in the actuator, and 0.13° for those that don´t have (condition of parallelism).

The last parameter that is needed for measuring the samples is the perpendicularity between faces and the axis of the specimen, and should comply with the equation:

$$\frac{\Delta i}{d} \leq \frac{1}{230} = 0.0043$$

In which Δ is the expression of a difference between the lowest and highest sided point located on one face.

The equipment developed for dimensional verification is illustrated in Figure 3- 4. It has the following elements:

1. A granite base of 400 x 400 mm, certified to have a flat surface where it can be achieve a certificate error flatness of 2.9 μm

according to UNE 82309/97 measured with electronic level and also with certificate of traceability ENAC 91710.

2. A granite base (150 x 120 x 50 mm) with articulated arm and clip for holding the electronic digital gauge.
3. A digital Mitutoyo Digimatic IDC 543-260b IP42 gauge, with data output cable, USB to COM adapter and foot switch pedal.

Several measurements are required and a pedal drive which transfers the data was placed to facilitate and speed the task.

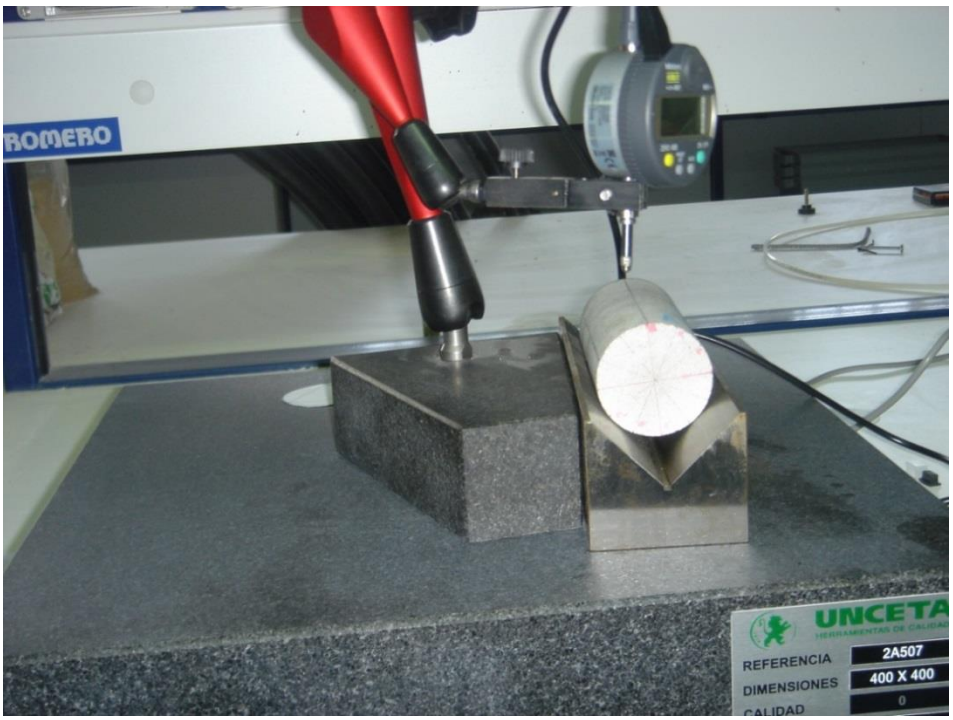

Figure 3- 4. Flatness table and elements associated with the dimensional verification of core plugs.

3.2 Experimental rig design

Most of the tests have been performed by applying differential stresses. Different confining pressure and axial load and isotropic conditions (σ_V/σ_H = 0.7 to 1). Therefore, a sample holder capable of withstanding the confining conditions set was used in conjunction with a loading frame and an axial actuator. All of these parts were the mechanisms through which the loads were transmitted. Furthermore, the pore pressure control has been effectuated by a system of dedicated pumps. A brief description of each element of the assay is followed below.

3.2.1 Loading frame

The axial force is transmitted to the tested specimens via a self-supporting steel frame has been used (Rogen US-243). The frame, with 30 tons load capacity, was equipped in origin with a manual hoist to change quickly and easily, the distance to the work bench (Figure 3- 5). The frame was coupled to a servo-controlled GDS-ADVDPC screw pump. It was placed on the system in order to replace the manual pump and with the purpose of a continuous control in pressure during the experiments.

Figure 3- 5. The UWV testing system configured for face-to-face velocity calibration at University of Coruña.

3.2.2 Core holder

A standard Hoek-Franklin cell (Hoek and Franklin 1967) manufactured by PROETI S.A. was chosen as workhorse core holder. The prescribed conditions for these tests involve a different magnitude for axial and confining pressures. This core holder has an effective sample diameter of 1.5" (38.1 mm; Figure 3- 6). It fits well with the supplement shrinkable material mentioned above.

A Hoek-Franklin cell is a hollow steel cylinder with two circular perforated caps. The diameter of the hole is slightly greater than the nominal diameter of the core to be tested. Two hardened steel cylinders pass through these end caps, and their role is to transmit the

axial load chosen. A hydraulic fluid is introduced into the steel cylinder, which is pressurized by pumps until reaching confining conditions. Both selected axial load and confining pressure are chosen to mimic reservoir depth and temperature condition. In order to avoid interaction of the hydraulic fluid, which is responsible for applying the confining pressure, and the cylinder itself, the cell has an inner sleeve made of flexible polyurethane, with dimensions adapted to the geometry of the cell and core plug employed. This sleeve was originally designed to prevent loss of fluid.

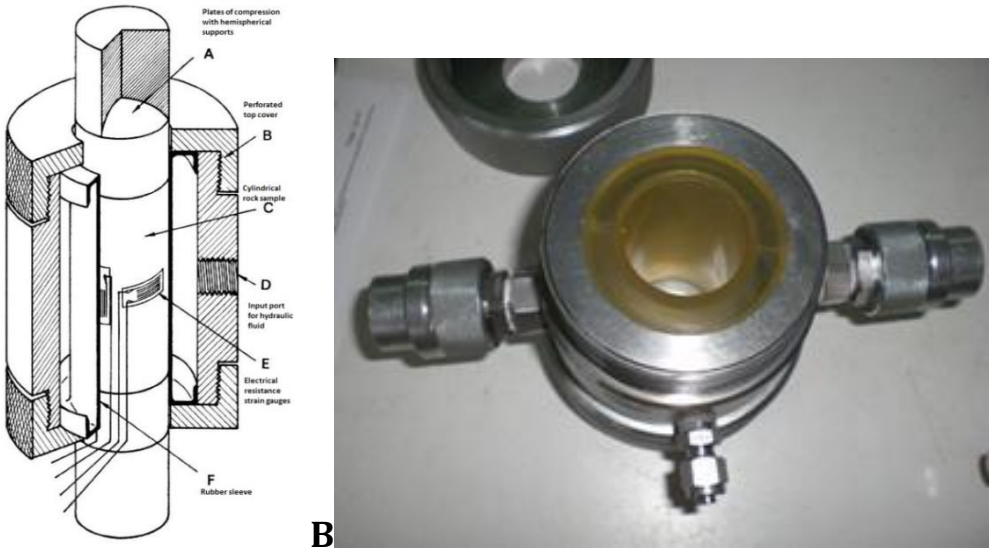

Figure 3- 6. A: Schematic of a Hoek-Franklin cell. B: Dismantled core holder.

The core holders used in this study have been modified to allow injection of fluid associated with a variable pore pressure through the load transmitting plates. Specifically, a stainless steel cylinder coupled with a pair of compression platens manufactured by ERGOTECH, were

used in this study. These platens are equipped with a system that measures the velocity of propagation of ultrasonic waves V_P, V_{S1}, and V_{S2}. The cylinders are longitudinally pierced by holes which, upon reaching the contact surface with the core plug, become grooves for proper distribution of fluid on the base and top of the specimen.

The cell is equipped with an aluminum heating jacket, which is connected to a temperature controller that receives the feedback of a PT100 temperature sensor, installed through the external wall of the cell.

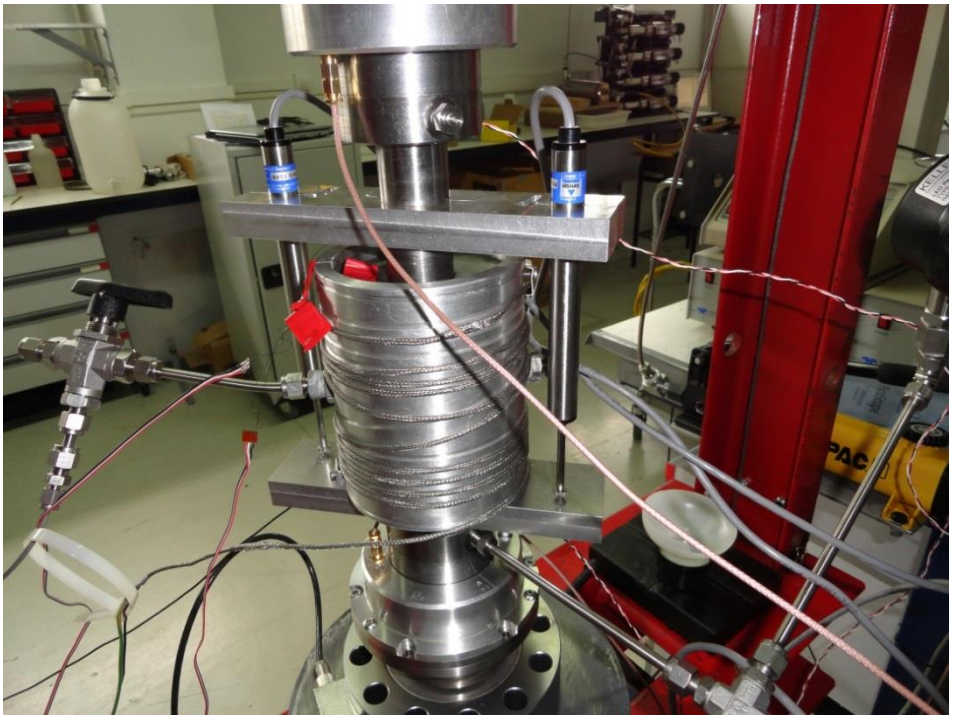

Figure 3- 7. Modified Hoek-Franklin cell with temperature control and axial strain monitoring.

3.2.3 Axial strain measurement

In some of the experiments reported, axial strain was recorded. That was possible with the aid of two-averaged Linear Displacement Transducers (Vishay LDT HS50). To separate the true sample strain from the deflection of the whole system, a series of sample-less calibration tests were performed in the load frame as well as the corresponding accessories, including load cell, spacers, platens, etc. The elastic response of the frame was evaluated by our LDT till the working limit of the complete system (30 ton) was reached. The sensors used illustrated in Figure 3- 7. Modified Hoek-Franklin cell with temperature control and axial strain monitoring is illustrated in Figure 3- 7.

3.2.4 Modified platens for load application

In order to make possible the determinations of permeability, pore pressure conditions need to be monitored. That required a modification of the load platens in order to make possible the transfer of fluid through them. The ultrasonic platens used have been manufactured by ERGOTECH (Figure 3- 8 and Figure 3- 9). These platens bear three stacked piezoelectric transducers (PZT) able to generate or receive ultrasonic pulses of compression (P) and shear waves (S_1, S_2), the latter two orthogonally polarized. The nominal resonant frequency of the PZT crystals is 1.3 MHz. A wave generator manufactured by the same company is used for creating quadratic

pulses. In order to record the arrival times of the waves a digital oscilloscope, PicoScope 3000 was used.

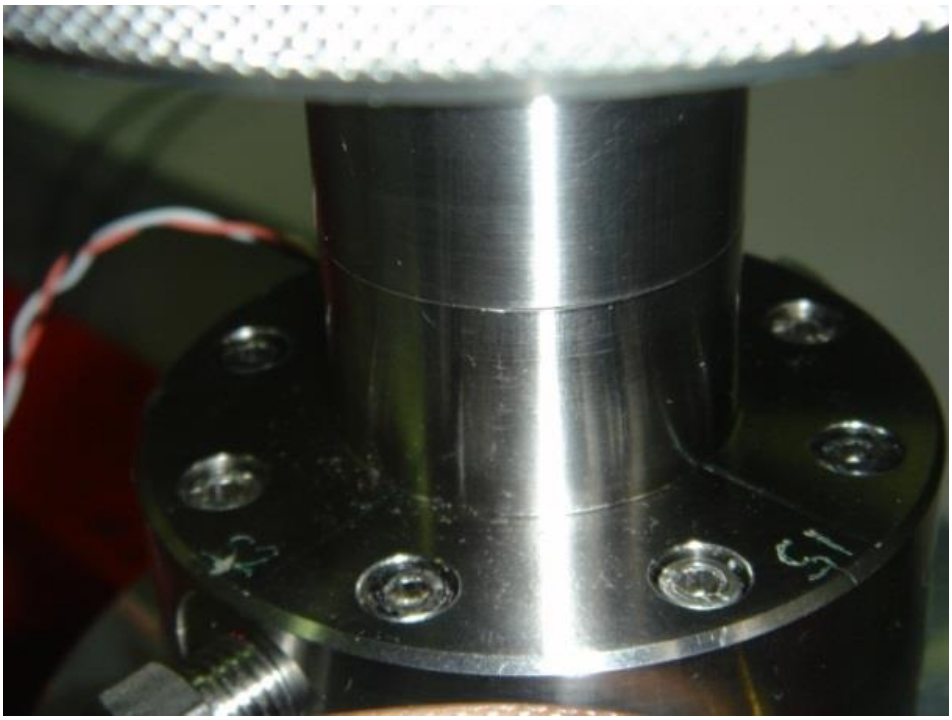

Figure 3- 8. Compression platen developed by Ergotech. Piezoelectric crystals are inside the plate for V_p and V_s measurements.

In the laboratory there are also alternate sets of compression platens with different diameter, all made of stainless steel AISI 316, which are also prepared for injection of different pore fluids. In this case, the contact surface between the piston and the cylinder is flat and grooved, with a geometric pattern which facilitates fluid distribution regularly along its entire surface. The shape of the opposite end of the cylinder bearing surface is a hemispher intended to facilitate the transmission of loads from the hydraulic actuator and correct small errors in alignment.

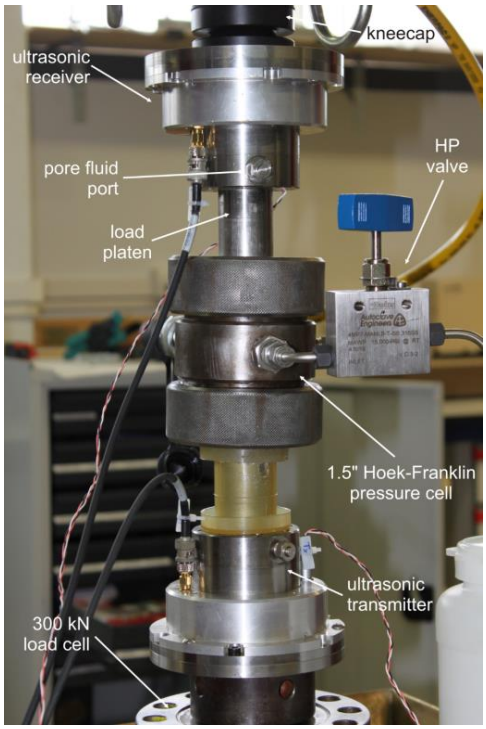

Figure 3- 9. General view of the UWV testing system configured for face-to-face velocity calibration.

3.2.5 Confining and Axial Pressure

In order to conduct the UWV tests under high-pressure and isotropically loaded conditions, we used the modified Hoek-Franklin-type triaxial cell described. Confining pressure and axial pressures are provided with a dual syringe pump Hastings-Teledyne ISCO 260 HP (V_{stroke}=100 mL; P_{max}=69 MPa; flow from 0.001 to 60 mL/min; precision 0.5%; highest volume resolution 9.6 nL). Axial load control was improved by cross-calibrating a dedicated 300 kN load cell (AEP Transducers TC4) with the output of the internal pressure transducers

of the ISCO pump. This calibration is illustrated in Figure 3- 10 and Figure 3- 12.

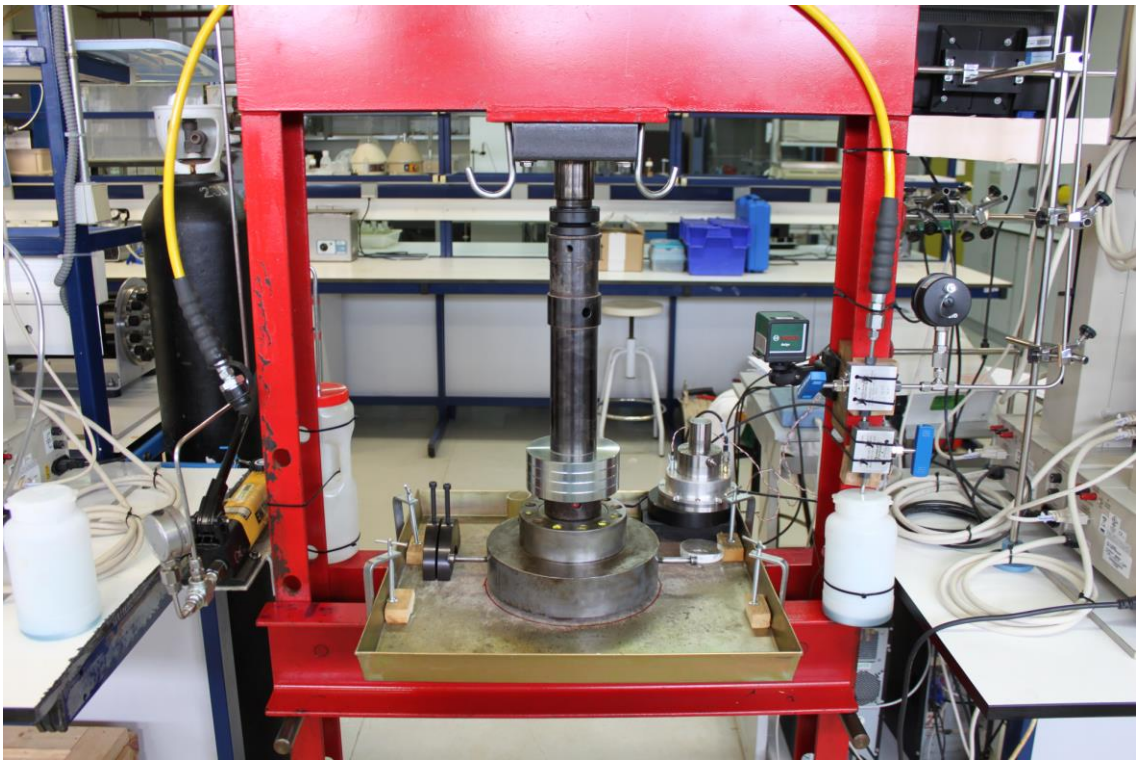

Figure 3- 10. Cross-calibration of the 300 kN load cell.

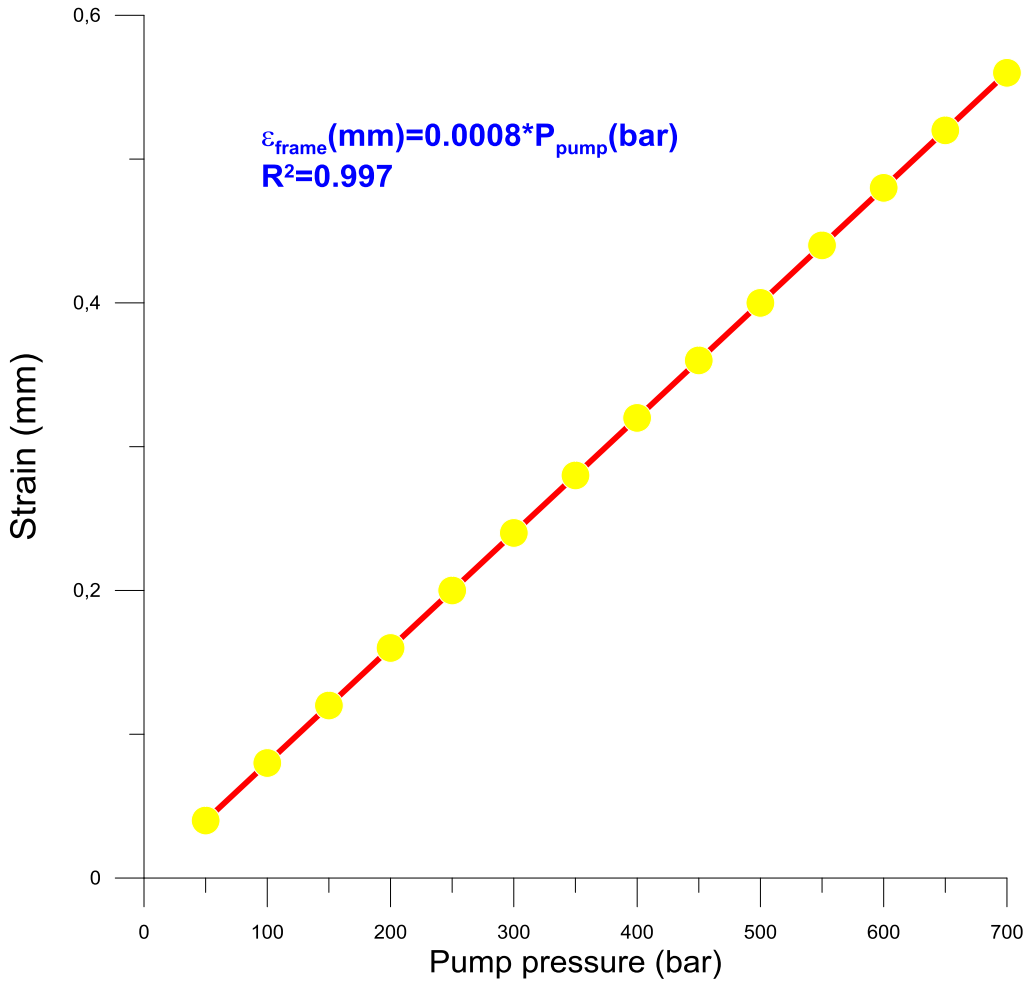

Figure 3- 11. Calibration of the frame and platens deformation with the pump pressure.

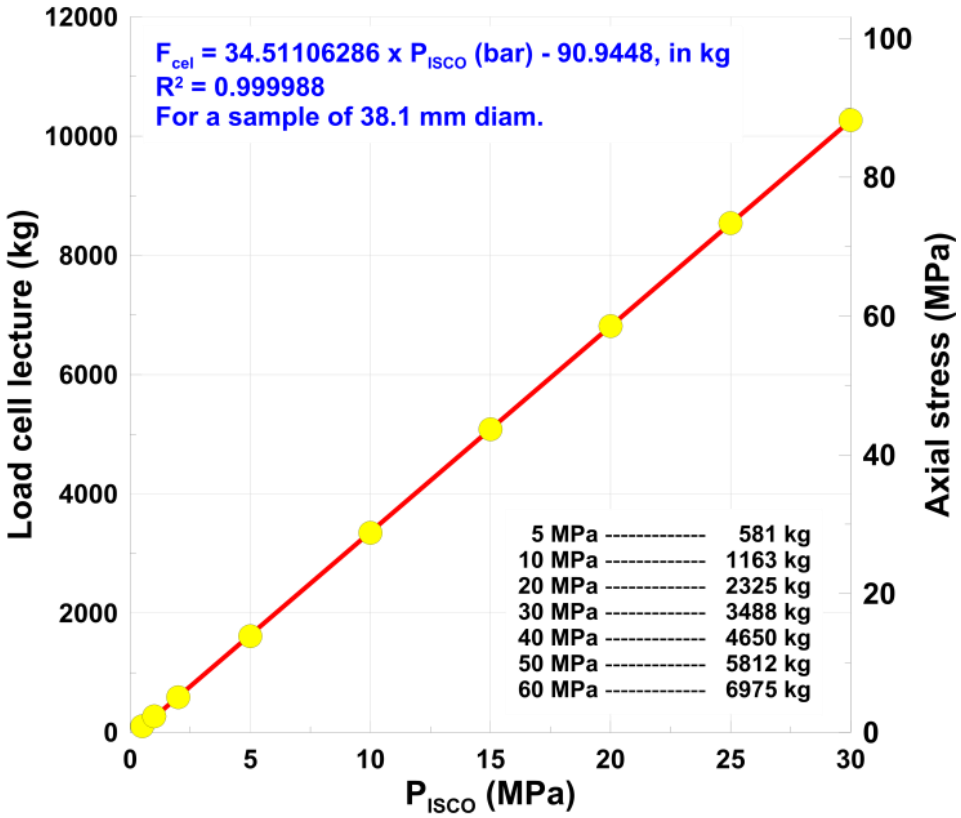

Figure 3- 12. Cross-calibration of the load cell with the values recorded with the internal pressure transducers of the ISCO pump. This is for a 38.1 mm sample.

A double check of the main parameters was implemented. That was necessary to verify the stability of the pressures applied during the execution of the tests. Thus, the indicators were complemented with other electronic transducers for absolute pressure monitoring: Keller Series 33X, with a range of measure from 0.1 to 70 MPa between -10°C and 80°C and with an accuracy of ± 0.1% full scale.

3.2.6 Control System for Interstitial Pressure

Fluid injection through the samples was accomplished with a number of elements which are briefly described hereafter.

When a gas is injected, it is pure N_2 provided in an industrial reservoir at 200 bar pressure (Carburos Metálicos S.A.). In order to have a dynamic range of injection pressures at the outlet of the bottle a back-pressure regulator, BPR, was inserted, manufactured by Parker. The BPR model used was VeriFlo ABP1, whose diaphragm is manufactured by Hastelloy C-22 and allows pressure regulation between 0.1 and 25 MPa.

On leaving the BPR, the gas flow is directed to a directional control valve coupled with a system of two syringe pumps which are working paired. Because the fluid injected is a gas, the arrival pressure at the injection pumps must be similar to the target injection pressure. BPR performs this function efficiently, improving performance of pumps and allowing better control of the injected flow.

ISCO pumps used (ISCO 100DX, manufactured by Hastings-Teledyne; allowed uninterrupted injection of fluid to a maximum pressure of 10,000 psi (68.9 Mpa). When the two cylinders of the pump work paired (the study case) the injection is carried out continuously without pulses, which allows better control of the experiments. Pumps also have extremely sensitive digital pressure transducers, as well as a

very precise system for the measurement of the flow of the fluid (liquid or gas) injected.

ISCO pumps are connected to a PC via an RS-232. Thus, the PC acts as a data acquisition system, storing information about the volume of gas injected, the pressure and flow rate, all of that as a function of time and a writing frequency prescribed by the user. The interface between the PC and the ISCO pump is a program developed under LabVIEW (National Instruments), who also provides immediate information (on the screen) of the variables stored.

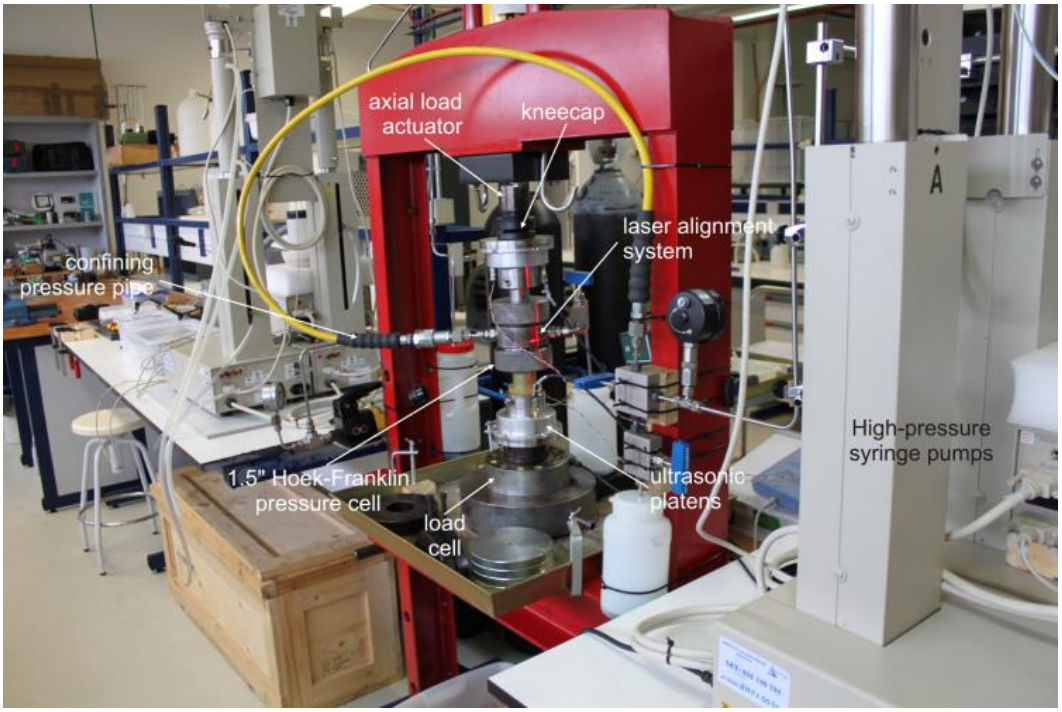

Figure 3- 13. ISCO pumps used for control of confining and pore pressure.

3.2.7 Flow Measurement

Measuring output flow through rock specimens is essential when you need to perform the necessary calculations aimed at obtaining its intrinsic permeability. The fluid used was N_2 and flow was measured using a mass flowmeter. The mass flow of gas was monitored using a device manufactured by Agilent Technologies (Figure 3- 14). This is a very precise and reliable device based on the viscosity, and it is capable of measuring different types of gas (N_2, CO_2, H_2, He, Ar, CH_4, N_2O, O_2, etc.). The detectable range of flow rates extends from 0 to 500 mL/min with an accuracy of ± 0.8% of reading and ± 0.2% full scale.

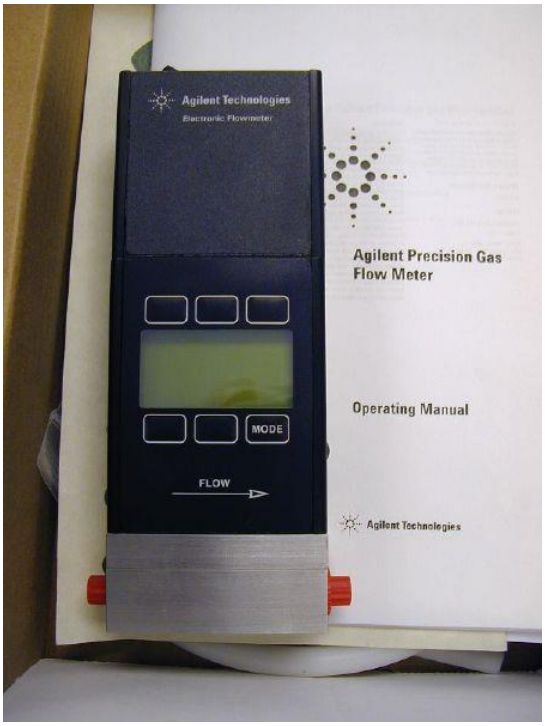

Figure 3- 14. Flowmeter AGILENT used for gas permeability determinations.

The electronic flow meter also allows communicating lectures to a computer via a serial RS-232 interface. The flowmeter reading is presented by default on a digital display. The data transferred to the computer include the values of volumetric and mass flow, temperature and absolute pressure, all versus time.

Pressure measurements made by the flowmeter are absolute, i.e., pressure 0 corresponds to the absolute vacuum. These absolute pressure values are used by the flowmeter when performing internal calculations and transform the electrical signal into a characteristic mass flow. Transforming the value of absolute pressure (P_{abs}) in a pressure relative to atmospheric ($P_{rel,1bar}$) can be performed by subtracting the measured absolute pressure and the existing atmospheric pressure (P_{atm}) at the time of measurement:

$$P_{rel,1bar}=P_{abs}-P_{atm}$$

The mass flow provided by the device Agilent are internally corrected by temperature and pressure, so they are standardized to the reference pressure and temperature of 25^0C, 0,1 MPa. This facilitates comparison between results. Device manufacturers do not recommend using the flowmeter with higher flow rates to 640 mL/min and pressures higher than 1 MPa entry.

3.2.8 Control Pressure in Injection Line

The injection pressure of N_2 through the specimens was monitored in two different ways. On one hand, we used the pressure transducers coupled to the ISCO pumps previously mentioned. Also, two high-precision pressure transducers (LEO Record (Ei) Keller-Drück) equipped with an internal data acquisition system were arranged. LEO Record devices are autonomous recorders with internal battery capable of measuring with high precision the temperature and pressure of liquids and gases for extended periods of time. The chosen model has a pressure range which goes from 0 to 70 MPa, with a measurement resolution of 0.01 MPa. Downloading data from the logger is done through specific software that communicates with the transducer / recorder via a USB type interface.

Two Leo Record transducers were placed: one to the input of the sample and the other to the output. The first one is redundant with the ISCO pumps. This transducer allows control, independently of the injection pressure, and it can detect possible malfunctions. The transducer located at the outlet of the pump allows verifying the pressure gradient between the ends of the specimen. It also warns of situations in which excess pressure, may damage the mass flowmeter aligned with it.

3.2.9 Microelectrodes for measuring pH and Conductivity

A group of electrodes, manufactured by Microelectrodes Inc., were attached to the experimental device in order to know the evolution of pH and conductivity (Figure 3- 15). These electrodes enable measurement of the specific conductivity and the pH, using a temperature sensor (PT-1000 sensor) as compensation system reading both parameters.

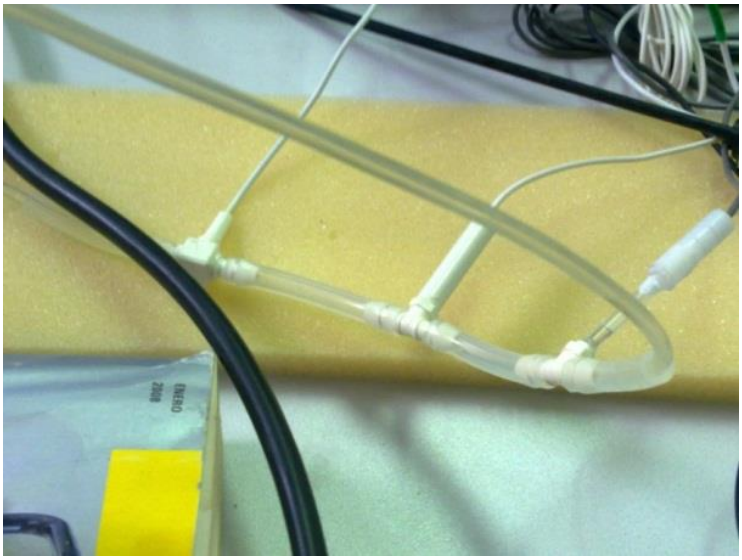

Figure 3- 15. Microelectrodes placed at the outlet line after the backpressure.

Table 3- 1 below shows the main characteristics of the microelectrodes.

deReference	Type	Cell volume (mL)	Diameter
8-900	Conductivity	0.093 mL	1/8”
16-900	Conductivity	0.093 mL	1/16”
8-705	pH	0.011 mL	1/8”
16-705	pH	0.011 mL	1/16”
8-702	Reference Ag/AgCl (KCl 3M)	0.093 mL	1/8”
16-702	ReferenceAg/AgCl (KCl 3M)	0.093 mL	1/16”

Table 3- 1. Main characteristics of the microelectrodes used in the experiments.

There are currently no systems that allow the measurement of chemical parameters under high pressure and in addition allow working with volumes as small as the one that flows through the specimens tested. Therefore, it is necessary to make a pressure adjustment to perform actions. This is especially important in the case of pH, but much less important in the case of the conductivity. In any case, pH data provided are susceptible to recalculation if the experimental conditions are known.

Throughout the experimental device is important that the electrodes are orderly placed. Thus, any fluid leakage from the reference electrode does not affect the readings of the electrodes located below in line.

An ELIT Aqualyser 9705c interface is coupled to the microelectrodes. It is used for the acquisition of data generated by

them, and it has 5 measurement channels of which three are occupied (pH, conductivity, reference) and two free (O_2, ORP). The interface also allows connecting a temperature sensor (PT100) for correcting the raw values. Aqualyser 9705c is connected to a computer through a RS-232 port and software provided by the manufacturer from which you can display and store data.

3.2.10 Ion chromatograph

For the chemical composition of the fluid used, an ion chromatograph ICS-1100 Dionex was used. Chromatograph determinations are performed through an attached conductivity cell, and it is provided with a separating column for anion analysis (AS23) and cation analysis (CS16). In general, in ion chromatography the ion concentration is determined by using a conductivity detector with electrochemical suppression. A typical ion chromatography system consists of an eluent, a high pressure pump, a sample injector, a system composed by a pre-column and a separating column, a suppression system, a conductivity cell and an acquisition system data.

Before carrying out an analysis, ion chromatography equipment must be calibrated using standard solutions. Comparing the data obtained from the sample with those obtained from standard, the sample ions can be identified and quantified. The data acquisition system (a computer with the chromatographic software) produces a chromatogram (detector signal regarding time). The software converts

each peak in the chromatogram into a concentration of anility and produces a report with the results.

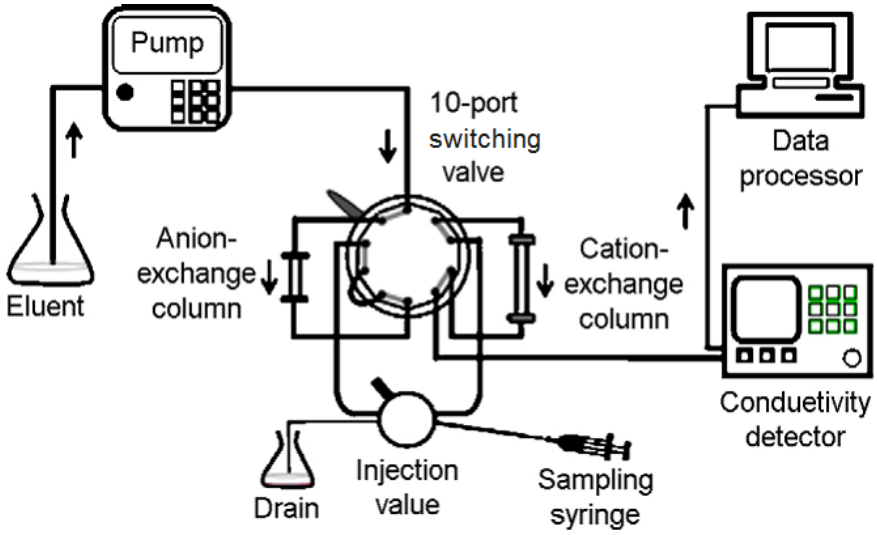

Figure 3- 16. Functional diagram of the ion chromatograph.

An ion chromatography (IC) analysis system is typically composed of 6 stages:

a) Eluent flow: This helps to separate the ions in the sample, drag the sample through the chromatographic system. ICS-1100 system is an isocratic supply. This means that the concentration of the eluent is maintained constant throughout the analysis.
b) Sample Injection: The liquid sample is loaded into a manual or automatic loop. At the time that the injection valve receives the signal, the sample is introduced into the IC system. The pump draws the sample and eluent through

the pre-column and the separating column (chemically inert tubes packed with polymeric resin). The pre-column retains contaminants that can damage the separating column.

c) Separation: As the eluent and the sample are pumped through the separating column, the sample ions drift apart. The ion exchange is the separation method used by the ICS-1100. This is based on the premise that sample ions migrate through the IC columns at different rates, depending on their interactions with exchange column points.

d) Suppression: After the eluent and the ions leave the column, the flow passes through the suppressor. This suppressor dynamically increases the ion signal and suppresses the conductivity of the eluent.

e) Detection: A conductivity cell measures the electric conductivity of the sample ions as they pass by the detector and it produces a signal based on the intrinsic properties of each species.

f) Data analysis: Conductivity cell transmits data to the data acquisition system. The data acquisition system ICS-1100 (Chromeleon Chromatography Management System) identifies the chromatogram peaks according to retention time, quantifying each species by comparison to the

chromatogram peaks pattern. The results are shown as a chromatogram, and the concentrations of the anilities are determined and automatically tabulated.

It is important to know that the solutions may have suffered variations analyzed for which interacted with the samples at higher pressure since the measurements must be made at ambient pressure.

3.2.11 Carbonation Tank

To perform various tests in which aqueous fluids may be saturated into CO_2 under various conditions of temperature and pressure, a carbonation tank was purposely designed. This tank holds a nominal pressure of 15 MPa, which is limited by a safety valve. The tank consists of a thick-walled steel cylinder and two lids attached through a series of high strength threaded rods. Both the upper and lower lid have multiple steps tube, which facilitates feeding of new fluid, gas or output for distribution to the test devices. The main water supply is by gravity using an auxiliary tank, which has a certain volume of the liquid previously deaerated. The carbonator has a manual syringe pump (HiP 62-6-10), with a capacity of 30 cc for each injection cycle. Its function is pressurized to reach the target value of work. This pump is capable of delivering pressures up to 10,000 psi (68.9 MPa).

Figure 3- 17. Fluid carbonation system coupled with the ISCO used for pore pressure.

The tank has different adjustable pressure valves to maintain the pressure (back pressure, BPR or positive pressure, PPR regulators). Furthermore, the supply of carbon dioxide takes place through a bottle, which provides liquid CO_2. The liquid CO_2 is introduced into the reservoir via a specific line provided with the corresponding valves that maintain the pressure. Some sintered porous cylinders were installed to facilitate the uniform distribution of CO_2 in the main water volume of the tank and to accelerate the dissolution (Figure 3- 18).

Figure 3- 18. CO_2 diffuser.

The line pressure control of CO_2 maintains a positive pressure regulator (Veriflo APR 66) that it aims is to adjust the pressure between 100 and 6000 psi, from the point of its location to the entrance in the pressure vessel. Similarly, there is another regulator with the same characteristics for the resulting balanced fluid in the reservoir, where its line ends in the manifold valve (ISCO 100DX).

3.2.12 Various equipment

In addition to the equipment described above, it was necessary to use other items of interest including:

a) Stainless steel pipes AISI 316: high pressure and diameter of 1/8" and 1/16". The fluid was transferred from the N_2 bottle to the ISCO pumps through those pipes, and from the ISCO pumps to the holder and to the mass flowmeter.
b) Valves, fittings and high pressure HiP connections, all made of stainless steel AISI 316. Their function is the distribution of flows and various operations required by the experimental operations (vent, sections isolation, etc.).

3.2.13 Systems integration

Figure 3- 19 represents a flow diagram in which most of the equipment and devices described in the previous sections are integrated into a single experimental rig. The system, which is highly modular, was design throughout our research in order to cope with the different problems as they arise.

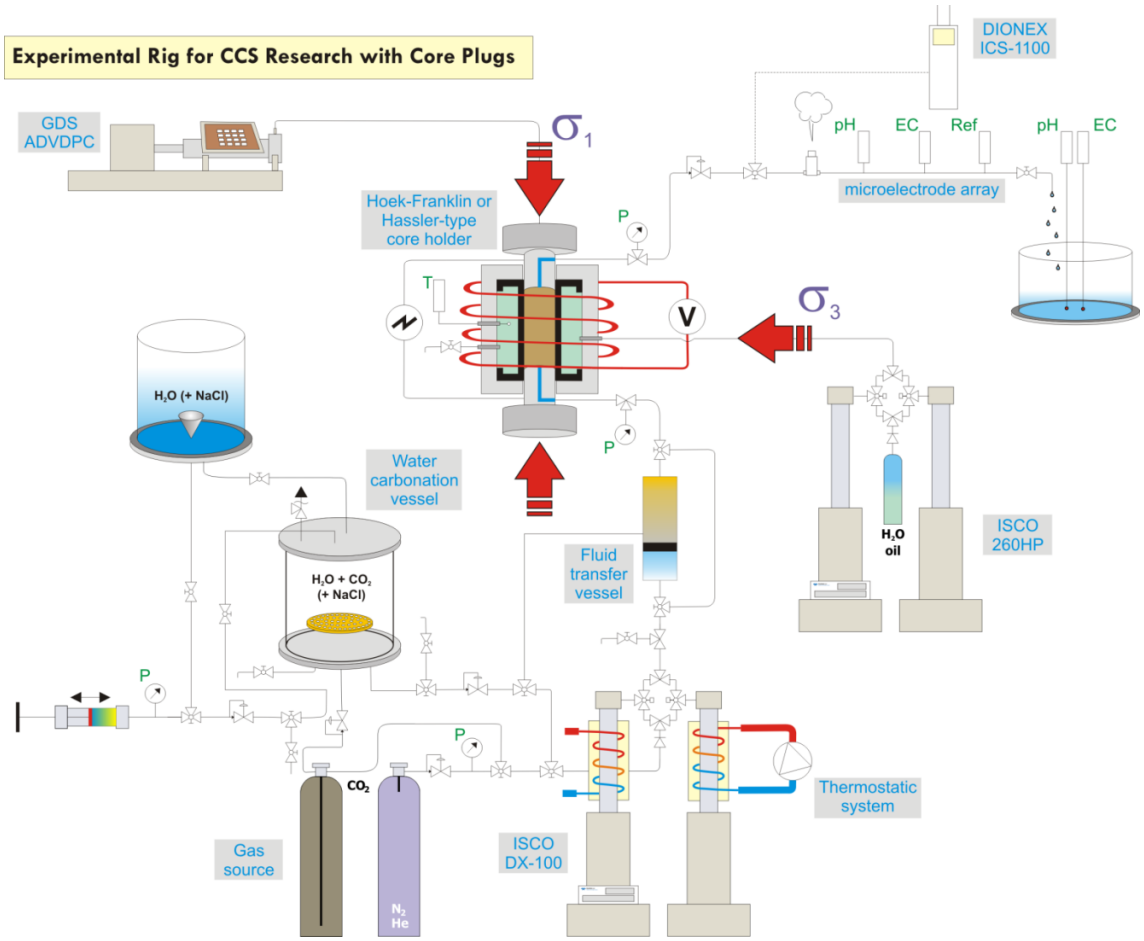

Figure 3- 19. Experimental rig developed at the UDC.

3.3 References

ASTM 4543. Practices for Preparing Rock Core as Cylindrical Test Specimens and Verifying Conformance to Dimensional and Shape Tolerances. ASTM International;

Hoek E, Franklin JA. A simple triaxial cell for field or laboratory testing of rock. Imperial College of Science and Technology, University of London;1967.

CHAPTER 4. INJECTION OF CO_2-SATURATED WATER THROUGH A SANDSTONE PLUG: EXPERIMENT AND MODELLING

4.1 Introduction

The geological setting beneath the Hontomín test storage site is a small, dome-shaped, structure (3x4 km) developed in a thick series of carbonated and detritic formations belonging to the Jurassic to lower Cretaceous cycles. Taking into account the information available from oil exploration reports, CIUDEN has identified two targets for CO_2 storage: Main and secondary reservoirs. The main reservoir is located between 1376 and 1502 m below the surface and corresponds to vuggy limestones and dissolution-collapse breccias (product of dedolomitization processes) of Hettangian-lower Sinemurian age. Towards the top of the reservoir the carbonates (skeletal and oolitic grainstones, mudstones, skeletal wackestones, stromatolitic limestones and dolostones) are well stratified. Its seal is constituted by a ~100 m thick package of marls alternating with limestones (Pliensbachian/Bajocian). The targets for CO_2 injection in the secondary reservoir are siliceous sandstone and conglomerate lenses, which are included in the red lutites of the Purbeck facies (Malm/Berriasian). Its corresponding seal are the central and upper lutitic formations of the Purbeck and marls of the Wealden (upper Berriasian/lower Aptian) megasequence (Beroiz and Permanyer 2011).

The nature and extent of $scCO_2$ or CO_2-bearing fluid/rock interactions is an important concern when considering injectivity,

containment and long-term safety of geological storage systems (Gaus 2010). Siliceous detritic formations are not expected to react massively with the injectate but the presence of lesser amounts of reactive minerals may play a significant role in their performance as geological storage. In fact, there is a wide body of evidence showing that coupled chemo-mechanical processes associated to CO_2 injection in sandstone reservoirs can trigger significant changes (some of them deleterious) in the transport properties of the storage system (Bowker and Shuler 1991; Le Guen et al. 2007; Hangx et al. 2010; Luquot et al. 2012). Among them, worth mentioning are the compaction of the rock grain skeleton induced by the dissolution/ collapse of cement phases (with a concomitant reduction of storage capacity and injectivity), the migration of fines in connection with their loosening from the rock framework or mineral scaling (Zemke et al. 2010).

Taking into account the specificity of the CO_2 storage systems, in this contribution we examine the behavior of a consolidated sandstone sample representative of the secondary reservoir of the Hontomín test storage site when flooded with CO_2-saturated water. Although similar studies are reported in the literature (Le Guen et al. 2007; Wigand et al. 2008; Hangx et al. 2010; Luquot et al. 2012) in our work we investigate and model the relevant mass transfer processes and we discuss the evolution of the hydrodynamic properties of the sample considering chemo-mechanical processes from the insight provided by the changes observed in the velocity of propagation of elastic P and S waves.

4.2 Materials and methods

Physical properties		Chemical composition (wt.%)[4]		Mineralogy (vol.%)[5]	
Diameter	38.30 mm	SiO_2	94,87	Quartz	92,1
Length	74.55 mm	Al_2O_3	2,13	Kaolinite	5
Volume	8.59 x 10^{-2} L	Fe_2O_3	0,92	Mg-Calcite	0,3
Initial porosity[1]	7,33%	MgO	0,06	K-feldspar	0,5
Dry density	2428 kg/m^3	CaO	0,12	Muscovite	0,1
Solid density	2620 kg/m^3	Na_2O	0,05	Goethite	0,9
Pore volume	6.31 x 10^{-3} L	K_2O	0,1	Apatite	0,03
Specific surface[2]	0.5 m^2/g	TiO_2	0,08	Rutile	0,1
Mean pore diameter[3]	0.5 mm	P_2O_5	0,03	Barite	traces
Mean intrinsic permeability	$10^{-16.7}$ m^2	LOI	1,2		

Table 4- 1. Summary of physical, chemical and mineralogical properties of the sample used in the experiment. Notes: 1) Based on the weigh difference between the dry and fluid-saturated sample; 2) BET isotherm performed on a rock chip; 3) Hg intrusion porosimetry; 4) XRF; 5) Normative calculation based on XRF data.

The experiment consisted in the successive injection of deionized water, DIW and CO_2-saturated DIW through a cylindrical, consolidated, quartzarenite sandstone plug of 38.30 mm diameter and 74.55 mm length. A summary of relevant physicochemical and mineralogical data of the rock is given in Table 4- 1. The rock block used to obtain the plug has the reference A1.3 and was collected near Hontomín (UTM-X: 0414003; UTM-Y: 4747617), in an outcrop of the Arcera Formation (lower Purbeck). The outcrop shows medium-coarse grained sandstone in 0.5 to 1 m thick banks and large-scale cross bedding. The plug was carefully cored and trimmed to fulfill standard geometric

constrains for rock mechanics studies: flatness, slenderness and cilindricity tolerances (Franklin 1983). The chemical composition of the sample was analyzed by X-ray fluorescence (Bruker AXS S4 Pioneer) while its mineralogy was identified by a combination of X-ray diffraction (Siemens D5000) and scanning electron microscopy (Jeol JSM 6400) techniques. Mineral abundances were computed from the XRF data using the MINSQ spreadsheet (Herrmann and Berry 2002). The mineralogy of the sample is dominated by quartz (~92%) with subordinated quantities of kaolinite (~5%). Scarce crystals of K-feldspar, muscovite, goethite, barite, ilmenite and rutile are also present in the rock (Figure 4- 1 B and D). The average inorganic carbon content of the rock is small (0.18 wt.%) and scanning electron microscope images show that the associated carbonates have a small grain size and they are always associated to the pore space of the rock, often in pore throats (Figure 4- 1 A). Quartz grains are cemented by microcrystalline silica and kaolinite fills a portion of the pore space (Figure 4- 1 B). The presence of illite or mixed-layer illite/smectite clays interstratified with kaolinite has not been recognized.

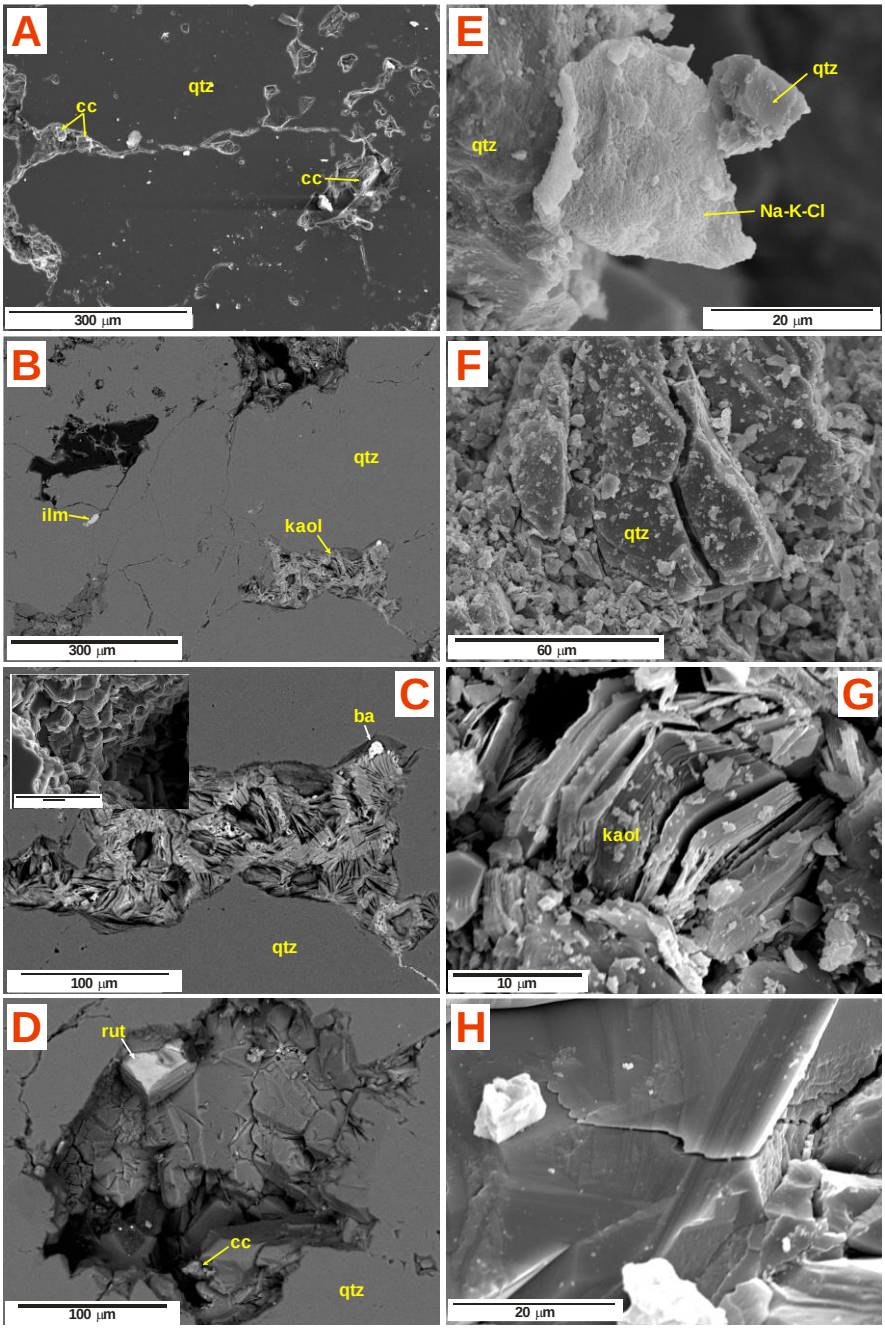

Figure 4- 1. Secondary (A, E, F, G, H) and backscattered electron (B, C, D) SEM images of the Arcera sandstone. Images A to E correspond to the sample before flooding while F to H were taken after the experiment. Cc: calcite; qtz: quartz; ilm: ilmenite; kaol: kaolinite; ba: barite; rut: rutile; Na-K-Cl: salt precipitate. See text for explanation.

The experiment lasted for nearly 49 days (7 days with DIW and 42 days with CO_2-saturated DIW) and a total of 2.7 L of fluid was forced to circulate through the sample. Taking into account that the initial porosity of the plug was 7.33%, its pore volume (PV) was flushed ~430 times during the experiment.

4.2.1 Experimental Rig

The sample, initially dry, was submitted to axi-symmetric (or pseudotriaxial) stress conditions by inserting the plug into a modified Hoek-Franklin-type core holder (Hoek and Franklin 1967) emplaced in a stiff reaction frame. The core holder transmit the stresses to the sample through two stainless-steel compression platens (axial stress; $\sigma 1$) and hydraulic oil (radial or confining stress; $\sigma_2 = \sigma_3 = \sigma_{2,3}$). To avoid contact between the confining fluid and the sample, this is jacketed with a polyurethane sleeve. The test was performed at room temperature (22 °C) and a constant deviatoric stress, Q ($\sigma_1 - \sigma_{2,3}$; σ_1=15 MPa; $\sigma_{2,3}$=10 MPa) of 5 MPa. The stress conditions were supplied by two independent ENERPAC Series P hand hydraulic pumps equipped with check valves (to maintain pressure) and analogic gauges (for monitoring). Loading of the sample was performed stepwise: In the first step the axial and confining pressures were rise simultaneously (Q=0) and at a constant rate to the target value of confining pressure. From hereafter σ_1 was increased while keeping constant $\sigma_{2,3}$.

Each of the compression platens incorporate two fluid ports connected to a thru hole. For a better distribution of the injected fluid, the surfaces in contact with the sample are grooved. During the loading process, in order to avoid an undesired increase of the pore pressure, the sample was kept drained (i.e. inlet and outlet ports open). The fluid ports of one of the compression platens were connected to a dual Teledyne Isco DX-100 high pressure syringe pump. This pump was used to inject, at a constant fluid pressure, P_F of 4 MPa the flooding fluids. Therefore, the effective mean stress, P', defined as $(\sigma_1+2\ \sigma_3)/3 - P_F$, was 4.3 MPa. The pressure drop between the inlet and outlet ports was monitored with two high resolution (±0.1%) absolute pressure transducers (Keller-Drück LEO Record Ei). At the opposite end, the fluid ports were connected to a tube line whose purpose was to collect the water circulated through the sample (outlet fluid). This line was equipped with a low volume flow-thru, temperature compensated, microelectrode array (Microelectrodes Inc. refs. 8-702, 8-705 and 8-900, corresponding to reference, pH and conductivity electrodes, respectively) all of them attached to an ELIT 9705b Aqualyser (Nico2000 Ltd.) for data acquisition purposes. Because these microelectrodes cannot attain pressures higher than 100 kPa, the fluid was decompressed prior to the measurements. However, the decompression of the fluid in the CO_2-saturated water injection phase triggered the outgassing of CO_2 and the growth and transient accumulation of small gas bubbles in the dead volume of the

microelectrodes. This turned out to increase the internal pressure and, as a result, small external leaks from the 3 M KCl reference electrode happened. That made necessary the continuous maintenance and recalibration of the electrodes, with long periods without measurements. We believe that the data recorded captured the general trend of the experiment but the problems reported make us to put a note of caution on what it can be concluded from its interpretation.

The top and bottom compression platens are instrumented each with a stack of 1.3 MHz resonant frequency piezoelectric transducers (PZT) for the measurement of direct (V_P) and shear (V_{S1}, V_{S2}) ultrasonic wave velocities. Squared-pulse waves were generated with a transducer-pulser unit (PT100-1000; ErgoTech Ltd.) and monitored with a digital oscilloscope (PicoScope 3204A; Pico Technologies Ltd.). Velocities were determined applying the time-of-flight technique, according to the recommendations given in (Rummel et al. 1978).

The saturation of water with CO_2 was accomplished in a 2.7 L carbonation vessel which was filled with DIW. To accelerate the saturation process, CO_2 was micronized at low pressure (~0.5 MPa) into small bubbles in the liquid using five TharSFC frits (ref. 01067-5). CO_2 was delivered in excess, what allowed the development of a CO_2 headspace. The compression of the system to the target pressure of 4 MPa was performed with a pressure generator (HiP mod. 62-6-10) at room temperature. The system was left to equilibrate for a week,

although different sources in the literature (Diamond and Akinfiev 2003) report that equilibrium can be reached in 24 to 48 h. The transfer of fluid from the carbonation vessel to the ISCO pump was performed by setting the later in constant pressure mode and a back-pressure regulator, both set to 4 MPa. According to the EOS described in (Duan and Sun 2003; Duan et al. 2006), the theoretical concentration of CO_2 in the carbonated fluid is 1.39 mol/kg H_2O or 61.1 g CO_2/kg H_2O. Similarly, the theoretical pH of the solution is 3.12.

4.2.2 Analytical Procedures

Different parameters were recorded during the experiment. Injection flow rates and pore pressure were directly monitored with the control software and the precision transducers of the ISCO pumps. This data was used to evaluate permeability using Darcy's Law for steady flow (Luquot and Gouze 2009). In short, the ratio of volumetric flow rate, Q (m^3/s) to the pressure drop, ΔP (Pa) between the inlet and outlet of a sample of cross sectional area, A (m^2) and length, L (m) is related with its intrinsic permeability, k (m^2) through the following expression:

$$k=\frac{\mu L Q}{A \Delta P}$$

Where μ represents the dynamic viscosity of the fluid (Pa·s). The fluid leaving the sample through the outlet port was collected and analyzed for its anionic (Cl, F, SO_4), cationic (Na, K, Ca, Mg, Al, Ba) and

silica concentrations (Table 4- 2). Anions were determined by ion chromatography (Dionex ICS-1100) while cations and silica by HR ICP-MS (Thermo Scientific Element XR).

Experimental phase	Flow	Cumulative volume	Time	Log k	k/k_0	ϕ/ϕ_0	Na	Mg	SiO_2	Ca	K	Al	Ba	F	Cl	SO_4	PO_4
I DIW	0.0210	0.021	0.68	-	1000	0.011	-3.30	-4.60	-4.35	-4.11	-3.47	-5.88	-7.16	-6.09	-3.24	< -5.3	-6.10
	0.0207	0.041	1.37	-16.67	1000	0.014	-3.66	-5.13	-4.90	-4.62	-3.93	-6.19	-7.62	-5.72	-3.66	< -5.3	< -6.3
	0.0249	0.096	2.90	-16.59	1204	0.013	-4.22	< -6.4	-5.36	-6.01	-5.04	-6.22	-8.34	-5.91	-4.14	< -5.3	< -6.3
	0.0303	0.114	3.31	-16.51	1464	0.013	-4.46	< -6.4	-5.65	-5.56	-4.95	-6.48	-8.25	-6.45	-4.14	< -5.3	< -6.3
	0.0280	0.184	5.01	-16.54	1351	0.013	-4.38	< -6.4	-5.57	-5.48	-4.59	-6.45	-8.00	-5.74	-4.11	< -5.3	-6.29
	0.0275	0.194	5.29	-16.55	1330	0.013	-4.39	< -6.4	-5.64	-5.48	-4.40	-6.45	-7.75	-5.50	-4.08	-4.54	-6.07
	0.0271	0.224	6.05	-16.55	1310	0.014	-4.79	< -6.4	-5.68	-5.82	-4.44	-6.44	-7.93	-5.75	-4.12	< -5.3	< -6.3
II CO_2-saturated DIW	0.0208	0.350	10.24	-16.67	1004	0.081	-4.90	-3.80	-5.12	-3.23	-3.92	-5.30	-6.57	-4.91	-4.10	-4.49	< -6.3
	0.0221	0.405	11.99	-16.64	1069	0.232	-4.63	-3.33	-4.09	-2.85	-2.79	-5.68	-6.27	-5.34	-2.95	-4.47	-5.55
	0.0218	0.453	13.50	-16.65	1053	0.289	-4.68	-3.45	-4.06	-2.89	-3.65	-5.78	-6.28	-5.35	-4.02	-4.49	-5.78
	0.0213	0.569	17.27	-16.66	1031	0.400	-4.54	-3.53	-4.00	-3.00	-3.75	-5.77	-6.26	-5.26	-4.10	-4.48	-5.66
	0.0240	0.680	20.50	-16.61	1159	0.501	-4.81	-3.62	-4.18	-3.00	-3.79	-5.61	-6.30	-5.98	-4.11	-4.49	-5.20
	0.0266	0.813	23.95	-16.56	1286	0.557	-4.80	-3.94	-4.75	-3.31	-4.10	-5.55	-6.37	-5.45	-4.10	-4.50	< -6.3
	0.0295	0.836	24.50	-16.52	1424	0.560	-4.83	-4.34	-5.11	-3.74	-4.55	-4.94	-6.42	-4.77	-4.12	-4.32	< -6.3
	0.0348	0.905	25.92	-16.45	1679	0.569	-4.85	-4.53	-4.98	-3.92	-4.70	-4.72	-6.42	-4.65	-4.12	-4.48	< -6.3
	0.0411	0.964	26.93	-16.37	1984	0.574	-4.64	-4.84	-5.24	-4.24	-4.78	-4.72	-6.49	-4.58	-4.07	-4.45	< -6.3
	0.0521	1210	30.39	-16.27	2516	0.599	-4.47	-4.67	-4.84	-4.06	-4.56	-4.71	-6.34	-4.38	-4.07	-4.45	< -6.3
	0.0509	1320	31.88	-16.28	2458	0.612	-4.80	-4.61	-4.27	-4.01	-4.73	-4.73	-6.35	-4.56	-4.11	< -5.3	-4.45
	0.0534	1746	37.50	-16.27	2513	0.681	-4.65	-4.31	-4.65	-3.74	-4.54	-5.28	-6.32	-4.73	-4.09	-4.47	< -6.3
	0.0534	1823	38.50	-16.27	2527	0.689	-4.65	-4.55	-5.02	-4.01	-4.54	-4.60	-6.35	-4.45	-4.12	-4.46	< -6.3
	0.0534	1900	39.50	-16.27	2540	0.698	-4.70	-4.56	-4.79	-4.00	-4.75	-4.66	-6.32	-4.50	-4.12	-4.46	< -6.3
	0.0575	2057	41.50	-16.23	2778	0.711	-4.68	-4.72	-4.95	-4.20	-4.70	-4.61	-6.38	-4.43	-4.12	-4.44	< -6.3
	0.0737	2464	45.50	-16.12	3561	0.742	-4.69	-4.77	-4.80	-4.34	-4.77	-4.65	-6.41	-4.39	-4.12	-4.44	< -6.3
	0.0777	2576	46.50	-16.10	3756	0.750	-4.70	-4.76	-4.83	-4.30	-4.85	-4.58	-6.42	-4.39	-4.12	-4.44	< -6.3
	0.0818	2744	47.92	-16.07	3952	0.765	-4.69	-4.70	-4.73	-4.23	-4.75	-4.53	-6.36	-4.38	-4.12	-4.43	-6.28

Table 4- 2. Measured flow (mL/min), cumulative water volume (L), log permeability (m^2), permeability ratio (-), porosity ratio (%) and outlet fluid composition. Element concentrations expressed in log molality.

For the purpose of plotting, the analytical concentrations have been represented against PV. Because each sample was collected after a variable period of time, its associated volume represents a certain number of pore volumes. This uncertainty has been incorporated to the plots as PV error bar.

4.2.3 Reactive Transport Modeling

The PHREEQC-2 code (version 2.18.3-5570) and its associated wateq4f.dat database were used to model the results of the experiment described in this work (Parkhurst and Appelo 1999). We took advantage of the reactive transport capabilities of the software by defining a one-dimensional model made of 20 cells, each one of them with a length equal to 1/20 of the total length of the sample. Relevant information of the model and associated parameters is provided in Table 4- 3. The experiment was segmented into five consecutive (I to V) modeling stages based on the visual inspection of the evolution of some relevant chemical constituents: Ca, Mg, SiO_2 and Al. All of them display a saw-tooth or stepped pattern (Figure 4- 3) whose boundaries, in terms of PV (I=0-35; II=35-150; III=150-200; IV=200-280; V=280-440), were used to constrain the model. Stage I considers only the injection of DIW while for stages II to V the model accounts for the flooding with CO_2-saturated water.

	Boundary water Phase I – DIW	Boundary water Phase II – CO2-saturated DIW
Temperature	22 °C	22 °C
pH	6.0	3.1
Na	0.02 mmol/L	0.02 mmol/L
K	0.015 mmol/L	0.015 mmol/L
Ca	0.00125 mmol/L	0.00125 mmol/L
Mg	0.01 mmol/L	0.01 mmol/L
Ba	$6.3x10^{-6}$ mmol/L	$6.3x10^{-6}$ mmol/L
Al	$3.2x10^{-4}$ mmol/L	$2.0x10^{-3}$ mmol/L
SiO_2	$2.0x10^{-3}$ mmol/L	$2.0x10^{-3}$ mmol/L
HCO_3	Log P_{CO2} = -3.5	Log P_{CO2} = 1.6
Cl	0.075 mmol/L	0.075 mmol/L
SO_4	0.028 mmol/L	0.033 mmol/L

Reactive Transport Parameters				
Number of cells		20	a_L	$7.5x10^{-3}$ m
Cell length		$3.73x10^{-3}$ m	D_e	$1.4x10^{-11}$ m^2/s
Modeling stages	I	0-35 PV (0-6 days)	v_I	$5x10^{-6}$ m/s
	II	35-150 PV (6-27 days)	v_{II}	$5x10^{-6}$ m/s
	III	50-200 PV (27-32 days	v_{III}	10^{-5} m/s
	IV	00-280 PV (32-38 days	v_{IV}	10^{-5} m/s
	V	80-440 PV (38-49 days	v_V	$1.25x10^{-5}$ m/s
Ion Exchange				
Half reaction		$logK_{H/K}$	CEC	
$K^+ + Y^- = KY$		0.0	0.05 mol/L	
$H^+ + Y^- = HY$		0.5		

Table 4- 3. Relevant data used to construct the reactive transport model of the experiment. Notes: PV: pore volume; αL: coefficient of longitudinal dispersion, De: effective diffusion coefficient; v: Darcy's velocity

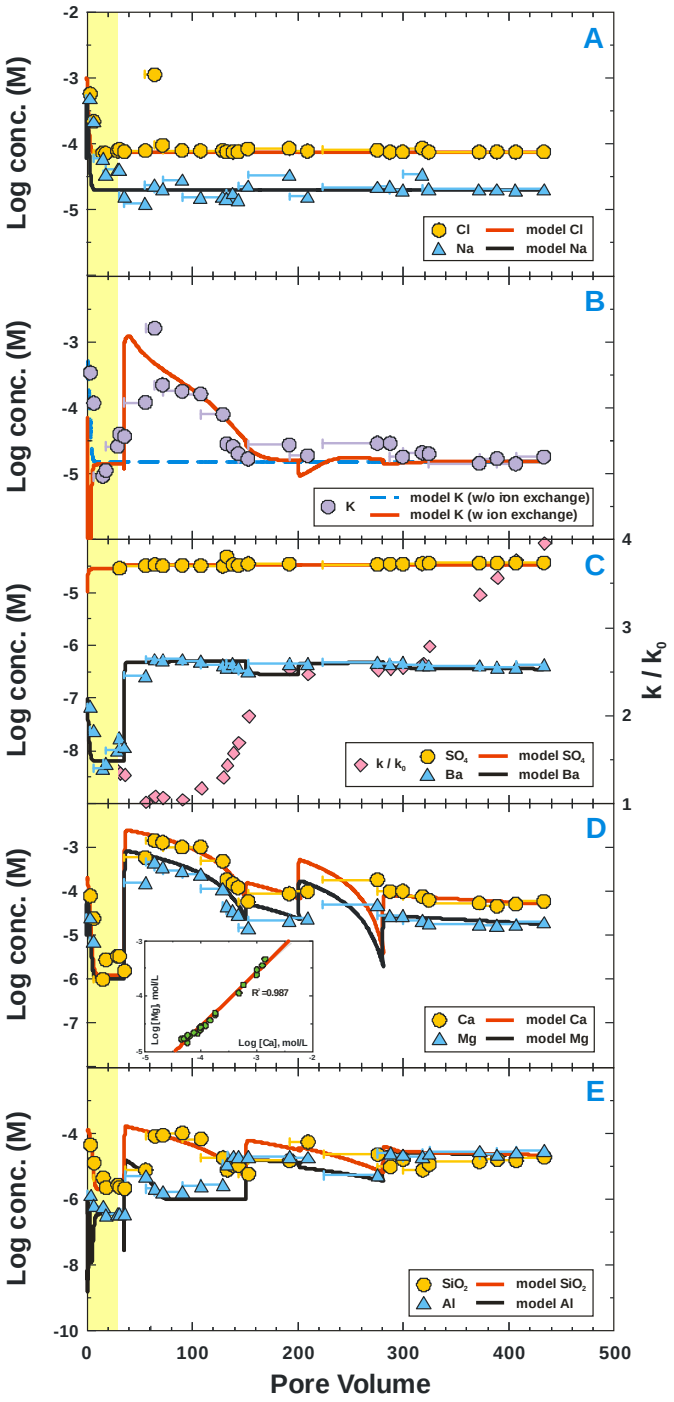

Figure 4- 2.Experimental data (symbols) and selected model results (lines). Horizontal error bars correspond to the PV range represented by each discrete analysis. The area shaded in light yellow identifies phase I of the experiment (injection of DIW).

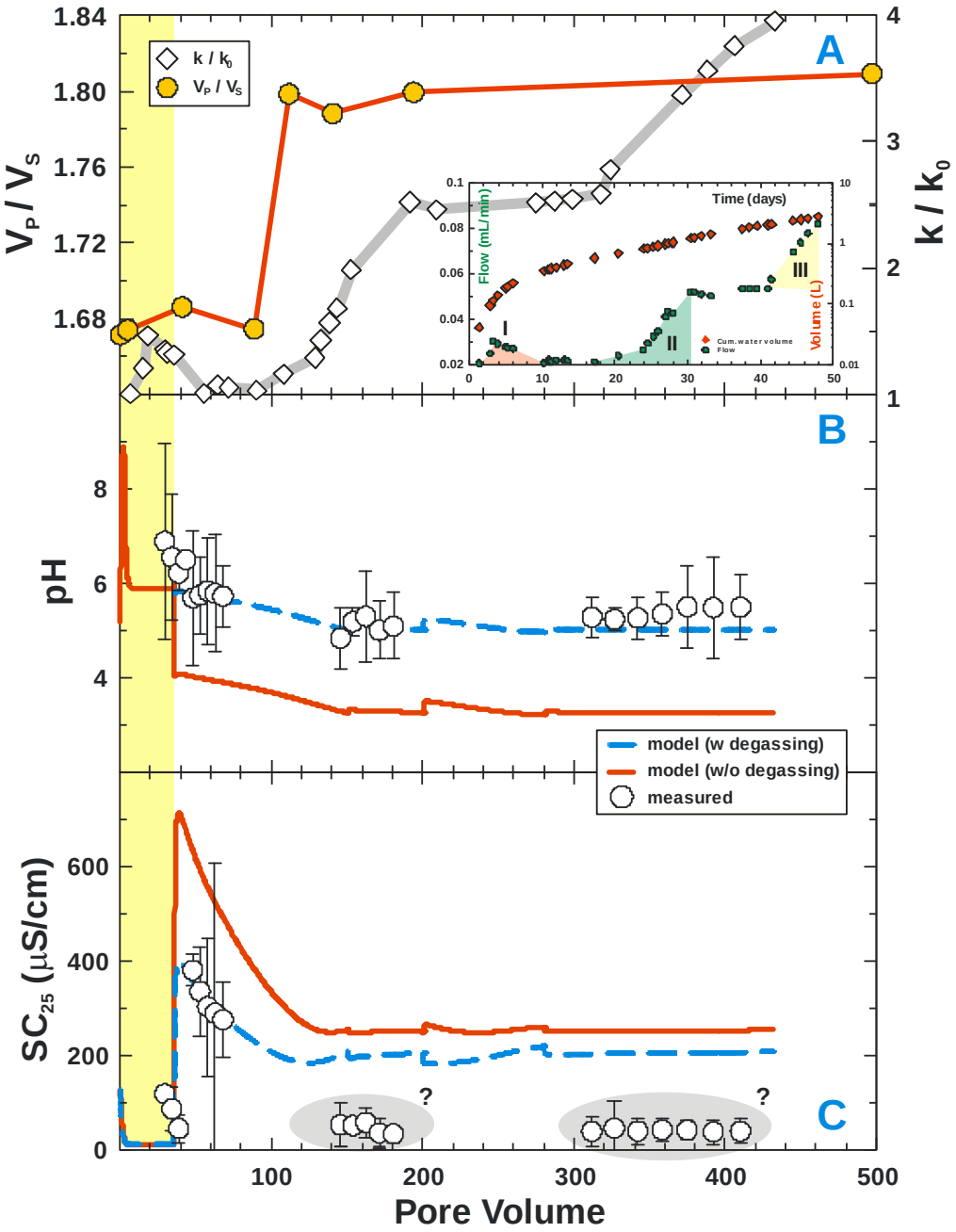

Figure 4- 3. Evolution of permeability, V_P/V_S ratio (A), pH (B) and specific conductance (C) during the experiment. The inset in A shows the compared flow and cumulative water volume as a function of time. I, II and III identify steps in the evolution of permeability. Dashed and continuous lines in B and C represent model results considering or not the effect of CO_2 degassing (blue and red, respectively). Question marks in C identify inconsistent data. The light yellow-shaded area illustrates phase I of the experiment (injection of DIW).

PHREEQC-2 does not allow the direct input of hydraulic conductivity (K) or pressure gradients (Δh/ΔL). These parameters have to be implicitly considered in the time and spatial discretization by relating the cell length, Δx (m) with the time step, Δt (s) through the pore flow or Darcy's velocity, v (m/s): $v=-K\Delta h/\Delta L$. Consequently, $v=\Delta x/\Delta t$. According to Appelo et al. (1998) and Appelo and Postma (2005) this is an advantageous approach because it reduces numerical dispersion and instability. Pore flow velocity was not constant throughout the experiment. Hence for modeling purposes we considered different values: $5x10^{-6}$ m/s for stages I and II; 10^{-5} m/s for stages III and IV (2xKI) and $1.25x10^{-5}$ m/s for stage V (2.5xKI). These values were selected to be consistent with the experimental observations.

PHREEQC-2 can simulate diffusive/dispersive transport by defining the hydrodynamic dispersion coefficient, D_L (m^2/s) that relates the effective diffusion coefficient, D_e (m^2/s), the velocity of the fluid, v (m/s) and the dispersivity of the porous media, α_L (m): $D_L=D_e+v\alpha_L$ (Appelo and Postma 2005). In the absence of sample-specific data, we assumed that dispersivity approaches 1/10 of the travel distance ($\alpha_L=7.5x10^{-3}$ m). Similarly, De is related to the molecular diffusion coefficient in free water, D_f by the relationship $D_e=D_f\varepsilon^m$, where ε represents porosity and m de Archie's law cementation exponent. Assuming m equal to 1.64 (Adler et al. 1992)

and for an average value of D_f of 10^{-9} m^2/s (Appelo and Postma 2005), D_e becomes equal to $1.4x10^{-11}$ m^2/s. The value of the diffusion coefficient and dispersity were kept constant for all the modeling stages.

The chemical composition of the boundary injectates (DIW and CO_2-saturated DIW) were determined from chemical analysis and the theoretical considerations outlined before. The model considered the presence of certain mineral phases: Mg-calcite, halite, sylvite, barite, amorphous silica and kaolinite. The rationale for their inclusion is given further on. These solids were considered to be present in the rock at the beginning of the experiment and they were modeled considering far from equilibrium kinetic rate laws. According to Appelo et al. (1998) and Appelo and Postma (2005) overall rates for kinetic reactions, R_k can be modelled using the transition-state theory derived expression:

$$R_i = \pm r_i \frac{A_0}{V} \left(\frac{m_i}{m_{0i}}\right)^n \left[1 - \left(\frac{IAP}{K_{sp,i}}\right)^\sigma\right]$$

where R_i represents the specific rate (positive for dissolution and negative for precipitation) of solid i (mol m^{-2} s^{-1}), A_0 its initial surface area (m^2), V the pore volume (m^3), m_{0i} the initial amount of solid i (mol), m_i the amount of solid i present at a given time (mol), n a shape factor (0.67 for spherical particles), and σ a stoichiometric factor of the kinetic reaction. $IAP/K_{sp,i}$ accounts for the saturation ratio of the solid i.

PHREEQC-2 incorporates a flexible scheme to help the inclusion of different formulations for the specific rates of minerals and other substances. In the case of Mg-calcite, we assumed that the rate equation described in Plummer et al. (1978) and Parkhurst and Appelo (1999) for calcite was applicable:

$$r_{cc}=k_1[H^+]+k_2[CO_{2,aq}]+k_3[H_2O]\left[1-\left(\frac{IAP}{K_{cc}}\right)^{2/3}\right]$$

The values of the natural logarithm of k_1, k_2 and k_3 are 0.198-444/T, 2.84-2177/T and -5.86-317/T, respectively. In the case of halite, sylvite (assumed equal to halite), barite, amorphous silica and kaolinite we used the parameters and sources reported in Palandri and Kharaka (2004), which are applicable to the following expression:

$$r_i=k_{25}^{nu}\exp\left[\frac{-E_a^{nu}}{R}\left(\frac{1}{T}-\frac{1}{298.15}\right)\right]+k_{25}^{ac}\exp\left[\frac{-E_a^{ac}}{R}\left(\frac{1}{T}-\frac{1}{298.15}\right)\right]a_{H^+}^{n_{ac}}+$$

$$+k_{25}^{ba}\exp\left[\frac{-E_a^{ba}}{R}\left(\frac{1}{T}-\frac{1}{298.15}\right)\right]a_{H^+}^{n_{ba}}$$

R represents the universal gas constant (8.314 J mol^{-1} K^{-1}), T the absolute temperature (K), k_{25} the rate constant of the substance at 25 °C (mol m^{-2} s^{-1}), E_a the activation energy (kJ mol^{-1}), a_{H+} the activity of the hydrogen ion and n an exponential factor. The acronyms nu, ac and ba account for the eventual acid, neutral and base dissolution/precipitation mechanisms. Because no information was

available on the reactive surface area of the minerals in the sample, their values were calibrated in the model.

In addition to speciation and dissolution/precipitation reactions the model included ion exchange processes in order to evaluate competitive proton exchange in clay minerals triggered by the flooding with the acidic fluid (Palandri and Kharaka 2004).

4.3 Results and discussions

The low flow conditions reproduced in the experiment (~0.4 m/day) can be representative of the circumstances prevailing in the bulk sandstone reservoir, at some distance of the CO_2 injection point.

No significant differences before and after the experiment were identified in the sample concerning its mineralogy or its relative abundance. However, a noticeable change in the hydrodynamic and acoustic properties of the sample took place as well as discernible patterns in the evolution of the outlet fluid (Figure 4- 2 and Figure 4- 3). Figure 4- 2A illustrates the evolution of permeability, expressed as permeability ratio, k/k_0, where k and k_0 represent the permeability at a given time and at the beginning of the experiment, respectively. We see that from 0 to ~20 PV permeability first rises and later drops to the reference value after ~60 PV (~10 days). From hereafter permeability displays a stepwise evolution, with steady and transient periods. The first steady period extends from ~60 to ~100 PV and the second from

~200 to ~320 PV. From ~100 to ~200 PV and from ~320 to the end of the experiment the permeability increases at an approximate rate of ~4 μD/day. At the end of the experiment permeability had increase by a factor of 4. It is likely that the first permeability fluctuation (from 0 to ~60 PV) is first related with the dissolution of readily soluble salts present in the initially dry rock (washout), followed by the migration of loosed fines that may have clogged some pore throats. Washout evidences are also observed in the evolution of certain constituents analyzed (Na, K, Cl, Ca, Mg; Table 4- 2). Similarly, rock damage associated to fines migration and pore throat clogging in sandstones have been previously described in the literature (Bowker and Shuler 1991). However, the permeability changes developed later need to be explained taking into account mechanical or coupled chemo-mechanical processes.

In Figure 4- 3 A we have represented the velocity ratio between direct (P) and shear (S) elastic waves monitored during the experiment. It is interesting to observe that the onset of permeability increase between ~60 and ~100 PV coincides in time with the climb of the V_P/V_S ratio from ~1.68 to ~1.8. An increase in the V_P/V_S ratio is generally considered indicative of rock microcracking and crack shearing dilatancy (Fortin et al. 2007; Guéguen et al. 2009). The post-experimental observation (Figure 4- 1 F-H) confirms that microcracking indeed occurred at the grain scale, but not immediately after loading the sample: According to the velocity data that happened

between ~80 and ~100 PV. From that point to the end of the experiment the V_P/V_S ration remained virtually constant, what suggests that microcracks did not propagate further or that their rate of growth was drastically reduced. Therefore, the coincidence in time of microcracking with the increase in permeability from ~60 and ~100 PV suggests a causal connection. However, this would not be apparent in the rise of permeability operated after ~320 PV up to the end of the experiment, because further sample damage is not supported by the velocity data.

Permeability enhancement associated to mineral dissolution may have also played a relevant role. In fact, the largest dissolution occurred at the beginning of the acidic flooding and up to ~150 PV, what points towards a clear chemo-hydro-mechanical coupling. However, the data available do not allow us to make precise inferences on the relative contribution of chemical vs. mechanical processes on the overall change of permeability. However, in the final part of the experiment it is clear that mechanical processes were subordinated with respect to permeability enhancement due to the porosity increase associated to mineral dissolution.

Although mechanical loading could account for some of the observed cracks (Figure 4- 1 G), it is not likely that this is the general case. The rock was submitted to stress conditions far away of its failure envelope and the onset of cracking happened nearly 20 days after

loading the sample. Similarly, if microcracking were associated to creep, we should expect a more or less gradual increase in the V_P/V_S ratio, which is not the case.

Different authors (Hangx et al. 2010) have pointed that, at the grain scale, microcracking could be chemically enhanced by the presence of aqueous fluids. The process, which is known as subcritical crack growth, is typically described for quartz as a "stress corrosion cracking" phenomena resulting from the weakening of strained Si-O bonds at the crack tips through chemical interactions with water, especially at low pH.

SEM images illustrate that microcracks are mainly open structures, with lengths shorter than ~100 μm, many of them not fully crossing grains (Figure 4- 1 G) and with orientations roughly parallel to σ_1. From the inversion of our velocity data, assuming a simplified model for crack distribution (isotropically distributed penny-shaped, non-interfering cracks), it is possible to compute the theoretical dimensionless crack density number (Stanchits et al. 2006; Ougier-Simonin et al. 2011). At the end of the experiment this number had a value of about 0.07 which, considering the sample volume (85.89 cm^3) and a hypothetical maximum crack length of 100 μm, would correspond to a total of ~5x104 cracks, that is less than 1 crack per cubic mm of sample.

Figure 4- 2 B and C show the evolution of pH and specific conductance (SC) of the outlet solution according to the measurements made with the microelectrode array. Due to the problems described earlier, it was not possible to obtain a continuous record and, when the measurements were possible, the data displayed a significant dispersion. In order to gain clarity in the representation the measured data was smoothed to mean daily values while the 5-95th percentile rank of the corresponding period was set as description of data dispersion.

pH data corresponding to the DIW flooding is not available. For the CO_2-saturated solution pH displays first a decreasing trend to later stabilize at a value slightly above 5. This value is different to that of 3.1 of the flooding fluid. Moreover, model results indicate that, after a certain time, the pH of the outlet fluid is expected to be acidic. The apparent inconsistency between the model and observations can be reconciled if we take into account that the pH measured corresponds to a previously degassed fluid, a phenomenon which is known to rise pH. Based on the equation of state of Duan et al. (Duan and Sun 2003; Duan et al. 2006) and the protolysis constants of relevant species for the aqueous carbon system, we can calculate that the magnitude of the pH change when dropping from 4 MPa to the equilibrium with the atmosphere is ~1.8 units. Once this correction is acknowledged, model and observation data becomes consistent, within the range of uncertainty. CO_2 degassing may also trigger the precipitation of

carbonates. Although mineral precipitates were not observed in the water collecting reservoir, it is hard to confirm whether carbonate scaling occurred or not in the tubes following fluid decompression. Model results indicate that the highest saturation index attained by calcite during the flooding with CO_2-saturated DIW was slightly higher than -4. In that case, the change in ~1.8 pH units associated to the P_{CO2} drop still lefts water undersaturated with respect calcite so that its precipitation is not to be expected.

SC values clearly identify phase I and II of the experiment. The PHREEQC-2 version used for this study is able to compute the SC of polyelectrolyte aqueous solutions based on the concentration, activity coefficient, and diffusion coefficients of the species present. To make possible the computation, we included the diffusion coefficients for aqueous species included in the phreeqc.dat database into our preferred database (wateq4f.dat). Figure 4- 2 C shows that model results are reasonably consistent with the first phase and the beginning of the second flooding phase of the experiment and that a much better agreement can be obtained when taking into account CO_2 degassing by stripping the relevant carbon species from the SC calculation. However, the SC corresponding to the measurements made after ~100 PV flooding is not consistent with the model either considering or not degassing. In fact, the experimental conductance values are exceedingly low to what it is expected from the analytical

concentrations. Consequently, we suspect that electrode malfunction, probably related with the permanence of gas bubbles, occurred.

Figure 4- 3 A to E illustrate the evolution of some chemical constituents in the outlet water. The outlet concentration is higher than that of the flooding water, what suggests that dissolution of mineral phases is a key geochemical process. Similarly, model results indicate that all the mineral phases considered (either present or potentially precipitating) remained undersaturated throughout the entire experiment. In agreement with what it has been observed elsewhere (Bowker and Shuler 1991; Kharaka et al. 2006; Wigand et al. 2008) the acidic flooding promotes the mobilization of certain minor and trace elements (F, P and Ba among the ones analyzed).

Figure 4- 3 A illustrates the evolution of Na and Cl. The first water samples collected have higher concentrations at the beginning of the experiment, with a fast drop in less than ten pore volumes. We interpret this feature as the result of the washout of tiny amount of Na-K-Cl salt precipitates (confirmed with SEM; Figure 4-1 E) initially present in the sample. The origin of these salts may not be geological but related with the oven-drying of the sample prior to the test. Assuming that the measured concentrations result from the dissolution of halite (NaCl) and sylvite (KCl), it is possible to compute their corresponding amounts either from mass balance (based on the concentrations observed during the first phase of the experiment) or

with the aid of the model. In either case, the mass required is ~0.78 and ~0.75 mg of halite and sylvite, respectively. After this initial washout period, the concentrations of Na and Cl become steady and the concentrations consistent with the chemical composition of the flooding water.

Figure 4- 3 B shows the evolution of potassium and, in contrast to what happens with Na and Cl, there is a noticeable rise in its concentration when the CO_2 saturated water is injected. This component attains its peak concentration after ~60 PV, dropping to a nearly steady concentration after ~150 PV. According to the mineralogy present in the rock, K-bearing phases are scarce and their contribution is not sufficient to explain the observed trend. It is well known, however, that kaolinite has a moderate cation exchange capacity, CEC. It is also known that, under acidic conditions, protons may compete with the monovalent cations of the exchange complex in a process described in the literature as hydrolytic exchange (McBride 1994). There is no available information on the CEC of the Arcera sandstone or its corresponding selectivity coefficients. These values were calibrated in the model from the experimental data. In a preliminary approach, we choose a simple one-site model to simulate the exchange reactions taking place in a hypothetical surface representing kaolinite between K and H^+. According to the PHREEQC-2 formalism (Parkhurst and Appelo 1999) exchange half-reactions were added to the working database. An acceptable match to the

experimental data can be obtained when considering 0.05 equivalents of exchange sites per liter of pore volume and selectivity constant for the H^+/K^+ exchange equal to 0.5. According to the characteristics of the sample (~5 vol. % kaolinite; ~ 7.3% porosity; 79.58 cm^3 bulk volume) this value equates to a CEC of ~0.03 eq/kg, which is consistent with the typical range attributed to kaolinite: 0.02 to 0.15 eq/kg (Sposito 1984). Therefore, H^+/K^+ exchange is a plausible candidate to explain the evolution of potassium during the experiment. Although ion exchange processes could also contribute to the behavior of other cations (Ca, Mg, Na…) attempts made to reproduce the experimental trends considering a variety of selectivity coefficients were unsuccessful. In turn, it has been possible to model reasonably well the behavior of these cations without the concourse of ion exchange.

Figure 4- 3 C displays the experimental concentrations of SO_4 and Ba in the outlet water. It is worth mentioning that, following the initial washout, the concentrations of both components steeply rise (in the case of SO_4 from below the detection limit) when the sample is flooded with the CO_2-saturated water. The similarity in the evolution of both components suggests a common mineral source, which is conjectured to be barite. Mass balances (based on the measured concentrations of SO_4 and Ba) are in excellent agreement with the model and both indicate that ~0.22 mg of barite would have been dissolved during the experiment.

There is an excellent correlation between the concentrations of Ca and Mg in the outlet fluid (Figure 4- 3 D). That points towards a common mineral source (Mg-calcite) and a co-dissolution process. Assuming that the dissolution is congruent, the theoretical stoichiometry of the carbonate would be $Ca_{0.78}Mg_{0.22}CO_3$. Following the washout stage, the evolution of these two components describes a distinct saw-tooth pattern which is different to what has been described so far. In a first step there is a sharp increase in concentrations that is attributed to the first arrival of the acidic fluid. After a short steady period, they go slowly down up to ~150 PV. Visual inspection of the remaining part of the experiment allows us to identify two-to-three additional steps, although their relative concentration change is rather small compared with the previous one. The origin of the stepped pattern is not clear although we speculate that it could be related to the access of fluid to new reactive surface in connection with a) microcracking (first step after washout), b) the dissolution of material containing carbonate crystals or c) changes in the flow path induced by the evolving pore connectivities.

In order to model the dissolution of Mg-calcite, we applied the stoichiometric saturation concept (Appelo et al. 1998). The solubility product was approximated from data published in (Morse and Mackenzie 1990) while the far from equilibrium dissolution rate was obtained from (Plummer et al. 1978; Parkhurst and Appelo 1999). Mass balance calculations suggest that the amount of carbonate

dissolved was ~0.10 g while the model indicates a slightly higher, but still consistent, value of ~0.14 g. Assuming that all the inorganic carbon present in the rock (0.18 wt.%) is in the form of carbonates, the mass initially available (scaled to the plug size) was ~3 g. Therefore, slightly more than 4% of the carbonate initially present in the rock was dissolved during the experiment. An outcome of this analysis is that only those grains more easily accessible to the flooding fluid (*i.e.* the ones located in pores within the main flow paths) would have been dissolved, while those isolated (inside less soluble phases, like siliceous cement) or located in dead ends would have not.

Figure 4- 3C presents the concentration of aqueous SiO_2 and Al. We observe the same general saw-tooth features described for Ca and Mg and we speculate similar origins. The reactive transport model provides a reasonably good match to the observations using amorphous silica and kaolinite as constraining minerals. The model predicts the cumulative dissolution of ~3.8 mg of amorphous silica and ~5.5 mg of kaolinite. Taking into account that the provenance of silica can be either from quartz or kaolinite, mass balances performed with the experimental data provides ~0.9 and ~4.7 mg of each mineral, respectively.

With the exception of certain trace minerals, the relatively simple mineralogy of the Arcera sandstone makes possible that the model is relatively successful in reproducing the experimental trends. For the

investigated conditions, the sandstone from the Hontomín test site does not experience a significant damage although this needs to be contrasted with new experiments under true reservoir conditions using the brackish resident fluid expected in situ.

According to the model, the mineral experiencing the largest mass transfer is Mg-calcite. If we add all the volumes associated with the minerals dissolved during the experiment we obtain that the corresponding porosity change is very small (~0.77%). This value becomes slightly larger (~0.85%) when we consider the pore volume associated to microcracks ($5x10^{-4}$ to $5x10^{-3}$ cm^3, computed for a total of $5x10^4$ penny-shaped cracks, 50 μm radius, 1 to 10μm aperture). It is worth to remark how such a small porosity change may have associated the large variation observed in permeability. To this respect, other authors (Colón et al. 2004) have observed similar effects in the siliceous Fontainebleau sandstone when flooded with a reactive alkaline fluid: Samples having the same range of porosity than ours (5.1 to 8.9%) but with permeability higher by one order of magnitude (0.27 to 0.57 mD) multiply their permeability by a factor of 2 to 3, while porosity changes only 1.2 to 1.4%. According to these authors, this phenomenon can be linked to the concentrated dissolution of minerals in pore throat locations, where a minimum increase in pore volume will determine a better connectivity and the concomitant increase in permeability.

With the exception of certain trace minerals, the relatively simple mineralogy of the Arcera sandstone makes it possible for the model to be relatively successful in reproducing the experimental trends. For the investigated conditions, the sandstone from Hontomin does not experience significant damage, although this needs to be contrasted with new experiments under true reservoir conditions using the brackish fluid expected in situ.

4.4 References

Adler PM, Jacquin CG, Thovert J. The formation factor of reconstructed porous media. Water Resour Res. Wiley Online Library; 1992; 28(6):1571–6.

Appelo CAJ, Postma D. Geochemistry, groundwater and pollution. CRC press; 2005.

Appelo CAJ, Verweij E, Schäfer H. A hydrogeochemical transport model for an oxidation experiment with pyrite/calcite/exchangers/organic matter containing sand. Appl geochemistry. Elsevier; 1998; 13(2):257–68.

Beroiz C, Permanyer A. Hydrocarbon habitat of the Sedano trough, Basque-Cantabrian basin, Spain. J Pet Geol. Wiley Online Library; 2011;34(4):387–409.

Bowker KA, Shuler PJ. Carbon dioxide injection and resultant alteration of the Weber Sandstone, Rangely Field, Colorado. Am. Assoc. Pet. Geol. Bull. American Association of Petroleum Geologists; 1991. p. 1489–99.

Colón CFJ, Oelkers EH, Schott J. Experimental investigation of the effect of dissolution on sandstone permeability, porosity, and reactive surface area. Geochim Cosmochim Acta. Elsevier; 2004;68(4):805–17.

Diamond LW, Akinfiev NN. Solubility of CO_2 in water from −1.5 to 100 °C and from 0.1 to 100 MPa: evaluation of literature data and thermodynamic modelling. Fluid Phase Equilib. 2003; 208(1–2):265–90.

Duan Z, Sun R. An improved model calculating CO_2 solubility in pure water and aqueous NaCl solutions from 273 to 533 K and from 0 to 2000 bar. Chem Geol. 2003; 193(3–4):257–71.

Duan Z, Sun R, Zhu C, Chou IM. An improved model for the calculation of CO_2 solubility in aqueous solutions containing Na^+, K^+, Ca^{2+}, Mg^{2+}, Cl^-, and SO_4^{2-}. Mar Chem. 2006; 98(2–4):131–9.

Fortin J, Guéguen Y, Schubnel A. Effects of pore collapse and grain crushing on ultrasonic velocities and V_P/V_S. J Geophys Res Solid Earth. Wiley Online Library; 2007; 112(B8).

Franklin. Suggested methods for determining the strength of rock materials in triaxial compression: Revised version. Int J Rock Mech Min Sci Geomech Abstr. 1983; 20(6):285–90.

Gaus I. Role and impact of CO_2–rock interactions during CO_2 storage in sedimentary rocks. Int J Greenh Gas Control. 2010 Jan; 4(1):73–89.

Guéguen Y, Sarout J, Fortin J, Schubnel A. Cracks in porous rocks: tiny defects, strong effects. Lead Edge. Society of Exploration Geophysicists; 2009; 28(1):40–7.

Le Guen Y, Renard F, Hellmann R, Brosse E, Collombet M, Tisserand D, et al. Enhanced deformation of limestone and sandstone in the presence of high fluids. J Geophys Res Solid Earth. Wiley Online Library; 2007; 112(B5).

Hangx SJT, Spiers CJ, Peach CJ. Creep of simulated reservoir sands and coupled chemical-mechanical effects of CO_2 injection. J Geophys Res. 2010 Sep 14; 115(B9):B09205.

Herrmann W, Berry RF. MINSQ – a least squares spreadsheet method for calculating mineral proportions from whole rock major element analyses. Geochemistry Explor Environ Anal. 2002 Nov 1; 2(4):361–8.

Hoek E, Franklin JA. A simple triaxial cell for field or laboratory testing of rock. Imperial College of Science and Technology, University of London; 1967.

Kharaka YK, Cole DR, Hovorka SD, Gunter WD, Knauss KG, Freifeld BM. Gas-water-rock interactions in Frio Formation following CO_2 injection: Implications for the storage of greenhouse gases in sedimentary basins. Geology. Geological Society of America; 2006; 34(7):577–80.

Luquot L, Andreani M, Gouze P, Camps P. CO_2 percolation experiment through chlorite/zeolite-rich sandstone (Pretty Hill Formation – Otway Basin–Australia). Chem Geol. 2012; 294–295:75–88.

Luquot L, Gouze P. Experimental determination of porosity and permeability changes induced by injection of CO_2 into carbonate rocks. Chem Geol. Elsevier; 2009;265(1):148–59.

McBride MB. Environmental chemistry of soils. Oxford university press; 1994.

Morse JW, Mackenzie FT. Geochemistry of sedimentary carbonates. Elsevier; 1990.

Ougier-Simonin A, Fortin J, Guéguen Y, Schubnel A, Bouyer F. Cracks in glass under triaxial conditions. Int J Eng Sci. Elsevier; 2011;49(1):105–21.

Palandri JL, Kharaka YK. A compilation of rate parameters of water-mineral interaction kinetics for application to geochemical modeling. DTIC Document; 2004.

Parkhurst BDL, Appelo CAJ. User's Guide To PHREEQC (version 2) — a Computer Program for Speciation, and Inverse Geochemical Calculations. Exch Organ Behav Teach J. 1999 ;D(Version 2):326.

Plummer LN, Wigley TML, Parkhurst DL. The kinetics of calcite dissolution in CO_2-water systems at 5 degrees to 60 degrees C and 0.0 to 1.0 atm CO_2. Am J Sci. American Journal of Science; 1978; 278(2):179–216.

Rummel F, Alheid HJ, Frohn C. Dilatancy and fracture induced velocity changes in rock and their relation to frictional sliding. pure Appl Geophys. Birkhauser-Verlag; 1978; 116(4-5):743–64.

Sposito G. The surface chemistry of soils. Oxford University Press; 1984.

Stanchits S, Vinciguerra S, Dresen G. Ultrasonic velocities, acoustic emission characteristics and crack damage of basalt and granite. Pure Appl Geophys. Springer; 2006; 163(5-6):975–94.

Wigand M, Carey JW, Schütt H, Spangenberg E, Erzinger J. Geochemical effects of CO_2 sequestration in sandstones under simulated in situ conditions of deep saline aquifers. Appl Geochemistry. Elsevier; 2008; 23(9):2735–45.

Zemke K, Liebscher A, Wandrey M. Petrophysical analysis to investigate the effects of carbon dioxide storage in a subsurface saline aquifer at Ketzin, Germany (CO2SINK). Int J Greenh Gas Control. 2010 Dec; 4(6):990–9.

CHAPTER 5. INJECTION OF CO_2-EQUILIBRATED BRINE INTO A VUGGY LIMESTONE

5.1 Introduction

Deep saline aquifers represent, by far, the most widely represented systems for CO_2 geosequestration. In the particular case of Spain, where conventional gas and oil fields are virtually non-existent, they represent the most realistic option for CCS. The EU GeoCapacity (2009) project determined that Spain had the highest onshore storage capacity of all European countries with a conservative estimate of 14,000 Mt in combined onshore and offshore deep saline reservoirs. The need for the native brine to be displaced by the injected CO_2 is greater in saline aquifers than in mature and depleted oil and gas fields, but applies to all. This may lead to pressure increases and far-field brine migration. The possible secondary effects of the large-scale pressure plume (on cap rock integrity, shallow water reservoir, etc.) and far field brine migration need to be properly understood in order to manage CO_2 injection and the development of formation pressure safely.

A CO_2 saturated brine is highly acidic and, therefore, aggressive with respect the media where it is injected (for instance, a carbonate reservoir). In a simplified first order approach, the injection of CO_2 will trigger the dissolution of carbonate minerals, what will increase the overall permeability but also reducing its strength. Depending on the minerals dissolved and the chemistry of the formation fluid, new minerals may also precipitate (some of them carbonates) which could

effectively lead to the effective mineralization of CO_2, reduction of permeability, overpressuring and concomitant mechanical processes (e.g. shearing, etc.). Eventually, upon the arrest of injection, the brine will tend to fill back the pore space, but a sizable amount of CO_2 may remain trapped by capillary forces as residual CO_2 bubbles. In summary, four basic trapping mechanisms are involved in the conventional concept of CO_2 geosequestration. Ranked according to their long term stability, these are (1) stratigraphic or tectonic trapping as a CO_2 phase; (2) water-dissolved CO_2; (3) capillary trapping; and (4) mineral trapping.

Within the context of the EU's OXYCFB 300 Compostilla Project, a number of sites have been investigated in Spain for the construction of a Technology Development Plant (TDP) as well as for commercial development. The place designed for the TDP is Hontomín (Burgos), a complex (but relatively small) carbonate structure where a broad number of techniques for CO_2 injection and monitorization have been tested. The understanding of the underground geology beneath the TDP is supported by log data from oil exploration wells drilled in the 1980's (numbered H-1, H-2, H-3 and H-4; Quesada et al. (1993, 1995, 1997); Quesada and Robles (1995)) and high resolution geophysical surveys specifically developed to characterize the TDP (Elío et al. 2013; Alcalde et al. 2014; Ogaya et al. 2014).

The geological setting beneath the Hontomín TDP is a small, dome-shaped, structure (~3x4 km) that has tectonically developed in a thick series of carbonated and detritic formations belonging to the Jurassic/lower Cretaceous cycles. The main potential reservoir of the TDP is located between 1376 and 1502 m b.s. and corresponds to vuggy limestones and dissolution-collapse breccias of Hettangian –lower Sinemurian age. Its seal is constituted by a ~100 m thick package of Pliensbachian/Bajocian marls and black shales alternating with limestones (Beroiz and Permanyer 2011; Permanyer et al. 2013). The expected thermo-mechanical conditions of this reservoir are about 40 ˚C, 15 MPa of confining pressure and 8.5 MPa of pore pressure.

Canal et al. (2013) have illustrated a preliminary core flooding experiment in which they used an upper Jurassic/lower Cretaceous (Purbeck Facies) quartzarenite plug that is representative of the secondary reservoir of the Hontomín test site (837 – 964 m b.s.). The sample, confined at high pressure, was successively injected with distilled water (DIW) and CO_2-saturated DIW (pH=3.1, [CO_2] =1.39 m) for 49 days while monitoring geophysical, chemical and hydrodynamic parameters.

Different petrophysical, hydrodynamic and geochemical parameters were recorded during this experiment. The plug experienced little change and show no discernable evidences of secondary carbonation. However, permeability increased by a factor of

4 and the V_P/V_S ratio rose from ~1.68 to ~1.8. Porosity slightly increased (7.3-8.1%) from the beginning to the end of the experiment. Fluid/rock reactions were also modelled and it was clear that they are dominated by the dissolution of Mg-calcite although mass balances show that only a small portion (~4%) of the initial carbonate present in the rock was consumed. The results of the experiments suggest that mineral dissolution coupled to mechanical effects (microcracking) may have acted in a synergistic way at the beginning of the acidic flooding. However, dissolution processes concentrated in pore throats can better explain the permeability enhancement observed over longer periods of time.

The work presented in Canal et al. (2013) is relevant in a number of ways. One of them is the elucidation of the need of the coupled monitoring the physic-chemical, petrophysical and hydro-geomechanical evolution of the system. However, at the time of performing this experiment the capability of measuring strains in the tested samples was not yet possible so that, to certain extent, the conjectures presented in the work require further experimental verifications. This requirement was partly fulfilled in the work presented in chapter 4. In addition, it was also necessary to test the behaviour of the rocks of the main reservoir (i.e. vuggy limestones) and to inject a fluid more akin to the one known to be present in the site at the reservoir depth (e.g. saline fluid).

In this chapter we present a new experiment using a vuggy limestone plug that has been flooded with a realistic formation fluid which is representative of the main TDP reservoir while we have measured a bundle of representative parameters amenable of use in advances T-H-M-G coupled models (a topic not covered in this research) as well as ultrasonic wave velocities.

5.2 Materials and methods

This experiment was developed in a similar frame/equipment configuration to that described in chapter 3. Some details of the equipment are explained further on.

The sample used in this new experiment consisted in a vuggy limestone plug (38.1 mm diameter and 76 mm length) representative of the main reservoir of Hontomín. The plug was carefully trimmed to fulfil standard geometric constrains (Franklin 1983).

A summary of the main properties of the sample is given in Table 5-1. The chemical composition of the rock was analysed by XRF, and the mineralogical composition was identified by a combination of powder-XRD and optical microscopy. Mineral abundances were computed from the XRF data using the MINSQ spreadsheet ((Herrmann and Berry 2002)). The heterogeneous pore distribution can be seen in Figure 5- 1 and also in the gas permeability results at Table 5- 2. This

phenomenon is due to the heterogeneous pore distribution and connectivity.

For this experiment, temperature was raised to 40 °C while axial and confining pressure were 30 and 10 MPa, respectively. While pore pressure is similar to the conditions expected at the PDT site (8.5 vs. 10 MPa) the confining pressure (30 MPa) was set higher than the one expected at the PDT (15 MPa). That was made to minimize the eventuality of preferential axial flows that could affect the evolution of permeability. The plug was pressurized and injected with pore fluid inside a Hoek-Franklin type cell following a methodology similar to that described in Canal et al. (2013).

Due to the high hydraulic conductivity of the tested sample, in order to reduce the Darcy's velocity to an acceptable value, a small constant pore pressure gradient of 4 bar was imposed (i.e. 4 MPa at the inlet and 3.6 MPa at the outlet of the core plug). Additional changes with respect to the experiment described in Canal et al. (2013) were: a) the injection of a synthetic proxy of the saline pore water of the Hontomín test site (Table 5- 3) either CO_2-free or CO_2-saturated; b) the monitoring of axial strain. Like in the previous experiment, the evolved fluid composition was monitored (pH, EC_{25} and the concentrations of Ca, Mg, Fe, SiO_2, F, Cl, Br and SO_4) likewise fluid flow (and permeability) and acoustic ultrasonic velocities.

Physical properties		**Chemical composition (wt.%)[3]**			**Mineralogy (vol.%)[4]**		
			c1	c2		c1	c2
Diameter	35,15 mm	CaO	49,06	51,12	Calcite	85,74	88,89
Length	66 mm	SiO_2	6,18	2,75	Ankerite	3,86	5,65
Volume	6,4 x 10^{-2} L	Al_2O_3	1,98	0,96	Muscovite	6,2	0,53
Initial weight	156,93 gr	Fe_2O_3	0,91	0,42	Albite	0,51	115,00%
Dry density	2450 kg/m^3	K_2O	0,69	0,43	Mg Chlorite	0,28	0,3
Solid density	2620 kg/m^3	MgO	0,65	1,44	Quartz	2,78	0
Pore volume	6.15x 10^{-3} L	SO_3	0,53	0,17	K feldspar	0	2,51
Specific surface[1]	0.984m^2/g	TiO_2	0,1	0,05	Rhodochrosite	0,07	0,26
Mean pore diameter[2]	0.076 μm	Na_2O	0,03	0,02			
		P_2O_5	0,03	0,02			
		LOI	39,5	42,01			

Table 5- 1. Summary of physical, chemical and mineralogical properties of the sample used in the experiment. Notes: 1) BET isotherm performed on a rock chip; 2) Hg intrusion porosimetry; 3) XRF; 4) Normative calculation based on XRF data.

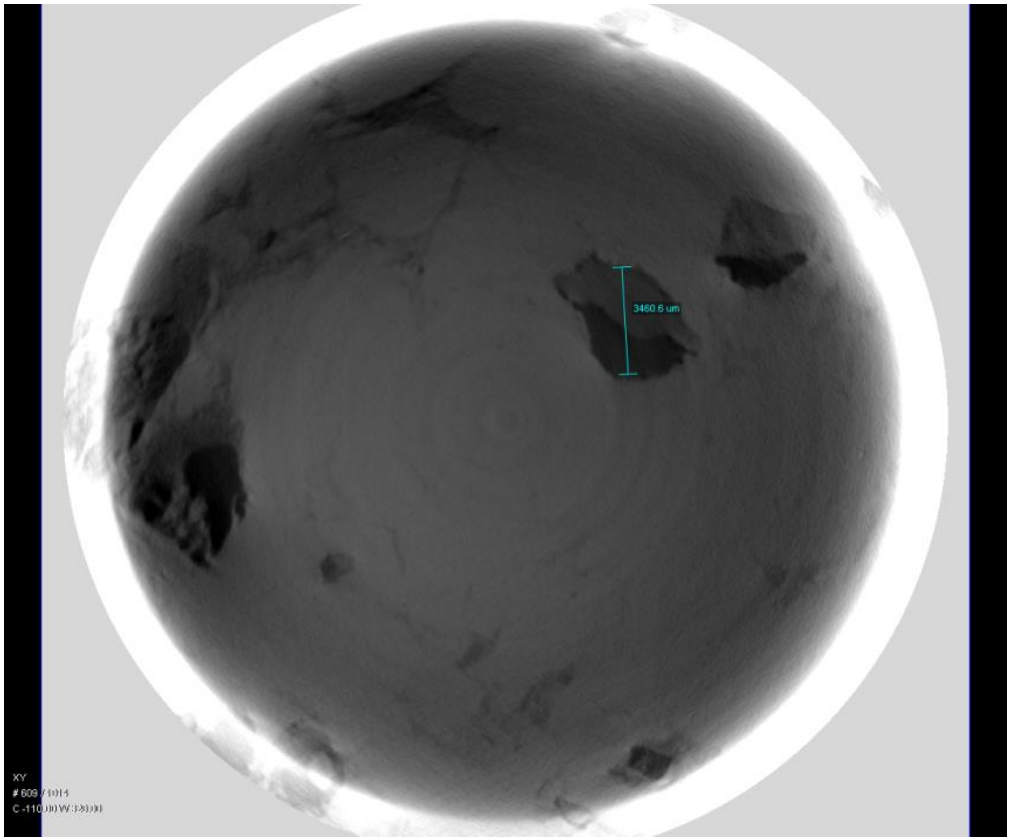

Figure 5- 1. Micro CT Scan image of vuggy limestone. Observe the high relative porosity but reduced connectivity. Scale bar corresponds to 3400 µm.

Sample nr	Lenght (mm)	diameter (mm)	Porosity based on Hg-porosimetry (%)	Porosity based on HE-pycnometry (%)	N_2 Klinkenberg permeability (mD)
B1.1A	46,447	37,197	11,793	17,38	0,667
B1.1B	47,257	37,187	10,405	11,3	0,741
B1.1C	47,373	37,22	7,969	15,562	0,066
B1.2A	44,947	37,307	7,042	14,586	5,456
B1.2B	43,83	37,27		10,058	0,026
B1.3A	46,24	37,25	6,974	8,55	0,008
B1.3B	45,087	37,297		12,587	<0,001
B1.4A	50,173	37,267	15,012	22,388	<0,001
B1.4B	49,833	37,29		25,897	2,202
B1.4C	49,66	37,263		29,887	0,531
B1.5A	47,493	37,23	9,754	22,283	0,16
B1.5B	47,227	37,207		14,365	0,017
B1.5C	47,113	37,223		12,356	<0,001
B1.6A	44,107	37,283		6,514	7,547
B1.6B	38,213	37,283		5,188	0,899
Mean				**15,26**	**1,527**

Table 5- 2.Results from different samples of the vuggy limestone formation. Hg-intrusion porosity was measured with a PoreMaster GT equipment. He porosity was measured by an Quantachrome Instruments Ultrapic 1200e. N_2 permeability was measured with a VINCI Technologies Gasperm steady state gas permeameter under 400 psi confining pressure.

Sample	T (°C)	pH	HCO_3^- mg/L	Na mg/L	Mg mg/L	Ca mg/L	Cl^- mg/L	SO_4^{2-} mg/L	K mg/L
S-1	22,6	7,16	244	8342,54	582,25	1397,08	15760,4	1519,78	342,88
S-2	21,5	8,7	27,35	6311,93	341,92	1089,06	11797	1058,36	277,6
S-3	21,6	9,33	23,69	6399,69	337,8	1149,24	12078,6	1084	276,38
S-4	21,6	6,77	351,77	9964	922,15	1948,03	19915,1	2112,91	466,02
S-5	21,7	6,73	349,73	9678,57	920,08	1866,78	19348,4	2041,61	479,79
S-6	21,4	6,77	246,03	9777,57	935,25	1951,48	19589,8	2062,85	479,76
S-7	21,3	6,67	367,02	8481,93	960,48	1709,28	16916,2	1790,72	493,8
S-8	21	7,16	134,2	8593,03	693,22	1540,97	16698,9	1645,39	405,83
S-9	21,5	7,04	277,55	9224,68	812,14	1734,41	18378,9	1865,35	457,63
S-10	21,7	6,82	329,4	9993,52	992,26	1991,67	19972	2182,76	524,51
S-11	22,1	6,98	335,5	10383,6	1004,24	2058,3	20839,9	2241,98	536,47
average	**21,64**		**244,2**	**8831,91**	**772,89**	**1676,03**	**17390,47**	**1782,34**	**430,97**

Table 5- 3. Brine composition from a prospection well in Hontomín. The samples were taken along 11 days and the results were average in order to elaborate synthetic brine for the experiments.

The experiment proceeded in three consecutive stages. First, N_2 was injected for the measurement of the gas permeability at experimental conditions. That was followed by the injection of deionized water (DIW) and then by a new injection and fluid substitution with a synthetic brine (SB) whose composition is similar to that reported for the Hontomín formation water (Table 5- 3). The SB solution was elaborated by the adding of NaCl, $CaCl_2.2H_2O$, $MgCl_2.6H_2O$, KBr, Na_2SO_4 and KBr to a DIW in order to elaborate a similar fluid in accordance with the composition of the formation fluid. After mixing the solution that was filtered using a cellulose nitrate filter of 0.45 microns. The electric conductivity (EC) of the brine is around 48.000 µS/cm. Finally, the SB solution was saturated with CO_2 (SBSC) after equilibration at 3.5 MPa and room temperature. This pressure was set lower than the injection pressure in order to avoid unmixing and formation of a biphasic fluid. Further details are provided later on. During the experiment, axial deformation, axial load, confining and pore pressure were measured.

The experiment was kept in operation during 24 days and, in that time, more than 180 pore volumes (PV) of the different fluids (DIW, SB, SBSC) were circulated through the sample. The average flow was 36 mL/day (~0.035 mL/min). The initial porosity of the rock was about 9.6%.

5.2.1 Experimental Setup

The experiment was performed under an axi-symmetric confining stress conditions by inserting the sample into a modified Hoek and Frankin-type cell (Hoek and Franklin 1967). The vertical force was applied by a piston rod connected to a loading frame. This element is actuated by one Enerpac P-80 hydraulic hand-operated pump. Additionally, this device was equipped with our own design of an aluminium shield covered by a resistance wire that can heat the Hoek cell. There is a temperature sensor inside the Hoek cell that´s connected to a temperature controller, also to the heat resistance. The confining pressure is applied to the cell by pressurizing the confining oil using a servo controlled pump (Teledyne Isco 260D). Axial pressure is transmitted to the sample by special platens designed also to apply the pore pressure to the sample in its edges. The test was conducted at 40 °C of temperature and constant stress conditions (σ_{ax}=30 MPa; σ_c=10MPa). Loading of the sample was performed stepwise: In the first step the axial and confining pressures were increased simultaneously (Q=0) and at a constant rate to the target value of confining pressure. From hereafter σ_1 was increased while keeping constant $\sigma_{2,3}$. These conditions are a step in the knowledge about the permeability change and the mechanical behaviour under reactivity changes due to the addition of the CO_2.

Each of the compression platens incorporate two fluid ports connected to a thru-hole. For a better distribution of the injected fluid, the surfaces in contact with the sample are grooved with concentric circles and radial lines connecting them. During the loading process, in order to avoid an undesired increase of the pore pressure, the sample was kept drained (i.e. inlet and outlet ports open). The fluid ports of one of the compression platens were connected to a dual Teledyne Isco DX-100 high pressure syringe pump. This pump was used to inject, at a constant fluid pressure (Pp) of 4 MPa the flooding fluids. The pressure drop between the inlet and outlet ports was monitored with two high resolution (0.01%) absolute pressure transducers (Keller-Drück LEO Record Ei). This data was used to evaluate permeability using Darcy's Law for steady flow (Luquot and Gouze 2009).

Due to the high hydraulic conductivity of the tested sample, in order to reduce the Darcy's velocity to an acceptable value, a small constant pore pressure gradient of 4 bar was imposed (i.e. 4 MPa at the inlet and 3.6 MPa at the outlet of the core plug). The outlet pore pressure is governed by a back pressure valve (BPV), after that, the exit of this valve is connected to a tube line whose purpose was to collect the water circulated through the sample (outlet fluid). This line was equipped with a low volume flow-thru, temperature compensated, microelectrode array (Microelectrodes Inc. refs. 8-702, 8-705 and 8-900, corresponding to reference, pH and conductivity electrodes, respectively) all of them attached to an ELIT 9705b Aqualyser

(Nico2000 Ltd.) for data acquisition purposes. Because these microelectrodes cannot attain pressures higher than 100 kPa, the fluid was decompressed prior to the measurements, after the BPV. However, the decompression of the fluid in the CO_2-saturated water injection phase triggered the outgassing of CO_2 and the growth and transient accumulation of small gas bubbles in the dead volume of the microelectrodes. This turned out to increase the internal pressure and, as a result, small external leaks from the 3 M KCl reference electrode happened. That made necessary the continuous maintenance and recalibration of the electrodes, with long periods without measurements. We believe that the data recorded captured the general trend of the experiment but the problems reported make us to put a note of caution on what it can be concluded from its interpretation.

The effluent water was collected on a daily basis pH and electrical conductivity (EC) were measured and the composition of the water samples was analysed (Ca, Mg, Fe, SiO_2, F, Cl, Br and SO_4), in order to understand the chemical change inside the rock under the experimental conditions. The pH was tested with a Crison GLP 22, the CE of the DIW with a pattern of 1413 µS/cm and 12.88 µS/cm, the sensor used was a Crison GLP 32 meanwhile for the brine we use a pattern of 50 mS/cm in a conductivity meter Hach Sension5.

The top and bottom compression platens are instrumented each with a stack of 1.3 MHz resonant frequency piezoelectric transducers

(PZT) for the measurement of direct (V_P) and shear (V_{S1}, V_{S2}) ultrasonic wave velocities. Squared-pulse waves were generated with a transducer-pulser unit (PT100-1000; ErgoTech Ltd.) and monitored with a digital oscilloscope (PicoScope 3204A; Pico Technologies Ltd.). Velocities were determined applying the time of flight technique, according to the recommendations given in Rummel et al. (1978).

The saturation of water with CO_2 was accomplished in a 2.7 L carbonation vessel which was filled with synthetic brine. To accelerate the saturation process, CO_2 was micronized at low pressure (~0.5 MPa) into small bubbles in the liquid using five sintered filters. CO_2 was delivered in excess, what allowed the development of a CO_2 headspace in order to saturate the brine in the conditions designed. The compression of the system to the target pressure of 3.5 MPa was performed with a manual pressure generator (HiP mod. 62-6-10) at room temperature. The system was left to equilibrate for a week, although different sources in the literature (Diamond and Akinfiev 2003) report that equilibrium can be reached in 24 to 48 h. The transfer of fluid from the carbonation vessel to the ISCO pump was performed by setting the later in constant pressure mode and a back-pressure regulator, both set to 4 MPa, because if the pressure would decrease it could be created a biphasic fluid. According to the EOS described in (Duan and Sun 2003; Duan et al. 2006), the theoretical concentration of CO_2.

5.3 Results and discussion

Figure 5- 2 to Figure 5- 5 summarize a part of the chemical information obtained during the experiment. Figure 5- 2 illustrates the evolution of pH and specific conductance following eluate decompression. Thus, these values need to be recomputed (see Canal et al., (2013)) in order to better describe the geochemical evolution of the system. In general, we observe a reasonably good correspondence between the microelectrode-measured parameters (continuous lines) and those obtained after collecting the eluate in a beaker for a given time (dots and dashed lines).

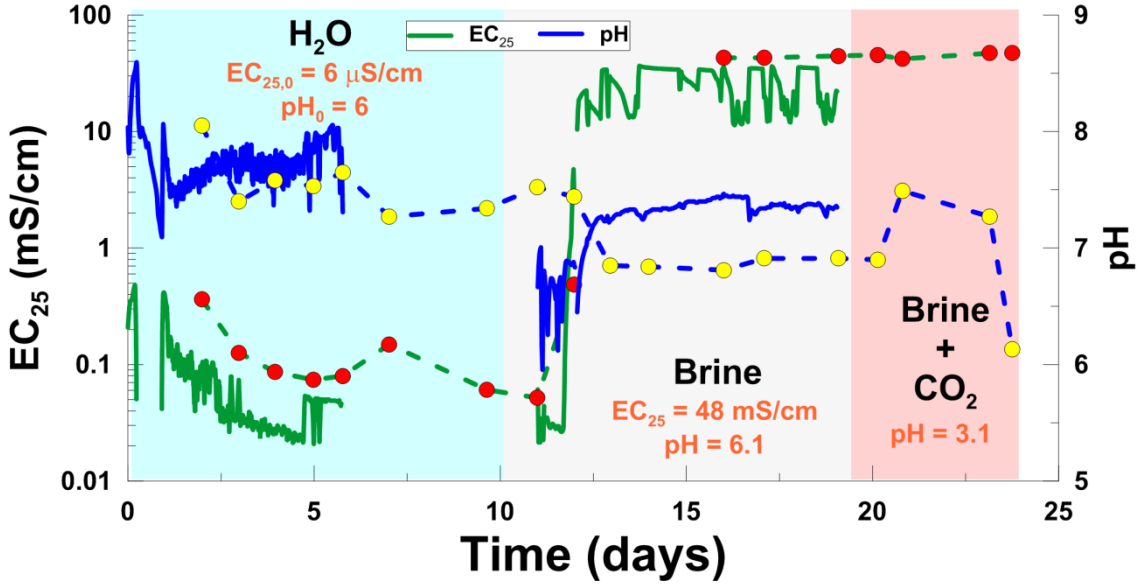

Figure 5- 2. Evolution of pH and specific conductance during the different injection stages of the experiment performed with a vuggy limestone of the Hontomín main reservoir. Dots and dash lines represent measurements performed after collection of eluates in a beaker while the continuous line correspond to 1-hour averaged values measured with a microelectrode array.

Microelectrodes are prone to bubble formation upon fluid decompression so care must be paid before using the experimental data. However, we see that the specific conductance has a rather neat tendency: A salt washout period (following the injection of DIW and up to ~5 days) and the attainment of a steady background value from hereafter and its sudden increase when the saline solution is injected (~12 days since the beginning of the test). From that point to the end of the experiment, EC_{25} remains constant with a value equal to that of the injected solution. That means that the dissolution processes occurring in the sample are not enough to trigger a significant change in this parameter. pH, on the other hand shows a more or less steady value of ~7.7 during most of the DIW injection stage and then drops to ~7 when the saline solution is injected. Both values are higher than the ones corresponding to the initial solutions what demonstrates the buffering effect of the carbonate rock upon the fluid. The injection of the CO_2-saturated saline solution makes pH to rise up to a final moment, when it suddenly drops following the sharp increase of hydraulic conductivity. We conjecture that this behaviour is related with the increase of the flow rate and the concomitant modification of the Damkhöler number.

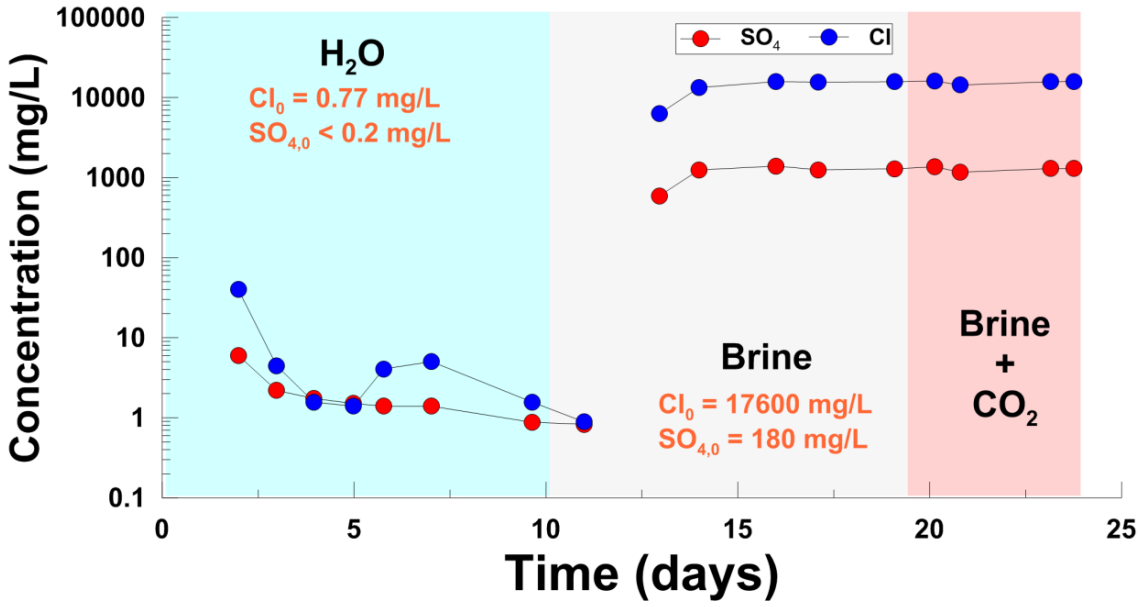

Figure 5- 3. Evolution of the aqueous concentrations of Cl and SO_4 during the different injection stages of the experiment performed with a vuggy limestone of the Hontomín main reservoir. Concentrations in the corresponding injectates are also illustrated.

Figure 5- 3 shows the evolution of two nearly conservative components. In fact, in the DIW injection stage, a progressive reduction in the concentrations of both components is observed what is associated to the washout of evaporitic minerals (gypsum, halite) already present in the porous space of the rock. The injection of the saline solution (either CO_2 saturated or not) makes increase their concentrations to its corresponding value but, because no further reactions involving these components occur, their concentrations remain steady up to the end of the experiment.

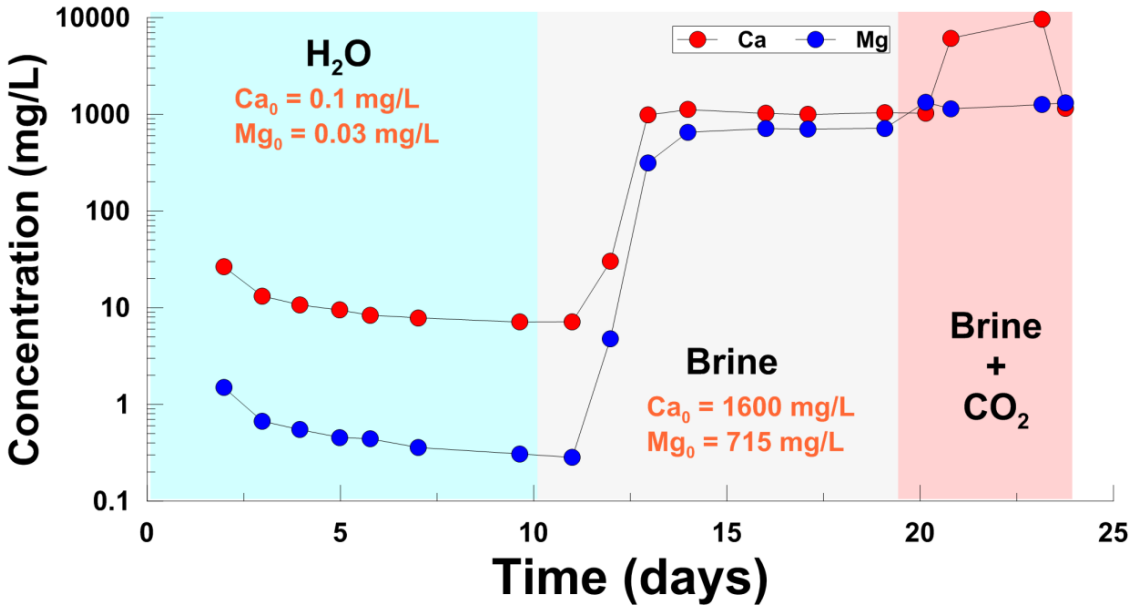

Figure 5- 4. Evolution of the aqueous concentrations of Ca and Mg during the different injection stages of the experiment performed with a vuggy limestone of the Hontomín main reservoir. Concentrations in the corresponding injectates are also illustrated.

Figure 5- 4 illustrates the evolution in the concentration of Ca and Mg. in general, their behaviour is similar to that described for the previous components. It is worth to mention that the SB saline solution is close to saturation with respect calcite so it is not to expect that mass transfers associated to the dissolution/precipitation of carbonates induce significant changes in relation with the chemical composition of the saline water. However, the injection of the SBSC, CO_2-saturated, saline solution conducts to a sharp rise in the concentration of Ca (much less in the case of Mg) evidencing the enhanced dissolution of calcite in this acidic media. At the end of the experiment, the

concentration of Ca drops, what it is likely connected with the commented change in the Damkhöler number.

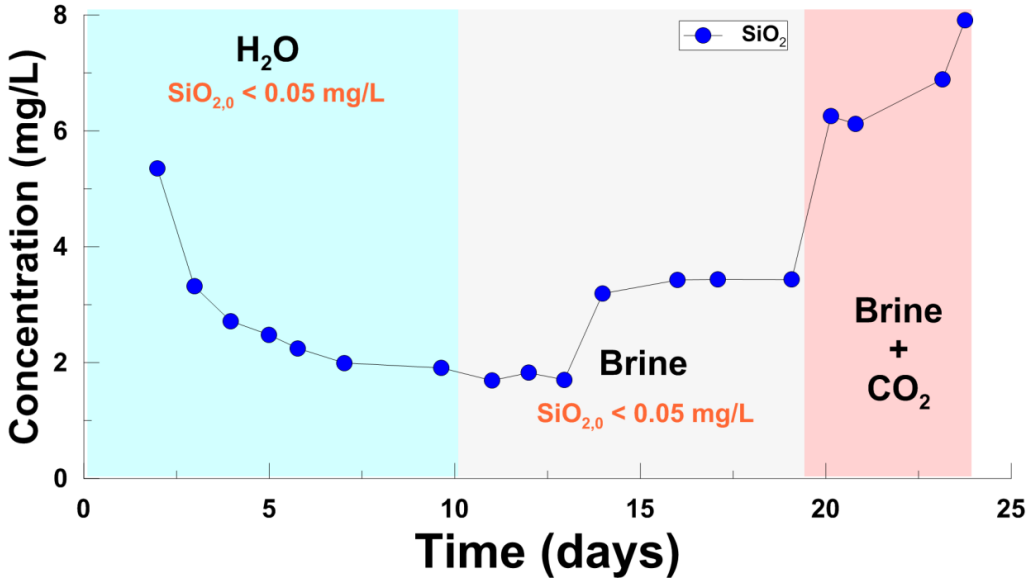

Figure 5- 5. Evolution of the aqueous concentrations of SiO_2 during the different injection stages of the experiment performed with a vuggy limestone of the Hontomín main reservoir. Concentrations in the corresponding injectates are also illustrated.

Figure 5- 5 shows the behaviour of SiO_2. It is interesting to remember that, although the most relevant components in this rock are carbonate minerals, clays may play also their role. Thus, following an initial period when the SiO_2 concentrations decrease (a phenomena likely linked to the early dissolution of SiO_2-bearing substances of source-limited poor crystallinity), we observe an increase in its concentration which is more pronounced when the P_{CO2} is higher.

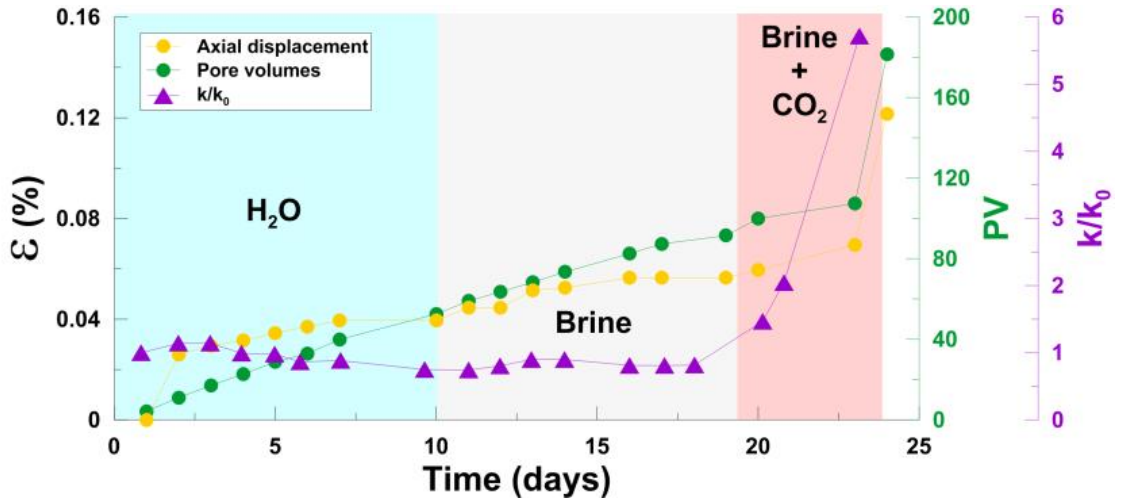

Figure 5- 6. Evolution of permeability and axial displacement during the different injection stages of the experiment performed with a vuggy limestone of the Hontomín main reservoir.

The evolution of permeability (expressed in relative change with respect that at the beginning of the test) is depicted in Figure 5- 6. We observe that, while for the major part of the test that remained steady ($\sim 10^{-9}$ m/s) the arrival of the CO_2-saturated saline (SBSC) solution promoted a dramatic increase in this parameter. This is connected with a concomitant increase in rate of the vertical displacement of the sample. In fact, such a steep rise determined the necessity of stopping the experiment due to the difficulties in keeping constant the pore pressure gradient. Obviously, this behaviour is connected with the massive dissolution of carbonate from the rock, which appears to be improved the connectivity among the big pores of the sample. Some evidences of wormholes were observed in the injection facet of the plug although X-ray tomographic information was not available at the time the test was performed.

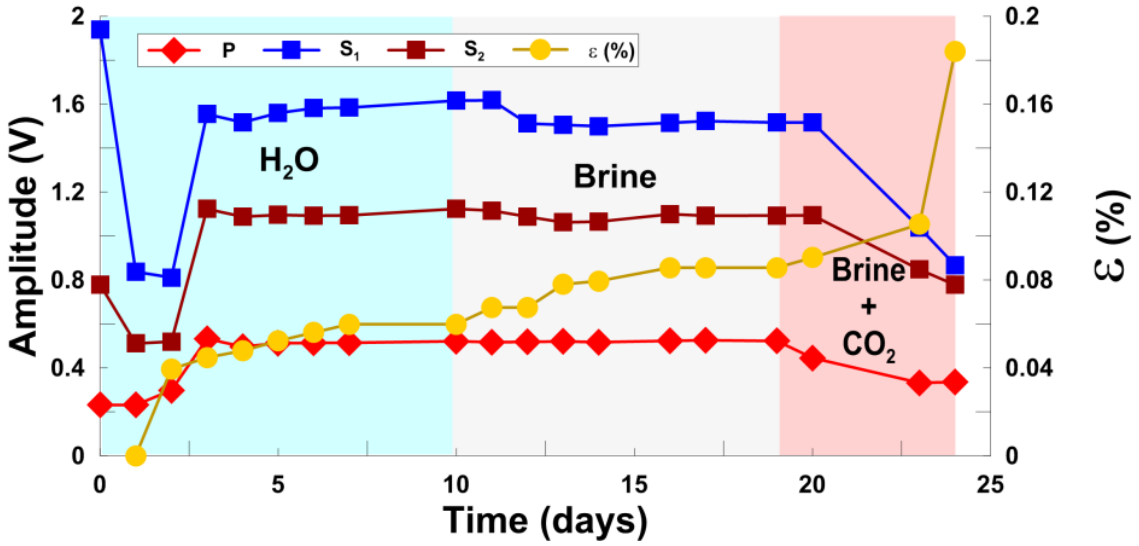

Figure 5- 7. Evolution of axial strain (yellow dots) and the amplitude of elastic V_P (green diamond) and V_S (red and blue squares) waves during the different injection stages of the experiment performed with a vuggy limestone of the Hontomín main reservoir.

Figure 5- 7 shows the evolution of axial strain in the studied sample and we observe that, although deformation occurs at a more or less constant rate since the early stages of the experiment, it suddenly accelerates when the SBCS solution is injected. This result is compatible with the observed hydrodynamic behaviour and we conjecture that the strength of the sample becomes reduced due to the accelerated dissolution of its carbonates. In the same figure we also observe an interesting evolution connected with the behaviour of elastic waves in the different stages. Thus, following a first stage in which the wave amplitudes change (probably due to the progressive saturation of the sample) they become steady both in the DIW and the SB solution injection stages. However, a significant drop in amplitudes

(damping) is observed upon the arrival of the SBSC solution. Attenuation has been recognized as a significant seismic indicator, which is not only useful for amplitude analysis and improving resolution, but also to obtain information on lithology, saturation (fluid type), permeability and pore pressure (Carcione and Gangi, 2000).

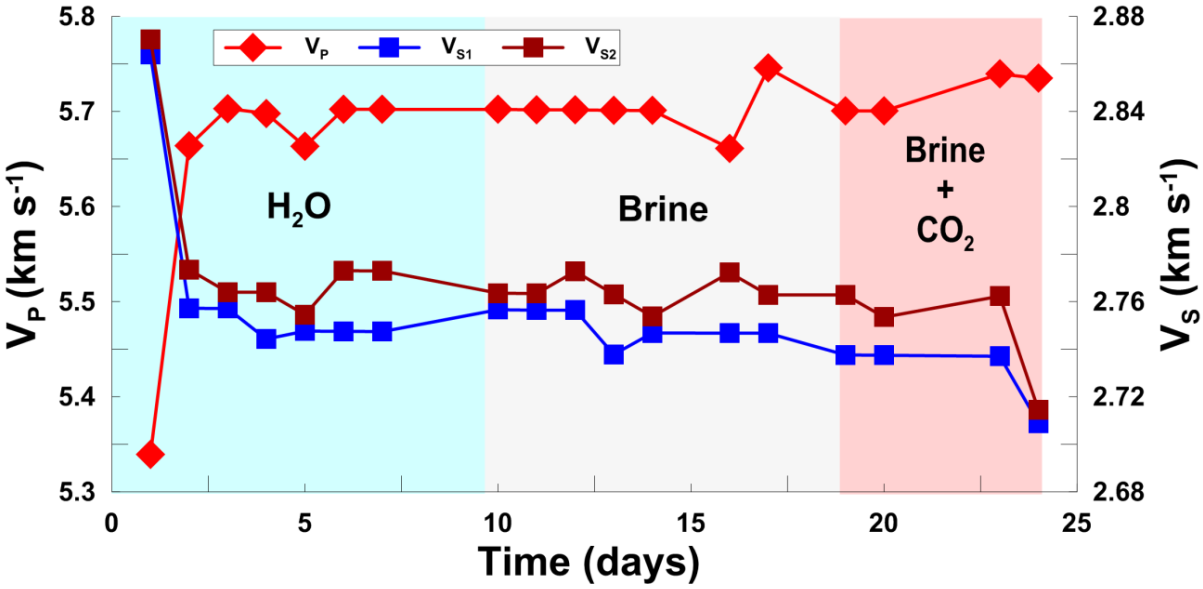

Figure 5- 8. Evolution of P (green circles) S_1 (blue squares) and S_2 (red diamonds) ultrasonic velocities during the experiment. These parameters were measured every day but the horizontal scale reflects the pore volume, and it varied during the experiment because the constant imposition of the experiment was the inlet and the outlet pressure.

The changes in the wave velocities during the experiment can be observed in Figure 5- 8. The first significant velocity change (about 2 days) is due to the saturation of the rock: At the beginning of the experiment, the connected pore space is not fully saturated, so the P velocity increases with saturation and the opposite occurs with the S-wave velocities. The SB injection stage does not result in any particular

change, but with the addition of CO_2 to the synthetic formation fluid (SBSC stage) determines a certain reduction in the P-wave velocity and increase of the corresponding S-wave velocities. This likely occurs as the result of changes in the pore space (carbonate dissolution) triggered by the injection of the acidic fluid.

The changes in velocities are also connected with a significant reduction in the amplitude of the waves as observed from the corresponding waveforms (Figure 5- 9)

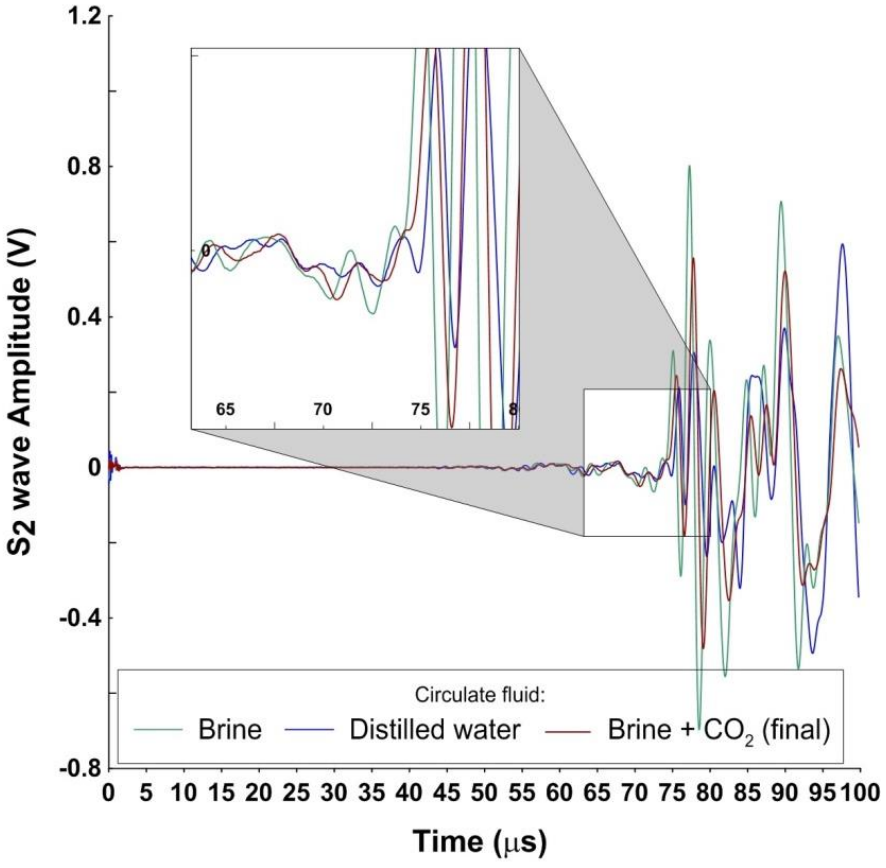

Figure 5- 9. Amplitude attenuation of three representative waveforms associated with the three stages of fluid injection in the experiment performed with a vuggy limestone of the main reservoir of the Hontomín PDT site. Note: DIW (blue line), SB (green line) and SBSC (red line).

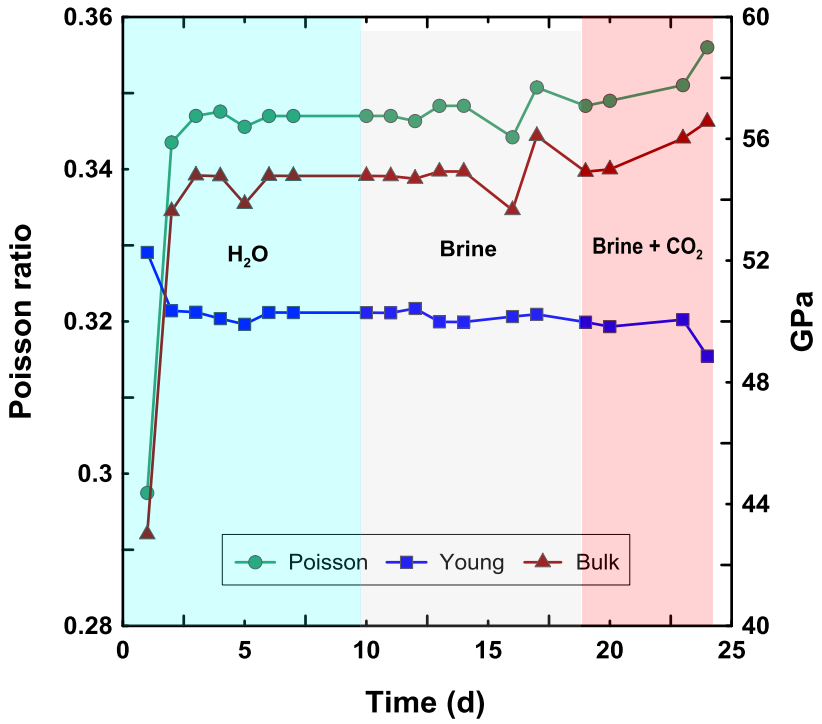

Figure 5- 10. Evolution of Poisson ratio (green), bulk modulus (red) and Young (blue) modulus during the experiment.

In Figure 5- 10 we observe the evolution of the computed dynamic Young's modulus. We observe that this parameter is nearly invariable although in the last day (coupled with the sudden increase in permeability and vertical strain) it suffers a decrease because of the dissolution of the rock. The Poisson´s ratio and bulk´s modulus show the same tendency. This increase would be due to the density rise in the pore fluid. Similar behaviours have been recently described by other authors (Hangx et al. 2013). On the other hand, we conjecture that the variation in the first days of the experiment may be explained by the full saturation of the sample.

Comparing the shape of the P and S-waves (Figure 5-11,Figure 5-12 and Figure 5- 13) when we switch the study into the frequency domain provides new insights about the fluid/rock interaction processes. For that purpose, FFT (Fast Fourier Transform) analyses have been performed using MATLAB (Santamarina and Fratta 2006a, 2006b). Table 5- 3 shows the peak frequency of each of the studied waveforms (P, S_1 and S_2). Frequencies have been studied along the 25 days that the experiment lasted and from them we can obtain a number of parameters. Each frequency corresponds with the peaks shown in Figure 5-11 to Figure 5- 13. The procedure and methodology to analyse this information is the same as the one presented in Chapter 7. The frequency peaks of the waves were transformed into wavelengths using the speed of the wave for each frequency (Table 5-4). In order to analyse the effect of the velocities in the wavelength, the full frequency spectrum was used to calculate the corresponding wavelength at maximum and minimum velocities. The attenuation is also represented in Table 5- 4. Attenuation has been recognized as a significant seismic indicator, which is not only useful for amplitude analysis and improving resolution, but also to obtain information on lithology, saturation (fluid type), permeability and pore pressure (Carcione and Gangi 2000).

	f (KHz)	Max. Ampl. (mV)	Min. Ampl. (mV)	amplitude decrease (%)	λ Vp max (mm)	λ Vp min (mm)
P wave						
f1	8,77	71889,05	15494,65	78,45	104,73	97,25
f2	40,08	178200,75	34113,04	80,86	22,91	21,27
f3	52,61	383604,42	78311,78	79,59	17,45	16,21
f4	68,89	425408,53	66524,14	84,36	13,33	12,38
f5	78,91	53478,45	10038,24	81,23	11,64	10,81
f6	91,43	361704,72	55583,70	84,63	10,04	9,33
f7	108,97	250609,57	46697,45	81,37	8,43	7,82
f8	129,01	173062,40	34909,44	79,83	7,12	6,61
f9	149,05	38916,70	8766,22	77,47	6,16	5,72
f10	155,31	49433,87	11126,12	77,49	5,91	5,49
S1 wave						
	f (KHz)	Max. Ampl. (mV)	Min. Ampl. (mV)	amplitude decrease (%)	λ Vs_1 max (mm)	λ Vs_1 min (mm)
f1	22,55	2,53	0,41	83,95	20,28	19,22
f2	33,82	0,63	0,13	79,00	13,52	12,81
f3	57,62	1,14	0,24	79,25	7,94	7,52
f4	78,91	1,31	0,29	77,97	5,80	5,49
f5	98,95	1,02	0,21	79,93	4,62	4,38
f6	126,50	0,86	0,05	94,77	3,61	3,43
f7	145,29	0,19	0,00	99,81	3,15	2,98
S2 wave						
	f (KHz)	Max. Ampl. (mV)	Min. Ampl. (mV)	amplitude decrease (%)	λ Vs_2 max (mm)	λ Vs_2 min (mm)
f1	23,80	1,99	0,36	82,06	19,26	17,96
f2	38,83	1,25	0,25	79,70	11,80	11,01
f3	62,63	0,57	0,10	83,41	7,32	6,82
f4	76,40	0,05	0,01	88,39	6,00	5,59
f5	87,68	0,14	0,03	81,54	5,23	4,87
f6	108,97	0,46	0,05	88,87	4,21	3,92
f7	160,32	0,13	0,00	99,99	2,86	2,67
f8	177,86	0,06	0,00	97,93	2,58	2,40

Table 5- 4. P, S_1 and S_2 frequency analysis. In the table is shown the frequency in Hz and KHz, the maximum and the minimum value of the amplitude during the 25 days, the difference between them in percentage (attenuation), the wavelength for the highest and the lowest wave velocity and the variation between them.

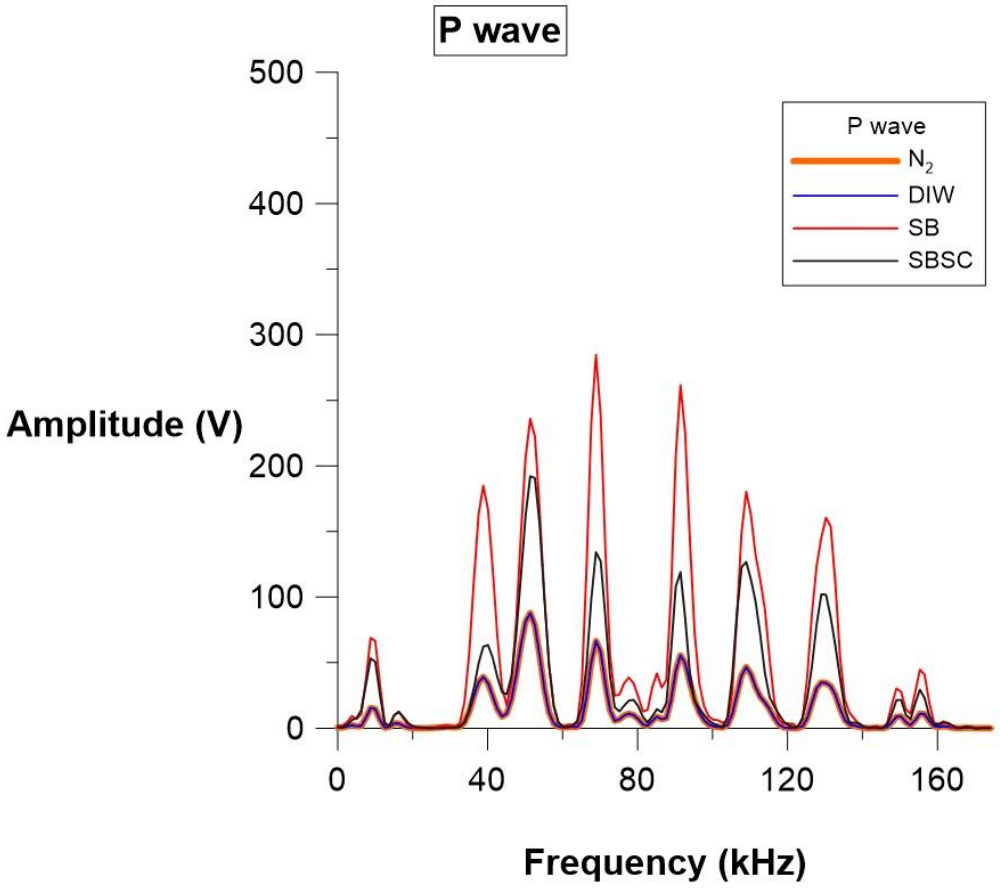

Figure 5- 11. Evolutions of the P wave frequency along the 25 days experiment.

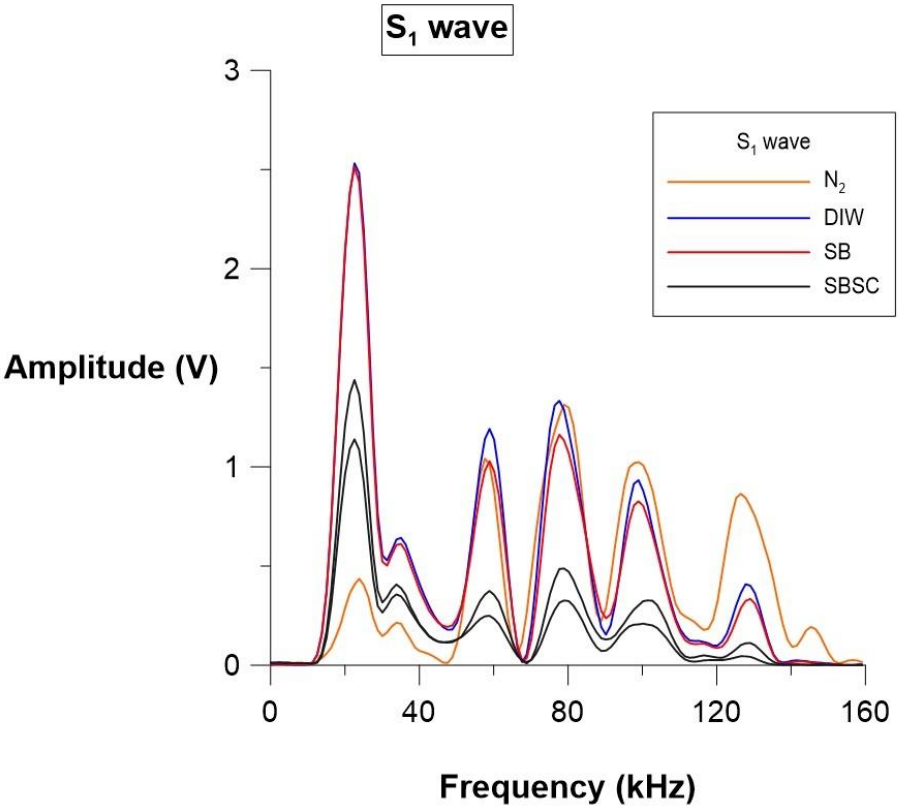

Figure 5- 12. Evolutions of the S_1 wave frequency along the 25 days experiment.

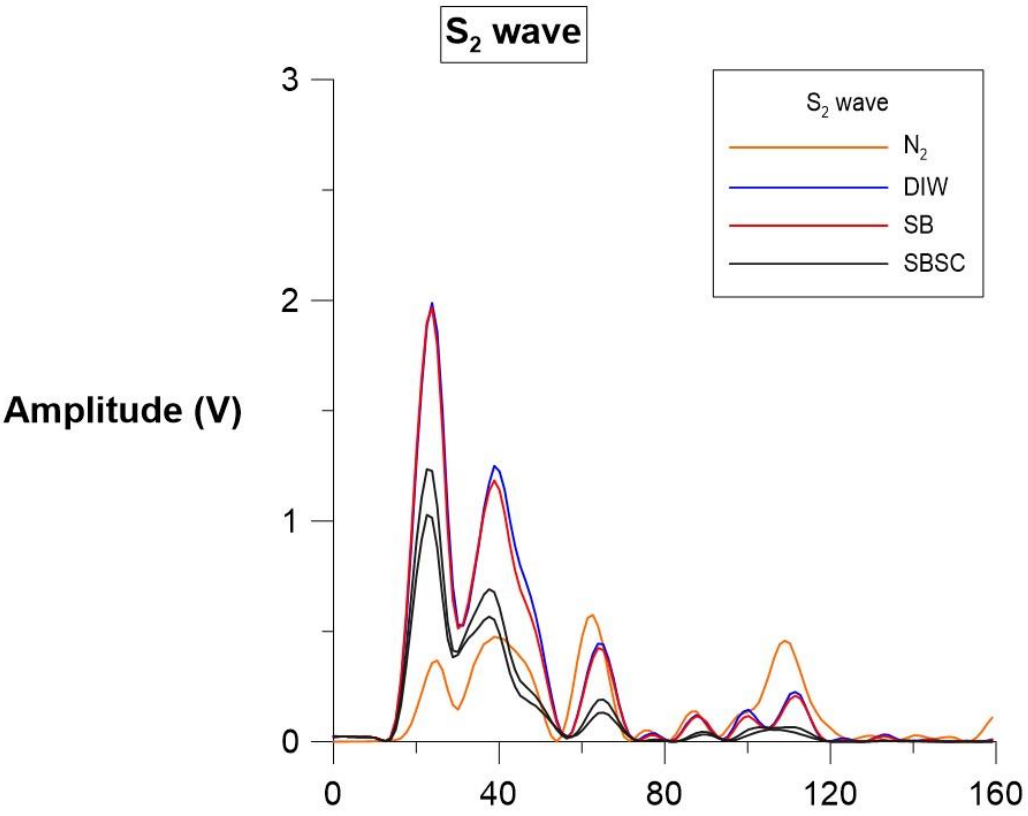

Figure 5- 13. Evolutions of the S_2 wave frequency along the 25 days experiment.

In Figure 5- 11 we observe that the P-wave is sensitive to fluid substitution. During the first day dry N_2 was used to determine the initial gas permeability. Then, during the DIW stage, we observe that the amplitude increases what is consistent with what happens during the following SB injection stage. However, it is worth to note that in the last SBSC injection stage the frequency distribution turns back to the pattern corresponding to the N_2 injection stage. The surface envelope associated with the frequency-amplitude-time corresponding to the P-wave during the 25 days of the experiment has been represented in Figure 5- 14.

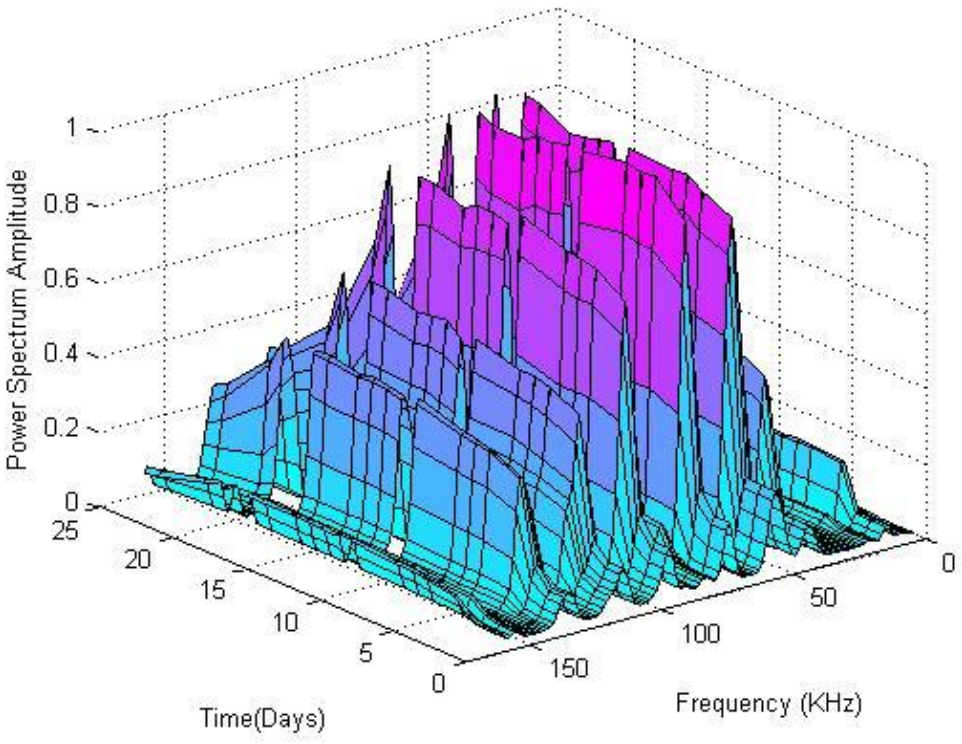

Figure 5- 14. Time evolution of the P wave frequency along the 25 days experiment.

A similar behaviour can be described for the S_1 and S_2-waves (Figure 5- 12 and Figure 5- 13) with the exception of the last reactive stage (SBSC injection). Here we observe that, for the low-frequency (the ones related with the wider wavelengths) the amplitude reduces. We speculate that the origin of this phenomenon is related with the fluid/rock interactions at the grain boundaries as they become progressively corroded (dissolved) by the acidic, CO_2-saturated saline fluid. Upon advancement of the dissolution process, pore collapse and grain reorganization may take place (with the concomitant compaction of the sample (Figure 5- 7) as well as an evolving situation by which changes at the grain-boundary level conduct to changes in the overall frequency spectrum.

5.4 Summary and conclusions

In this chapter we focus in the investigation about the THMC effects of the injection of a reactive, CO_2-saturated, saline fluid into a carbonated rock while monitoring the changes operated in their elastic, ultrasonic and geochemical properties. The selected sample can be considered representative of the main reservoir for the Ciuden CCS project. Our investigation reports chemical and rock physics parameters simultaneously determined during a complex flow through experiment with a vuggy limestone. We observe a significant dissolution coupled with the injection of the acidic fluid what turns out to trigger a significant compaction of the sample. This is connected

with a fast change in its permeability. Likewise, P and S-wave velocities (and their amplitudes) appear to be sufficiently sensitive to detect the weakening of the material. Therefore, it is important that the short term effect of CO_2 injection on mechanical properties is investigated for such formations. The study of the P and S frequency spectrum provide with complementary information. Thus, while with the P-wave fluid substitution is observed, the change of the S-wave amplitudes may reveal internal rock change during the acidic injection perhaps at the grain boundary level.

The previous examples illustrate well what we believe is the way forward for a better understanding of coupled THMC processes. Such an approach encompasses added values when we combine with the geophysical prospecting tools intended to use for monitoring, accounting and verification of CCS or oil & gas industry related projects.

At present, our work is mainly addressed to the improvement of the experimental rig in order to make possible the simultaneous examination of hydrodynamic (flow and permeability), mechanic (strain), wave propagation (V_P, V_S) and electrical (i.e. resistivity) properties in core plugs of variable size while keeping track of the chemical composition of the eluates in long-lasting experiments (weeks to months). Special attention is being devoted to the continuous monitoring of aqueous chemical parameters (specific

conductance and pH) under in situ conditions by implementing high pressure/high temperature electrodes.

While the typical core plugs used so far for us have a typical diameter of 38.1 mm diameter, this is insufficient for working with vuggy carbonates for which the minimum acceptable diameter would be ~100 mm if its greatest vug is in the order of 1 cm.

5.5 References

Alcalde J, Marzán I, Saura E, Martí D, Ayarza P, Juhlin C, et al. 3D geological characterization of the Hontomín CO_2 storage site, Spain: Multidisciplinary approach from seismic, well-log and regional data. Tectonophysics. 2014;627:6–25.

Beroiz C, Permanyer A. Hydrocarbon habitat of the Sedano trough, Basque-Cantabrian basin, Spain. J Pet Geol. Wiley Online Library; 2011;34(4):387–409.

Canal J, Delgado J, Falcón I, Yang Q, Juncosa R, Barrientos V. Injection of CO_2-saturated water through a siliceous sandstone plug from the Hontomin test site (Spain): Experiment and modeling. Environ Sci Technol. 2013;47(1):159–67.

Carcione JM, Gangi AF. Non-equilibrium compaction and abnormal pore-fluid pressures: effects on rock properties1. Geophys Prospect. Blackwell Science Ltd; 2000;48(3):521–37.

Diamond LW, Akinfiev NN. Solubility of CO_2 in water from −1.5 to 100 °C and from 0.1 to 100 MPa: evaluation of literature data and thermodynamic modelling. Fluid Phase Equilib. 2003;208(1–2):265–90.

Duan Z, Sun R. An improved model calculating CO_2 solubility in pure water and aqueous NaCl solutions from 273 to 533 K and from 0 to 2000 bar. Chem Geol. 2003;193(3–4):257–71.

Duan Z, Sun R, Zhu C, Chou IM. An improved model for the calculation of CO_2 solubility in aqueous solutions containing Na^+, K^+, Ca^{2+}, Mg^{2+}, Cl^-, and SO_4^{2-}. Mar Chem. 2006;98(2–4):131–9.

Elío J, Nisi B, Ortega MF, Mazadiego LF, Vaselli O, Grandia F. CO_2 soil flux baseline at the technological development plant for CO_2 injection at Hontomin (Burgos, Spain). Int J Greenh Gas Control. 2013;18:224–36.

Franklin. Suggested methods for determining the strength of rock materials in triaxial compression: Revised version. Int J Rock Mech Min Sci Geomech Abstr. 1983;20(6):285–90.

Hangx S, van der Linden A, Marcelis F, Bauer A. The effect of CO_2 on the mechanical properties of the Captain Sandstone: Geological storage of CO_2 at the Goldeneye field (UK). Int J Greenh Gas Control. 2013;19(0):609–19.

Herrmann W, Berry RF. MINSQ – a least squares spreadsheet method for calculating mineral proportions from whole rock major element analyses. Geochemistry Explor Environ Anal. 2002 Nov 1;2(4):361–8.

Hoek E, Franklin JA. A simple triaxial cell for field or laboratory testing of rock. Imperial College of Science and Technology, University of London; 1967.

Luquot L, Gouze P. Experimental determination of porosity and permeability changes induced by injection of CO_2 into carbonate rocks. Chem Geol. Elsevier; 2009;265(1):148–59.

Mavko G, Mukerji T. Bounds on low-frequency seismic velocities in partially saturated rocks. Geophysics. 1998;63(3):918–24.

Ogaya X, Queralt P, Ledo J, Marcuello Á, Jones AG. Geoelectrical baseline model of the subsurface of the Hontomín site (Spain) for CO_2 geological storage in a deep saline aquifer: A 3D magnetotelluric characterisation. Int J Greenh Gas Control. 2014;27:120–38.

Permanyer A, Márquez G, Gallego JR. Compositional variability in oils

and formation waters from the Ayoluengo and Hontomín fields (Burgos, Spain). Implications for assessing biodegradation and reservoir compartmentalization. Org Geochem. Elsevier; 2013;54:125–39.

Quesada S, Dorronsoro C, Robles S. Genetic relationship between the oil of the Ayoluengo field and the Liassic source-rock of the Southwestern Basque-Cantabrian Basin (Northern Spain). Org Geochemistry Dev Appl to Energy, Clim Environ Hum Hist. AIGOA, Donostia-San Sebastian; 1995;461–3.

Quesada S, Dorronsoro C, Robles S, Chaler R, Grimalt JO. Geochemical correlation of oil from the Ayoluengo field to Liassic black shale units in the southwestern Basque-Cantabrian Basin (northern Spain). Org Geochem. Elsevier; 1997;27(1):25–40.

Quesada S, Robles S. Organic geochemistry, distribution and depositional dynamics of the Liassic organic facies of the Basque-Cantabrian Basin (Northern Spain). Org Geochemistry Dev Appl to Energy, Clim Environ Hum Hist. AIGOA, Donostia-San Sebastian; 1995;464–5.

Quesada S, Robles S, Pujalte V. El Jurásico Marino del margen suroccidental de la Cuenca Vasco-Cantábrica y su relación con la exploración de hidrocarburos. Geogaceta. 1993;13(1993):92–6.

Rummel F, Alheid HJ, Frohn C. Dilatancy and fracture induced velocity changes in rock and their relation to frictional sliding. pure Appl Geophys. Birkhauser-Verlag; 1978;116(4-5):743–64.

Santamarina JC, Fratta D. Frequency Domain Analysis of Signals (Discrete Fourier Transform). Discret Signals Inverse Probl. John Wiley & Sons, Ltd; 2006a. p. 103–36.

Santamarina JC, Fratta D. Frequency Domain Analysis of Systems. Discret Signals Inverse Probl. John Wiley & Sons, Ltd; 2006b. p. 137–74.

CHAPTER 6. CHARACTERIZATION AND MULTIFACETED ANISOTROPY ASSESSMENT OF CORVIO SANDSTONE

6.1 Introduction

The injection of reactive fluids like CO_2 into geological formations within the context of operations for enhanced oil recovery (EOR) or carbon capture and storage (CCS) projects has been widely studied in the recent past. Before implementing CO_2 on large scale sites, it is crucial to assess the viability of the associated geological context. In this regard, the main concern is that the injection may potentially trigger a series of interlinked phenomena that affect the physical (or mechanical) and hydraulic properties of the reservoir, its seal or even the cementing materials used in wellbores (Kutchko et al. 2008; Hangx et al. 2010; Liu et al. 2012; Rutqvist 2012; Song and Zhang 2013). Because water is always present in the porous space of these systems, the forced injection of CO_2 (whether in gas, liquid or supercritical state) induces significant acidification and onsets reactive processes which are especially notorious in the presence of carbonate or carbonate-bearing rocks (Gaus 2010). Siliciclastic formations are not expected to react significantly with CO_2 injection, although the presence of lesser amounts of reactive minerals may play a significant role in their geological storage performance (Canal et al. 2013). Because they are low reactive formations with high storage capacities, brine saturated sandstone reservoirs constitute target CO_2 storage formations.

The success in the assessment of a reservoir heavily relies on an adequate understanding of the coupled thermal, hydrodynamic, mechanical and geochemical (THMG) coupled processes that occur during fluid-rock interaction. Typically, laboratory studies of reservoir and seal formation rocks are a major input to the assessment process. The limited availability (or even absence) of in situ samples is commonly solved by using rock analogues to the ones found in the target reservoir. A significant amount of literature can be found on the use of rocks with well-known properties for conducting a range of laboratory tests (strength, permeability, etc.), to understand the behaviour of reservoir core flooding or to check instrument performance (Churcher et al. 1991). Also, in recent years, digital rock physics has evolved rapidly through the increasing resolution of X-ray computed tomography (CT) imaging , and has become a valuable tool for quick, non-destructive assessment of many rock properties (Andrä et al. 2013). However, these digital imaging techniques still require standard rock samples for calibration purposes and complementary destructive/non-destructive tests.

The specialist literature includes a wide number of reference rock materials used in many research works so that they now constitute de facto standard materials within the discipline of rock mechanics/rock physics. Among many other rocks, Berea sandstone (Krevor et al. 2012; Pini et al. 2012; Akbarabadi and Piri 2013; Nakagawa et al. 2013; Oh et al. 2013), Tako sandstone (Xue and Ohsumi 2004; Xue and Lei

2006; Lei and Xue 2009; Nakatsuka et al. 2010) Bentheim sandstone (Klein et al. 2001), Bleurswiller sandstone (Fortin et al. 2005), Fontainebleau sandstone (Fredrich et al. 1993; Song and Renner 2008), Donnybrook sandstone (Mikhaltsevitch et al. 2014) and Navajo sandstone (Lu et al. 2011) have been used to investigate CO_2 injection in sandstone reservoirs, as well as for general reference materials in the petroleum industry. However, despite their widespread use and availability, none of them can be considered to be truly traceable standard materials because they display significant heterogeneity and anisotropy (although these are in themselves valid properties). Indeed, most sedimentary rocks of interest in exploration geophysics are considered to be weakly anisotropic, i.e., with less than 20% anisotropy (Thomsen 1986). Sample heterogeneity is the greater problem because of what constitutes a representative laboratory sample volume for valid upscaling of measured properties to large geological formations. The key point is that both heterogeneity and anisotropy must be accurately quantified for a valid standard material, not always achieved in the above mentioned works.

Sample anisotropy can be assessed from the contrast in P- and S-wave velocities propagating in directions orthogonal and parallel to bedding planes (Thomsen 1986; Wang 2002; Schubnel et al. 2006; Martínez and Schmitt 2013), and similarly for P- and S-wave attenuation (Q^{-1}, the reciprocal of the quality factor Q; Zhu and Tsvankin 2006; Best et al. 2007; Zhu et al. 2007; Chichinina et al.

2009). Electrical resistivity (Ellis et al. 2010) and magnetic susceptibility (e.g. Louis et al. 2004) have also been employed for this purpose. Although weak anisotropy can lead to negligible effects in some instances (Thomsen 1986), especially at the laboratory scale, it can be significant for the accurate calibration of geophysical techniques, fluid transport phenomena (e.g., fingering) and when studying THMG coupled processes.

Corvio sandstone was chosen as a local reference material during the commissioning a CO_2 injection pilot plant in Northern Spain (Alcalde et al. 2014). We present a comprehensive laboratory characterization of the properties of Corvio sandstone including anisotropy. The aims of this work is to summarize the most relevant physical, chemical, geomechanical and hydrodynamic properties of Corvio sandstone to provide a baseline database for subsequent studies, and to identify the extent and magnitude of anisotropy to inform studies of its possible impact on THMG coupled processes associated with CO_2 storage in siliceous sandstone reservoirs.

6.2 Materials and methods

Most of the work presented in the present chapter has been developed at the Laboratory of Rock Mechanics (LAMEROC) of the University of A Coruña and, to a limited extent, at the National Oceanography Center (NOC) of Southampton (United Kingdom).

Description of the equipment and experimental methods will consider the place of execution of the given test.

6.2.1 Corvio sandstone

Corvio sandstone (CS) forms a c. 20 m thick unit (Corvio Formation) that appears in the top section of the Frontada Formation (Campoó Group; Lower Cretaceous) located in Northern Spain in the southern margin of the BasqueCantabrian Basin. It is composed of siliceous sandstones and conglomerates. It displays decimetric to metric trough-type cross bedding associated with braided fluvial channels (Hernández et al. 1999). A total of 228 cylindrical plugs of diameter 38.1 and 50 mm, with an approximately length to diameter ratio of 2.0, were cored from four blocks (dimensions 0.3 x 0.2 x 0.5 m) of Corvio sandstone, orthogonally to the three independent surfaces of the sample block (arbitrarily denoted as X, Y, Z). Onwards, we denote samples as X-, Y- and Z-plugs to refer to the corresponding coring direction. The core plugs were carefully trimmed to meet geometric standards for rock mechanics studies (Franklin 1983).

6.2.2 Physical and chemical characterization

Knowledge of the physical and chemical properties of Corvio sandstone is important for CO_2 injection studies, since CO_2 is a reactive fluid whether in a liquid, gaseous or supercritical state. Hence, core chips were employed to determine mineralogy, density, porosity and

pore size distribution. The following techniques were used: X-ray diffraction and fluorescence (XRD and XRF; Siemens D5000 and Bruker-AXS S4 Pioneer, respectively); thermogravimetric analysis; differential thermal analysis and outgas analyses via Fourier transform infrared spectroscopy (TGA-DTA-FTIR; TA Inst. SDT 2960 coupled to Bruker Vector 22), which also provide information on water evaporation mechanisms under controlled heating (Barrientos et al. 2010); Brunauer-EmmettTeller (BET, Micromeritics Gemini VII 2390a) specific surface area; scanning electron microscopy coupled to energy dispersive microanalysis (SEM-EDS, JEOL JSM-6400); petrography (Olympus BX51); He pycnometry (Quantachrome Ultrapyc 1200e); Hg porosimetry (Quantachrome Poremaster-60); and X-Ray μCT-scans (XRadia MicroXCT-300). A total of 10 samples were used to assess the statistical significance of the measured properties.

6.2.3 Mechanical characterization

The long-term integrity of CO_2 repositories is linked to the potential mechanical deformation induced during the injection process. The mechanical stability of reservoirs is addressed through geomechanical modelling. The accuracy of these models depends on the available information about stresses and rock mechanical properties, based on geomechanical studies. This is crucial to identify the linear elasticity field from which static elastic moduli of the rock are calculated; but also to quantify deviations from perfect linear

behaviour associated with compliant fractures and pores (Angus et al. 2010). Geomechanical tests were performed on a total of 28 cylindrical plugs (diameter 50 mm; length to diameter ratio ~2) of Corvio sandstone, which were prepared to meet the recommendations of the International Society for Rock Mechanics (1978): 11 for tensile strength (Brazilian test), 10 for unconfined compressive strength (UCS) and 6 for confined compressive strength (CCS). The tests were carried out using a MTS 815 testing system located at the facilities of the Rock Mechanics Laboratory (LaMEROC) of the University of A Coruña (Figura 6-1). During compressive strength tests, the axial strains were recorded with a dual-averaging knife-edge type extensometer, while the lateral strain was measured using a circumferential chain-type extensometer. Some plugs were equipped additionally with four 350 Ω strain gages (two axial and two radial). Tensile strength was calculated indirectly (Brazilian test) by applying radial compression to induce tensile stresses in a thin discs of rocks (Hakala et al. 2007; Cai 2010; Bednárik and Kohút 2012). Based on the measured stress-strain information, we computed the static elastic moduli, and the critical stress states as presented in Hakala et al. (2007). Tangent Young's modulus (E) and Poisson's ratio (ν) were calculated at the strength level equal to 50% of UCS. The slope of the stress-strain curves was determined as the first derivative at a stress value equivalent to 50% of the peak strength, using a 3rd degree polynomial approximation. We also determined the characteristic

stress levels describing the brittle behaviour of the rock, based on the work presented by Martin and Chandler (1994), further developed by Lau and Chandler (2004), Cai (2010) and Nicksiar and Martin (2012). These stress levels are known as crack closure stress (σ_{cc}), crack initiation stress (σ_{ci}), crack damage stress (σ_d) and failure (or peak) stress (σ_f). The crack closure stress corresponds to the load level up to which the strain occurs as a result of pore compaction and compliant crack closing.

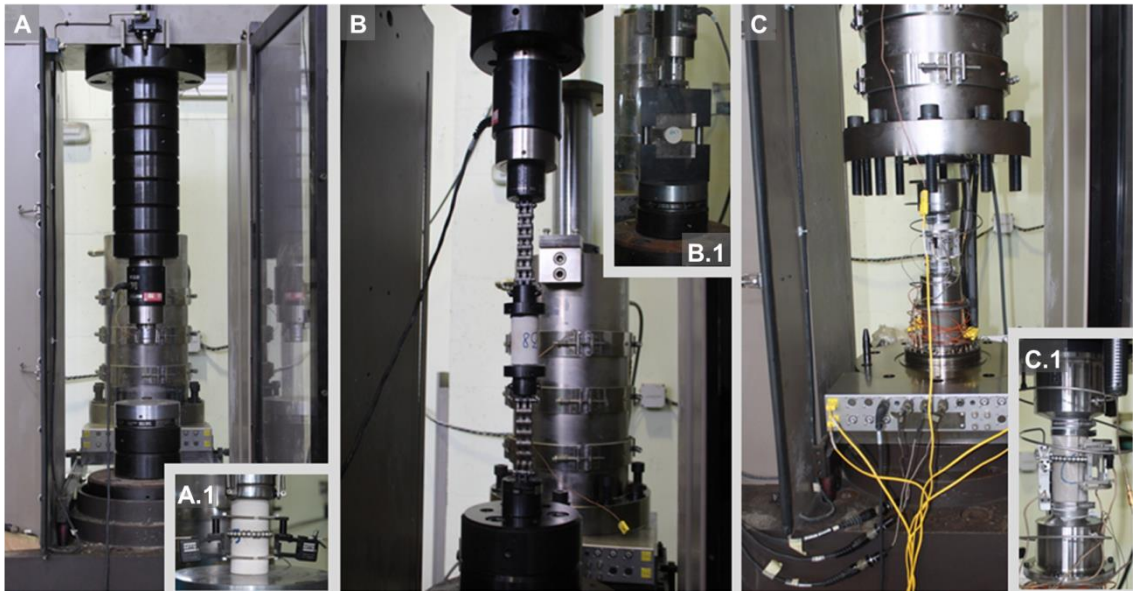

Figure 6- 1. MTS 815 Rock Mechanics Testing System. A, uniaxial configuration and sample (A.1) equipped with extensometers dual-averaging knife-edge type (longitudinal deformation) and chain-type (circumferential deformation); B and B.1, direct and indirect (Brazilian) tensile configurations; C, open-chamber vision of the triaxial configuration and sample (C.1) ready for testing (same type of extensometers as the uniaxial configuration).

6.2.4 Elastic wave

There is widespread use of seismic methods to monitor CO_2 movement and distribution in reservoir formations. Seismic properties of rocks are pressure dependent, and so elastic wave velocities were measured on dry and water saturated Corvio sandstone samples over a wide range of confining pressures, both under hydrostatic and non-hydrostatic conditions. These velocities were also employed to compute the corresponding dynamic moduli (E_{dyn}, ν_{dyn}, K_{dyn} and μ_{dyn}) assuming isotropic homogeneous materials and standard relationships (e.g. Batzle et al. 2006; Rae et al. 2007). Ultrasonic wave velocities (V_P, V_{S1} and V_{S2}: P-wave, fast S-wave and slow S-wave, respectively) were measured on 38.1 mm diameter core plugs with the aid of a pair of ErgoTech compression platens both equipped with one P-wave, and two orthogonally polarized S-wave, 1.3 MHz PZT transducers in pulse-transmission mode; time-of-flight was determined by picking first breaks (LaMEROC). The ultrasonic pulse-echo technique was used at the National Oceanography Centre, Southampton (NOC) on 50 mm diameter plugs, as presented in McCann and Sothcott (1992).

6.2.5 Permeability

Permeability is pressure-dependent and controls the rate of fluid advance through the reservoir formation. When mixed phase fluids (e.g., brine and CO_2) are injected into a porous medium, the permeability to water (absolute permeability or hydraulic

conductivity) is needed to calculate the relative permeability curves of the corresponding fluids. Hence, we measured the absolute permeability to water for different pairs of hydrostatic confining and pore fluid pressures. Permeability was determined by the steady state flow method (i.e., Darcy's law) using water. We assumed a homogenous contribution to the flow of the full core cross-sectional area, and the absence of hydro-mechanical end-effects (Nguyen et al. 2014). In short, the ratio of volumetric flow rate, Q (m^3 s^{-1}), to the pressure drop, ΔP (Pa), between the inlet and outlet of a sample of cross sectional area, A (m^2), and length, L (m), for a fluid dynamic viscosity, μ (Pa s), is related to absolute permeability, k (m^2), through the expression:

$$k = \frac{\mu L Q}{\Delta P A}$$

The equipment used to conduct these tests combines a high pressure Hassler (LaMEROC) or Hoek-Franklin-type (NOC) core holders together with a number of high-pressure, high-resolution syringe pumps (ISCO 100DX, Quizix SP-5400, GDS ADVDPC) for maintaining confining pressure and fluid injection rates. Confining and pore pressure were continuously monitored with several pressure transducers (Keller-Drück series 33X). The system was configured to set a constant pore pressure gradient, while recording the flow rate

upstream and downstream of the sample. For permeability calculations, only the steady flow condition was considered within a single step.

6.2.6 Anisotropy assessment

Assessing the potential of Corvio sandstone as a reference material requires an evaluation of how the main properties of the rock vary with orientation. Hence, we used a multicore approach similar to that described by Louis et al. (2004). We cored additional 38.1 and 50 mm diameter plugs orthogonal to the three independent surfaces of the sample block (arbitrarily denoted as X, Y, Z), trimmed to a length to diameter ratio of 2 and 0.4, respectively. Dry ultrasonic measurements were conducted at LaMEROC (pulse-transmission method) on long core plugs, including a set of measurements on three orthogonal plugs whereby the samples were rotated 20° stepwise around the longitudinal axial under minimum loading (~1 MPa) to ensure good coupling between the platen and sample. This results in 9 measurements per core plug and a total of 27 for the three X-, Y-, and Z-plugs. Long plugs were also used for permeability assessment and tracer injection tests.

Dry and fluid saturated short plugs were used for the pulse-echo technique at NOC for different combinations of confining and pore pressure. Short plugs were also employed to assess the dynamic coefficients, permeability and bulk electrical resistivity.

As a preliminary step, unconfined dry ultrasonic velocity was measured to assess weak anisotropy in the samples of interest. Based on these results, we designed two main sets of experiments to better characterize the observed anisotropy: (i) combined electrical resistivity, ultrasonic velocity and permeability on brine-saturated plugs under nearly hydrostatic confining conditions at NOC; (ii) tracer injection tests at LaMEROC.

P-wave velocity and attenuation, electrical resistivity and permeability were together analysed on three short orthogonal brine saturated samples using the experimental rig at NOC described in Falcon-Suarez et al. (2014). This rig employs a triaxial cell with a specially adapted rubber sleeve with a 16-electrode array, and bespoke data acquisition systems and software developed at the NOC. This enabled the determination of the full 9-component resistivity anisotropy tensor without bias from measurements on a single core sample (North et al. 2013; North and Best 2014a). Because we employed a set of orthogonal plugs, we can also compare the equivalent isotropic resistivity by fitting a homogeneous, isotropic model to the resistivity data. This yields a crude estimate of the overall resistivity of the sample, although it must be acknowledged that this is biased by the geometry of the electrode array and the measurement protocol.

The combined electrical resistivity, ultrasonic P-wave velocity and attenuation, and permeability experiments (referred as RuVAK tests) were performed at room temperature on three 50 mm diameter, 20 mm length plugs (X-plug porosity ϕ = 0.23; Y-plug ϕ = 0.21; Z-plug ϕ = 0.22). The test procedure consisted of a drainage steady state flow test, setting a constant upstream flow of 0.5 cm^3min^{-1} and a constant downstream pressure of 5 MPa. The pore fluid was 35 gL^{-1} NaCl brine solution. The test was repeatedly conducted for a loading/unloading path of differential pressure ($P_{diff}=\sigma_c - P_p$), by increasing the confining pressure 5 MPa stepwise from 10 to 25 MPa and back to 10 MPa, while keeping the P_p constant at 5 MPa. Furthermore, confining conditions were quasi-hydrostatic ($\sigma_1 - \sigma_3$ = 0.5 MPa) to emphasize the effect of the anisotropy along the longitudinal axis of each plug. For each loading/unloading step, a fluid volume of no less than 10 mL was circulated through the sample, corresponding to approximately one pore volume. Permeability was continuously monitored based on the final change in pore pressure gradient and corresponding flow.

The tracer tests performed were pulse-type (Shackelford et al. 1999; Ptak et al. 2004) and are referred to here as TPT tests. The tests used a brackish NaCl solution of 1000 µS cm^{-1} as injectate for the three 38.1 mm diameter X-, Y- and Z-plugs confined at 10 MPa under hydrostatic conditions. This confining pressure makes possible the closing of compliant cracks in order to better assess the relevance of

small-scale porosity heterogeneities over fluid and solute transport. Rather than monitoring a chemical constituent, we continuously monitored the electrical conductivity of the effluent using a low-volume, flow-through, temperature compensated conductivity sensor (MicroElectrodes Inc. mod. 8-900) coupled to a data acquisition system (ELIT 9705c Aqualyser) set to 1 Hz.

6.3 Results

6.3.1 Rock characterization

Corvio sandstone is light grey with occasional purple veins and has a medium grain size. It can be classified as a grain-supported quartzarenite with microcrystalline silica cement. The mineralogy of the Corvio sandstone is summarized in Table 6- 1. Based on X-ray diffraction, the main mineral constituents are quartz (~94 wt. %) with subordinated kaolinite (~3.5 wt. %) and K-feldspar (~1.7 wt. %). Trace amounts of ilmenite (~0.2 wt. %) were observed in the µCT scans, while ~0.5 wt. % of carbonates, ~0.5 wt. % of hydrated minerals and <0.05 wt. % of C, N and S-compounds are inferred from the TGA-DTA-FTIR (Figure 6- 2; weight loss sensitivity 0.1 µg or 0.0002%). The rock typically comprises sub-rounded quartz grains, is well sorted with an average grain size around 0.15 - 0.3 mm. In the studied samples, fossils comprised scarce cm-sized spots with remnants of tree debris (Hernández et al. 1999).

Mineralogy	wt.%	Method
Quartz	94.0	XRD
Kaolinite	3.5	XRD
K-Feldspar	1.7	XRD
Ilmenite	0.2	mCT scan
Carbonates	0.5	TDA-TG-FTIR
N, S-compounds	<0.05	CHNS

Table 6- 1. Mineralogical composition of Corvio sandstone.

Based on ATD-TG-FTIR, the weight % of hydrated minerals is ~0.5 while C, N and S-compounds are below 0.05 wt. %.

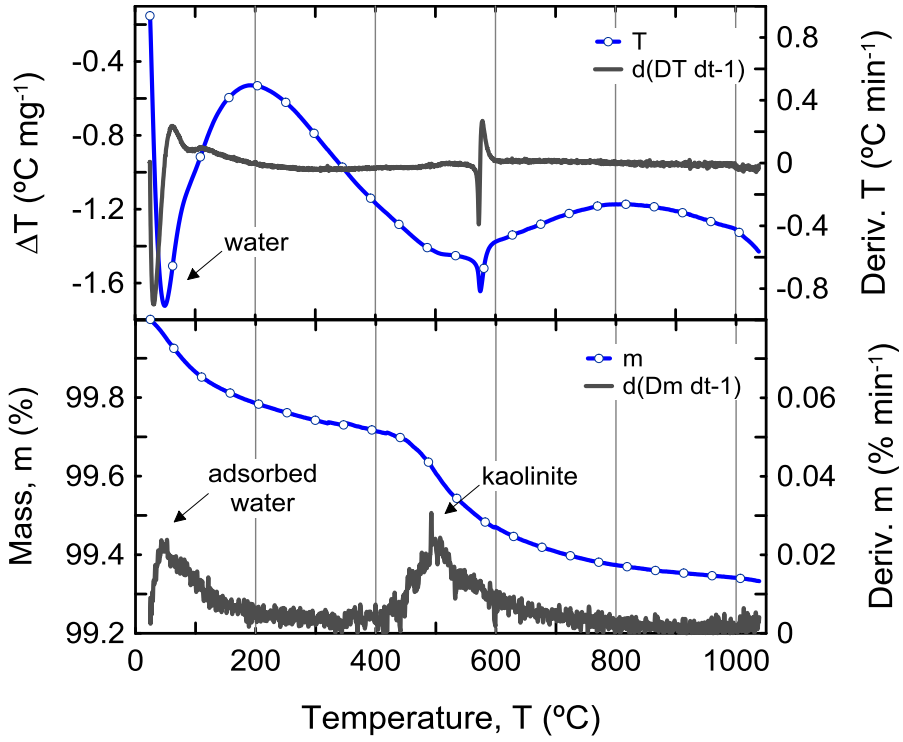

Figure 6- 2. Typical TDA–TG analyses of Corvio sandstone. The prescribed heating rate was 5 K min^{-1} from room temperature to 1050 °C.

The average BET specific surface is 1.09 ± 0.07 m^2 g^{-1} (n = 12) while porosity and dry density are 21.7 ±1.2 % (n = 224) and 2036 ±32 kg m^{-3} (n = 227) on average (Figure 6- 3;Figure 6- 4). Available BET sorption/ desorption isotherms show low hysteresis and correspond to the IUPAC's Type III (Rouquerol et al. 1994). This is typical of macroporous absorbents with weak surface affinity. The values obtained are comparable with that reported for the Berea (Zhan et al. 2010) and other sandstones.

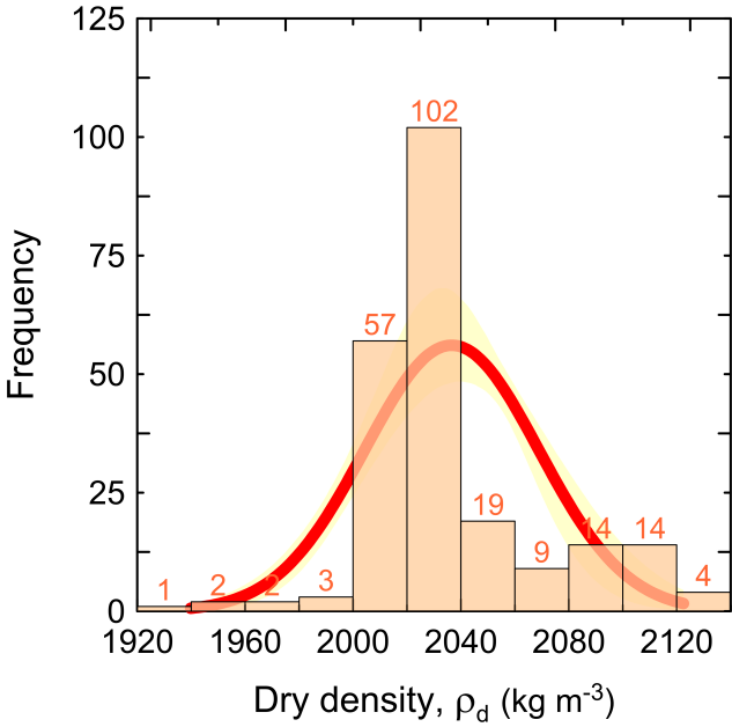

Figure 6- 3. Measured dry density of 227 samples of the Corvio sandstone. The red line shows the trace of a normal distribution function and the yellow shadow the associated 95% confidence band. Samples belonging to each class is indicated by a number accompanying bars.

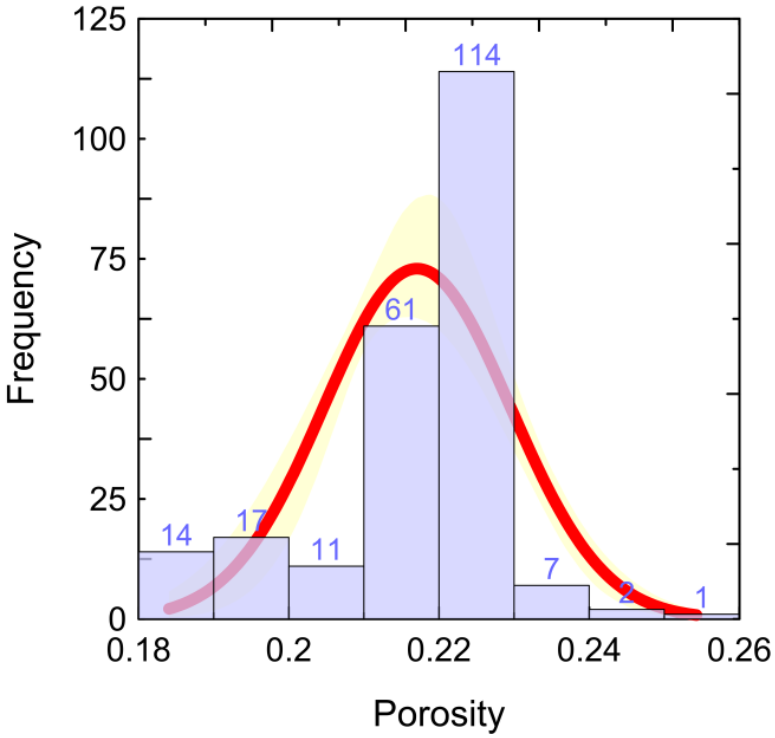

Figure 6- 4. Measured porosity of 227 samples of the Corvio sandstone. The red line shows the trace of a normal distribution function and the yellow shadow the associated 95% confidence band. Samples belonging to each class is indicated by a number accompanying bars.

From mercury porosimetry, we observed pore sizes from 0.1 to 1000 µm with a median pore size of ~20 µm (Figure 6- 5). Additionally, 3D and 2D-sections from the µCT-scanner (Figure 6- 6) revealed that, although pores tend to show an equant shape, some larger open areas can be distinguished. These may lead to a compliant behaviour upon loading as confirmed by the stress-strain results presented below.

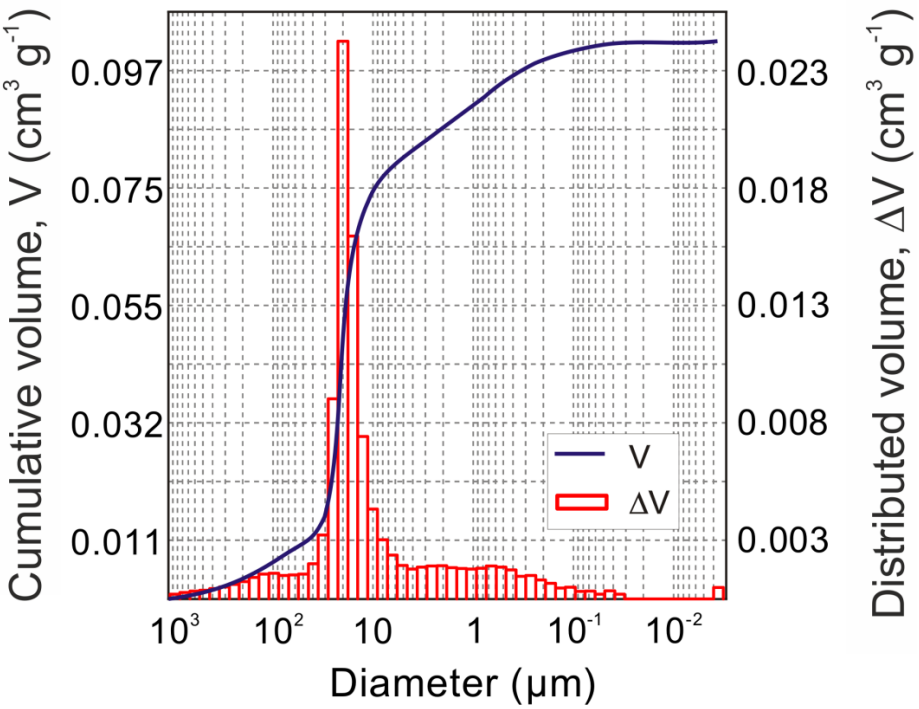

Figure 6- 5. Pore size distribution of a Corvio sandstone.

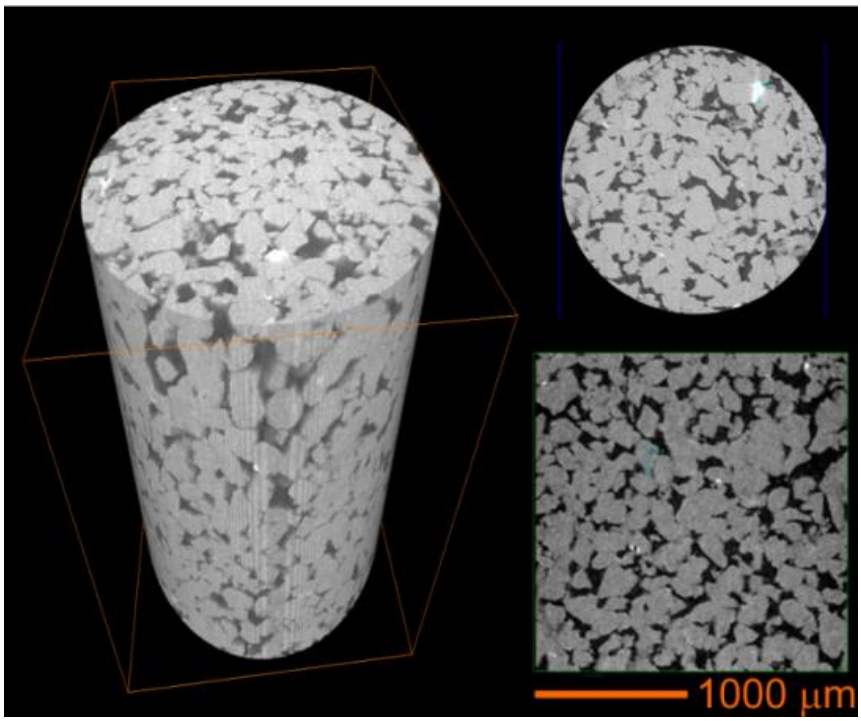

Figure 6- 6. X-Ray μCT-scan (small cylinder of 2 mm diameter, radial and transversal sections) of the Corvio sandstone.

6.3.2 Rock strength and stress-strain behaviour

The mean tensile strength of Corvio sandstone is 2.3 ± 0.14 MPa, while UCS is 41.15 ± 3.28 MPa. Drained CCS values vary according with confining pressure (see Table 6- 2). Figure 6- 7 illustrates the corresponding strength envelope based on the Hoek-Brown model (Hoek and Brown 1980; Hoek et al. 2002) according to the equationbellow, which results in a m_b value of 13.2 by setting the s and a constants to 1 and 0.5, respectively (m_b, s and a are the Hoek-Brown material constants):

$$\sigma_1 = \sigma_3 + \sigma_c \left(m_b \frac{\sigma_3}{\sigma_c} + s \right)$$

Sample	ρ_d (kg m^{-3})	f (%)	σ_3 (MPa)	σ_1 (MPa)	E (GPa)	n	G (GPa)	K (GPa)
Confined compressive strength				*(CCS)*				
C91	2026.2	17.7	5	90.6	-	-	-	-
C78	2030.2	16.5	10	107.3	14.71	0.34	5.48	15.44
C87	1998.7	17.2	15	129.9	-	-	-	-
C74	2023.4	17.3	30	153.1	14.62	0.34	5.47	14.99
T115	2122.5	11.0	38	181.4	17.54	0.34	6.57	17.72
C64	2052.7	16.7	50	221.9	13.99	0.34	5.23	14.41
Unconfined compressive strength				*(UCS)*				
C1	2008.8	15.2	0.1	36.0	9.33	0.35	3.47	10.08
C4	2022.7	15.0	0.1	41.1	11.11	0.35	4.11	12.39
C8	2032.0	15.2	0.1	43.7	12.04	0.35	4.47	13.12
C11	2021.4	15.6	0.1	43.3	11.09	0.35	4.10	12.65
C12	2030.9	16.0	0.1	44.4	11.38	0.34	4.25	11.63
C15	2025.3	15.5	0.1	35.4	19.72	0.34	7.34	20.90
C21	2035.3	16.4	0.1	41.4	10.81	0.33	4.08	10.36
C25	2037.5	15.9	0.1	43.7	10.99	0.35	4.08	11.94
C26	1939.8	15.0	0.1	39.4	9.47	0.34	3.53	10.01
C32	2032.3	14.2	0.1	42.9	12.03	0.35	4.46	13.29
Tensile strength (Brazilian)				*(TS)*				
C68-1	2043.5	16.6	9.1	3.0	-	-	-	-
C68-3	2043.5	16.6	5.5	1.8	-	-	-	-
C75-1	2020.8	17.6	5.7	1.9	-	-	-	-
C75-2	2020.8	17.6	6.2	2.1	-	-	-	-
C75-3	2020.8	17.6	8.2	2.7	-	-	-	-
C76-1	2016.2	17.2	6.8	2.3	-	-	-	-
C76-2	2016.2	17.2	5.7	1.9	-	-	-	-
C76-3	2016.2	17.2	7.3	2.4	-	-	-	-
C77-1	2035.7	16.8	6.7	2.2	-	-	-	-
C77-2	2035.7	16.8	6.7	2.2	-	-	-	-
C77-3	2035.7	16.8	9.4	3.1	-	-	-	-

Table 6- 2. Geomechanical characterization of Corvio sandstone

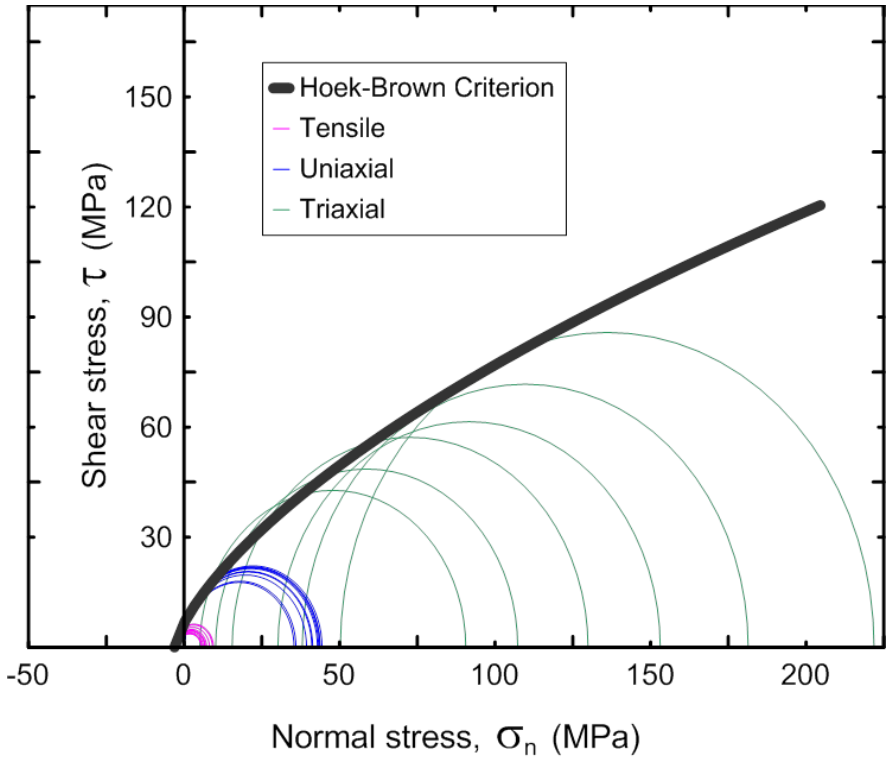

Figure 6- 7. Mohr circles corresponding to the different mechanical tests performed: Tensile (Brazilian tests), Uniaxial (UCS) and Triaxial (CCS) with the Corvio sandstone. The computed strength envelope, computed from the Hoek-Brown model is also shown

Static moduli were computed from the stress-strain curves from the UCS tests. For such conditions, the static Young's modulus (E) and Poisson's ratio (ν) are 11.8 ± 2.8 GPa and 0.34 ± 0.01, respectively; however, under confined conditions, E increases slightly (15.2 ± 2.8 GPa), while ν remains unchanged.

A further study of the stress levels presented by Corvio sandstone, shown in Figure 6- 8, reveals that crack closure occurs up to a stress level, σ_{cc}, of 9.7 ± 1 MPa. With increasing stress, the rock shows elastic behaviour to a maximum value of 17.7 ± 2.3 MPa, which corresponds

to the crack initiation stress, σ_{ci}; the crack damage onset stress, σ_d, initiates at 26.0 ± 2.4 MPa up to failure (i.e., peak strength, σ_f). The peak strength of Corvio sandstone is consistently attained during the UCS tests at 41.15 ± 3.28 MPa under uniaxial conditions, although it rises to 222 MPa at 50 MPa confining pressure under dry conditions.

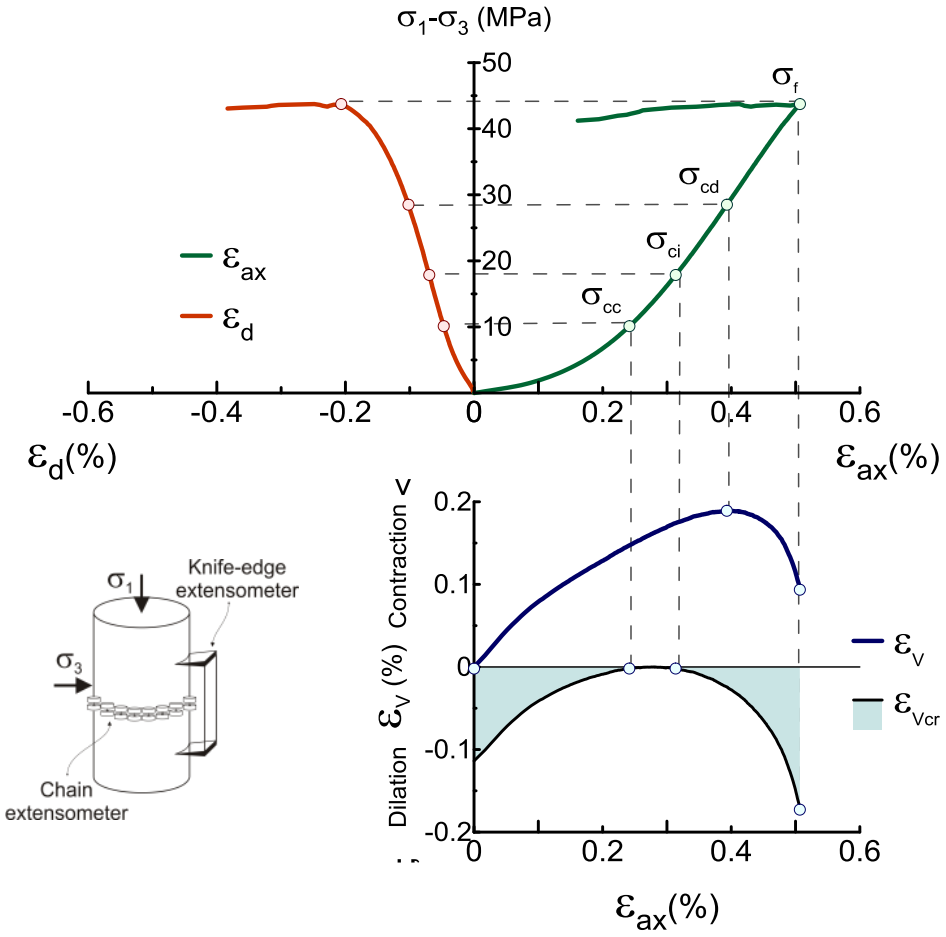

Figure 6- 8. Typical UCS strain-stress curves of the CS (sample C8) and identification of the critical stress states.

6.3.3 P- and S- wave velocities

V_P and V_S velocities were axially measured on 50 mm diameter X-plugs following a loading/unloading path from 0.5 to 35 MPa; the pressure steps were 2.5 and 5 MPa for non-hydrostatic and hydrostatic conditions, respectively. Figure 6- 9 and Figure 6- 10 show wiggle-trace plots corresponding to the change in V_P and V_S of Corvio sandstone for 5 MPa steps, following the display used by Njiekak et al. (2013). We observe that, when increasing confining pressure, both velocities increase from 2.92 to 3.69 km s^{-1} and 1.51 to 2.09 km s^{-1}, respectively. Below 10 MPa, the loading effect follows an exponential curve consistent with the previously described crack closure stress stage, an effect that has been reported or inferred from experimental data in a number of (King 1983; Xue and Lei 2006; Mikhaltsevitch et al. 2014). The unloading path is slightly different from the loading one, with higher average velocities. This hysteresis is associated with irreversible damage suffered by the rock above the ~18 MPa limit associated with the crack initiation stress (Xu et al. 2006; Fortin et al. 2007).

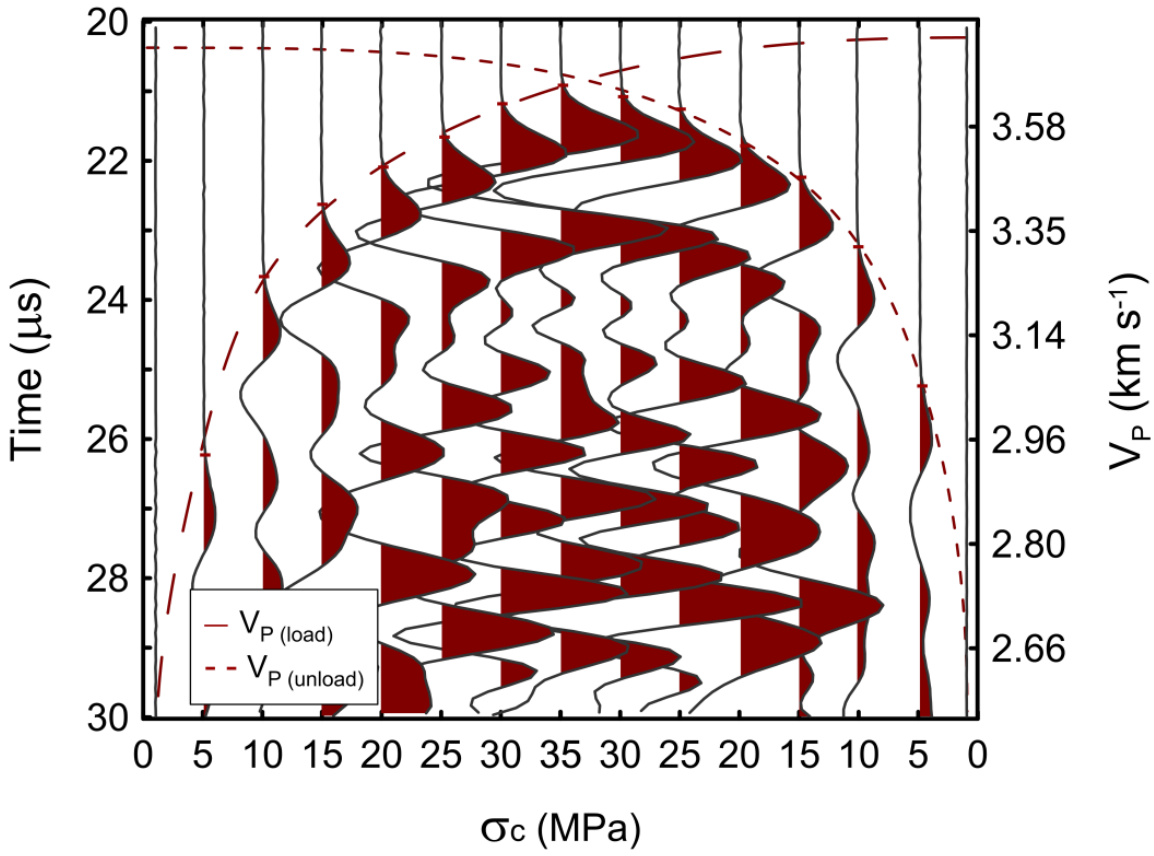

Figure 6- 9. Wiggle-trace plot corresponding to the change in P wave velocities in the CS. Loading/unloading test performed under hydrostatic conditions ($\sigma_1=\sigma_2=\sigma_3$). Discontinuous and dotted lines indicate the first pulse arrival during the loading and unloading sequence, respectively.

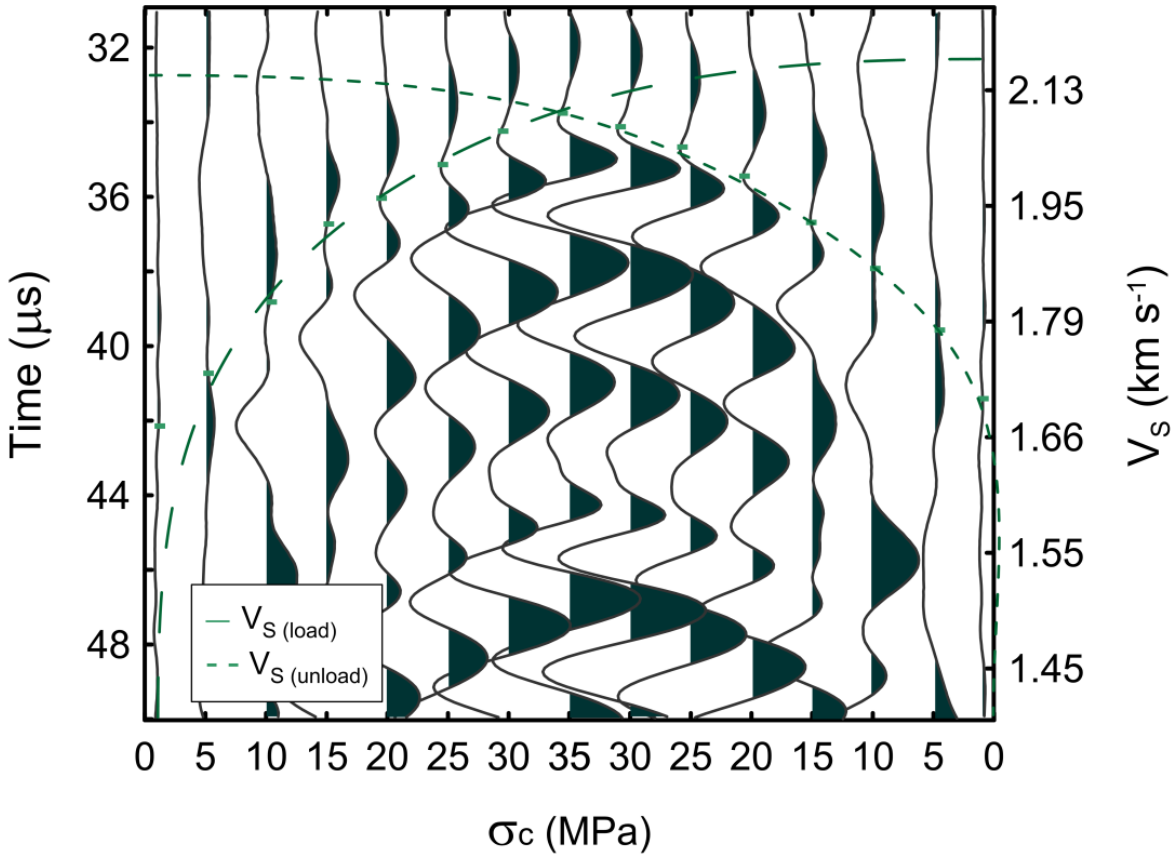

Figure 6- 10. Wiggle-trace plot corresponding to the change in S velocities in the CS. Loading/unloading test performed under hydrostatic conditions ($\sigma_1=\sigma_2=\sigma_3$).

Figure 6- 11 and Figure 6- 12 illustrate the V_P and V_S curves obtained under non-hydrostatic conditions by increasing the axial load while keeping constant the radial confining pressure (i.e., increasing the deviatoric stress). We observe that for low load (<10 MPa) and low confining pressure (0.1 MPa) there is a significant dependence of velocity with stress. This effect becomes less pronounced above 10 MPa loading, or at higher confining pressures. That means that closing of compliant cracks and pore compaction must be kept in mind when considering the ultrasonic characterization of plugs in the laboratory (King 1983; Asef and Najibi 2013).

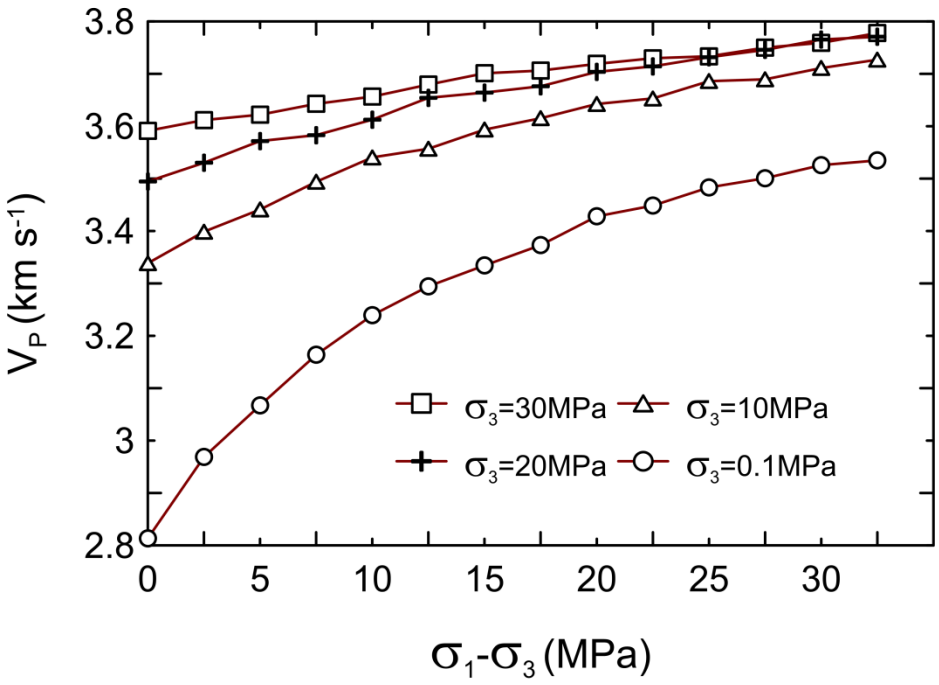

Figure 6- 11. V_P plotted vs. deviatoric stress ($\sigma_1 \neq \sigma_2 = \sigma_3$) for different confining conditions.

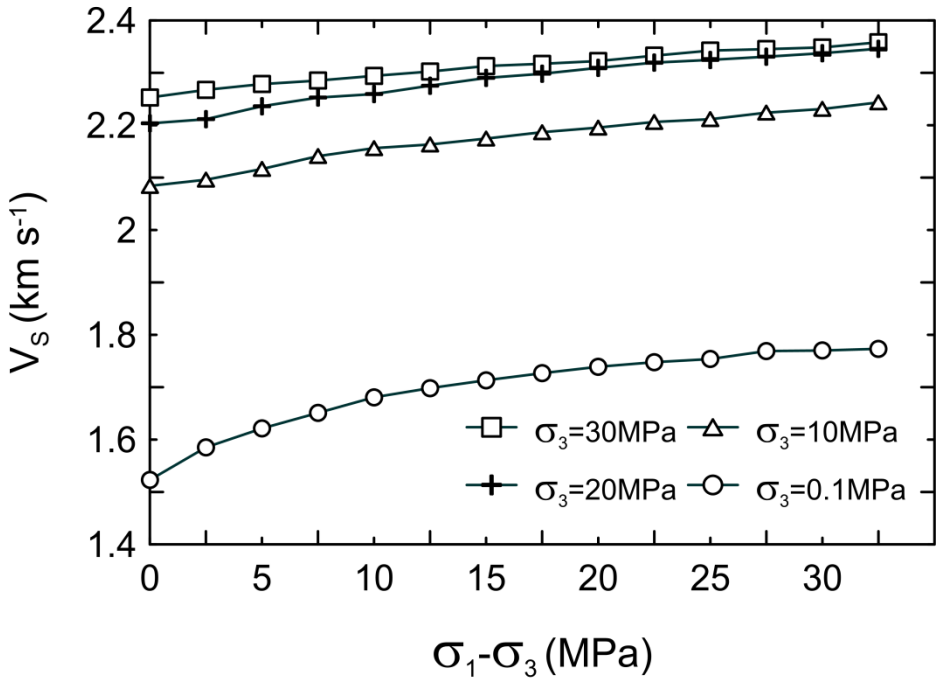

Figure 6- 12. V_S plotted vs. deviatoric stress ($\sigma_1 \neq \sigma_2 = \sigma_3$) for different confining conditions.

Based on the previous elastic wave velocities and the dry density of the samples, we calculated the dynamic moduli of the rock: Young's modulus and Poisson's ratio (E_{dyn} and ν_{dyn}; Figure 6- 13;Figure 6- 14), and the bulk modulus and shear modulus (K_{dyn} and G_{dyn}; Figure 6- 15;Figure 6- 16). Furthermore, comparing dynamic to static moduli we observe E_{dyn} is higher than E_{st} while ν_{dyn} is lower than ν_{st}, which has been largely identified in the past (King 1983; Eissa and Kazi 1988; Fjær 2009; Asef and Najibi 2013). The differences are related with deformation amplitudes between static and dynamic methods (at ultrasonic frequencies), and also with the heterogeneities between the different components of porous rocks, which lead to local non-elastic

behaviours - stress-induced anisotropy - when subjected to external stress changes (Fjær et al. 2013; Blake and Faulkner 2016). In our case, the static moduli are determined at the strength level equal to 50% of UCS, laying above the elastic limit of the rock in all the cases. Hence, to correlate static and dynamic moduli, a further analysis of the sensitivity of static moduli to the stress level (measure point along the failure envelope) is needed (Fjær 2009), using damage controlled tests (Lau and Chandler 2004).

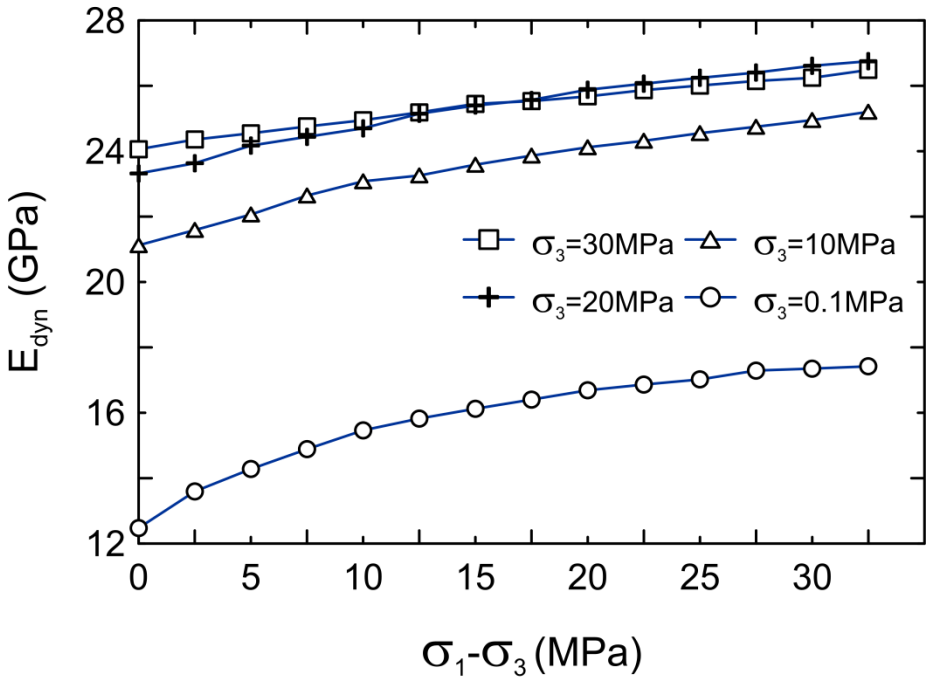

Figure 6- 13. Young's modulus (E_{dyn}) versus deviatoric stress for different confining conditions (σ_1=σ_2=σ_3).

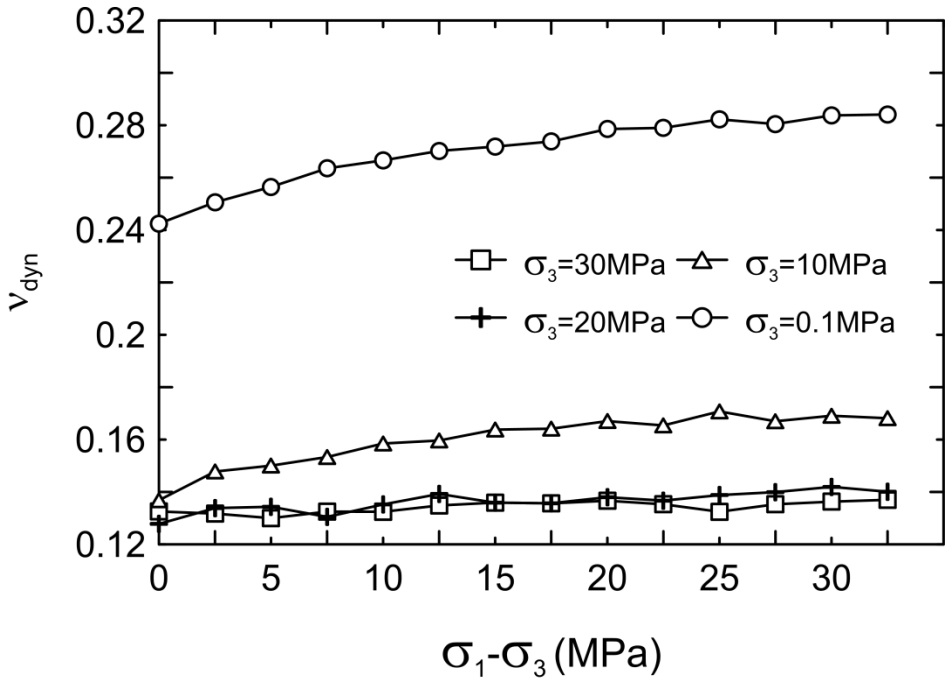

Figure 6- 14. Poisson's ratio (ν_{dyn}) versus deviatoric stress for different confining conditions ($\sigma_1=\sigma_2=\sigma_3$).

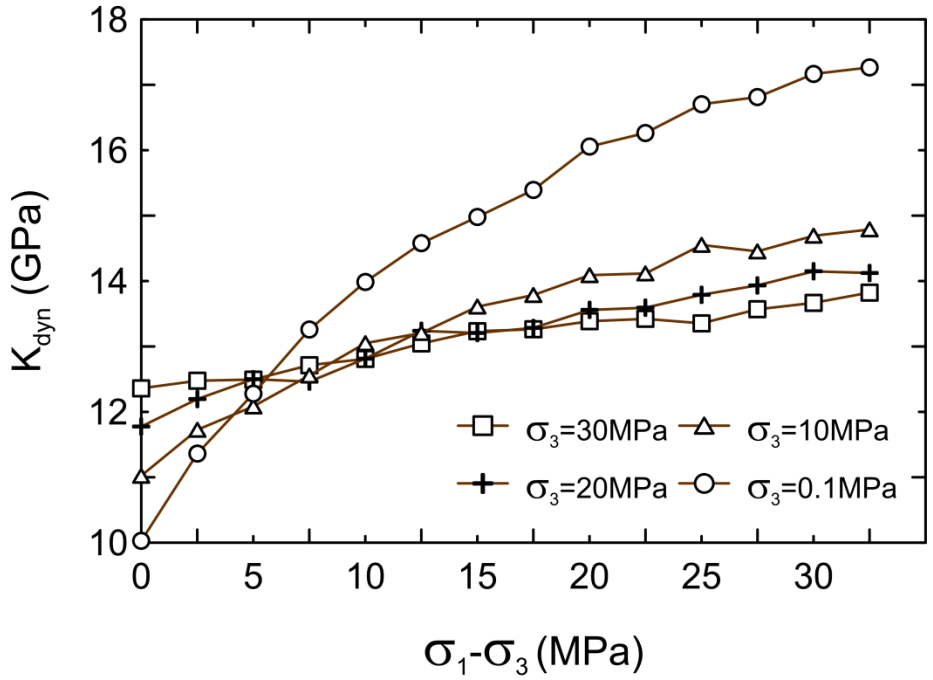

Figure 6- 15. Bulk modulus (K_{dyn}) versus deviatoric stress for different confining conditions ($\sigma_1 \neq \sigma_2 = \sigma_3$)

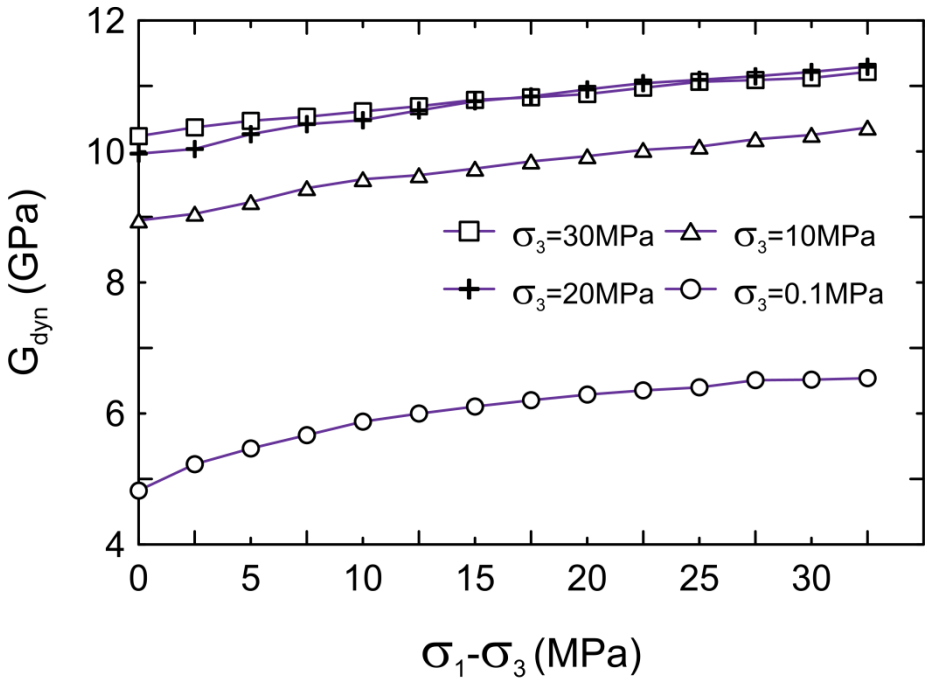

Figure 6- 16. . Shear modulus (G_{dyn}) versus deviatoric stress for different confining conditions ($\sigma_1 \neq \sigma_2 = \sigma_3$).

6.3.4 Permeability

The permeability of 38.1 mm diameter X-type plugs was evaluated with a series of 4 consecutive steady state flow tests performed along step wise loading/unloading cycles (between 5 and 30 MPa of hydrostatic confining pressure, i.e., $\sigma_c = \sigma_1 = \sigma_2 = \sigma_3$). Each one has a constant pore pressure (P_p, from 1 to 16 MPa), which is increased from one to the next to repeat the differential stress sequence ($P_{diff} = \sigma_c - P_P$). Figure 6- 17 shows that permeability progressively varies from 4 to 0.8 mD (~810-16 to ~410-15 m^2) while increasing confining pressure. There is a significant drop in permeability once the first loading/unloading cycle is completed,

thought to be associated with pore closing and crack compliance. The permeability change after the 2nd, 3rd and 4th loading/unloading cycles is much smaller, although the P_{diff} is kept constant along the sequence, which provides further evidence of the permanent deformation of the sample during initial loading due to pore closure. Hysteresis upon unloading is relatively small, below 15%. Overall, the observed permeability evolution can be attributed to compaction of pore space and favourably oriented cracks, already documented in other sandstones (Bernabe 1991; Ojala et al. 2004).

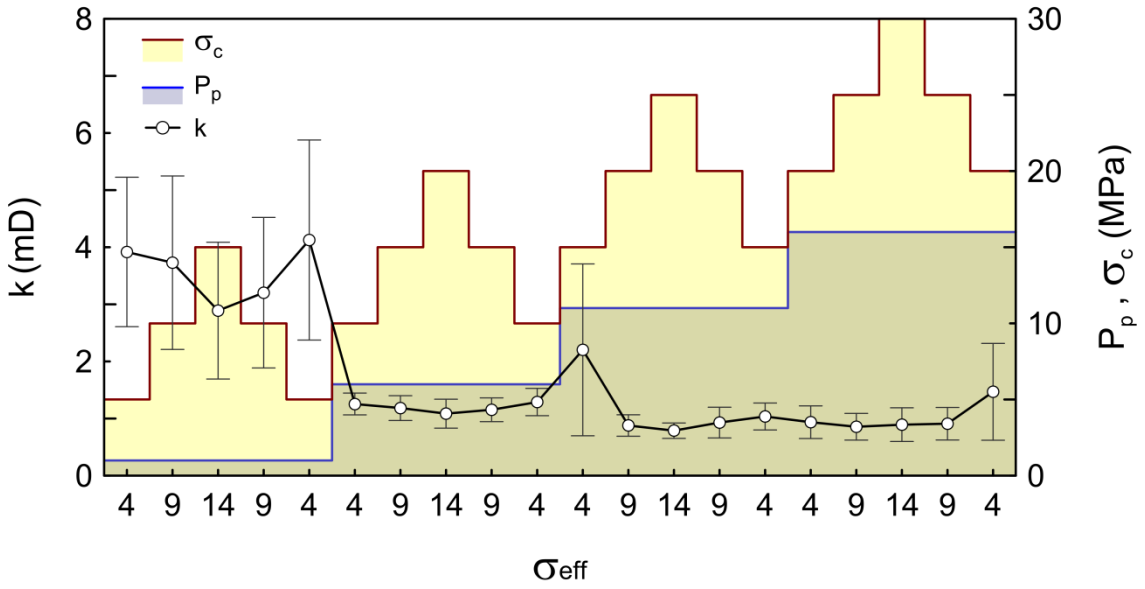

Figure 6- 17. Permeability of Corvio sandstone as resulting from 4 consecutive loading/unloading each one of them performed at constant pore pressure.

6.4 Anisotropy assessment

6.4.1 Exploratory approach

None of the 4 Corvio sandstone blocks used to core the plugs displayed clear evidences of heterogeneity (especially cross bedding) and that was also the case of the small scale μCT X-ray scans. In order to make evident the existence of anisotropy we performed an exploratory survey by taking several plugs which were sampled orthogonally to the three independent surfaces (denoted as X, Y and Z) of the parallelepiped sandstone block. Figure 6- 18 shows the vector-distribution of V_P, V_{S1} and V_{S2} (transverse to V_{S1}) resulting from the non-saturated unconfined test in which three X-, Y- and Z-plugs were revolved in steps of 20° around their longitudinal axes. Calculations show that V_P and V_S (average of V_{S1} and V_{S2}) are 2986 ±18 and 1515 ± 32 m s^{-1} for the X-plug; 3289 ± 48 and 1716 ± 21 m s^{-1}, for the Y-plug; and 3360 ± 32 and 1729 ± 20 m s^{-1}, for the Z-plug. Hence, V_p in the longitudinal direction of the X-plug is ~10% slower than in the Z-plug, and ~8% slower than in the Y-plug. Similarly, V_S is about 12% slower in both the Y- and Z-plugs. Further observation of the same figure lets us conclude that the rock is transversely isotropic in the longitudinal direction of Z-plugs, since the P and S-wave velocities are relatively insensitive to rotation, while the X- and Y-plugs are slightly orthotropic. It is worth noting that the X-plug shows 90° crossed symmetric values, indicating some sort of preferential void alignment

perpendicular to the axis. Besides, the difference between V_{S1} and V_{S2} is a proof of anisotropy, since different velocities along different wave paths may imply heterogeneity. The case of the Y-plug is more difficult to explain since V_P should be unaffected by axial rotation, but the results show the contrary (V_P is higher at 45°).

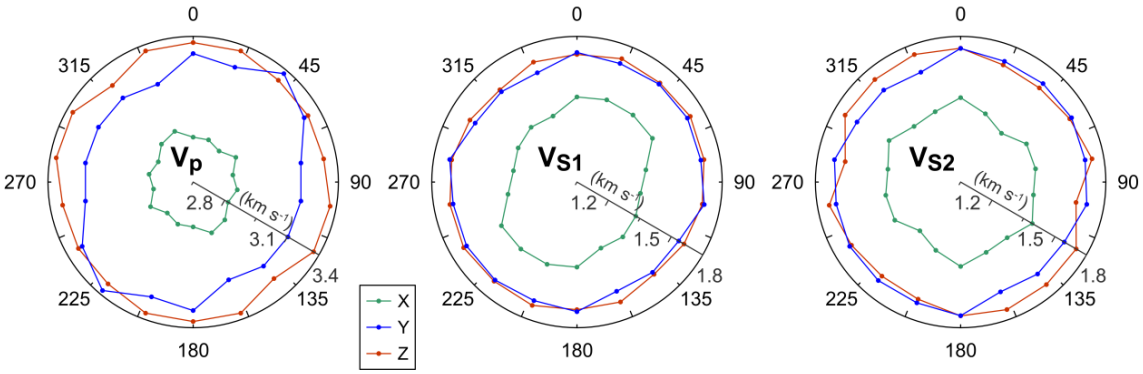

Figure 6- 18. Acoustic wave velocities for X, Y and Z oriented samples of CS, measured at 20° axially-rotating-steps. The measurements were carried out under unconfined conditions and a load of 1 MPa.

In a collaborative paper by Falcón-Suárez et al. (accepted, in press) we have also performed a more detailed assessment of the anisotropy characteristics of the Corvio sandstone. It is out os the scope of the present dissertation to discuss the details of this work and we refer interested readers to the corresponding paper. Nonetheless, taking into account the sedimentary fabric models presented by North et al. (2013), the main conclusion attained in this work is the identification of several sedimentary structures in Corvio sandstone: (i) the X-plugs have bedding orthogonal to the axis of the plug; (ii) the Y-plugs have tubular micro-structure slightly oblique to the axis of the plug; and (iii)

the Z-plugs have laminated micro-structure along the axis of the plug. Based on that and other information, we infer the presence of a weak cross-bedding structure that would somehow reflect the macroscale cross bedding previously reported for the Corvio sandstone by Hernández et al. (1999)

The tracer TPT tests also provide an alternative mean to test the anisotropy of Corvio sandstone. These tests are significant as they directly emphasize the transport properties of the rock, providing information about actual flow-paths and fluid-flow through. Hence, it is possible to obtain information on the pore space (and transport properties) of the rock from the shape of the breakthrough curve (Ptak et al. 2004). It is far from the scope of this contribution to provide a detailed assessment of TPT tests although some general ideas can be presented. Assuming that the movement of the tracer conforms to piston-type flow, the injection of a discrete stepped pulse at the inlet of the sample translates into a tailed bell-shape breakthrough curve at its outlet (Fetter 1993). The change from a squared to a, more or less pronounced, tailed bell-shape curve depends on the relative importance of diffusive/dispersive effects while the tracer is crossing the pore space of the sample.

The tracer injection tests were repeated up to five times for the X-, Y- and Zplugs, obtaining comparable results in each case. Representative breakthrough curves are illustrated in Figure 6- 19.

From a merely descriptive point of view, we see in our experiments that the faster travel time occurs for the Y-plug and is followed by the Z- and X-plugs. The relative height of the peak conductivity has the opposite order (highest for the X-plug and lowest for the Y-plug). Because electrical conductivity is a conservative tracer in our test (were chemical reactions are negligible according to the mineralogy of the rock, at the time-scale of the test) the surface area covered by each breakthrough curve is nearly identical. Permeability results show that the plug showing the lowest value was the Xplug. This is consistent with the slowest arrival time of the same orientation in the TPT tests. However, the Y-plug has lower k than the Z-plug which is in apparent contradiction with the TPT results from the same plugs. Furthermore, if we focus on the shape of the Y-plug breakthrough curve, the recession curve shows a protuberance (i.e., the trailing limb after the peak value) which points towards a double-porosity system. One porosity, well connected, would contribute providing fast trackways for tracer transport (also responsible for the early breakthrough) and a second one, less well connected, providing a delayed arrival of tracer with a peak value (the first inflexion point in the recession curve) located between the peak times for the X- and Z-plugs. The double porosity effect on permeability is imperceptible since the measurements are conducted in a constant flow mode, so dominated by preferential path flows (primary porosity), instead of a single pulse

(TDT tests). Nonetheless, such a feature is consistent with our previous interpretation of weak cross-bedding.

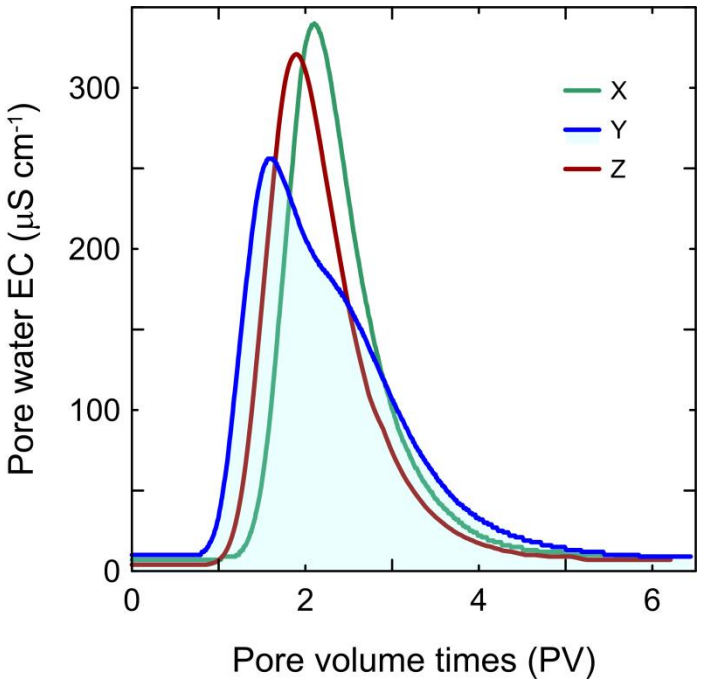

Figure 6- 19. Breakthrough electrical conductivity curves corresponding to pulse-injection tracer tests performed along the three main orthogonal directions (X-, Y- and Z-plugs) of Corvio sandstone.

6.4.2 Weak anisotropy assessment. Detailed approach

The previous results encouraged the development of a more detailed anisotropy investigation. Based on these, we assumed that Corvio sandstone is transversely isotropic (TI), allowing the application of weak anisotropy formulae (Thomsen 1986). Accordingly, since V_P is normally lower in the direction perpendicular to bedding (Thomsen 1986; Wang 2002; King 2009; Martínez and Schmitt 2013), the direction along the X-plug (or vector V) would

correspond to the symmetry axis, while the isotropic plane containing the Y- and Z-plugs axial directions (with velocities about 10% higher) defines the bedding plane (i.e., two perpendicular directions to the anisotropy symmetry axis H_1 and H_2). Then, taking the Thomsen (1986) notation and equations, it is possible to evaluate the anisotropy for P-wave velocity (ε) and S-wave velocity (γ) from four of the five elastic constants of the material (C_{11}, C_{33}, C_{44} and C_{66}) as follows:

$$\varepsilon = \frac{C_{11} - C_{33}}{2C_{33}}$$

$$\gamma = \frac{C_{66} - C_{44}}{2C_{44}}$$

where $C_{11} = \rho V_{p(H1,2)}^{\ 2}$; $C_{33} = \rho V_{p(V)}^{\ 2}$; $C_{66} = \rho V_{s(H1,2)}^{\ 2}$; and $C_{44} = \rho V_{p(V)}^{\ 2}$. A more detailed explanation of the notation and equations is given in Thomsen (1986), Wang (2002) and Louis et al. (2004). It is worth noting that we independently compute ε and γ for H_1 and H_2 (i.e., Y- and Z-plugs) since both directions are orthogonal to the symmetry axis. In this study we lack a sample cored at 45°, hence the third Thomsen's anisotropy parameter δ (Thomsen 1986) cannot be calculated. Likewise, to analyse the anisotropy of the rock in terms of P- and S-wave attenuations (Q_p^{-1} and Q_s^{-1}), we use the Thomsen-style

parameters proposed by Zhu and Tsvankin (2006), as presented in Best et al. (2007):

$$\varepsilon_Q = \frac{Q_p^{-1}\left(H_{1,2}\right) - Q_p^{-1}(V)}{Q_p^{-1}(V)}$$

$$\gamma_Q = \frac{Q_s^{-1}\left(H_{1,2}\right) - Q_s^{-1}(V)}{Q_s^{-1}(V)}$$

The computed velocity and attenuation anisotropies are represented in Figure 6- 20 and Figure 6- 21, as ε, γ, ε_Q, γ_Q percentages versus differential stress. The P- and S- wave velocity anisotropy parameters ε and γ display similar evolution versus P_{diff}, decreasing from 12 to 8% and 8 to 4%, respectively, when P_{diff} increases 15 MPa. Furthermore, the changes of ε and γ in the plane defined by the X- and Y-plugs (ε_{xy} and γ_{xy}) are less pronounced (i.e., less anisotropic) than those observed for the plane defined by the X- and Z-plugs (ε_{xz} and γ_{xz}); this suggests that pore compaction is more significant along the former plane. Additionally, the low hysteresis observed at the end of the unloading path (~2%) would suggest that the reduction of anisotropy due to compression is largely controlled by the compliance of equant pores. In this regard, the non-linear trends are likely indicating that microcrackclosing is also playing a role (Martínez and Schmitt 2013). Nevertheless, our data suggest that all core plugs evolve

to a more isotropic state when confining pressure is increased as ε and γ tend to decrease. The attenuation parameters (ε_Q and γ_Q) show similar trends to those described previously for velocities, although ε_Q is positive (<12%) and γ_Q negative (20 – 25%). The parameter γ_Q ranges between -5 to 5% for the plane defined by the X- and Yplugs, and stays around -10% for that defined by the X- and Z-plugs, without showing a clear dependence on P_{diff}. As noted by Best et al. (2007), for P_{diff} increments greater than those used in this study, attenuation anisotropy in sandstones is more sensitive to pressure changes than velocity anisotropy. So that P- and S-wave attenuation parameters provide more information about the magnitude of the anisotropy. Nonetheless, whether the velocity or attenuation anisotropy is considered, Corvio sandstone seems to be weakly anisotropic according to Martínez and Schmitt (2013).

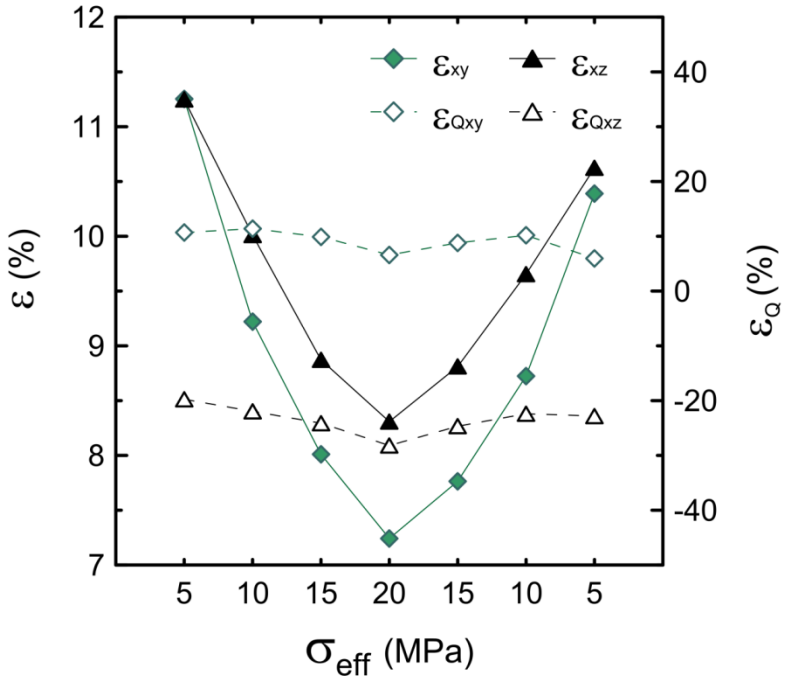

Figure 6- 20. P-wave velocity and attenuation anisotropy (ε and ε_Q) of the Corvio.

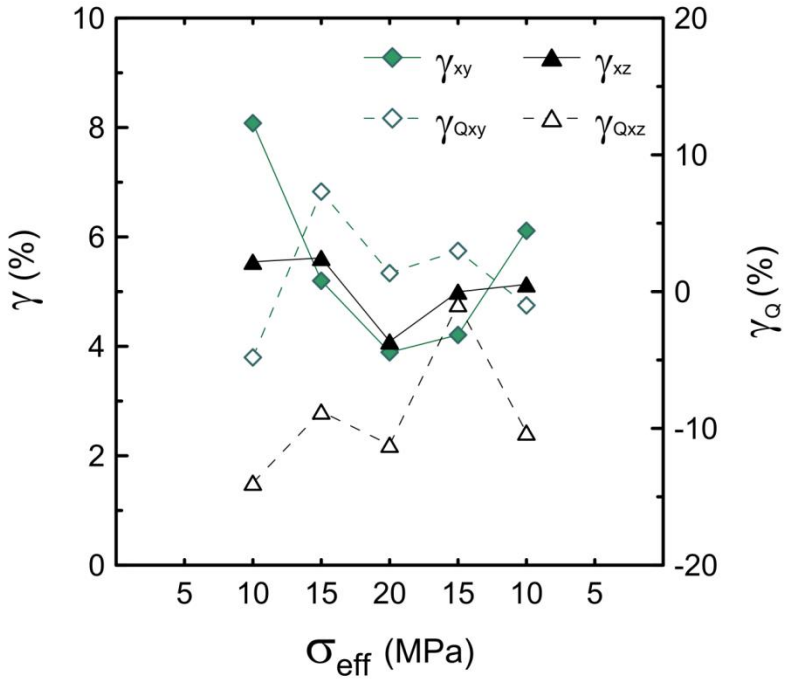

Figure 6- 21. S-wave velocity and attenuation anisotropy (Υ and Υ_Q).

6.5 Summary and conclusions

We have reported a comprehensive characterization for the Corvio sandstone and we have deserved a special attention to the assessment of weak anisotropy from a multifaceted perspective. The average mineralogy is dominated by quartz (~94%), kaolinite (~3.5%) and k-feldspar (~1.7%) what suggests that its chemical reactivity when submitted to the injection of CO_2 or CO_2-saturated fluids is expected to be low, at least on short time scales. This is useful when trying to focus the interest in thermos-hydro-mechanical processes associated to CO_2 injection with minimum impact of chemical processes.

The standard geomechanical characterization provides also with relevant information. The crack closing stress (which refers to pore compaction and compliant crack closing) occurs at 10 MPa while the onset of crack initiation takes place at ~18 MPa. These values have been indirectly verified by different techniques. Direct application of these results imply a better assessment of experimental conditions in order to reduce undesired effects like enhanced permeability due to non-closed cracks at low stress levels or associated with rock damage induced by high stresses.

The average permeability of the CS sandstone varies from 4 to 0.8 mD, decreasing with confining pressure. It is worth to note that, within the studied testing range, the main process inducing a hysteretic behaviour in the rock (either in terms of hydrodynamic or

wave propagation velocity responses) is related with pore compaction/compliant crack closing.

Although no sedimentary structures were detected at block-scale or through the X-ray μCT-scans, we have developed a multifaceted anisotropic analysis (multicore analysis) and conclude that the Corvio sandstone is weakly anisotropic: Our results show that the anisotropies of ultrasonic P-wave velocity is <12% (<8% for the S-wave), attenuation <20%, electrical resistivity <18% and that of permeability slightly oscillates (±1 mD) depending on the direction considered. In addition, the bulk ER analysis performed as well as the tracer injection tests support that weak cross-bedding is present in the studied rock.

These characterization results constitute a useful baseline for CO_2 injection studies using this sedimentary rock. Our results are of direct application when working with this rock in the laboratory, as they help us: (i) to understand nonobvious processes such as thresholds for pore compaction, compliant crack closure, and physicochemical coupling; (ii) to better calibrate geophysical techniques by reducing uncertainty and providing a well-constrained fabric model; (iii) to improve experimental design parameters such as stress ranges, plug orientation, and vector properties, among others. Furthermore, we want to highlight the importance of weak anisotropy when considering naturally homogeneous materials (at least in appearance). These

observations can be scaled up to field scenarios in order to improve reservoir models. This comprehensive characterization of Corvio sandstone covers geomechanical, geochemical, geophysical and hydrodynamic properties. Together with the detailed assessment of anisotropy presented here, the results indicate that Corvio sandstone could be used as a particularly interesting rock-standard to improve the understanding of reservoirs subjected to complex thermo-hydromechano-geochemical coupled phenomena, typically associated with CO_2 storage practices.

6.6 References

Akbarabadi M, Piri M. Relative permeability hysteresis and capillary trapping characteristics of supercritical CO_2/brine systems: An experimental study at reservoir conditions. Adv Water Resour. Elsevier Ltd; 2013;52:190–206.

Alcalde J, Marzán I, Saura E, Martí D, Ayarza P, Juhlin C, et al. 3D geological characterization of the Hontomín CO_2 storage site, Spain: Multidisciplinary approach from seismic, well-log and regional data. Tectonophysics. 2014;627:6–25.

Alemu BL, Aker E, Soldal M, Johnsen Ø, Aagaard P. Effect of sub-core scale heterogeneities on acoustic and electrical properties of a reservoir rock: A CO_2 flooding experiment of brine saturated sandstone in a computed tomography scanner. Geophys Prospect. 2013;61(1):235–50.

Andrä H, Combaret N, Dvorkin J, Glatt E, Han J, Kabel M, et al. Digital rock physics benchmarks—Part I: Imaging and segmentation. Comput Geosci. 2013;50:25–32.

Angus DA, Kendall J, Fisher QJ, Segura JM, Skachkov S, Crook AJL, et al.

Modelling microseismicity of a producing reservoir from coupled fluid-flow and geomechanical simulation. Geophys Prospect. Wiley Online Library; 2010;58(5):901–14.

Asef MR, Najibi AR. The effect of confining pressure on elastic wave velocities and dynamic to static Young's modulus ratio. 2013;78(3).

Barrientos V, Delgado J, Navarro V, Juncosa R, Falcon Suarez I, Vazquez A. Characterization and geochemical-geotechnical properties of granite sawdust produced by the dimension stone industry of O Porrino (Pontevedra, Spain). Q. J. Eng. Geol. Hydrogeol. 2010.

Batzle ML, Han D-H, Hofmann R. Fluid mobility and frequency-dependent seismic velocity -- Direct measurements. Geophysics. 2006;71(1):N1–9.

Bednárik M, Kohút I. Three-dimensional colour functions for stress state visualisation. Comput Geosci. 2012;48:117–25.

Bernabe Y. Pore geometry and pressure dependence of the transport properties in sandstones. Geophysics. Society of Exploration Geophysicists; 1991;56(4):436–46.

Best AI, Sothcott J, McCann C. A laboratory study of seismic velocity and attenuation anisotropy in near-surface sedimentary rocks. Geophys Prospect. Blackwell Publishing Ltd; 2007;55(5):609–25.

Blake OO, Faulkner DR. The effect of fracture density and stress state on the static and dynamic bulk moduli of Westerly Granite. J Geophys Res Solid Earth. 2016 Mar 22;121(4).

Cai M. Practical Estimates of Tensile Strength and Hoek–Brown Strength Parameter m i of Brittle Rocks. Rock Mech Rock Eng. 2010;43(2):167–84.

Canal J, Delgado J, Falcón I, Yang Q, Juncosa R, Barrientos V. Injection of CO_2-saturated water through a siliceous sandstone plug from the Hontomin test site (Spain): Experiment and modeling. Environ Sci Technol. 2013;47(1):159–67.

Chichinina T, Obolentseva I, Gik L, Bobrov B, Ronquillo-Jarillo G. Attenuation anisotropy in the linear-slip model: Interpretation of physical modeling data. Geophysics. 2009;74(5):WB165.

Churcher PL, French PR, Shaw JC, Schramm LL. Rock Properties of Berea Sandstone, Baker Dolomite, and Indiana Limestone. Society of Petroleum Engineers. 1991; 20-22 February, SPE 21044.

Eissa EA, Kazi A. Relation between static and dynamic Young's moduli of rocks. Int J Rock Mech Min Sci Geomech Abstr. Pergamon; 1988 Dec;25(6):479–82.

Ellis MH, Sinha MC, Minshull TA, Sothcott J, Best AI. An anisotropic model for the electrical resistivity of two-phase geologic materials. Geophysics. 2010;75(6):E161–70.

Falcon-Suarez I, North L, Best A. Experimental Rig to Improve the Geophysical and Geomechanical Understanding of CO_2 Reservoirs. Energy Procedia. 2014;59:75–81.

Farrell NJC, Healy D, Taylor CW. Anisotropy of permeability in faulted porous sandstones. J Struct Geol. 2014;63:50–67.

Fetter CW (Charles W. Contaminant hydrogeology / C.W. Fetter. New York: Macmillan Pub. Co.; Maxwell Macmillan Canada; Maxwell Macmillan International; 1993.

Fjær E. Static and dynamic moduli of a weak sandstone. Geophysics. Society of Exploration Geophysicists; 2009 Mar 1;74(2):WA103–12.

Fjær E, Stroisz AM, Holt RM. Elastic Dispersion Derived from a Combination of Static and Dynamic Measurements. Rock Mech Rock Eng. 2013;46(3):611–8.

Fortin J, Guéguen Y, Schubnel A. Effects of pore collapse and grain crushing on ultrasonic velocities and Vp/Vs. J Geophys Res Solid Earth. Wiley Online Library; 2007;112(B8).

Fortin J, Schubnel A, Guéguen Y. Elastic wave velocities and permeability evolution during compaction of Bleurswiller

sandstone. Int J Rock Mech Min Sci. 2005;42(7-8):873–89.

Franklin. Suggested methods for determining the strength of rock materials in triaxial compression: Revised version. Int J Rock Mech Min Sci Geomech Abstr. 1983;20(6):285–90.

Fredrich JT, Greaves KH, Martin JW. Pore geometry and transport properties of Fontainebleau sandstone. Int J Rock Mech Min Sci Geomech Abstr. 1993 Dec;30(7):691–7.

Gaus I. Role and impact of CO_2–rock interactions during CO_2 storage in sedimentary rocks. Int J Greenh Gas Control. 2010 Jan;4(1):73–89.

Hakala M, Kuula H, Hudson JA. Estimating the transversely isotropic elastic intact rock properties for in situ stress measurement data reduction: A case study of the Olkiluoto mica gneiss, Finland. Int J Rock Mech Min Sci. 2007;44(1):14–46.

Hangx SJT, Spiers CJ, Peach CJ. Creep of simulated reservoir sands and coupled chemical-mechanical effects of CO_2 injection. J Geophys Res. 2010 Sep 14;115(B9):B09205.

Hernández JM, Pujalte V, Robles S, Martín-Closas C. División estratigráfica genética del Grupo Campóo (Malm-Cretácico inferior; SW Cuenca Vascocantábrica). Rev la Soc Geológica España. 1999;12(3-4):377–96.

Hoek E, Brown ET. Underground excavations in rock. 1980.

Hoek E, Carranza-Torres C, Corkum B. Hoek-Brown failure criterion – 2002 Edition. 5th North Am Rock Mech Symp. 2002;1:267–73.

King MS. Static and dynamic elastic properties of rocks from the Canadian shield. Int J Rock Mech Min Sci Geomech Abstr. Pergamon; 1983 Oct;20(5):237–41.

King MS. Recent developments in seismic rock physics. Int J Rock Mech Min Sci. 2009 Dec;46(8):1341–8.

Klein E, Baud P, Reuschlé T, Wong T. Mechanical behaviour and failure mode of bentheim sandstone under triaxial compression. Phys Chem Earth, Part A Solid Earth Geod. 2001 Jan;26(1-2):21–5.

Krevor SCM, Pini R, Zuo L, Benson SM. Relative permeability and trapping of CO_2 and water in sandstone rocks at reservoir conditions. WATER Resour Res. 2012;48.

Kutchko BG, Strazisar BR, Lowry G V, Dzombak DA, Thaulow N. Rate of CO_2 Attack on Hydrated Class H Well Cement under Geologic Sequestration Conditions. Environ Sci Technol. 2008;42(16):6237–42.

Lau JSO, Chandler NA. Innovative laboratory testing. Int J Rock Mech Min Sci. 2004 Dec;41(8):1427–45.

Lei X, Xue Z. Ultrasonic velocity and attenuation during CO_2 injection into water-saturated porous sandstone: Measurements using difference seismic tomography. Phys Earth Planet Inter. 2009;176(3-4):224–34.

Liu F, Lu P, Griffith C, Hedges SW, Soong Y, Hellevang H, et al. CO_2--brine--caprock interaction: reactivity experiments on Eau Claire shale and a review of relevant literature. Int J Greenh Gas Control. Elsevier; 2012;7:153–67.

Louis L, Robion P, David C. A single method for the inversion of anisotropic data sets with application to structural studies. J Struct Geol. 2004;26(11):2065–72.

Lu P, Fu Q, Seyfried Jr W, Hereford A, Zhu C. Navajo Sandstone–brine–CO_2 interaction: implications for geological carbon sequestration. Environ Earth Sci. Springer-Verlag; 2011;62(1):101–18.

Martin CD, Chandler NA. The progressive fracture of Lac du Bonnet granite. Int J Rock Mech Min Sci Geomech Abstr. 1994 Dec;31(6):643–59.

Martínez JM, Schmitt DR. Anisotropic elastic moduli of carbonates and evaporites from the Weyburn-Midale reservoir and seal rocks. Geophys Prospect. Blackwell Publishing Ltd; 2013;61(2):363–79.

McCann C, Sothcott J. Laboratory measurements of the seismic properties of sedimentary rocks. Geol Soc London, Spec Publ. 1992 Jan 1;65(1):285–97.

Mikhaltsevitch V, Lebedev M, Gurevich B. A Laboratory Study of the Elastic and Anelastic Properties of the Sandstone Flooded with Supercritical CO_2 at Seismic Frequencies. Energy Procedia. 2014;63:4289–96.

Nakagawa S, Kneafsey TJ, Daley TM, Freifeld BM, Rees E V. Laboratory seismic monitoring of supercritical CO_2 flooding in sandstone cores using the Split Hopkinson Resonant Bar technique with concurrent x-ray Computed Tomography imaging. Geophys Prospect. Blackwell Publishing Ltd; 2013;61(2):254–69.

Nakatsuka Y, Xue Z, Garcia H, Matsuoka T. Experimental study on CO_2 monitoring and quantification of stored CO_2 in saline formations using resistivity measurements. Int J Greenh Gas Control. 2010 Mar;4(2):209–16.

Nguyen VH, Gland N, Dautriat J, David C, Wassermann J, Guélard J. Compaction, permeability evolution and stress path effects in unconsolidated sand and weakly consolidated sandstone. Int J Rock Mech Min Sci. 2014 Apr;67:226–39.

Nicksiar M, Martin CD. Evaluation of Methods for Determining Crack Initiation in Compression Tests on Low-Porosity Rocks. Rock Mech Rock Eng. Springer Vienna; 2012;45(4):607–17.

Njiekak G, Schmitt DR, Yam H, Kofman RS. CO_2 rock physics as part of the Weyburn-Midale geological storage project. Int J Greenh Gas Control. 2013;16:S118–33.

North L, Best AI, Sothcott J, MacGregor L. Laboratory determination of the full electrical resistivity tensor of heterogeneous carbonate rocks at elevated pressures. Geophys Prospect. Blackwell Publishing Ltd; 2013;61(2):458–70.

North LJ, Best AI. Anomalous electrical resistivity anisotropy in clean reservoir sandstones. Geophys Prospect. 2014a Nov 20;62(6):1315–26.

North LJ, Best AI. Anomalous electrical resistivity anisotropy in clean reservoir sandstones. Geophys Prospect. 2014b;62(6):1315–26.

Oh J, Kim KY, Han WS, Kim T, Kim JC, Park E. Experimental and numerical study on supercritical CO_2/brine transport in a fractured rock: Implications of mass transfer, capillary pressure and storage capacity. Adv Water Resour. Elsevier Ltd; 2013;62:442–53.

Ojala IO, Ngwenya BT, Main IG, Ojala IO, Ngwenya BT, Main IG. Loading rate dependence of permeability evolution in porous aeolian sandstones. J Geophys Res. 2004 Jan 1;109(B1):1–14.

Pini R, Krevor SCM, Benson SM. Capillary pressure and heterogeneity for the CO_2/water system in sandstone rocks at reservoir conditions. Adv Water Resour. 2012;38:48–59.

Ptak T, Piepenbrink M, Martac E. Tracer tests for the investigation of heterogeneous porous media and stochastic modelling of flow and transport - A review of some recent developments. J Hydrol. 2004;294(1-3):122–63.

Rae PJ, Brown EN, Orler EB. The mechanical properties of poly(ether-ether-ketone) (PEEK) with emphasis on the large compressive strain response. Polymer (Guildf). 2007 Jan;48(2):598–615.

Rouquerol J, Avnir D, Fairbridge CW, Everett DH, Haynes JM, Pernicone N, et al. Recommendations for the characterization of porous solids (Technical Report). Pure Appl Chem. 1994;66(8):1739–58.

Rutqvist J. The Geomechanics of CO_2 Storage in Deep Sedimentary Formations. Geotech Geol Eng. Springer Netherlands; 2012;30(3):525–51.

Schubnel A, Benson P, Thompson B, Hazzard J, Young RP. Quantifying Damage, Saturation and Anisotropy in Cracked Rocks by Inverting Elastic Wave Velocities. In: Dresen G, Zang A, Stephansson O, editors. Rock Damage Fluid Transp Part I SE - 3. Birkhäuser Basel; 2006. p. 947–73.

Shackelford BCD, Malusis MA, Majeski MJ, Stern RT, Member A. E c b c. 1999;(April):260–70.

Song I, Renner J. Hydromechanical properties of Fontainebleau

sandstone: Experimental determination and micromechanical modeling. J Geophys Res. 2008 Sep 26;113(B9):B09211.

Song J, Zhang D. Comprehensive Review of Caprock-Sealing Mechanisms for Geologic Carbon Sequestration. Environ Sci Technol. American Chemical Society; 2013 Jan 2;47(1):9–22.

Thomsen L. Weak elastic anisotropy. Geophysics. 1986;51(10):1954.

Wang Z. Seismic anisotropy in sedimentary rocks, part 1: A single-plug laboratory method. Geophysics. 2002 Sep 1;67(5):1415–22.

Xu X, Hofmann R, Batzle M, Tshering T. Influence of pore pressure on velocity in low-porosity sandstone: Implications for time-lapse feasibility and pore-pressure study. Geophys Prospect. Blackwell Publishing Ltd; 2006;54(5):565–73.

Xue Z, Lei X. Laboratory study of CO_2 migration in water-saturated anisotropic sandstone, based on P-wave velocity imaging. Explor Geophys. 2006 Jan 1;37(1):10–8.

Xue Z, Ohsumi T. Seismic wave monitoring of CO_2 migration in water-saturated porous sandstone. Explor Geophys. Australian Society of Exploration Geophysicists; 2004 Mar 1;35(1):25–32.

Zhan X, Schwartz L, Toksöz M, Smith W, Morgan F. Pore-scale modeling of electrical and fluid transport in Berea sandstone. Geophysics. Society of Exploration Geophysicists; 2010 Sep 1;75(5):F135–42.

Zhu Y, Tsvankin I. Plane-wave propagation in attenuative transversely isotropic media. Geophysics. 2006;71(2):T17.

Zhu Y, Tsvankin I, Dewangan P, Wijk K. Physical modeling and analysis of P-wave attenuation anisotropy in transversely isotropic media. Geophysics. Society of Exploration Geophysicists; 2007 Nov 15;72(1):D1–7.

Suggested methods for determining the strength of rock materials in triaxial compression. Int J Rock Mech Min Sci Geomech Abstr. 1978 Apr;15(2):47–51.

CHAPTER 7. EFFECT OF THE SUPERCRITICAL CO_2 INJECTION IN THE CORVIO SANDSTONE DURING A FLOW-THRU TRIAXIAL EXPERIMENT

7.1 Introduction

Deep saline aquifers represent, by far, the most typical scenario for CO_2 geosequestration. They also have the largest volumetric storage capacity. In the case of Spain, where conventional gas and oil fields are virtually non-existent, they represent the most realistic option for CCS. The EU GeoCapacity (2009) project assessed that Spain had the highest onshore storage capacity of all European countries, with a conservative estimate of 14,000 Mt in combined onshore and offshore deep saline reservoirs. In December 2010 Spain also became the first European country to transpose the CCS Directive 2009/31/EC. Most of the storage capacity is associated to deep saline aquifers of the major sedimentary basins (Douro, Ebro, Guadalquivir and Tagus). The Douro basin, in particular, is of interest as it has an extension of approximately 50,000 km^2 and is the largest Cenozoic basin on the Iberian Peninsula.

It is well known that the injection of reactive fluids, like CO_2, into geological formations trigger a series of interlinked phenomena (thermo-hydro-chemo-mechanical or THCM) that affects the properties of the reservoir, its seal or even the cementitious materials used in wellbores. Because water is always present in the porous space of these systems, the forced injection of CO_2 (either as gas, liquid or supercritical fluid) induces a significant acidification and the onset of reactive processes which are especially notorious when carbonate or

carbonate-bearing rocks are present. The co-injection of subordinated gasses accompanying CO_2 (O_2, SO_2…) might exacerbate this reactivity due to the oxidation of reduced mineral phases already present in the rocks or by promoting an enhanced acidity associated to S-bearing gasses.

Petrophysics and rock mechanics provide with invaluable toolbox with which to assess key rock properties and to elaborate integrated reservoir models. However, in their classical use they do not consider the crucial importance of the THCM couplings which are inherent, however, to reactive systems. Routinely, laboratory data is used to correlate model logs or the seismic response to study the feasibility of monitoring a dynamic reservoir with geophysical methods (e.g. production, enhanced oil recovery, CO_2 sequestration). During injection or extraction, fluids in the reservoir change what induces changes in the elastic and visco-elastic rock moduli. In seismic data or full-waveform sonic logs the preferential loss of amplitude with frequency is referred to as apparent (or effective) attenuation. This attenuation is the combination of intrinsic and scattering loss.

Core-flooding experiments performed at P-T conditions similar to those in situ have a great potential in helping us to unravel complex THCM processes, provided that it is feasible the separation of each of their corresponding contributions. To this respect, based on previous experiences (Canal et al. 2013), in this study we focus on the evolution

of different properties of a reference rock material (Corvio Sandstone) during a core-flooding test in which we sequentially inject deionized water (DIW) and CO_2-saturated DIW. The studied rock was selected among several candidates in order to minimize, as much as possible, chemical couplings so that the observed phenomena could be mostly related with non-reactive processes.

7.2 Material and methods

The tested core plug was carefully trimmed to fulfill standard geometric constrains in rock mechanics experiments (flatness, slenderness and cilindricity; (Franklin 1983)). The core flooding experiment was performed under axisymmetric confining stress conditions by inserting the polyolefin-sleeved rock plug (37.4 mm diameter; 70.2 mm length; ϕ=12.1 %; ρ_d=2094 kg/m^3) into a modified Hoek-Franklin-type cell (Hoek and Franklin 1967). The axial force is applied with a hydraulic jack supported by a loading frame equipped with a 30 ton load cell. The jack was connected to a servo-controlled GDS-ADVDPC screw pump. The axial pressure is transmitted to the sample by drilled load platens allowing (via circular and radial grooves) a homogeneous access of the pore fluid to the edges of the plug. The confining pressure is applied to the core holder with the aid of a high pressure, servo-controlled syringe pump cell (Teledyne Isco 260D) by pressurizing the confining fluid using a servo controlled

pump. The cell is equipped with an aluminium heating jacket which is connected to a temperature controller that receives the feedback of a PT1000 temperature sensor installed through the external wall of the cell.

The experimental setup is shown and described with more details in Chapter 3. The test was performed at 40 °C and under hydrostatic stress conditions ($\sigma_1=\sigma_2=\sigma_3$=15 MPa) and a pore pressure ~8 MPa (P_F=8.2-9.4 MPa). Loading of the sample was performed stepwise: In the first step the axial and confining pressures were increased simultaneously (Q=0), at a constant rate and under drained conditions to the target stress value. Then, following a short period to allow the mechanical re-conditioning of the plug, deionized water (DIW) was injected at a constant flow rate (0.04 mL/min) through the bottom platen in order to saturate the sample. For the injection, a high pressure syringe pump (Teledyne Isco DX-100) was used. The pressure drop between the inlet and outlet ports was monitored with two high resolution (±0.01%) absolute pressure transducers (Keller-Drück LEO Record Ei).

In order to ensure that the experimental conditions inside the plug were compatible with CO_2 supercritical conditions (>7.38 MPa; >31.1 °C) the outlet port was equipped with a back pressure valve (BPV) rated to a maximum fluid pressure of 7.6 MPa at the sample side. The small pore pressure gradient inside the sample made it difficult to

obtain accurate information about the evolution of permeability. After the BPV the pipeline was allowed to drop to ambient pressure in order to collect the water circulated through the sample. This section of the pipeline was equipped with a low volume flow-thru, temperature compensated, microelectrode array (Micro-electrodes Inc.) allowing the inline (although depressurized) measurement of pH and electrical conductance (EC_{25}). The electrodes were connected to an ELIT 9705b Aqualyser (Nico2000 Ltd.) data conditioning and acquisition system. The calibration of these electrodes was done periodically (2-3 days) due to the harsh working conditions. In addition, the cumulative effluent water was collected on a daily basis for analysis (Na, K, Ca, Mg, SiO_2, Fe, Mn, Al, F, Cl, SO_4) and its pH and EC_{25} also recorded.

The top and bottom compression platens are instrumented each with a stack of 1.3 MHz resonant frequency piezoelectric transducers (PZT) for the measurement of direct (V_P) and shear (V_{S1}, V_{S2}) ultrasonic wave velocities. Squared-pulse waves were generated with a transducer-pulser unit (PT100-1000; ErgoTech Ltd.) and monitored with a digital oscilloscope (PicoScope 3204A; Pico Technologies Ltd.). Velocities were determined once a day by applying the time of flight technique (Rummel et al. 1978).

Only axial strains were recorded in this experiment with the aid of two-averaged Linear Displacement Sensors (Vishay LDS HS50). To separate the true sample strain from system deflection, a series of

sample-less calibration tests were performed in the load frame (plus the corresponding accessories: load cell, spacers, platens, etc.). Therefore, strains reported in this work are frame-corrected values.

The saturation of DIW with CO_2 was accomplished in a 2.7 L carbonation vessel for several days (different sources in the literature report that equilibrium can be reached in 24 to 48 h.; (Diamond and Akinfiev 2003)). To speed-up the equilibration process, CO_2 was micronized inside the vessel at low pressure (~0.5 MPa). CO_2 was supplied in excess, what allowed the development of a gaseous headspace. The vessel was then driven at room temperature to the target condition of 8 MPa with the aid of a manual pressure generator (HiP mod. 62-6-10). The transfer of fluid from the carbonation vessel to the ISCO pump was performed by setting the later in constant pressure mode and a back-pressure regulator. According to the EOS (Duan and Sun 2003; Duan et al. 2006), the theoretical concentration of CO_2 in the injected fluid is ~1.2 m and the corresponding pH ~3.1.

7.3 Coupled effects of core flooding test

The experiment lasted for 35 days and during that time ~140 pore volumes of fluid (~2.02 L) circulated through the porous space of the plug. The light blue-shadowed area represents the DIW injection stage (~50 PV), which is followed by the CO_2-saturated DIW injection period (from ~50 to ~140 PV). Circulated fluid shows evidences of chemical

reactivity, although this is limited. Nonetheless, the time-evolution of recorded parameters provided with interesting information. The evolution of pH and EC_{25} was monitored during the experiment (Figure 7- 1) With respect pH, the DIW stage shows a slight tendency of acidification, which is a typical situation during the injection of weakly buffered fluid into siliciclastic rocks. In the second stage, there is a significant pH increase that can be related with the dissolution of carbonates that can be inferred from the sharp increase in Ca and Mg concentrations (Figure 7- 2). EC_{25} shows virtually no changes during the first stage and a sharp rise (although to a moderate value of ~110 µS/cm) immediately after the beginning of the injection of the carbonated fluid. This is interpreted as being the result of mineral dissolution reactions. Then, EC_{25} drops steadily for the remaining of the test. That suggests that the mineral phases available for reaction are being exhausted and that chemical processes have a very limited impact in this experiment.

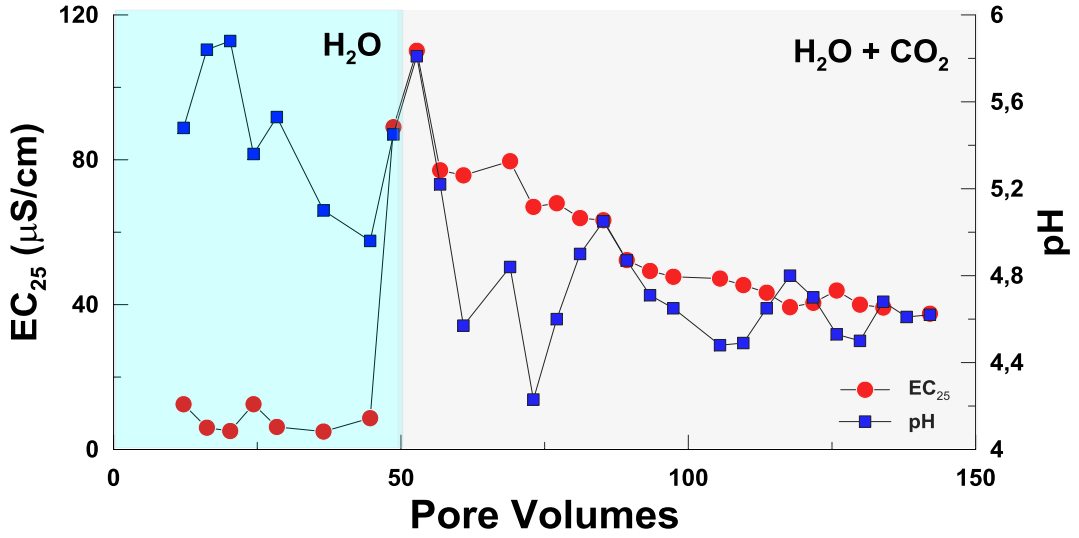

Figure 7- 1. Evolution of pH and EC_{25}.

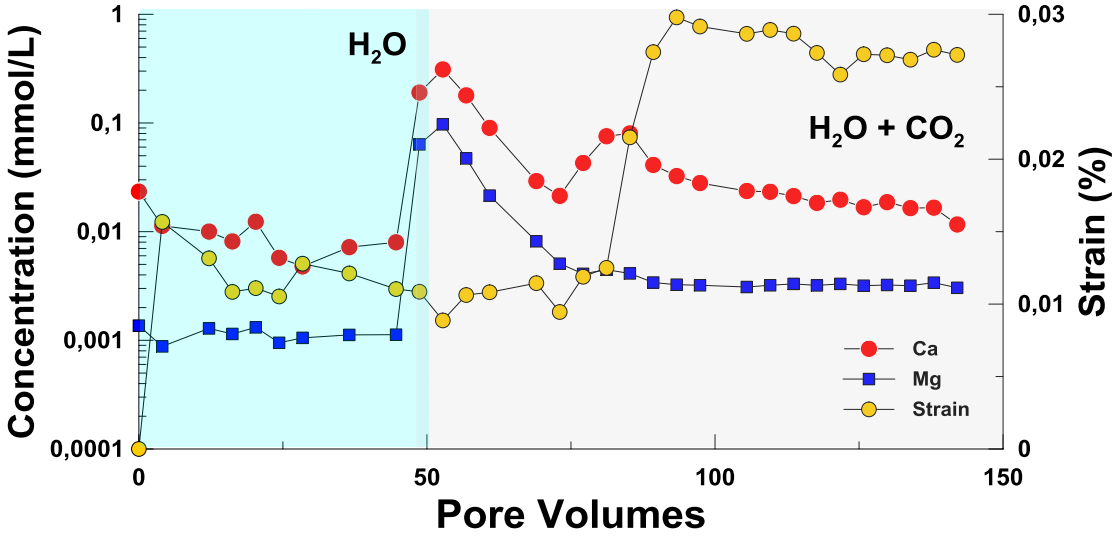

Figure 7- 2. Evolution of Ca and Mg compared with the deformation of the sample.

The evolution of Ca and Mg follows a parallel trend what points towards co-dissolution phenomena. In the case of Ca, the appearance of a two-peak pattern suggests that dissolution occurred in two main steps: The first one upon CO_2-saturated DIW injection and the second

slightly later on. Following previous conjectures (Canal et al. 2013) and the strain evidences observed in this experiment (Figure 7- 2), we conclude that the second step is connected with the late access to new carbonate surfaces following cracking or micro-cracking of the plug.

The evolution of other parameters is also illustrated (Na and K, (Figure 7- 3); SiO_2 (Figure 7- 4) Fe and Mn (Figure 7- 5) and major anions (Figure 7- 6). Following the previous considerations, we observe that no major elemental mobilization occurred during the test and that the major constituent of the rock (SiO_2, present in quartz and other silicates) experiences a slight increase in concentration trend which is to be expected as the result of the undersaturation of silica of the injected fluids. Other features include the mobilization of Fe, Mn and F upon arrival of the carbonated fluid and virtual absence of contributions from the rock to the measured concentration of SO_4 and Cl. Na and K show also a very small washout from the rock, probably associated with the re-equilibration of the exchange complex linked to the presence of kaolinite in the rock.

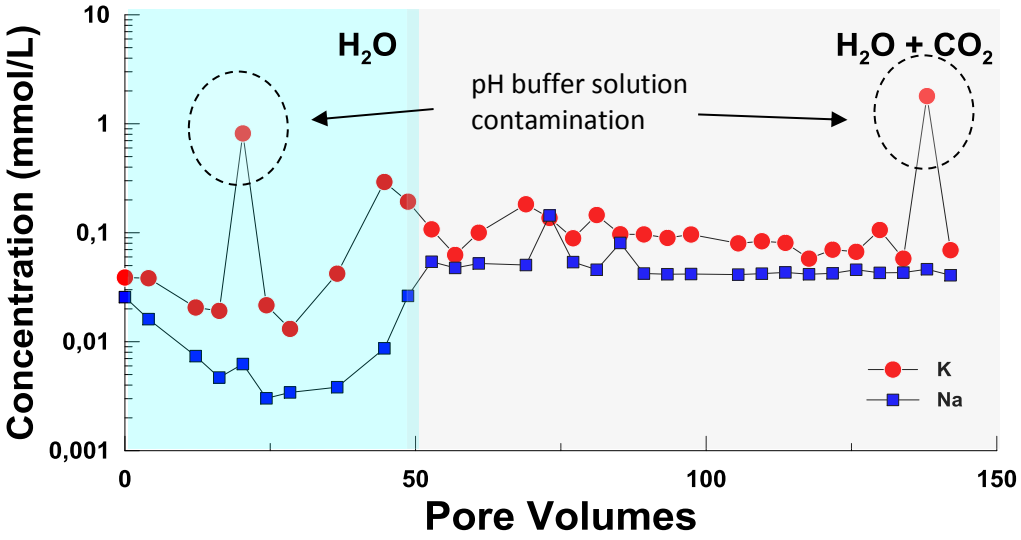

Figure 7- 3. Evolution of K and Na. The ellipses highlight water samples affected by electrode leakage.

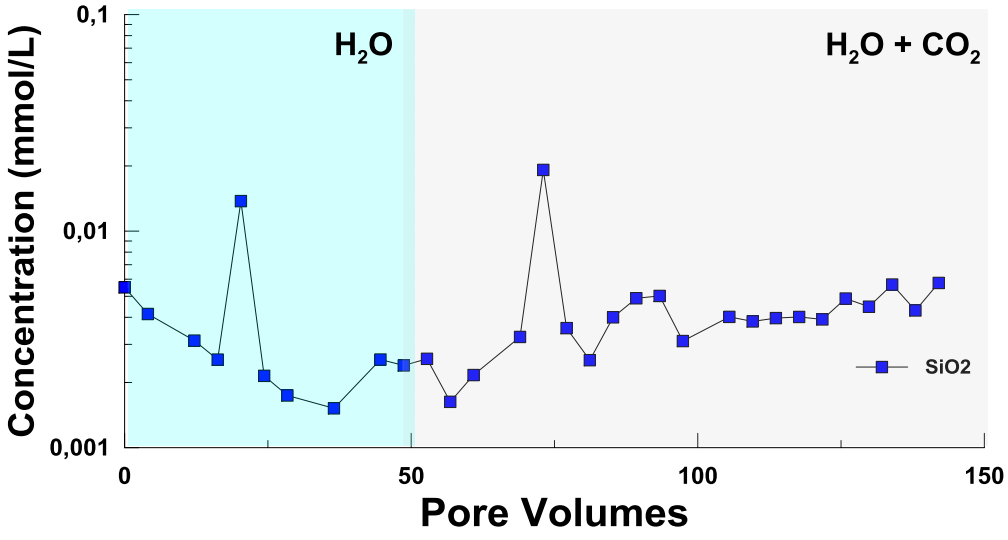

Figure 7- 4. SiO_2 evolution.

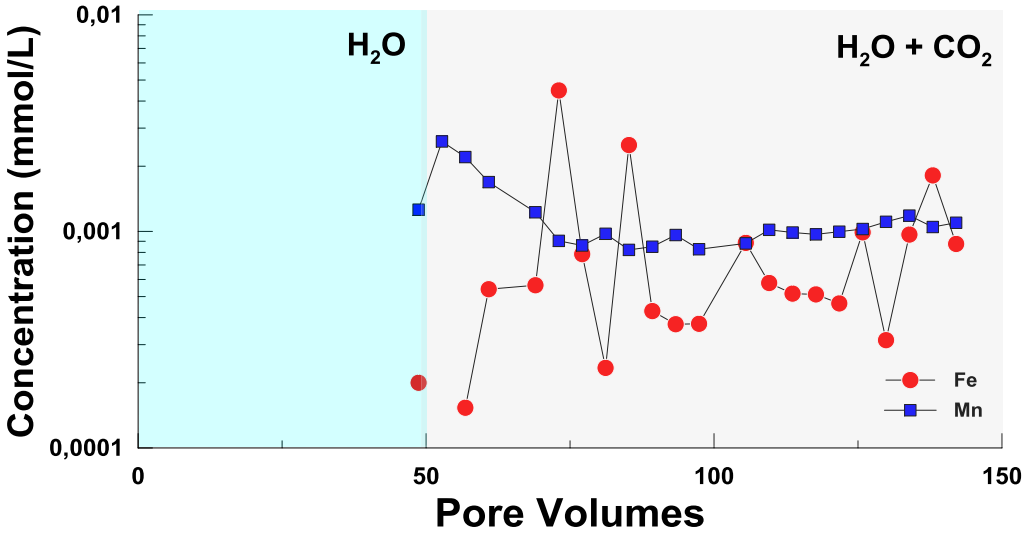

Figure 7- 5. Evolution of Fe and Mn.

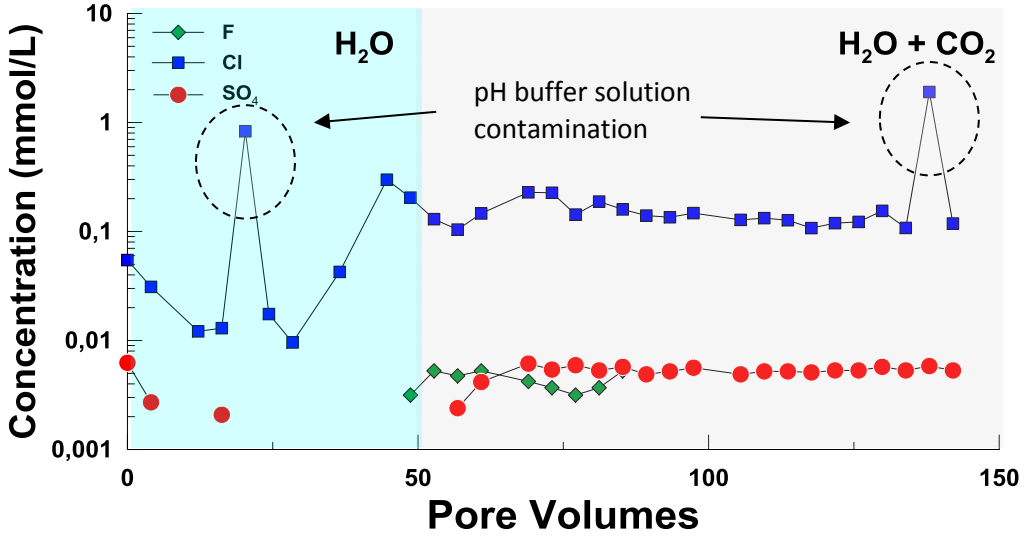

Figure 7- 6. Evolution of F and Cl compared with SO_4. The ellipses highlight water samples affected by electrode leakage.

Two peaks have been identified (for K and F) in which we identify the existence of perturbations in the concentrations measured in the water samples. This is likely due to a contamination accident associated to the entrance into the sample beaker of some drops of the calibration fluid of the EC_{25} electrode (a KCl solution).

Figure 7- 7 shows the evolution of P and S wave velocities (expressed as relative velocities computed from the velocity at time t, V, with respect velocity at time 0 of the experiment, V_0) during the experiment. We observe that both, compressional and shear velocities remain constant (even slightly increase) during the DIW injection stage but they significantly decrease (~100 m/s) during the injection of the carbonated fluid. Attenuation has been recognized as a significant seismic indicator, which is not only useful for amplitude analysis and improving resolution, but also to obtain information on lithology, saturation (fluid type), permeability and pore pressure (Carcione and Gangi 2000). The P and S wave amplitude evolution is illustrated in Figure 7- 8 and compared with the observed axial plug strain. It is interesting to pay attention to the fact that wave amplitudes remain virtually constant at the beginning of the injection of CO_2-saturated DIW and that they drop coinciding with the sudden strain increase developed after ~75 pore volumes (PV) of injection. The decrease-in-amplitude effect is also visualized in Figure 7- 8 where three P-waveforms illustrate the two stages of the experiment and the post-experiment condition. We have recognized this effect before in

previous experiments and it has been also described in recent literature (Hangx et al. 2013). However, it is worth noting that while wave velocity reduction occurs at the beginning of the injection of the carbonated fluid (fluid substitution effect) the largest change in amplitude shows a significant delay with respect this event. The good time-correspondence between amplitude drop and axial strain rise suggests that wave attenuation is more likely associated to mechanical rather than to fluid-substitution effects.

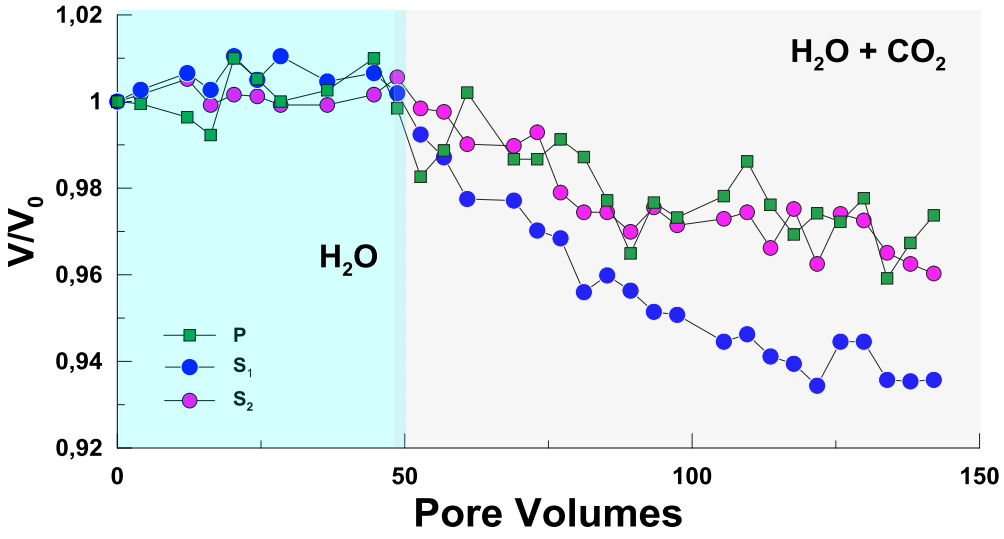

Figure 7- 7. Evolution of compressional (P) and shear (S_1 and S_2) relative wave velocities (top) compared with the velocity measured on the first day experiment.

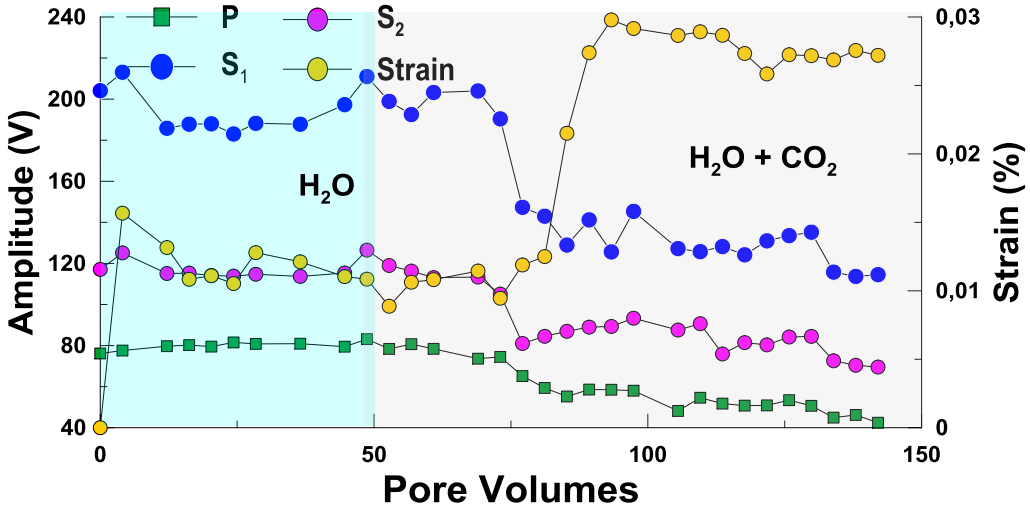

Figure 7- 8. Amplitude data is compared with strain evolution during the experiment.

Comparing the shape of the P and S waves (Figure 7- 9; Figure 7- 10; Figure 7- 11) in the frequency domain throughout the experiment provides new interesting insights. For that purpose FFT (Fast Fourier Transform) analyses have been performed using MATLAB (Santamarina and Fratta 2006a, 2006b). We observe that frequency distribution does not change in a significant way when we consider the water and CO_2-saturated injection stages.

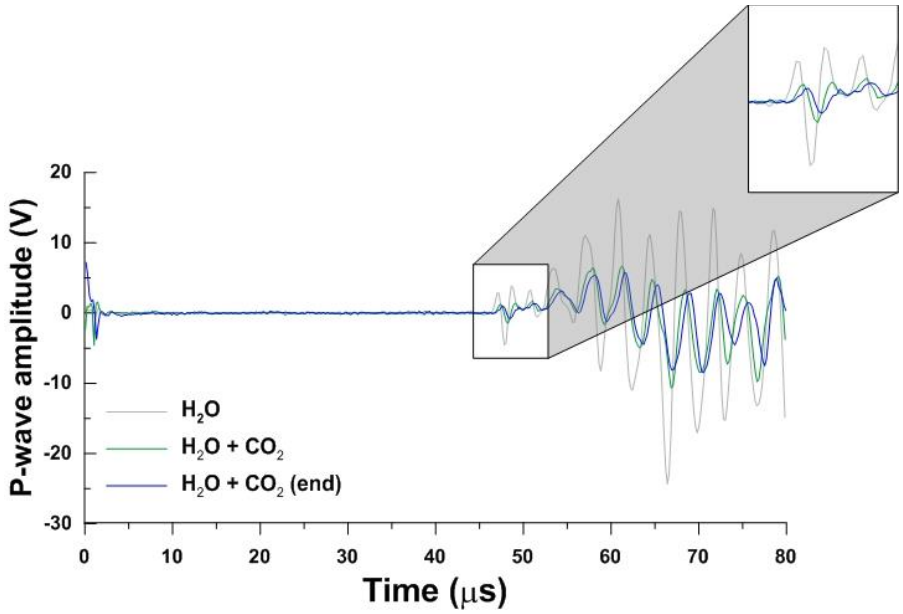

Figure 7- 9. Comparison of experimental P-waveforms associated to the two stages of the experiment and at the end. Delay of the velocity is also observed.

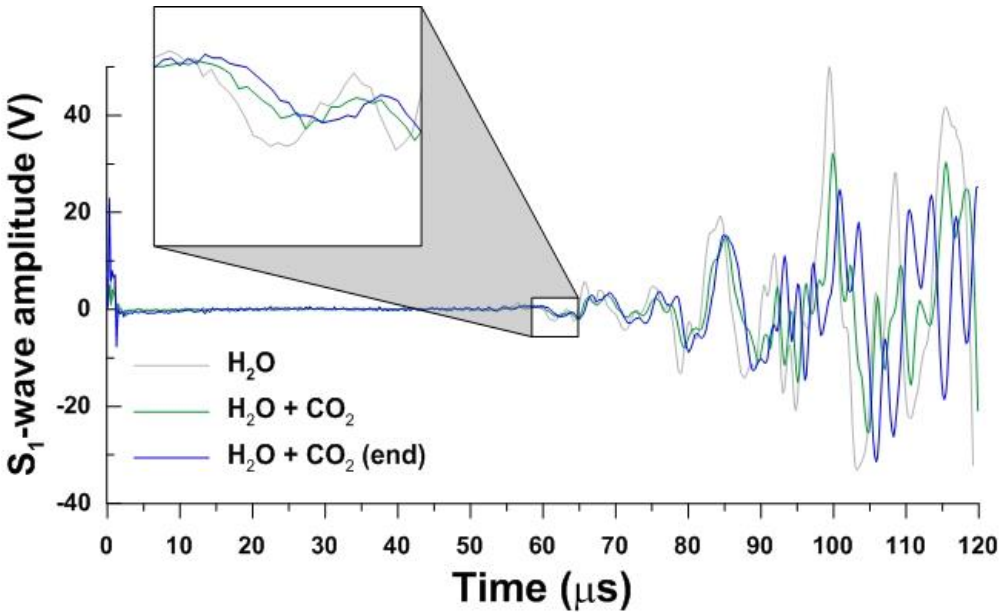

Figure 7- 10. Comparison of experimental S_1-waveforms associated to the two stages of the experiment and at the end. Delay of the velocity is also observed.

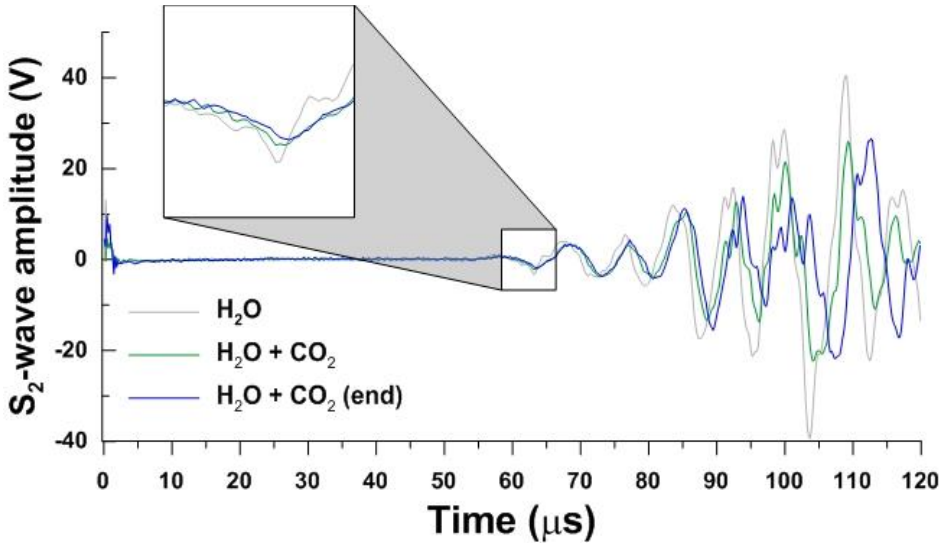

Figure 7- 11. Comparison of experimental S_2-waveforms associated to the two stages of the experiment and at the end. Delay of the velocity is also observed.

However, while during the water injection stage amplitude remains constant, this parameter drops significantly with the onset of the acidic CO_2 injection (Figure 7- 15, Figure 7- 16 and Figure 7- 17) The frequency peaks of the waves were transformed into wavelength using the speed of the wave for each frequency (Table 7- 1). In order to analyse the effect of the velocities in the wave length all the frequency were used to calculate the wavelength at maximum velocity and minimum. The difference between them is 7.5% in the worst scenario. The drop in amplitude is summarized in Table 7- 1 where wavelengths and corresponding peak frequencies are presented (Figure 7- 12; Figure 7- 13 and Figure 7- 14). The attenuation process is happening in the acidic phase; it´s noticeable also that this attenuation is also happening with a compaction of the sample. The trend during this

phase shows a drop of the amplitude (for P and S wave), especially for the frequencies that are related with the smallest wavelength that correspond to the millimeter-length order of magnitude. For the P waves, those frequencies with wavelengths smaller than 4mm result in an attenuation larger than 94%. For both S_1 and S_2 waves (both mutually consistent what suggests a significant isotropy in the vertical plane) the observed attenuations for frequencies related with wavelengths smaller than 4 mm are bigger than 85%.

P wave						
	f (KHz)	Max. Ampl. (mV)	Min. Ampl. (mV)	amplitude decrease (%)	λ Vp max (mm)	λ Vp min (mm)
f1	19,90	2038,96	1202,16	41,04	29,43	27,95
f2	29,85	5513,23	1761,83	68,04	19,62	18,63
f3	149,25	1135,60	72,47	93,62	3,92	3,73
f4	161,69	9311,85	528,88	94,32	3,62	3,44
f5	199,00	16137,15	184,05	98,86	2,94	2,80
f6	211,44	2927,23	4,18	99,86	2,77	2,63
f7	236,32	538,08	34,38	93,61	2,48	2,35
f8	256,22	2857,48	30,72	98,93	2,29	2,17
f9	266,17	3259,09	85,96	97,36	2,20	2,09
f10	273,63	5344,81	53,08	99,01	2,14	2,03
f11	298,51	569,82	28,39	95,02	1,96	1,86
f12	318,41	3250,15	98,55	96,97	1,84	1,75
S1 wave						
	f (KHz)	Max. Ampl. (mV)	Min. Ampl. (mV)	amplitude decrease (%)	λ Vs_1 max (mm)	λ Vs_1 min (mm)
f1	72,14	263996,47	38197,03	85,53	6,00	5,55
f2	92,04	67838,30	26709,57	60,63	4,71	4,35
f3	116,92	22266,72	2395,75	89,24	3,70	3,43
f4	126,87	3581,41	360,48	89,93	3,41	3,16
S2 wave						
	f (KHz)	Max. Ampl. (mV)	Min. Ampl. (mV)	amplitude decrease (%)	λ Vs_2 max (mm)	λ Vs_2 min (mm)
f1	69,65	72698,18	13910,33	80,87	6,41	6,12
f2	97,01	7890,23	1674,35	78,78	4,60	4,40
f3	116,92	11421,82	1486,65	86,98	3,82	3,65
f4	136,82	3723,84	200,27	94,62	3,26	3,12

Table 7- 1. Wavelength conversion from P, S_1 and S_2 frequency analysis.

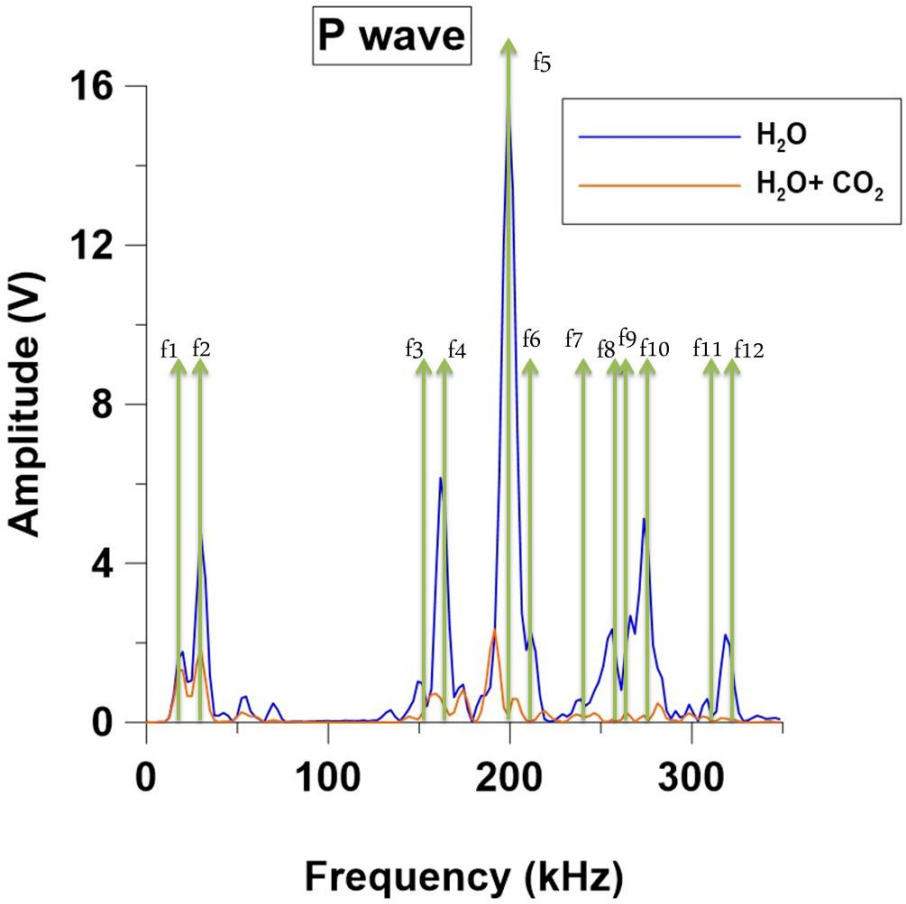

Figure 7- 12. P wave in frequency domain that illustrate the peaks that were studying during the 35 days experiment

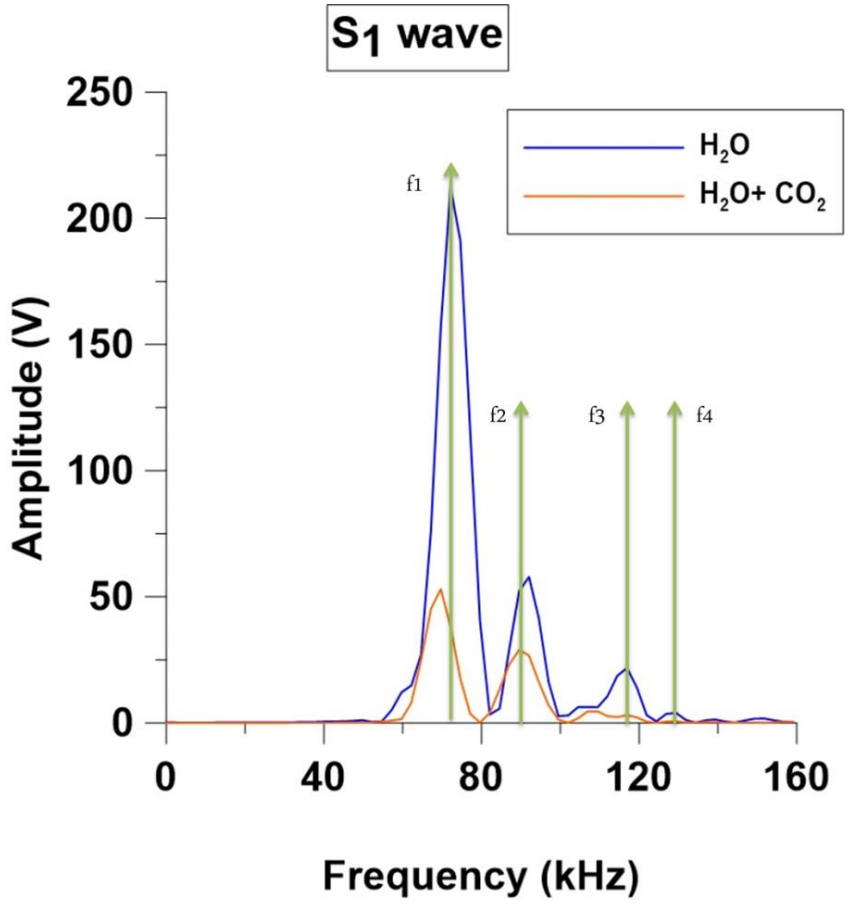

Figure 7- 13. S_1 wave in frequency domain that illustrate the peaks that were studying during the 35 days experiment.

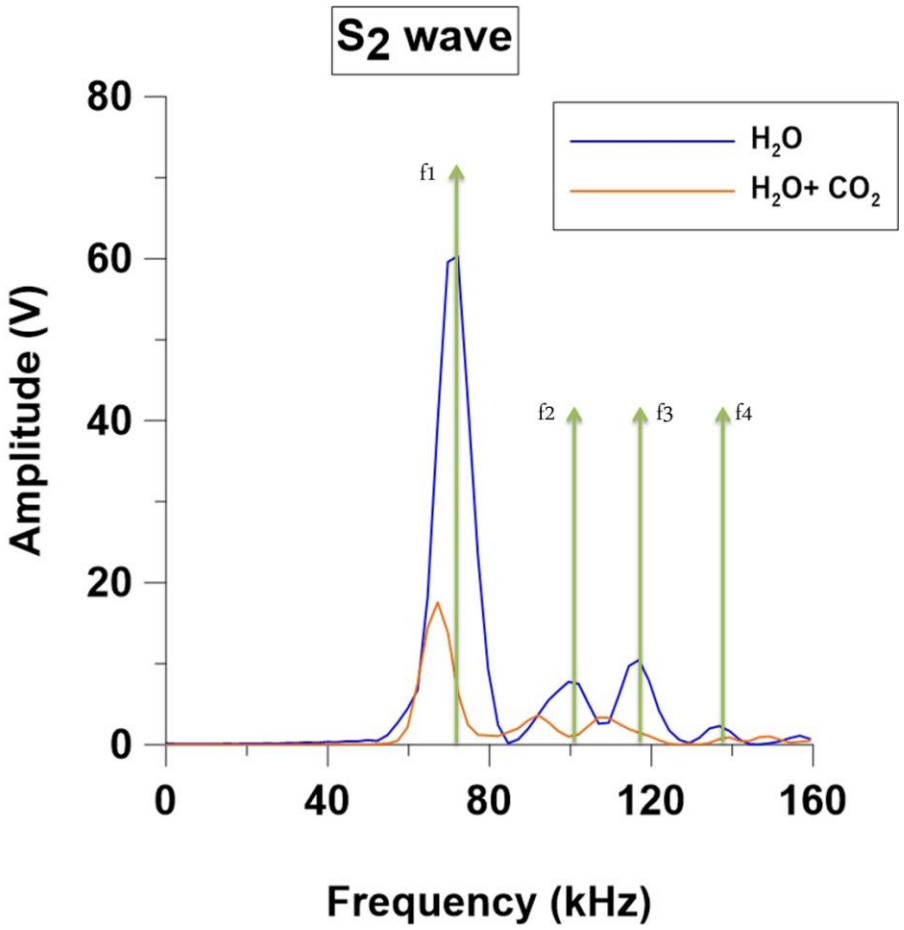

Figure 7- 14. S_2 wave in frequency domain that illustrate the peaks that were studying during the 35 days experiment.

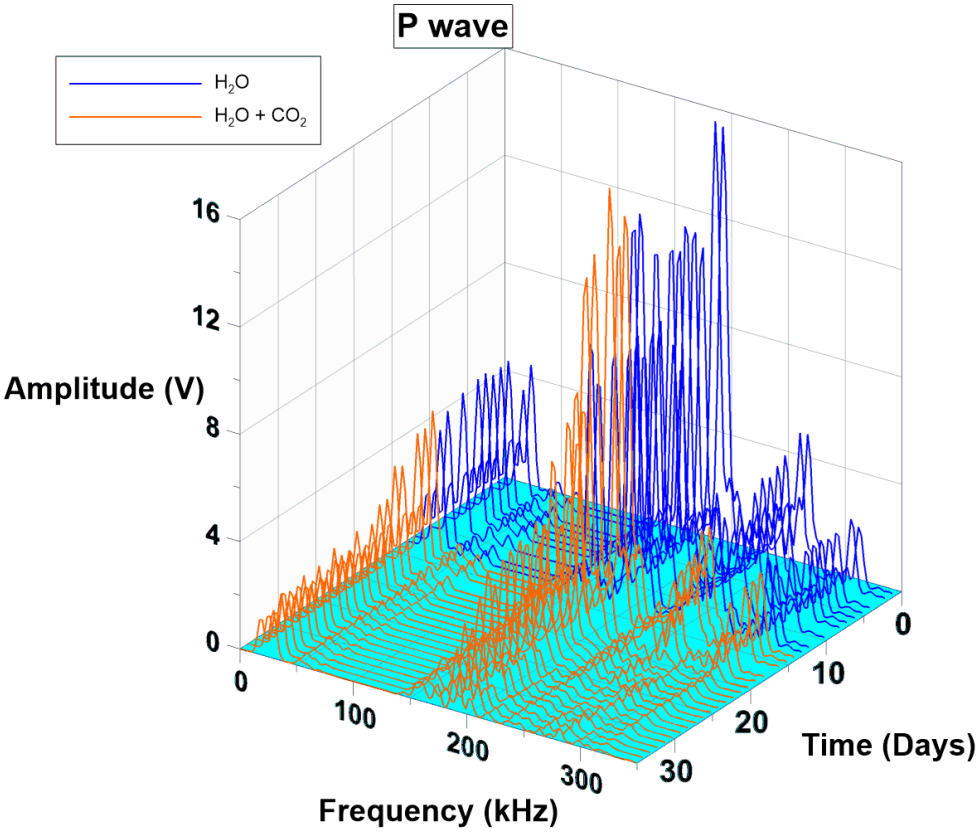

Figure 7- 15. Evolutions of the P wave frequency along the 35 days experiment.

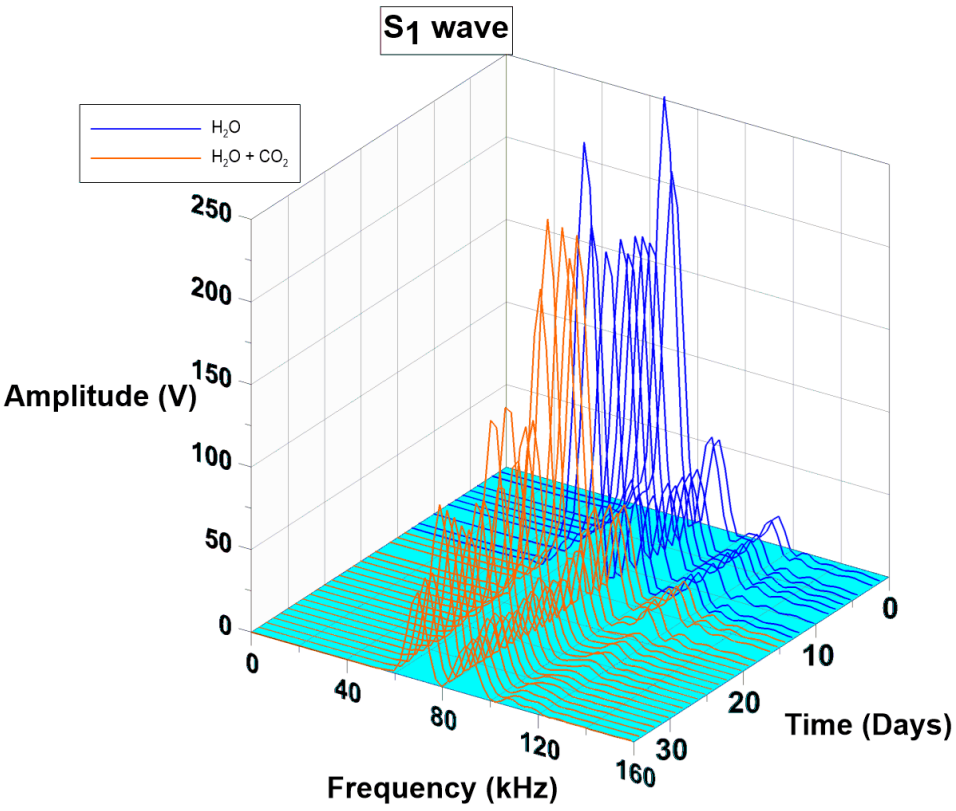

Figure 7- 16. Evolutions of the S_1 wave frequency along the 35 days experiment.

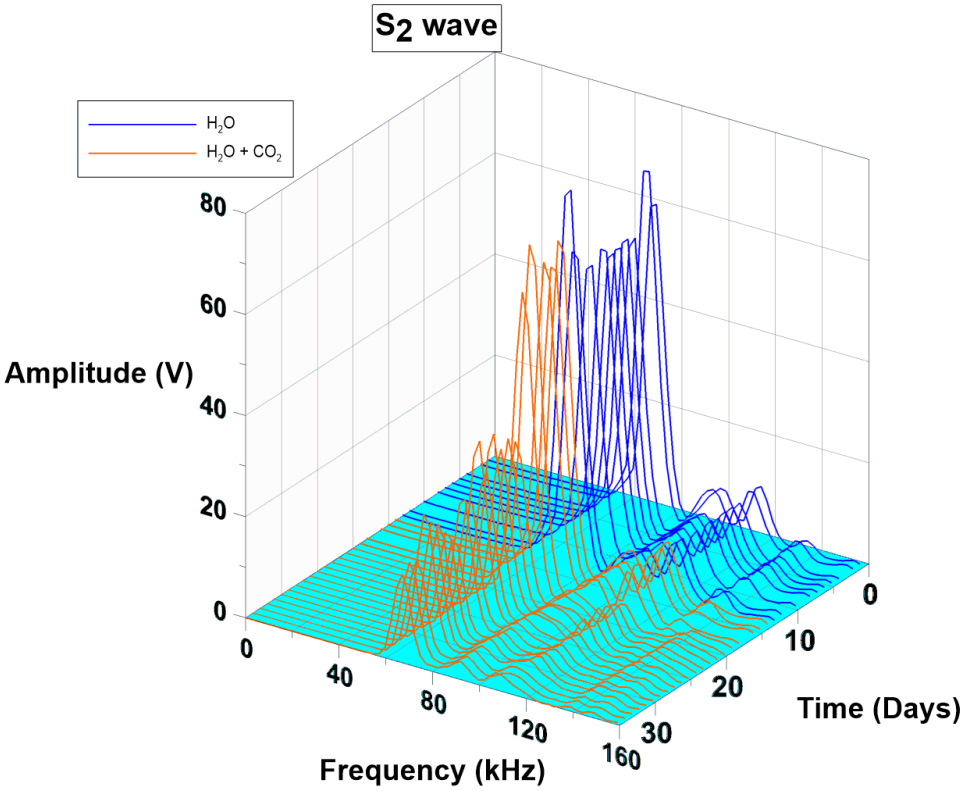

Figure 7- 17. Evolutions of the S_2 wave frequency along the 35 days experiment.

We conjecture that the wave attenuation observed in this experiment is caused by the reactive loss of cement (i.e. dissolution reactions) while the wavelengths are giving us an idea of the size of the spatial domain where the dissolution process is occurring. Overall, there is a reduction in the contact area among grains even though the sample is reducing the volume due to compaction. At this point it is worth to stress the cause-effect relationship and the derived impact over other parameters like strain, permeability and fluid chemistry.

The relationship between strains, pore pressure at the inlet of the plug and computed permeability (Figure 7- 18) illustrates the hydromechanical effects. Following an initial dilatation likely associated with the pass from ambient pressure to the constant flow condition (P_F ~8.2 MPa), the average strain rise to a value of ~0.015% and then steadily drops up to ~50 PV (pore volumes). This drop is likely associated with the compaction of the sample. From 50 to 75 PV, strain remains more or less constant, although this is the period in which reactive processes (due to the injection of the carbonated fluid) have the largest impact (Figure 7- 8). As it was mentioned earlier, the experiment was conducted under constant flow conditions. That means that the pore pressure at the inlet was not constant. We observe (Figure 7- 18) that, while the inlet pressure was nearly constant (~ 8.2 MPa) during the DIW injection stage, it was appreciably higher in the CO_2 -saturated DIW injection phase (~ 9.4 MPa). Thus, the strain increase in the interval from 75 to ~90 PV is likely due to a

supplementary dilation of the plug due to the pore pressure increase. From ~90 PV to the end of the experiment strain experiences again a steady drop that we interpret as being the result of plug compaction.

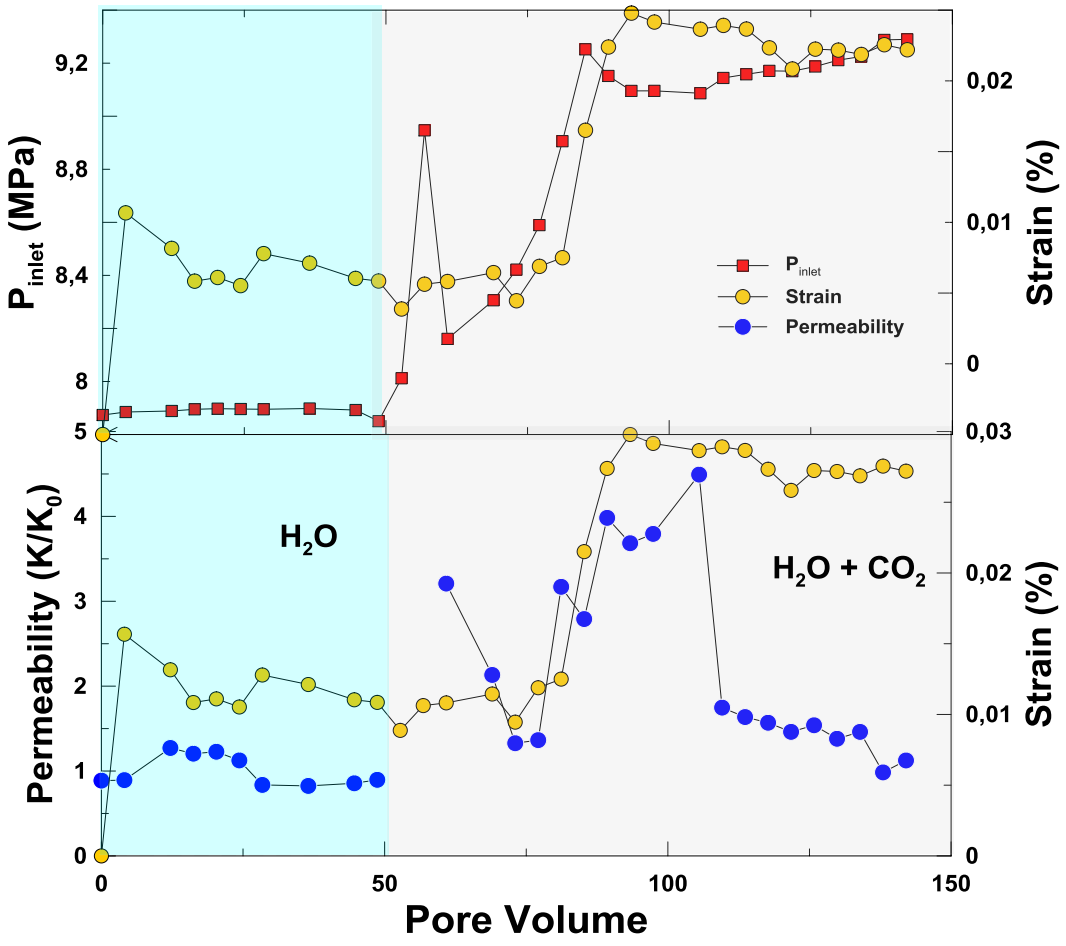

Figure 7- 18. Evolution of strain and pore pressure at the inlet port of the plug during the experiment (top) and computed permeability (bottom) referred to the permeability measured the first day (K_0).

7.4 Summary and conclusions

We observe that there is a small (and transient) permeability increase between 10 and 30 PV (Figure 7- 18). Following the considerations made in previous works (Canal et al. 2013), we conjecture that this could obey to small-scale fines-migration processes (clogging/unclogging of flow paths associated with the release of clayey particles). This process could be connected also with the inlet pressure peak observed at ~60 PV. We observe also that there is a significant permeability increase following the sharp rise in strain between 75-90 PV. This effect requires the enhancement of flow paths, probably associated with the onset of microcracking in the plug. After~ 110 PV, permeability suddenly drops, decreasing from hereafter steadily and, probably, as a consequence of the observed sample compaction. Overall, in this experiment, reactive processes do not seem very important taking into account total amount of dissolved materials. However, this (coupled to associated mechanical effects) turns out to significantly affect the evolution of permeability. The reason would stand in the fact that the mass that is being dissolved is located in critical grain-supporting positions : If this material is being lost, the rock will experience compaction.

We have performed a complex coupled-phenomena (hydro-chemo-mechanical) multi-stage, long-lasting experiment with the Corvio sandstone in which, presuming a limited reactivity, the extent of

hydromechanical couplings would be stressed. It turns out that, even considering the low reactivity of this rock, chemical reactions associated to the dissolution of trace-amount minerals (particularly in the case of the injection of a CO_2-saturated fluid) have a significant impact over the evolution of permeability. Similarly, fluid substitution has a significant effect over wave propagation properties, specifically, wave amplitude. This effect cannot be solely attributed to mechanical (strain, crack development) or chemical processes (dissolution-enhanced porosity, etc.). This experiment illustrates interlinked hydro-mechanical processes with a minor influence of reactive (chemical) phenomena. This is a relevant approach when trying to quantify the relative contribution of mixed hydro-chemo-mechanical processes.

7.5 References

Canal J, Delgado J, Falcón I, Yang Q, Juncosa R, Barrientos V. Injection of CO_2-saturated water through a siliceous sandstone plug from the Hontomin test site (Spain): Experiment and modeling. Environ Sci Technol. 2013;47(1):159–67.

Carcione JM, Gangi AF. Non-equilibrium compaction and abnormal pore-fluid pressures: effects on rock properties1. Geophys Prospect. Blackwell Science Ltd; 2000;48(3):521–37.

Diamond LW, Akinfiev NN. Solubility of CO_2 in water from −1.5 to 100 °C and from 0.1 to 100 MPa: evaluation of literature data and thermodynamic modelling. Fluid Phase Equilib. 2003;208(1–2):265–90.

Duan Z, Sun R. An improved model calculating CO_2 solubility in pure water and aqueous NaCl solutions from 273 to 533 K and from 0 to

2000 bar. Chem Geol. 2003;193(3–4):257–71.

Duan Z, Sun R, Zhu C, Chou IM. An improved model for the calculation of CO_2 solubility in aqueous solutions containing Na^+, K^+, Ca^{2+}, Mg^{2+}, Cl^-, and SO_4^{2-}. Mar Chem. 2006;98(2–4):131–9.

Franklin. Suggested methods for determining the strength of rock materials in triaxial compression: Revised version. Int J Rock Mech Min Sci Geomech Abstr. 1983;20(6):285–90.

Hangx S, van der Linden A, Marcelis F, Bauer A. The effect of CO_2 on the mechanical properties of the Captain Sandstone: Geological storage of CO_2 at the Goldeneye field (UK). Int J Greenh Gas Control. 2013;19(0):609–19.

Hoek E, Franklin JA. A simple triaxial cell for field or laboratory testing of rock. Imperial College of Science and Technology, University of London; 1967.

Rummel F, Alheid HJ, Frohn C. Dilatancy and fracture induced velocity changes in rock and their relation to frictional sliding. pure Appl Geophys. Birkhauser-Verlag; 1978;116(4-5):743–64.

Santamarina JC, Fratta D. Frequency Domain Analysis of Signals (Discrete Fourier Transform). Discret Signals Inverse Probl. John Wiley & Sons, Ltd; 2006a. p. 103–36.

Santamarina JC, Fratta D. Frequency Domain Analysis of Systems. Discret Signals Inverse Probl. John Wiley & Sons, Ltd; 2006b. p. 137–74.

CHAPTER 8. CONCLUSIONS

8.1 Introduction

The most significant results, findings and conclusions obtained during the development of this thesis are summarized next:

-We have designed, constructed and tested a versatile experimental rig useful to develop coupled thermos-hydro-chemo-mechanical experiments, with special attention to the CCS research field.

-The experimental system developed is modular, scalable and can be enhanced through the integration of additional observation/monitoring systems. Although significant electronic improvements still need to be introduced (data acquisition and sensor integration, volume strain monitoring, additional petro-geophysical properties –e.g. electrical resistivity, acoustic emission…-, high T&P geochemical sensors,…) the system has proved to be both simple and reliable to perform long-lasting coupled experiments.

-Based on the experiments performed, the study of rock-mechanics-related coupled processes requires significant background information about the materials tested. The assessment of homogeneity/inhomogeneity and isotropy/anisotropy relationships and, in general, a comprehensive materials characterization is critical in order to set up a sound basis to discuss and understand the behaviour of the studied system. Likewise, a good *ex ante* knowledge on the mechanical properties of the tested materials is critical to

identify whether or not the changes observed during the development of a coupled phenomenon experiment are due to the selection of experimental conditions (e.g. P, T and P_{pore} above or below initial cracking stress, yield stress, closeness to ultimate strength…). There are very few references in the literature paying attention to this circumstance. Although this could be understandable due to the inherent complexity of experimentation and difficulties to access to reservoir-related core materials, it must be acknowledged that this fact introduces uncertainties that affect the generalization of the derived conclusions and eventually justify contradictory observations attained by different authors.

-Based on the previous consideration, we have performed a systematic characterization (which is presented in chapter 6) of one of the selected testing materials (Corvio sandstone) followed by 1 core-flow experiments (chapters 7).

-The crack closing stress for Corvio sandstone (which refers to pore compaction and compliant crack closing) occurs at 10 MPa while the onset of crack initiation takes place at ~18 MPa. These values have been indirectly verified by different techniques. Direct application of these results imply a better assessment of experimental conditions in order to reduce undesired effects like enhanced permeability due to non-closed cracks at low stress levels or associated with rock damage induced by high stresses.

-These characterization results constitute a useful baseline for CO_2 injection studies using this sedimentary rock. Our results are of direct application when working with this rock in the laboratory, as they help us: (i) to understand processes such as thresholds for pore compaction, compliant crack closure, and physicochemical coupling; (ii) to better calibrate geophysical techniques by reducing uncertainty and providing a well-constrained fabric model; (iii) to improve experimental design parameters such as stress ranges, plug orientation, and vector properties, among others. Furthermore, we want to highlight the importance of weak anisotropy when considering naturally homogeneous materials (at least in appearance). These observations can be scaled up to field scenarios in order to improve reservoir models. This comprehensive characterization of Corvio sandstone covers geomechanical, geochemical, geophysical and hydrodynamic properties. Together with the detailed assessment of anisotropy presented here, the results indicate that Corvio sandstone could be used as a particularly interesting rock-standard to improve the understanding of reservoirs subjected to complex thermo-hydromechano-geochemical coupled phenomena, typically associated with CO_2 storage practices.

Taking the different experiments performed as self-contained entities, we draw the following conclusions from each one of them:

Experiment described in chapter 4

- The rock was submitted to stress conditions far away of its failure envelope and the onset of cracking happened nearly 20 days after loading the sample. However, if this microcracking were associated to creep, we should expect a more or less gradual increase in the V_P/V_S ratio, which is not the case. Therefore, following different authors, we conjecture that, at the grain scale, microcracking could be chemically enhanced by the presence of aqueous fluids in a process known as subcritical crack growth (*i.e.* "stress-corrosion cracking"). In the case of quartz (the dominant mineral in the Arcera Sandstone) would occur as a result of the weakening of strained Si-O bonds at the crack tips through chemical interactions with water, especially at the low pH of the carbonated fluid.
- No significant differences before and after the experiment were identified in the sample concerning its mineralogy or its relative abundance. However, a noticeable change in the hydrodynamic and acoustic properties of the sample took place as well as discernible patterns in the evolution of the outlet fluid.
- Permeability enhancement associated to mineral dissolution may have also played a relevant role. It is clear that mechanical processes were subordinated with respect to permeability enhancement due to the porosity increase associated to mineral dissolution.

- With the exception of certain trace minerals, the relatively simple mineralogy of the Arcera sandstone makes possible that the model is successful in reproducing the experimental trends. According to this model, the mineral experiencing the largest mass transfer is Mg-calcite. It is worth to remark how such a small porosity change (~0.85%) may have associated the large variation observed in permeability. This phenomenon can be linked to the concentrated dissolution of minerals in pore throat locations, where a minimum increase in pore volume will determine a better connectivity and the concomitant increase in permeability.

Experiment described in Chapter 5:

- We observe a significant dissolution coupled with the injection of the acidic fluid (CO_2) what turns out to trigger a significant compaction of the sample. This is connected with a fast change in its permeability.
- P and S-wave velocities appear not to be sufficiently sensitive to detect the weakening of the material.
- CO_2 effects appear in short term with highly reactive formation. The experiment needs a very small amount of fluid to be able to monitor the reactivity.
- While with the P-wave fluid substitution is observed, the change of the S-wave amplitudes may reveal internal rock change during

the acidic injection perhaps for a dissolution that occurs in the cement that is supporting the grains.

- It is interesting to remember that, although the most relevant components in this rock are carbonate minerals, clays may play also their role. Thus, following an initial period when the SiO_2 concentrations decrease (a phenomena likely linked to the early dissolution of SiO_2-bearing substances of source-limited poor crystallinity), we observe an increase in its concentration which is more pronounced when the P_{CO2} is higher.

Analysing the core flooding experiment in Chapter 7 we observe that:

- In this experiment, reactive processes do not seem to be very important because of the amount of dissolved mass. However, this minor mass transfer appears to play a significant role in terms of permeability evolution. The reason for that would be grounded in the circumstance that this is being dissolved from points located in critical grain-supporting positions. If this material is being lost, it will trigger compaction.
- It is also noticeable the delay in response between mineral dissolution and rock compaction. This reinforces the conjecture that the first material dissolved is the cement that is supporting the grains, when it becomes unstable the sample suffers compaction.

- It turns out that, even considering the low reactivity of this rock, chemical reactions associated to the dissolution of trace-amount minerals (particularly in the case of the injection of a CO_2-saturated fluid) have a significant impact over the evolution of permeability. Similarly, wave attenuation occurs due to a loss of contact between grains. This effect cannot be solely attributed to mechanical (strain, crack development) or chemical processes (dissolution-enhanced porosity, etc.). This experiment illustrates interlinked hydro-mechanical processes with a minor influence of reactive (chemical) phenomena. This is a relevant approach when trying to quantify the relative contribution of mixed hydro-chemo-mechanical processes.
- In this experiment, we assume that the observed wave attenuation is caused by the loss of cement and the wavelength would give us an idea about the relative size-domain (i.e. order of magnitude) where the dissolution phenomena would be happening. This would reduce the contact area among grains even though the sample is reducing the volume due to compaction.

Piling up all the information obtained along the experiment we can reach to these general conclusions:

- The low flow conditions and a fluid saturated with CO_2 have been reproduced through experimental conditions that are

representative of the circumstances prevailing reservoir, at some distance of the CO_2 injection point.

- V_P/V_S body wave velocities is not a good indicator for detecting changes in the pore space.
- V_P/V_S body wave frequency domain analysis (amplitude) is a good indicator for rock/fluid properties change.
- Chapters 5 and 7 illustrate different behaviours when performing the same frequency analysis. In the case of the vuggy limestone (chapter 5) frequency attenuation occurs throughout all the recorded spectra. However, in the case of the Corvio sandstone (chapter 7) the largest attenuation occurs for those frequencies corresponding to smaller wavelengths. This would be related with the type of damage affecting each sample. In the case of the sandstone damage would be generalized (i.e. affecting the whole core plug) while in the case of the limestone damage would be focus because dissolution will be concentrated in those pore-throats and necks with faster flow (i.e. where the acidic solution renewal is more effective)
- The trigger mechanism for changes in the hydro-mechanical behaviour of the tested samples appears always to be fluid/rock chemical disequilibrium. In this case, coupled hydro-chemo-mechanical processes would occur independently of the stress state and this can be accentuated in cases were sample stresses are close to failure.

8.2 Future work

In the following paragraphs we provide a few ideas concerning future developments and approaches starting from the works presented ere:

-A triaxial test with body wave at variable frequencies for P and S wave will give us the response of the sample in the order of Hz to MHz. This will be helpful information that can be more representative for the seismic monitoring of CO_2 plumes.

-While the typical core plugs used so far in our experiments have a typical diameter of 38.1 mm diameter, this is insufficient for working with vuggy carbonates for which the minimum acceptable diameter would be ~100 mm if its greatest vug is in the order of 1 cm.

-The use of high resolution digital image (micro CT scanning) of test samples before and after the experiments can help to understand the phenomena and measure internal changes.

-Implementation of pH meter and resistivimeter in the pore pressure line that can resist pressure and temperature. This can give us information of fluid before and after the plug. The data will be a input for a mass balance model.

-Measure continuously the resistivity of the rock. If there is variation along the experiment phases will give the starting point for a screening of the reservoir with a resistivity tool in a pilot project.

-The experiments can be designed taking into consideration the importance of the wave analysis in frequency domain so we can think to obtain an acquisition card with higher resolution and to acquire all the waveform.

CHAPTER 9. BIBLIOGRAPHY

Akbarabadi M, Piri M. Relative permeability hysteresis and capillary trapping characteristics of supercritical CO_2/brine systems: An experimental study at reservoir conditions. Adv Water Resour.

Alcalde J, Marzán I, Saura E, Martí D, Ayarza P, Juhlin C, et al. 3D geological characterization of the Hontomín CO_2 storage site, Spain: Multidisciplinary approach from seismic, well-log and regional data. Tectonophysics. 2014;627:6–25.

Alemu BL, Aker E, Soldal M, Johnsen Ø, Aagaard P. Effect of sub-core scale heterogeneities on acoustic and electrical properties of a reservoir rock: A CO_2 flooding experiment of brine saturated sandstone in a computed tomography scanner. Geophys Prospect. 2013;61(1):235–50.

Andrä H, Combaret N, Dvorkin J, Glatt E, Han J, Kabel M, et al. Digital rock physics benchmarks—Part I: Imaging and segmentation. Comput Geosci. 2013;50:25–32.

Adler PM, Jacquin CG, Thovert J. The formation factor of reconstructed porous media. Water Resour Res. Wiley Online Library; 1992; 28(6):1571–6.

Andreani M, Luquot L, Gouze P, Godard M, Hoisé E, Gibert B. Experimental Study of Carbon Sequestration Reactions Controlled by the Percolation of CO_2-Rich Brine through Peridotites. Environ Sci Technol. 2009;43(4):1226–31.

Angus DA, Kendall J, Fisher QJ, Segura JM, Skachkov S, Crook AJL, et al. Modelling microseismicity of a producing reservoir from coupled fluid-flow and geomechanical simulation. Geophys Prospect. Wiley Online Library; 2010;58(5):901–14.

Appelo CAJ, Postma D. Geochemistry, groundwater and pollution. CRC press; 2005.

Appelo CAJ, Verweij E, Schäfer H. A hydrogeochemical transport model for an oxidation experiment with pyrite/calcite/exchangers/organic matter containing sand. Appl

geochemistry. Elsevier; 1998; 13(2):257–68.

ASTM 4543. Practices for Preparing Rock Core as Cylindrical Test Specimens and Verifying Conformance to Dimensional and Shape Tolerances. ASTM International.

Asef MR, Najibi AR. The effect of confining pressure on elastic wave velocities and dynamic to static Young's modulus ratio. 2013;78(3).

Bachu S. Sequestration of CO_2 in geological media in response to climate change: road map for site selection using the transform of the geological space into the CO_2 phase space. 2002;43:87–102.

Barrientos V, Delgado J, Navarro V, Juncosa R, Falcon Suarez I, Vazquez A. Characterization and geochemical-geotechnical properties of granite sawdust produced by the dimension stone industry of O Porrino (Pontevedra, Spain). Q. J. Eng. Geol. Hydrogeol. 2010.

Batzle ML, Han D-H, Hofmann R. Fluid mobility and frequency-dependent seismic velocity -- Direct measurements. Geophysics. 2006;71(1):N1–9.

Bednárik M, Kohút I. Three-dimensional colour functions for stress state visualisation. Comput Geosci. 2012;48:117–25.

Bernabe Y. Pore geometry and pressure dependence of the transport properties in sandstones. Geophysics. Society of Exploration Geophysicists; 1991;56(4):436–46.

Beroiz C, Permanyer A. Hydrocarbon habitat of the Sedano trough, Basque-Cantabrian basin, Spain. J Pet Geol. Wiley Online Library; 2011;34(4):387–409.

Best AI, Sothcott J, McCann C. A laboratory study of seismic velocity and attenuation anisotropy in near-surface sedimentary rocks. Geophys Prospect. Blackwell Publishing Ltd; 2007;55(5):609–25.

Blake OO, Faulkner DR. The effect of fracture density and stress state on the static and dynamic bulk moduli of Westerly Granite. J Geophys Res Solid Earth. 2016 Mar 22;121(4).

Bowker KA, Shuler PJ. Carbon dioxide injection and resultant alteration of the Weber Sandstone, Rangely Field, Colorado. Am. Assoc. Pet. Geol. Bull. American Association of Petroleum Geologists; 1991. p. 1489–99.

Cai M. Practical Estimates of Tensile Strength and Hoek–Brown Strength Parameter m i of Brittle Rocks. Rock Mech Rock Eng. 2010;43(2):167–84.

Canal J, Delgado J, Falcón I, Yang Q, Juncosa R, Barrientos V. Injection of CO_2-saturated water through a siliceous sandstone plug from the Hontomin test site (Spain): Experiment and modeling. Environ Sci Technol. 2013;47(1):159–67.

Carcione JM, Gangi AF. Non-equilibrium compaction and abnormal pore-fluid pressures: effects on rock properties1. Geophys Prospect. Blackwell Science Ltd; 2000;48(3):521–37.

Chichinina T, Obolentseva I, Gik L, Bobrov B, Ronquillo-Jarillo G. Attenuation anisotropy in the linear-slip model: Interpretation of physical modeling data. Geophysics. 2009;74(5):WB165.

Churcher PL, French PR, Shaw JC, Schramm LL. Rock Properties of Berea Sandstone, Baker Dolomite, and Indiana Limestone. Society of Petroleum Engineers. 1991; 20-22 February, SPE 21044.

Colón CFJ, Oelkers EH, Schott J. Experimental investigation of the effect of dissolution on sandstone permeability, porosity, and reactive surface area1. Geochim Cosmochim Acta. 2004 Feb 15;68(4):805–17.

Diamond LW, Akinfiev NN. Solubility of CO_2 in water from −1.5 to 100 °C and from 0.1 to 100 MPa: evaluation of literature data and thermodynamic modelling. Fluid Phase Equilib. 2003; 208(1–2):265–90.

Duan Z, Sun R. An improved model calculating CO_2 solubility in pure water and aqueous NaCl solutions from 273 to 533 K and from 0 to 2000 bar. Chem Geol. 2003; 193(3–4):257–71.

Duan Z, Sun R, Zhu C, Chou IM. An improved model for the calculation

of CO_2 solubility in aqueous solutions containing Na^+, K^+, Ca^{2+}, Mg^{2+}, Cl^-, and SO_4^{2-}. Mar Chem. 2006; 98(2–4):131–9.

Eissa EA, Kazi A. Relation between static and dynamic Young's moduli of rocks. Int J Rock Mech Min Sci Geomech Abstr. Pergamon; 1988 Dec;25(6):479–82.

Elío J, Nisi B, Ortega MF, Mazadiego LF, Vaselli O, Grandia F. CO_2 soil flux baseline at the technological development plant for CO_2 injection at Hontomin (Burgos, Spain). Int J Greenh Gas Control. 2013;18:224–36.

Ellis MH, Sinha MC, Minshull TA, Sothcott J, Best AI. An anisotropic model for the electrical resistivity of two-phase geologic materials. Geophysics. 2010;75(6):E161–70.

Falcon-Suarez I, North L, Best A. Experimental Rig to Improve the Geophysical and Geomechanical Understanding of CO_2 Reservoirs. Energy Procedia. 2014;59:75–81.

Farrell NJC, Healy D, Taylor CW. Anisotropy of permeability in faulted porous sandstones. J Struct Geol. 2014;63:50–67.

Fetter CW (Charles W. Contaminant hydrogeology / C.W. Fetter. New York: Macmillan Pub. Co.; Maxwell Macmillan Canada; Maxwell Macmillan International; 1993.

Fjær E. Static and dynamic moduli of a weak sandstone. Geophysics. Society of Exploration Geophysicists; 2009 Mar 1;74(2):WA103–12.

Fjær E, Stroisz AM, Holt RM. Elastic Dispersion Derived from a Combination of Static and Dynamic Measurements. Rock Mech Rock Eng. 2013;46(3):611–8.

Fortin J, Guéguen Y, Schubnel A. Effects of pore collapse and grain crushing on ultrasonic velocities and V_p/V_s. J Geophys Res Solid Earth. Wiley Online Library; 2007; 112(B8).

Franklin. Suggested methods for determining the strength of rock materials in triaxial compression: Revised version. Int J Rock Mech

Min Sci Geomech Abstr. 1983; 20(6):285–90.

Fredrich JT, Greaves KH, Martin JW. Pore geometry and transport properties of Fontainebleau sandstone. Int J Rock Mech Min Sci Geomech Abstr. 1993 Dec;30(7):691–7.

Gaus I. Role and impact of CO_2–rock interactions during CO_2 storage in sedimentary rocks. Int J Greenh Gas Control. 2010 Jan; 4(1):73–89.

Gouze P, Luquot L. X-ray microtomography characterization of porosity, permeability and reactive surface changes during dissolution. J Contam Hydrol. Elsevier; 2011;120:45–55.

Guéguen Y, Sarout J, Fortin J, Schubnel A. Cracks in porous rocks: tiny defects, strong effects. Lead Edge. Society of Exploration Geophysicists; 2009; 28(1):40–7.

Le Guen Y, Renard F, Hellmann R, Brosse E, Collombet M, Tisserand D, et al. Enhanced deformation of limestone and sandstone in the presence of high fluids. J Geophys Res Solid Earth. Wiley Online Library; 2007;112(B5).

Hakala M, Kuula H, Hudson JA. Estimating the transversely isotropic elastic intact rock properties for in situ stress measurement data reduction: A case study of the Olkiluoto mica gneiss, Finland. Int J Rock Mech Min Sci. 2007;44(1):14–46.

Hangx SJT, Spiers CJ, Peach CJ. Creep of simulated reservoir sands and coupled chemical-mechanical effects of CO_2 injection. J Geophys Res. 2010 Sep 14;115(B9):B09205.

Hangx S, van der Linden A, Marcelis F, Bauer A. The effect of CO_2 on the mechanical properties of the Captain Sandstone: Geological storage of CO_2 at the Goldeneye field (UK). Int J Greenh Gas Control. 2013;19(0):609–19.

Heiland J. Laboratory testing of coupled hydro-mechanical processes during rock deformation. Hydrogeol J. Springer; 2003;11(1):122–41.

Hernández JM, Pujalte V, Robles S, Martín-Closas C. División

estratigráfica genética del Grupo Campóo (Malm-Cretácico inferior; SW Cuenca Vascocantábrica). Rev la Soc Geológica España. 1999;12(3-4):377–96.

Herrmann W, Berry RF. MINSQ – a least squares spreadsheet method for calculating mineral proportions from whole rock major element analyses. Geochemistry Explor Environ Anal. 2002 Nov 1; 2(4):361–8.

Hoek E, Brown ET. Underground excavations in rock. 1980.

Hoek E, Carranza-Torres C, Corkum B. Hoek-Brown failure criterion – 2002 Edition. 5th North Am Rock Mech Symp. 2002;1:267–73.

Hoek E, Franklin JA. A simple triaxial cell for field or laboratory testing of rock. Imperial College of Science and Technology, University of London; 1967.

Izgec O, Demiral B, Bertin H, Akin S. CO_2 injection into saline carbonate aquifer formations I: laboratory investigation. Transp Porous Media. Springer; 2008;72(1):1–24.

Kharaka YK, Cole DR, Hovorka SD, Gunter WD, Knauss KG, Freifeld BM. Gas-water-rock interactions in Frio Formation following CO_2 injection: Implications for the storage of greenhouse gases in sedimentary basins. Geology. Geological Society of America; 2006; 34(7):577–80.

Kieffer B, Jové CF, Oelkers EH, Schott J. An experimental study of the reactive surface area of the Fontainebleau sandstone as a function of porosity, permeability, and fluid flow rate. Geochim Cosmochim Acta. 1999 Nov;63(21):3525–34.

King MS. Static and dynamic elastic properties of rocks from the Canadian shield. Int J Rock Mech Min Sci Geomech Abstr. Pergamon; 1983 Oct;20(5):237–41.

King MS. Recent developments in seismic rock physics. Int J Rock Mech Min Sci. 2009 Dec;46(8):1341–8.

Klein E, Baud P, Reuschlé T, Wong T. Mechanical behaviour and failure

mode of bentheim sandstone under triaxial compression. Phys Chem Earth, Part A Solid Earth Geod. 2001 Jan;26(1-2):21–5.

Krevor SCM, Pini R, Zuo L, Benson SM. Relative permeability and trapping of CO_2 and water in sandstone rocks at reservoir conditions. WATER Resour Res. 2012;48.

Kummerow J, Spangenberg E. Experimental evaluation of the impact of the interactions of CO_2-SO_2, brine, and reservoir rock on petrophysical properties: A case study from the Ketzin test site, Germany. Geochemistry, Geophys Geosystems. Wiley Online Library; 2011;12(5).

Kutchko BG, Strazisar BR, Lowry G V, Dzombak DA, Thaulow N. Rate of CO_2 Attack on Hydrated Class H Well Cement under Geologic Sequestration Conditions. Environ Sci Technol. 2008;42(16):6237–42.

Lau JSO, Chandler NA. Innovative laboratory testing. Int J Rock Mech Min Sci. 2004 Dec;41(8):1427–45.

Lei X, Xue Z. Ultrasonic velocity and attenuation during CO_2 injection into water-saturated porous sandstone: Measurements using difference seismic tomography. Phys Earth Planet Inter. 2009;176(3-4):224–34.

Liu F, Lu P, Griffith C, Hedges SW, Soong Y, Hellevang H, et al. CO_2--brine--caprock interaction: reactivity experiments on Eau Claire shale and a review of relevant literature. Int J Greenh Gas Control. Elsevier; 2012;7:153–67.

Louis L, Robion P, David C. A single method for the inversion of anisotropic data sets with application to structural studies. J Struct Geol. 2004;26(11):2065–72.

Lu P, Fu Q, Seyfried Jr W, Hereford A, Zhu C. Navajo Sandstone–brine–CO_2 interaction: implications for geological carbon sequestration. Environ Earth Sci. Springer-Verlag; 2011;62(1):101–18.

Luquot L, Andreani M, Gouze P, Camps P. CO_2 percolation experiment through chlorite/zeolite-rich sandstone (Pretty Hill Formation –

Otway Basin–Australia). Chem Geol. 2012;294–295:75–88.

Luquot L, Gouze P. Experimental determination of porosity and permeability changes induced by injection of CO_2 into carbonate rocks. Chem Geol. Elsevier; 2009;265(1):148–59.

Martin CD, Chandler NA. The progressive fracture of Lac du Bonnet granite. Int J Rock Mech Min Sci Geomech Abstr. 1994 Dec;31(6):643–59.

Martínez JM, Schmitt DR. Anisotropic elastic moduli of carbonates and evaporites from the Weyburn-Midale reservoir and seal rocks. Geophys Prospect. Blackwell Publishing Ltd; 2013;61(2):363–79.

Mavko G, Mukerji T. Bounds on low-frequency seismic velocities in partially saturated rocks. Geophysics. 1998;63(3):918–24.

McBride MB. Environmental chemistry of soils. Oxford university press; 1994.

McCann C, Sothcott J. Laboratory measurements of the seismic properties of sedimentary rocks. Geol Soc London, Spec Publ. 1992 Jan 1;65(1):285–97.

Mikhaltsevitch V, Lebedev M, Gurevich B. A Laboratory Study of the Elastic and Anelastic Properties of the Sandstone Flooded with Supercritical CO_2 at Seismic Frequencies. Energy Procedia. 2014;63:4289–96.

Milsch H, Blöcher G, Engelmann S. The relationship between hydraulic and electrical transport properties in sandstones: An experimental evaluation of several scaling models. Earth Planet Sci Lett. Elsevier; 2008;275(3):355–63.

Morse JW, Mackenzie FT. Geochemistry of sedimentary carbonates. Elsevier; 1990.

Nakagawa S, Kneafsey TJ, Daley TM, Freifeld BM, Rees E V. Laboratory seismic monitoring of supercritical CO_2 flooding in sandstone cores using the Split Hopkinson Resonant Bar technique with concurrent x-ray Computed Tomography imaging. Geophys Prospect.

Blackwell Publishing Ltd; 2013;61(2):254–69.

Nakatsuka Y, Xue Z, Garcia H, Matsuoka T. Experimental study on CO_2 monitoring and quantification of stored CO_2 in saline formations using resistivity measurements. Int J Greenh Gas Control. 2010 Mar;4(2):209–16.

Newell DL, Carey JW. Experimental evaluation of wellbore integrity along the cement-rock boundary. Environ Sci Technol. ACS Publications; 2012;47(1):276–82.

Nguyen VH, Gland N, Dautriat J, David C, Wassermann J, Guélard J. Compaction, permeability evolution and stress path effects in unconsolidated sand and weakly consolidated sandstone. Int J Rock Mech Min Sci. 2014 Apr;67:226–39.

Nicksiar M, Martin CD. Evaluation of Methods for Determining Crack Initiation in Compression Tests on Low-Porosity Rocks. Rock Mech Rock Eng. Springer Vienna; 2012;45(4):607–17.

Njiekak G, Schmitt DR, Yam H, Kofman RS. CO_2 rock physics as part of the Weyburn-Midale geological storage project. Int J Greenh Gas Control. 2013;16:S118–33.

Noiriel C, Bernard D, Gouze P, Thibault X. Hydraulic properties and microgeometry evolution accompanying limestone dissolution by acidic water. Oil gas Sci Technol. IFP; 2005;60(1):177–92.

Noiriel C, Gouze P, Madé B. Time-resolved 3D characterisation of flow and dissolution patterns in a single rough-walled fracture. In: Jir'i Krásný (Editor) JMS (Editor), editor. Groundw Fract rocks [Internet]. Taylor & Francis; 2007. p. 629–42.

Noiriel C, Luquot L, Madé B, Raimbault L, Gouze P, Van Der Lee J. Changes in reactive surface area during limestone dissolution: An experimental and modelling study. Chem Geol. Elsevier; 2009;265(1):160–70.

North L, Best AI, Sothcott J, MacGregor L. Laboratory determination of the full electrical resistivity tensor of heterogeneous carbonate rocks at elevated pressures. Geophys Prospect. Blackwell

Publishing Ltd; 2013;61(2):458–70.

North LJ, Best AI. Anomalous electrical resistivity anisotropy in clean reservoir sandstones. Geophys Prospect. 2014a Nov 20;62(6):1315–26.

North LJ, Best AI. Anomalous electrical resistivity anisotropy in clean reservoir sandstones. Geophys Prospect. 2014b;62(6):1315–26.

Ogaya X, Queralt P, Ledo J, Marcuello Á, Jones AG. Geoelectrical baseline model of the subsurface of the Hontomín site (Spain) for CO_2 geological storage in a deep saline aquifer: A 3D magnetotelluric characterisation. Int J Greenh Gas Control. 2014;27:120–38.

Oh J, Kim KY, Han WS, Kim T, Kim JC, Park E. Experimental and numerical study on supercritical CO_2/brine transport in a fractured rock: Implications of mass transfer, capillary pressure and storage capacity. Adv Water Resour. Elsevier Ltd; 2013;62:442–53.

Ojala IO, Ngwenya BT, Main IG, Ojala IO, Ngwenya BT, Main IG. Loading rate dependence of permeability evolution in porous aeolian sandstones. J Geophys Res. 2004 Jan 1;109(B1):1–14.

Ougier-Simonin A, Fortin J, Guéguen Y, Schubnel A, Bouyer F. Cracks in glass under triaxial conditions. Int J Eng Sci. Elsevier; 2011;49(1):105–21.

Palandri JL, Kharaka YK. A compilation of rate parameters of water-mineral interaction kinetics for application to geochemical modeling. DTIC Document; 2004.

Parkhurst BDL, Appelo CAJ. User's Guide To PHREEQC (version 2) — a Computer Program for Speciation, and Inverse Geochemical Calculations. Exch Organ Behav Teach J. 1999 ;D(Version 2):326.

Permanyer A, Márquez G, Gallego JR. Compositional variability in oils and formation waters from the Ayoluengo and Hontomín fields (Burgos, Spain). Implications for assessing biodegradation and reservoir compartmentalization. Org Geochem. Elsevier;

2013;54:125–39.

Perrin J-C, Benson S. An experimental study on the influence of sub-core scale heterogeneities on CO_2 distribution in reservoir rocks. Transp porous media. Springer; 2010;82(1):93–109.

Peysson Y, Bazin B, Magnier C, Kohler E, Youssef S. Permeability alteration due to salt precipitation driven by drying in the context of CO_2 injection. Energy Procedia. Elsevier; 2011;4:4387–94.

Pini R, Krevor SCM, Benson SM. Capillary pressure and heterogeneity for the CO_2/water system in sandstone rocks at reservoir conditions. Adv Water Resour. 2012;38:48–59.

Plummer LN, Wigley TML, Parkhurst DL. The kinetics of calcite dissolution in CO_2-water systems at 5 degrees to 60 degrees C and 0.0 to 1.0 atm CO_2. Am J Sci. American Journal of Science; 1978; 278(2):179–216.

Pruess K, Garcia J. Multiphase flow dynamics during CO_2 disposal into saline aquifers. Environ Geol. Springer; 2002;42(2-3):282–95.

Ptak T, Piepenbrink M, Martac E. Tracer tests for the investigation of heterogeneous porous media and stochastic modelling of flow and transport - A review of some recent developments. J Hydrol. 2004;294(1-3):122–63.

Quesada S, Dorronsoro C, Robles S. Genetic relationship between the oil of the Ayoluengo field and the Liassic source-rock of the Southwestern Basque-Cantabrian Basin (Northern Spain). Org Geochemistry Dev Appl to Energy, Clim Environ Hum Hist. AIGOA, Donostia-San Sebastian; 1995;461–3.

Quesada S, Dorronsoro C, Robles S, Chaler R, Grimalt JO. Geochemical correlation of oil from the Ayoluengo field to Liassic black shale units in the southwestern Basque-Cantabrian Basin (northern Spain). Org Geochem. Elsevier; 1997;27(1):25–40.

Quesada S, Robles S. Organic geochemistry, distribution and depositional dynamics of the Liassic organic facies of the Basque-Cantabrian Basin (Northern Spain). Org Geochemistry Dev Appl to

Energy, Clim Environ Hum Hist. AIGOA, Donostia-San Sebastian; 1995;464–5.

Quesada S, Robles S, Pujalte V. El Jurásico Marino del margen suroccidental de la Cuenca Vasco-Cantábrica y su relación con la exploración de hidrocarburos. Geogaceta. 1993;13(1993):92–6.

Rae PJ, Brown EN, Orler EB. The mechanical properties of poly(ether-ether-ketone) (PEEK) with emphasis on the large compressive strain response. Polymer (Guildf). 2007 Jan;48(2):598–615.

Rouquerol J, Avnir D, Fairbridge CW, Everett DH, Haynes JM, Pernicone N, et al. Recommendations for the characterization of porous solids (Technical Report). Pure Appl Chem. 1994;66(8):1739–58.

Rummel F, Alheid HJ, Frohn C. Dilatancy and fracture induced velocity changes in rock and their relation to frictional sliding. pure Appl Geophys. Birkhauser-Verlag; 1978; 116(4-5):743–64.

Rutqvist J. The Geomechanics of CO_2 Storage in Deep Sedimentary Formations. Geotech Geol Eng. Springer Netherlands; 2012;30(3):525–51.

Santamarina JC, Fratta D. Frequency Domain Analysis of Signals (Discrete Fourier Transform). Discret Signals Inverse Probl. John Wiley & Sons, Ltd; 2006a. p. 103–36.

Santamarina JC, Fratta D. Frequency Domain Analysis of Systems. Discret Signals Inverse Probl. John Wiley & Sons, Ltd; 2006b. p. 137–74.

Schubnel A, Benson P, Thompson B, Hazzard J, Young RP. Quantifying Damage, Saturation and Anisotropy in Cracked Rocks by Inverting Elastic Wave Velocities. In: Dresen G, Zang A, Stephansson O, editors. Rock Damage Fluid Transp Part I SE - 3. Birkhäuser Basel; 2006. p. 947–73.

Shackelford BCD, Malusis MA, Majeski MJ, Stern RT, Member A. E c b c. 1999;(April):260–70.

Shiraki R, Dunn TL. Experimental study on water–rock interactions

during CO_2 flooding in the Tensleep Formation, Wyoming, USA. Appl Geochemistry. Elsevier; 2000;15(3):265–79.

Song I, Renner J. Hydromechanical properties of Fontainebleau sandstone: Experimental determination and micromechanical modeling. J Geophys Res. 2008 Sep 26;113(B9):B09211.

Song J, Zhang D. Comprehensive Review of Caprock-Sealing Mechanisms for Geologic Carbon Sequestration. Environ Sci Technol. American Chemical Society; 2013 Jan 2;47(1):9–22.

Sposito G. The surface chemistry of soils. Oxford University Press; 1984.

Stanchits S, Vinciguerra S, Dresen G. Ultrasonic velocities, acoustic emission characteristics and crack damage of basalt and granite. Pure Appl Geophys. Springer; 2006; 163(5-6):975–94.

Thomsen L. Weak elastic anisotropy. Geophysics. 1986;51(10):1954.

Wang Z. Seismic anisotropy in sedimentary rocks, part 1: A single-plug laboratory method. Geophysics. 2002 Sep 1;67(5):1415–22.

Wigand M, Carey JW, Schütt H, Spangenberg E, Erzinger J. Geochemical effects of CO_2 sequestration in sandstones under simulated in situ conditions of deep saline aquifers. Appl Geochemistry. Elsevier; 2008;23(9):2735–45.

Xie SY, Shao JF, Xu WY. Influences of chemical degradation on mechanical behaviour of a limestone. Int J Rock Mech Min Sci. Elsevier; 2011;48(5):741–7.

Xu X, Hofmann R, Batzle M, Tshering T. Influence of pore pressure on velocity in low-porosity sandstone: Implications for time-lapse feasibility and pore-pressure study. Geophys Prospect. Blackwell Publishing Ltd; 2006;54(5):565–73.

Xue Z, Lei X. Laboratory study of CO_2 migration in water-saturated anisotropic sandstone, based on P-wave velocity imaging. Explor Geophys. 2006 Jan 1;37(1):10–8.

Xue Z, Ohsumi T. Seismic wave monitoring of CO_2 migration in water-

saturated porous sandstone. Explor Geophys. Australian Society of Exploration Geophysicists; 2004 Mar 1;35(1):25–32.

Zemke K, Liebscher A, Wandrey M. Petrophysical analysis to investigate the effects of carbon dioxide storage in a subsurface saline aquifer at Ketzin, Germany (CO_2SINK). Int J Greenh Gas Control. 2010 Dec; 4(6):990–9.

Zhan X, Schwartz L, Toksöz M, Smith W, Morgan F. Pore-scale modeling of electrical and fluid transport in Berea sandstone. Geophysics. Society of Exploration Geophysicists; 2010 Sep 1;75(5):F135–42.

Zhu Y, Tsvankin I. Plane-wave propagation in attenuative transversely isotropic media. Geophysics. 2006;71(2):T17.

Zhu Y, Tsvankin I, Dewangan P, Wijk K. Physical modeling and analysis of P-wave attenuation anisotropy in transversely isotropic media. Geophysics. Society of Exploration Geophysicists; 2007 Nov 15;72(1):D1–7.

ANNEX 1. RESÚMENES EXTENDIDOS

Introducción

A lo largo de las pasadas décadas, la complejidad en la dinámica del cambio climático y su evolución ha influido profundamente en el desarrollo de nuevos campos de conocimiento, así como en el desarrollo de nuevos enfoques tecnológicos y metodológicos. La contribución de los gases de efecto invernadero al calentamiento global constituye una preocupación creciente. El dióxido de carbono es uno de los más significativos (aunque no el único) contribuyentes gases de efecto invernadero y, de acuerdo con la percepción actual, la principal causa del calentamiento global. A pesar de que la naturaleza, alcance y sentido de estos cambios son aún inciertos, a lo largo de las próximas décadas se espera un aumento de la temperatura media global de la Tierra en superficie.

Los expertos coinciden en que es necesario actuar pronto con el fin de reducir las emisiones de CO_2 a la atmósfera. Para ello se considera una amplia batería de técnicas de entre las cuales, las principales son:

- La reducción del consumo de servicios energéticos
- El aumentar de la eficiencia de conversión de energía o en su uso
- La migración hacia combustibles de bajo contenido de carbono, por ejemplo, el gas natural en lugar de carbón
- La mejora y expansión de los sumideros naturales de CO_2, por ejemplo, los bosques, los suelos, etc.

- El uso de fuentes de energía con emisiones de CO_2 muy bajas, como las energías renovables o la energía nuclear
- La captura y almacenamiento de las emisiones de gases de efecto invernadero producto de la combustión de combustibles fósiles y otras actividades industriales.

La captura y almacenamiento de carbono (CCS en inglés) es una de las tecnologías más prometedoras actualmente en desarrollo. Es una de las medidas correctivas que se menciona explícitamente en el protocolo de Kyoto. El objetivo del CCS es separar el CO_2 producido en diferentes procesos para obtener una corriente de gas con una concentración suficientemente alta de CO_2 para comprimirlo y transportarlo (a través de conductos) hasta el punto donde quede almacenado de forma permanente... o al menos, almacenado durante un tiempo suficientemente largo para asegurar un impacto positivo sobre las tasas de emisión (decenas de miles de años). El CCS puede definirse como un conjunto de tecnologías que integra tres etapas: 1) la captura de CO_2; 2) el transporte de CO_2 y 3) el almacenamiento geológico. La captura de CO_2 y almacenamiento subterráneo puede realizarse con la tecnología actualmente disponible, aunque sólo recientemente han sido consideradas de forma seria como métodos potenciales para la reducción de emisiones. Su importancia radica en el hecho de que, en la actualidad, aproximadamente el 85% de las necesidades energéticas comerciales del mundo son suministrados por

los combustibles fósiles. Un cambio rápido de las fuentes de energía no fósiles, incluso si ello fuera posible, daría lugar a grandes trastornos en la infraestructura de suministro de energía, con importantes repercusiones sobre la economía mundial. La tecnología de captura y almacenamiento de CO_2 permitiría al mundo seguir utilizando combustibles fósiles aunque reduciendo de forma muy significativa las emisiones de CO_2 hacia la atmósfera. En vista de las muchas incertidumbres sobre el curso del cambio climático, parece más que recomendable un mayor desarrollo del conocimiento de la captura de CO_2 y de las tecnologías asociadas a su almacenamiento geológico.

Esta tesis se desarrolla en el contexto de un contrato de I+D suscrito entre la Fundación Ciudad de la Energía (CIUDEN) y la Universidade da Coruña (Laboratorio de Mecánica de Rocas) al amparo del Proyecto OXYCFB 300 (Compostilla) del Programa Europeo para la Recuperación Económica.

Organización de la Tesis

Esta tesis se estructura en 8 capítulos correspondiendo la introducción al **Capítulo 1**.

El **Capítulo 2** está dedicado a hacer un breve resumen sobre el estado del arte en algunos campos pertinentes relacionados con el trabajo desarrollado en esta tesis.

Es conveniente señalar que, al inicio de los trabajos que han conducido a la redacción de este documento, se consideró necesario el diseñar y construir una nueva plataforma experimental. El equipo experimental fue siendo mejorado progresivamente durante el tiempo de su realización de modo que, en la actualidad, su capacidad para acometer ensayos progresivamente más complejos ha aumentado significativamente. De acuerdo con ello, el **Capítulo 3** está dedicado a la descripción de las características del equipo experimental y su funcionalidad. En el mismo se expone también una serie de cuestiones relativas a la preparación de las muestras para su ensayo.

El primer experimento exitoso realizado con la plataforma experimental se describe y analiza en el **Capítulo 4**. Este experimento, que se desarrolló a temperatura ambiente, se realizó con una arenisca en el que se inyecta una salmuera saturada con CO_2 bajo condiciones subcríticas (CO_2). En el mismo se realizó un seguimiento de las velocidades de propagación de la onda P y S, la deformación axial, así como el análisis químico del agua intersticial. Asimismo, se analizaron los resultados mediante su modelización del transporte reactivo.

El **Capítulo 5** presenta un nuevo experimento tipo "core flooding" a través de una muestra de carniola en el que se inyecta secuencialmente una sucesión de líquidos (N_2, agua desionizada, salmuera, y salmuera saturada en CO_2). Este experimento se realizó también bajo

condiciones subcríticas empleando la plataforma experimental descrita en el **Capítulo 3**.

De acuerdo con los resultados obtenidos en los ensayos anteriores (que condujeron a la necesidad de realizar una caracterización de profundidad de los materiales experimentales), el **Capítulo 6** presenta los resultados de una gran variedad de ensayos mecánicos y otros de caracterización y análisis los cuales fueron realizados para conocer en profundidad un material experimental de referencia (Arenisca de Corvio) a partir de la cual se realizaron nuevos ensayos de inyección.. De ese modo, el **Capítulo 7** presenta los resultados de un nuevo experimento tipo "core flooding" empleando la citada arenisca, la cual, debido a su composición mineralógica (cuarzo), debía dar lugar a una limitada reactividad química. En este caso, las etapas de inyección fueron de agua desionizada y agua desionizada saturada con CO_2. La inyección se realizó bajo condiciones supercríticas para el CO_2 al tiempo que se impuso un caudal de inyección constante a lo largo de todo el experimento. Esta condición experimental fue diferente a las anteriores (es decir, los experimentos descritos en los capítulos 4 y 5 se realizaron bajo condiciones de presión de inyección constante)..

Por último, las conclusiones más importantes y propuestas futuras líneas de investigación se resumen en el **Capítulo 8**

Preparación de muestras y desarrollo experimental

El estudio del comportamiento geomecánico de las rocas conlleva una minuciosa preparación de los materiales a ensayar (dimensiones) así como un amplio conocimiento del contexto geológico y otras propiedades relevantes. Por ello, los distintos materiales de ensayo fueron caracterizados desde diversos puntos de vista los cuales incluyen aspectos mineralógicos, químicos, texturales y petrofísicos.

Para la realización de los ensayos de flujo a través (o "core flooding") se ha empleado una celda triaxial en la que se somete a una muestra cilíndrica de roca a una presión de confinamiento radial y vertical a través de unos pistones que apoyan en las superficies superior e inferior de la muestra. Estas tensiones se corresponden con los esfuerzos principal mayor y menor, respectivamente, siendo el intermedio, σ_2, igual en magnitud a σ_3 debido a la simetría radial de la muestra y la manera homogénea de aplicación de la carga (empleando un fluido). En un ensayo triaxial típico, se obtiene información de las deformaciones producidas en función de la carga aplicada y la presión de confinamiento. No obstante, otras variables, como la temperatura o la existencia de una presión intersticial diferente a la de confinamiento juegan un papel importante a la hora de ilustrar el comportamiento mecánico del material. Durante la realización de un ensayo convencional, tienen lugar distintos fenómenos los cuales son susceptibles de estudiar mediante distintas técnicas de caracterización.

Entre las más interesantes se encuentra el estudio de la velocidad de propagación de ondas sísmicas.

Con el fin de poder realizar un amplio rango de ensayos y poder realizar experimentos de larga duración, se desarrolló un dispositivo experimental modular y escalable, donde se han acoplado equipos de diversa índole con el objetivo de poder realizar ensayos acoplados (hidrogeoquímicos). La adquisición de datos y calibración de los equipos también ha sido objeto de este trabajo. A continuación se menciona las partes más significativas de las que consta dicho sistema (Figura R- 1):

- Bastidor de carga
- Celda portamuestras
- Equipo de adquisición de señal de desplazamientos
- Platos de carga axial con presión de poro y ondas ultrasónicas (P, S_1 y S_2)
- Sistema de presión axial y confinamiento
- Sistema de presión de poro
- Medidor de flujo másico de gas
- Reguladores de presión
- Microelectrodos de pH y conductividad
- Cromatógrafo iónico

Los ensayos realizados en este dispositivo han sido de muy diversa índole:

- Ensayos de permeabilidad bajo condiciones triaxiales.
- Inyección de CO_2 líquido y CO_2 supercrítico.
- Inyección de agua saturada en CO_2.
- Inyección de salmuera saturada en CO_2.

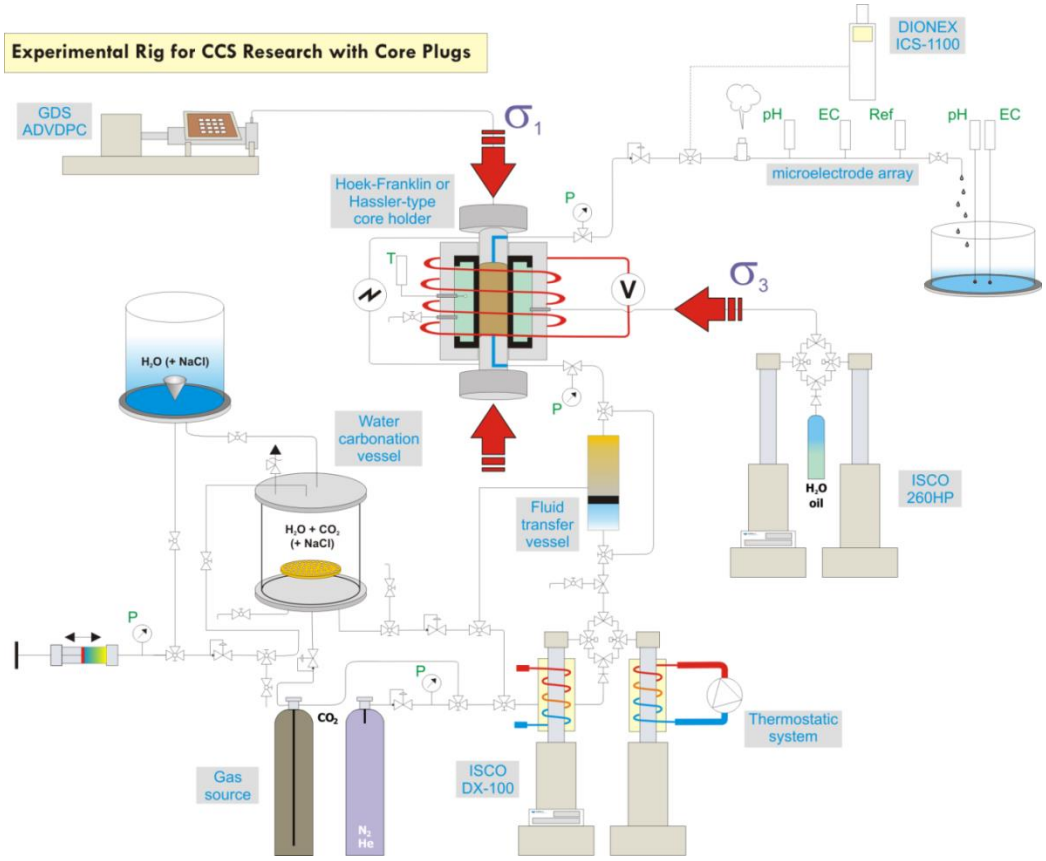

Figura R- 1. Diseño experimental realizado en la UDC para la realización de ensayos

Todos estos ensayos de permeabilidad tiene como objetivo conocer el comportamiento de la formación a estudiar bajo varios supuesto de fluido permeante y de este modo caracterizar su comportamiento, aunque desde el punto de vista del almacenamiento

de CO_2 los ensayos más completos son aquellos en los que el fluido residente y la roca reaccionan con el CO_2 que se intenta almacenar. Es el caso de los ensayos descritos en los capítulos 4, 5 y 7. En estos casos, además del control de las medidas de permeabilidad y presión, se ha realizado un seguimiento de la evolución del pH y conductividad a lo largo del ensayo así como la determinación de las velocidades de ondas ultrasónicas cada día. A partir de esta última información ha podido deducirse la evolución de los parámetros elásticos dinámicos del material analizado.

Dentro de los ensayos de laboratorio y con el objeto de abarcar distintas litologías y condiciones, se realizaron ensayos en areniscas y carniolas a distintas condiciones de presión, temperatura, fluidos con la intención de abarcar un rango amplio de condiciones y fenómenos que pueden suceder en un potencial almacén geológico de CO_2.

Ensayo de inyección en la arenisca de la formación Arcera

Este capítulo describe el experimento correspondiente con el ensayo realizado en una probeta de arenisca de la Formación Arcera (Purbeck Inferior), correspondiente a niveles superiores a la formación objetivo de la Planta de Desarrollo Tecnológico de Hontomín.

Las condiciones de ensayo prescritas fueron constantes durante la duración del ensayo: 10 MPa de presión de confinamiento; 15 MPa de presión axial; 4 MPa de presión de poro y temperatura ambiente.

Respecto del campo de estabilidad del CO_2, estas condiciones son subcríticas, presumiéndose un flujo de tipo monofásico (H_2O+CO_2 disuelto).

La muestra ensayada corresponde a una cuarzoarenita. Su densidad seca, antes del ensayo era de 2.428 g/cm^3. Suponiendo una densidad media de los sólidos que componen la roca de ~2.6 g/cm^3, el volumen de huecos de la probeta sería del orden de 6.3 cm^3 por lo que su porosidad inicial sería de, aproximadamente, 7.3 %.

El fluido circulado a través de la probeta (agua desionizada) fue analizado con carácter previo a su carbonatación. Su saturación con CO_2 se produjo a una a presión de 4 MPa (igual a la presión de poro objetivo) y temperatura ambiente (~22 °C). Bajo esas condiciones, el contenido teórico de CO_2 en el fluido es del 2 % (molar).

El experimento se desarrolló en dos etapas, con una duración conjunta de más de dos meses. En la primera etapa se inyectó sólo agua desionizada (~7 días) mientras que en la segunda se inyectó la solución saturada en CO_2. A lo largo de ese tiempo se midió cuidadosamente el volumen de fluido circulado, su composición química (analizada mediante cromatografía iónica e ICP-MS) así como las velocidades de propagación de ondas. Dichos datos permitieron evaluar el valor de la permeabilidad de la roca y cómo ésta cambia en función de la inyección, así como los procesos reactivos que en el seno de la misma tuvieron lugar. La medida de velocidades de ondas

permitió, asimismo, tener una primera aproximación al conocimiento de procesos de carácter químico-mecánico.

En la Figura R- 2 se ha indicado el momento que separa la inyección del agua desionizada respecto del de la inyección del agua carbonatada. Es interesante observar que, en la primera etapa, la permeabilidad aumenta ligeramente, para disminuir y estabilizarse cuando se inicia la inyección del fluido carbonatado. Transcurridas unas 2.5 semanas desde el inicio de la segunda etapa, tuvo lugar un notable incremento del valor de la permeabilidad, el cual se estabilizó al cabo de otra semana. Tras ~1.5 semanas adicionales, se produjo un nuevo aumento del valor de la permeabilidad. Conjeturamos que ese comportamiento obedece al acoplamiento entre distintos procesos siendo el más destacable el desarrollo de reacciones químicas que propician la disolución de elementos de la probeta.

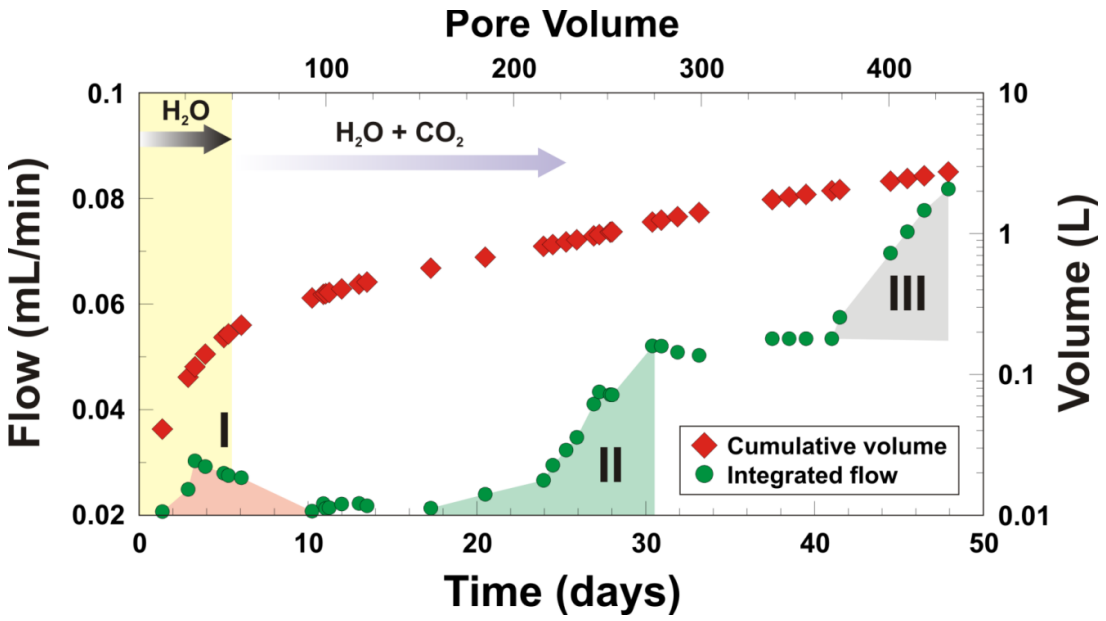

Figura R- 2 . Evolución de la permeabilidad (y el caudal drenado) de la muestra en función del tiempo.

De forma simultánea al incremento de la concentración de Ca y Mg (Figura R- 3), se produce un ligero aumento en la permeabilidad de la probeta, lo cual sugiere que el aumento de la porosidad y de la permeabilidad están relacionados.

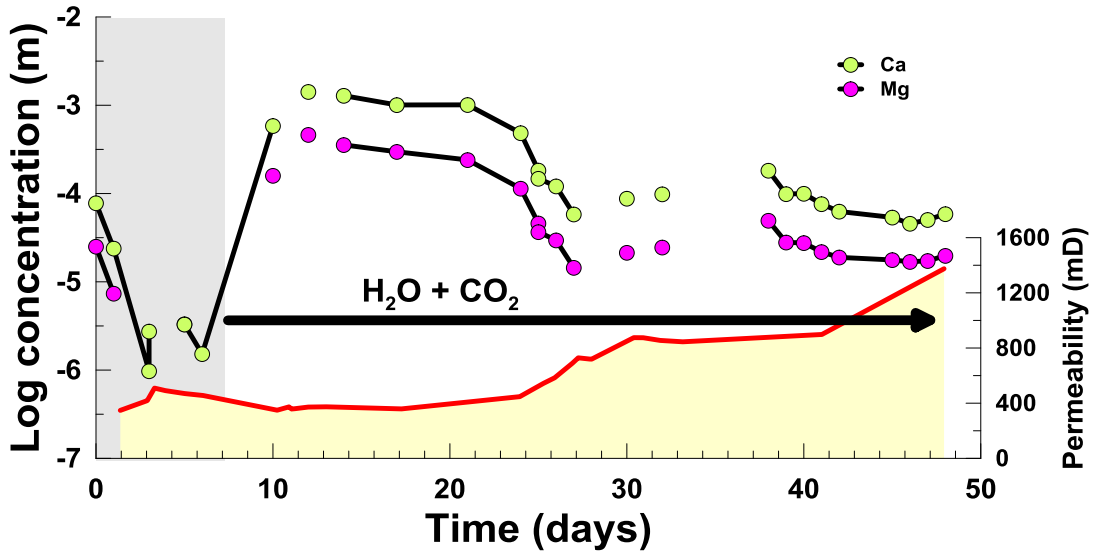

Figura R- 3. Evolución de la permeabilidad y del Ca y Mg, ambos cationes muestran un patrón evolutivo simétrico.

De modo general, es posible identificar el momento a partir del cual se produce la llegada del fluido saturado en CO_2 dado que se produce una marcada disminución en el pH y un aumento en la conductividad; dichos parámetros fueron analizados en continuo a la salida de la línea de presión intersticial. Por otro lado, V_P aumenta notoriamente (coincidiendo con la etapa de inyección de agua carbonatada) mientras que lo contrario sucede con V_{S1} y V_{S2}. Es interesante también el observar que la magnitud de V_P no se mantiene constante a lo largo de la etapa de inyección de agua saturada en CO_2, experimentando descensos y ascensos.

Si observamos de forma detallada la evolución de las concentraciones de sílice y potasio podremos verificar una pauta de evolución geoquímica compleja. En la primera fase del ensayo, cuando

sólo circuló agua destilada, la concentración de ambos componentes tiende a disminuir de forma acusada, aunque, en el caso del K, se inicia una recuperación al cabo de tres a cuatro días desde el inicio del ensayo. La llegada de la solución carbonatada en la etapa 2 marca un comportamiento variado en el que, en una primera fase, las concentraciones de ambos componentes se mantiene estable (~5-6 mg/L). Esa etapa coincide, aproximadamente, con un muy leve aumento de la permeabilidad de la probeta, la cual asociamos con la disolución de carbonatos (probablemente calcita magnesiana). En el momento en el que parecen haberse agotado los carbonatos, tiene lugar un abrupto descenso en la concentración acoplada de SiO_2 y K, apuntando los datos disponibles hacia un incremento posterior, relacionado con el aumento de permeabilidad.

Ensayo de inyección en Carniolas

Este capítulo se centra en un ensayo reactivo de carniola, el reservorio objetivo del programa de almacenamiento de la Fundación Ciuden. La muestra en la que se realizó en el ensayo presentaba una porosidad del 9.6% y una densidad aparente de 2.45gr/cm^3. Se trata de una muestra con un contenido en calcita de aproximadamente 86%.

Las etapas de inyección han sido 1) agua desionizada 2) salmuera sintética de formación y 3) salmuera sintética de formación saturada en CO_2.

Al igual que en el ensayo del capítulo 4 es un experimento de inyección continua (25 días) en el que los fluidos utilizados fueros agua desionizada, salmuera de formación y dicha salmuera saturada con CO_2. La temperatura de ensayo fue de 40 °C, la presión axial de 30 MPa, una presión de confinamiento de 10 MPa y una presión de poro de 4 MPa, lo que nos lleva a realizar el ensayo en unas condiciones subcríticas desde el punto de vista del CO_2.

La etapa de inyección de salmuera saturada en CO_2 da lugar a cambios notables en la evolución de la muestra:

-La velocidad de la deformación es prácticamente constante hasta la aparición de la etapa de CO_2 (Figura R- 4), en esta última se observa una fase reactiva elevada en comparación con las anteriores y se observan los mayores cambios desde el punto de vista químico, hidrodinámico y mecánico.

-La conductividad hidráulica aumenta abruptamente en esta etapa mientras que a lo largo de los primeros 20 días permanece constante.

-Al analizar en dominio de frecuencias las ondas P, S_1 y S_2 también se observan ciertas variaciones a lo largo del ensayo. En el caso de la onda P se observa perfectamente el efecto de la sustitución de fluidos mientras que en el caso de la onda S_1 y S_2 se observan fenómenos que se achacan a procesos de disolución.

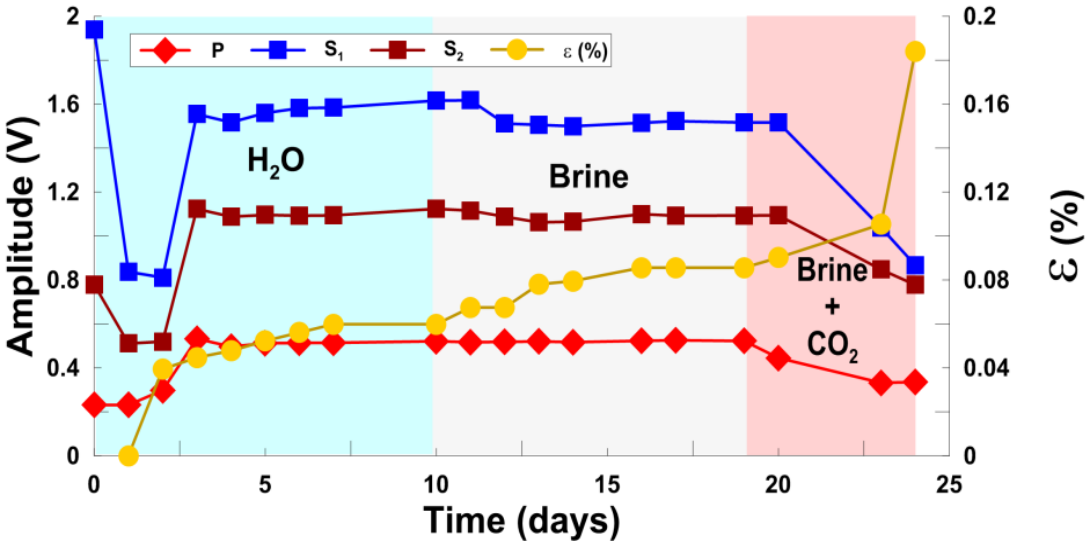

Figura R- 4. Evolución de la deformación axial junto con la amplitud de las ondas P, S_1 y S_2.

Caracterización geomecánica y anisotrópica de arenica de Corvio

Los experimentos realizados ponen en evidencia las complejas interacciones que tienen lugar cuando un fluido carbonatado ácido interactúa con una roca y como, a raíz de ello, se desarrollan importantes acoplamientos hidrodinámicos, mecánicos y químicos. Con objeto de realizar ensayos sobre una roca donde la parte reactiva sea menor y en busca de caracterizar su parte mecánica en profundidad, nace el capítulo 6. Dicho capítulo se centra en una arenisca comercial de la Formación Corvio. En él se presenta una caracterización completa de la física, mineralogía, propiedades geomecánicas, geofísicas e hidrodinámicas de la Arenisca de Corvio. Esta información, junto con una evaluación detallada de su

anisotropía, es necesaria para establecer este material como un estándar de referencia para ensayos de laboratorio enfocados hacia los fenómenos termo-hidro-mecánico-geoquímicos acoplados de interés para el almacenamiento geológico de CO_2 y otros estudios geológicos en general. Más de 200 muestras de arenisca de Corvio (diámetro 38.1 y 50 mm, 2:1 de longitud a diámetro) se utilizaron en este estudio de caracterización, con una roca porosidad de 21,7 ± 1,2%, densidad en seco 2036 ± 32 kg m^{-3}, y resistencia a compresión simple y resistencia a la tracción de 41 ± 3,28 y 2,3 ± 0,14 MPa, respectivamente. Los ensayos geomecánicos muestran que la roca se comporta elásticamente entre ~10 y ~18 MPa bajo condiciones de confinamiento (Figura R- 5) con un módulo de Young y coeficiente de Poisson asociados de 11,8 ± 2,8 GPa y 0,34 ± 0,01, respectivamente. La permeabilidad disminuye abruptamente con presión de confinamiento hasta ~ 10 MPa y luego se estabiliza en ~ 1 MD. Velocidades Ultrasónica P y S varían desde alrededor de 2.8 hasta 3.8 km s^{-1} y de 1,5 a 2,4 km s^{-1}, respectivamente, a lo largo de confinamiento y presiones diferenciales entre 0,1-35 MPa, permitiendo derivar de estos los parámetros elásticos dinámicos asociados. La anisotropía se investigó usando testigos orientados en diversas direcciones para la resistividad eléctrica, velocidad de la onda elástica y la atenuación, la permeabilidad y ensayos de inyección de trazadores. La Arenisca de Corvio muestra débil anisotropía transversal (simetría eje normal a la estratificación) de <10% de la velocidad y <20% de la atenuación.

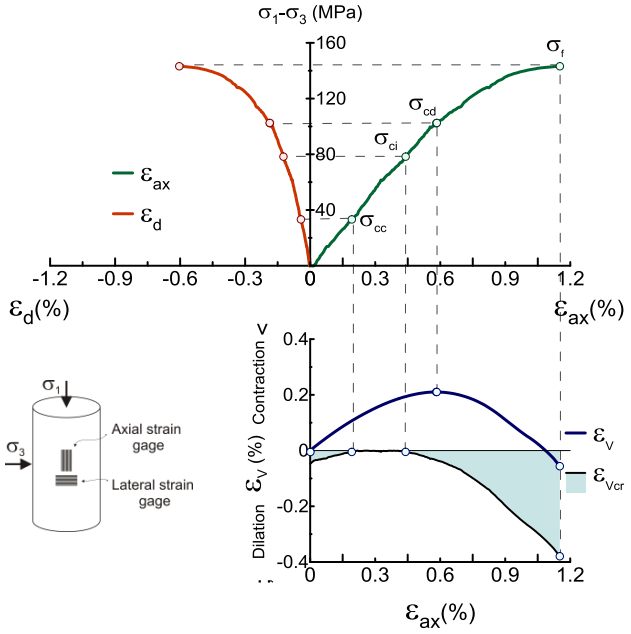

Figura R- 5. Ensayo triaxial de la Arenisca de Corvio (σ_3=38 MPa) usando galgas extensométricas para la medida de deformación. σ_{cc}, cierre de fisuras; σ_{ci}, inicio de fisuración; σ_d, daño en las fisuras; σ_f, colapso.

Ensayo de inyección en la Arenisca de Corvio

En el capítulo 7 se presenta un ensayo de inyección continúa (35 días) y multietapa de esta arenisca se realiza a una temperatura de 40 °C, a una presión de confinamiento de 10 MPa, una presión axial de 15 MPa y una presión de poro de 8 MPa. Este ensayo se realiza en caudal impuesto de 0.04 mL/min y con dos etapas diferenciadas, la primera de agua desionizada y una segunda de agua desionizada saturada en CO_2. Estas condiciones garantizan un régimen supercrítico en el CO_2.

La cuarzo arenisca ensayada en este test tenía un diámetro de 37.4 mm, una longitud de 70.2 mm, porosidad 12.1% y una densidad aparente de 2.094 gcm^{-3}.

En el experimento se analizan los fenómenos acoplados y se aprecia pequeña disolución en el material cementante intergranular. Dicha disolución tiene cambios en la permeabilidad, deformación axial (Figura R- 6), cambios de amplitud en las frecuencias de las ondas P, S_1 y S_2 como consecuencia de un peor contacto entre los granos.

Como resultados reseñables se observa que el cambio de las amplitudes de las ondas P y S es un indicador de un aumento de la deformación de la muestra, produciéndose una reordenación y re-compactación de los granos. Los procesos que desencadenan los fenómenos acoplados son de origen químicos y estos, a su vez, dan lugar a cambios hidro-mecánicos. La respuesta entre ambos presenta un cierto desfase, dado que el colapso del material no se produce en el inicio del proceso de disolución.

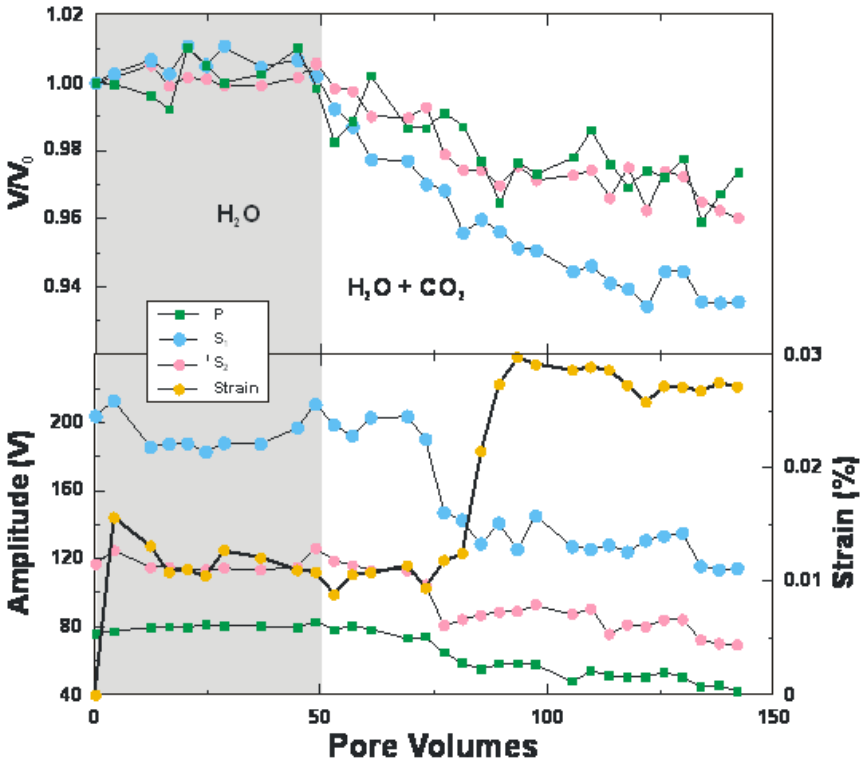

Figura R- 6. Evolución de la deformación axial junto con la amplitud de las ondas P, S_1 y S_2.

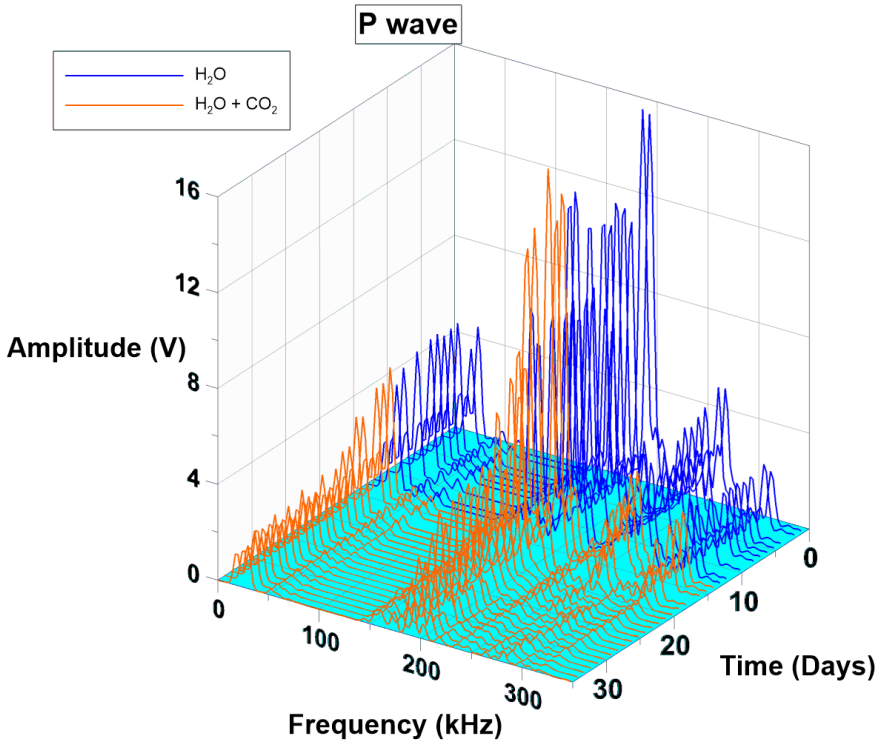

Figura R- 7. Evolución de las frecuencias de ondas P a lo largo de los 35 dias de duración del experimento de inyección con la Arenisca de Corvio.

Conclusiones

Como conclusiones generales del trabajo se establecen las siguientes:

-Hemos Diseñado, construido y probado una plataforma experimental versátil que permite desarrollar ensayos acoplados (termo-hidro-quimio-mecánicos), con especial atención al campo de la investigación de CCS.

-El Sistema experimental desarrollado es modular, escalable. El sistema ha demostrado ser a la vez simple y fiable para llevar a cabo experimentos acoplados de larga duración.

-Las condiciones impuestas de bajo flujo y un fluido saturado con CO_2 pretenden reproducir unas condiciones de ensayo representativas de las circunstancias imperantes en el almacén, a cierta distancia del punto de inyección de CO_2.

-El cociente de velocidades de onda V_p/V_s no es un buen indicador para la detección de cambios en el espacio poroso.

-El análisis en dominio de la frecuencia de la ondas V_p/V_s (amplitud) es un buen indicador para los cambios de propiedades derivadas de la interacción fluido/roca.

-Los experimentos ilustrados en los Capítulos 5 y 7 muestran un comportamiento sensiblemente diferente en el análisis de frecuencias: La atenuación en las frecuencias de la carniola ocurre para todo el

rango de frecuencias; En la Arenisca de Corvio la atenuación mayor se produce para las frecuencias correspondientes a las longitudes de onda más pequeñas. Esto parece estar relacionado con el tipo de daño interno en la muestra. En un caso este sería de tipo general (arenisca) mientras que en el otro, el daño estaría más focalizado (carniola) a tenor de los fenómenos de disolución localizada que, de forma preferente, tienen lugar en la carniola.

-En una roca con contactos entre granos de gran tamaño (carniola) se puede observar la sustitución de fluidos (onda P) al contrario que en la arenisca.

-El proceso químico es el detonante de todos los demás cambios en las propiedades de la roca y por lo tanto el que gobierna la reacción en cadena.

Introdución

Ao longo das pasadas décadas, a complexidade na dinámica do cambio climático e a súa evolución influíu profundamente no desenvolvemento de novos campos de coñecemento, así como no desenvolvemento de novos enfoques tecnolóxicos e metodolóxicos. A contribución dos gases de efecto invernadoiro ao quecemento global constitúe unha preocupación crecente. O dióxido de carbono é un dos máis significativos (aínda que non o único) contribuíntes gases de efecto invernadoiro e, de acordo coa percepción actual, a principal causa do quecemento global. Malia que a natureza, alcance e sentido destes cambios son aínda incertos, ao longo das próximas décadas espérase un aumento da temperatura media global da Terra en superficie.

Os expertos coinciden en que é necesario actuar pronto co fin de reducir as emisións de CO_2 á atmosfera. Para iso considérase unha ampla batería de técnicas de entre as cales, as principais son:

- A redución do consumo de servizos enerxéticos
- O aumentar da eficiencia de conversión de enerxía ou no seu uso
- A migración cara a combustibles de baixo contido de carbono, por exemplo, o gas natural en lugar de carbón
- Mellora e expansión dos sumidoiro naturais de CO_2, por exemplo, os bosques, os chans, etc.

- O uso de fontes de enerxía con emisións de CO_2 moi baixas, como as enerxías renovables ou a enerxía nuclear
- Captura e almacenamento das emisións de gases de efecto invernadoiro produto da combustión de combustibles fósiles e outras actividades industriais.

Captura e almacenamento de carbono (CCS en inglés) é unha das tecnoloxías máis prometedoras actualmente en desenvolvemento. É unha das medidas correctivas que se menciona explicitamente no protocolo de Kyoto. O obxectivo do CCS é separar o CO_2 producido en diferentes procesos para obter unha corrente de gas cunha concentración suficientemente alta de CO_2 para comprimilo e transportalo (a través de condutos) ata o punto onde quede almacenado de forma permanente... ou polo menos, almacenado durante un tempo suficientemente longo para asegurar un impacto positivo sobre as taxas de emisión (decenas de miles de anos). O CCS pode definirse como un conxunto de tecnoloxías que integra tres etapas: 1) captura de CO_2; 2) o transporte de CO_2 e 3) o almacenamento xeolóxico. Captura de CO_2 e almacenamento subterráneo pode realizarse coa tecnoloxía actualmente dispoñible, aínda que só recentemente foron consideradas de forma seria como métodos potenciais para a redución de emisións. A súa importancia radica no feito de que, na actualidade, aproximadamente o 85% das necesidades enerxéticas comerciais do mundo son fornecidos polos

combustibles fósiles. Un cambio rápido das fontes de enerxía non fósiles, ata si iso fose posible, daría lugar a grandes trastornos na infraestrutura de fornezo de enerxía, con importantes repercusións sobre a economía mundial. A tecnoloxía de captura e almacenamento de CO_2 permitiría ao mundo seguir utilizando combustibles fósiles aínda que reducindo de forma moi significativas as emisións de CO_2 cara á atmosfera. En vista das moitas incertezas sobre o curso do cambio climático, parece máis que recomendable un maior desenvolvemento do coñecemento de captúraa de CO_2 e das tecnoloxías asociadas á súa almacenamento xeolóxico.

Esta tese desenvólvese no contexto dun contrato de I + D subscrito entre a Fundación Cidade da Enerxía (CIUDEN) e a Universidade da Coruña (Laboratorio de Mecánica de Rocas) ao amparo do Proxecto OXYCFB 300 (Compostilla) do Programa Europeo para a Recuperación Económica.

Organización da Tese

Esta tese se estrutura en 8 capítulos correspondendo a introdución ao **Capítulo 1**.

O **Capítulo 2** está dedicado a facer un breve resumo sobre o estado da arte nalgúns campos pertinentes relacionados co traballo desenvolvido nesta tese.

É conveniente sinalar que, ao comezo dos traballos que conduciron á redacción deste documento, considerouse necesario o deseñar e construír unha nova plataforma experimental. O equipo experimental foi sendo mellorado progresivamente durante o tempo da súa realización de modo que, na actualidade, a súa capacidade para acometer ensaios progresivamente máis complexos aumentou significativamente. De acordo con iso, o **Capítulo 3** está dedicado á descrición das características do equipo experimental e o seu funcionalidade. No mesmo exponse tamén unha serie de cuestións relativas á preparación das mostras para o seu ensaio.

O primeiro experimento exitoso realizado coa plataforma experimental descríbese e analízase no **Capítulo 4**. Este experimento, que se desenvolveu a temperatura ambiente, realizouse cunha arenisca no que se inxecta unha salmuera saturada con CO_2 baixo condicións subcríticas (CO_2). No mesmo realizouse un seguimento das velocidades de propagación da onda P e S, a deformación axial, así como a análise química do auga intersticial. Así mesmo, analizáronse os resultados mediante o seu modelización do transporte reactivo.

O **Capítulo 5** presenta un novo experimento tipo "core flooding" a través dunha mostra de carniola no que se inxecta secuencialmente unha sucesión de líquidos (N_2, auga desionizada, salmuera, e salmuera saturada en CO_2). Este experimento realizouse tamén baixo condicións

subcríticas empregando a plataforma experimental descrita no **Capítulo 3**.

De acordo cos resultados obtidos nos ensaios anteriores (que conduciron á necesidade de realizar unha caracterización de profundidade dos materiais experimentais), o **Capítulo 6** presenta os resultados dunha gran variedade de ensaios mecánicos e outros de caracterización e análises os cales foron realizados para coñecer en profundidade un material experimental de referencia (Arenisca de Corvio) a partir da cal realizáronse novos ensaios de inxección. . Dese modo, o **Capítulo 7** presenta os resultado dun novo experimento tipo "core flooding" empregando a citada arenisca a cal, debido á súa composición mineralóxica (cuarzo), debía dar lugar a unha limitada reactividade química. Neste caso, as etapas de inxección foron de auga desionizada e auga desionizada saturada con CO_2. A inxección realizouse baixo condicións supercríticas para o CO_2 á vez que se impuxo un un caudal de inxección constante ao longo de todo o experimento. Esta condición experimental foi diferente ás anteriores (é dicir, os experimentos descritos nos **capítulos 4 e 5** realizáronse baixo condicións de presión de inxección constante)..

Para rematar, as conclusións máis importantes e propostas futuras liñas de investigación resúmense no **Capítulo 8**.

Preparación de mostras e desenrolo experimental

O estudo do comportamento xeomecánico das rocas conleva unha minuciosa preparación dos materiais a ensaiar (dimensións) así como un amplo coñecemento do contexto xeolóxico e outras propiedades relevantes. Por iso, os distintos materiais de ensaio foron caracterizados desde diversos puntos de vista os cales inclúen aspectos mineralóxicos, químicos, texturales e petrofísicos.

Para a realización dos ensaios de fluxo a través (ou "core flooding") empregouse unha cela triaxial na que se somete a unha mostra cilíndrica de roca a unha presión de confinamento radial e vertical a través duns pistóns que apoian nas superficies superior e inferior da mostra. Estas tensións correspóndense cos esforzos principal maior e menor, respectivamente, sendo o intermedio, σ_2, igual en magnitude a σ_3 debido á simetría radial da mostra e o xeito homoxénea de aplicación da carga (empregando un fluído). Nun ensaio triaxial típico, obtense información das deformacións producidas en función da carga aplicada e a presión de confinamento. No entanto, outras variables, como a temperatura ou a existencia dunha presión intersticial diferente á de confinamento xogan un papel importante á hora de ilustrar o comportamento mecánico do material. Durante a realización dun ensaio convencional, teñen lugar distintos fenómenos os cales son susceptibles de estudar mediante distintas técnicas de

caracterización. Entre as máis interesantes atópase o estudo da velocidade de propagación de ondas sísmicas.

Co fin de poder realizar un amplo rango de ensaios e poder realizar experimentos de longa duración, desenvolveuse un dispositivo experimental modular e escalalo, onde se axustaron equipos de diversa índole co obxectivo de poder realizar ensaios axustados (hidroxeoquímicos). A adquisición de datos e calibración dos equipos tamén foi obxecto deste traballo. A continuación menciónase as partes máis significativas das que consta devandito sistema (Fig. R.1):

- Bastidor de carga
- Cela portamostras
- Equipo de adquisición de sinal de desprazamentos
- Pratos de carga axial con presión de poro e ondas ultrasónicas (P, S_1 e S_2)
- Sistema de presión axial e confinamento
- Sistema de presión de poro
- Medidor de fluxo másico de gas
- Reguladores de presión
- Microelectrodos de pH e condutividade
- Cromatógrafo iónico

Os ensaios realizados neste dispositivo foron de moi diversa índole:

- Ensaios de permeabilidade baixo condicións triaxiales.
- Inxección de CO_2 líquido e CO_2 supercrítico.
- Inxección de auga saturada en CO_2.
- Inxección de salmuera saturada en CO_2.

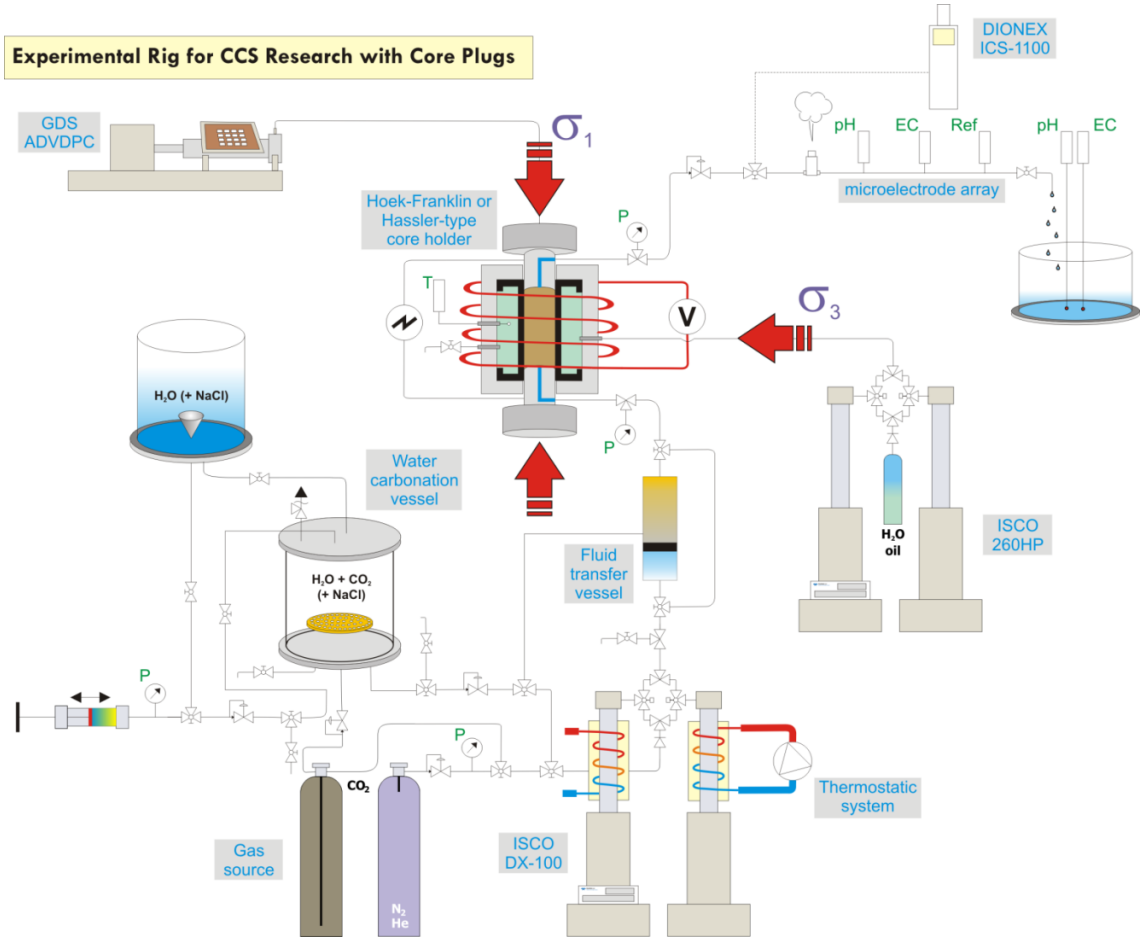

Figura R.1. Deseño experimental realizado na UDC para a realización dos ensaios

Todos estes ensaios de permeabilidade teñen como obxectivo coñecer o comportamento da formación a estudar baixo varios suposto de fluído permeante e deste xeito caracterizar o seu comportamento,

aínda que desde o punto de vista do almacenamento de CO_2 os ensaios máis completos son aqueles en os que o fluído residente e a roca reaccionan co CO_2 que se intenta almacenar. É o caso dos ensaios descritos nos capítulos 4, 5 e 7. Nestes casos, ademais do control das medidas de permeabilidade e presión, realizouse un seguimento da evolución do pH e condutividade ao longo do ensaio así como a determinación das velocidades de ondas ultrasónicas cada día. A partir desta última información puido deducirse a evolución dos parámetros elásticos dinámicos do material analizado.

Dentro dos ensaios de laboratorio e co obxecto de abarcar distintas litoloxías e condicións, realizáronse ensaios en areniscas e carniolas a distintas condicións de presión, temperatura, fluídos coa intención de abarcar un rango amplo de condicións e fenómenos que poden suceder nun potencial almacén xeolóxico de CO_2.

Ensaio de inxección na arenisca da formación Arcera

Este capítulo describe o experimento correspondente co ensaio realizado nunha probeta de arenisca da Formación Arcera (Purbeck Inferior), correspondente a niveis superiores á formación obxectivo da Planta de Desenvolvemento Tecnolóxico de Hontomín.

As condicións de ensaio prescritas foron constantes durante a duración do ensaio: 10 MPa de presión de confinamento; 15 MPa de presión axial; 4 MPa de presión de poro e temperatura ambiente.

Respecto do campo de estabilidade do CO_2, estas condicións son subcríticas, presumíndose un fluxo de tipo monofásico (H_2O+CO_2 disolto).

A mostra ensaiada corresponde a unha cuarzoarenita. O seu densidade seca, antes do ensaio era de 2.428 g/cm^3. Supoñendo unha densidade media dos sólidos que compoñen a roca de 2.6 g/cm^3, o volume de ocos da probeta sería da orde de 6.3 cm^3 polo que a súa porosidade inicial sería de, aproximadamente, 7.3 %.

O fluído circulado a través da probeta (auga desionizada) foi analizado con carácter previo ao seu carbonatación. O seu saturación con CO_2 produciuse a unha a presión de 4 MPa (igual á presión de poro obxectivo) e temperatura ambiente (22 °C). Baixo esas condicións, o contido teórico de CO_2 no fluído é do 2 % (molar).

O experimento desenvolveuse en dúas etapas, cunha duración conxunta de máis de dous meses. Na primeira etapa inxectouse só auga desionizada (7 días) mentres que na segunda inxectouse a solución saturada en CO_2. Ao longo dese tempo mediuse coidadosamente o volume de fluído circulado, a súa composición química (analizada mediante cromatografía iónica e ICP-MS) así como as velocidades de propagación de ondas. Devanditos datos permitiron avaliar o valor da permeabilidade da roca e como esta cambia en función da inxección, así como os procesos reactivos que no seo da mesma tiveron lugar. A medida de velocidades de ondas permitiu, así mesmo, ter unha

primeira aproximación ao coñecemento de procesos de carácter químico-mecánico.

Na figura R.2 indicouse o momento que separa a inxección do auga desionizada respecto do da inxección do auga carbonatada. É interesante observar que, na primeira etapa, a permeabilidade aumenta lixeiramente, para diminuír e estabilizarse cando se inicia a inxección do fluído carbonatado. Transcorridas unhas 2.5 semanas desde o inicio da segunda etapa, tivo lugar un notable incremento do valor da permeabilidade, o cal estabilizouse ao cabo doutra semana. Tras 1.5 semanas adicionais, produciuse un novo aumento do valor da permeabilidade. Conxeturamos que ese comportamento obedece ao acoplamento entre distintos procesos sendo o máis destacable o desenvolvemento de reaccións químicas que propician a disolución de elementos da probeta.

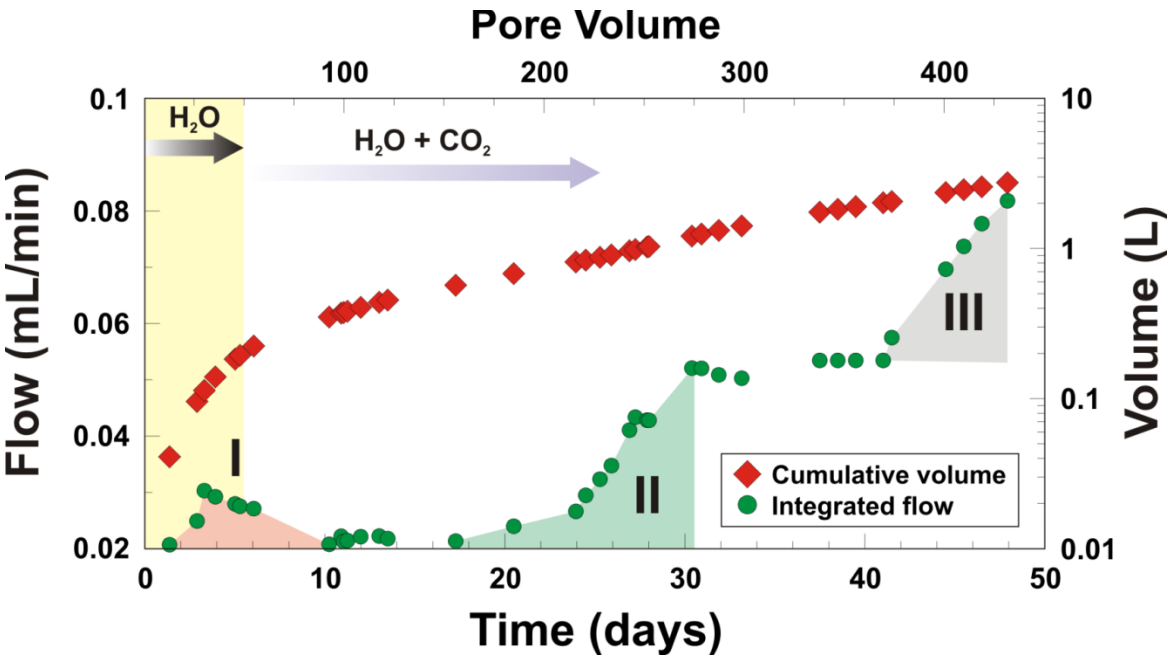

Figura R.2. Evolución da permeabilidade (e o caudal drenado) da mostra en función do tempo.

De forma simultánea ao incremento da concentración de Ca e Mg (figura R.3), prodúcese un lixeiro aumento na permeabilidade da probeta, o cal suxire que o aumento da porosidade e da permeabilidade están relacionados.

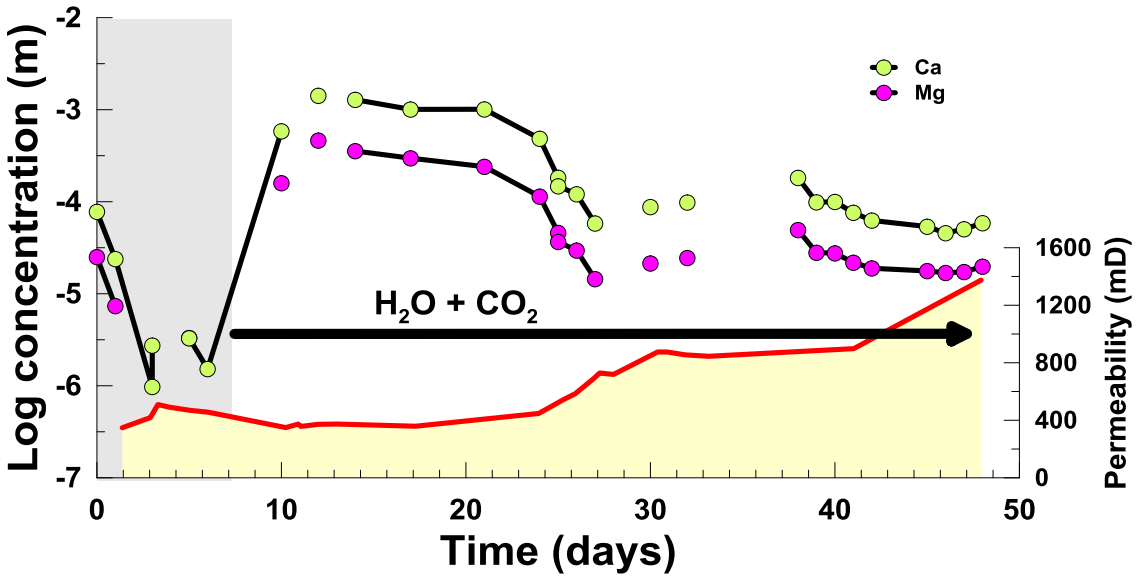

Figura R.3. Evolución da permeabilidade y del Ca y Mg, ambos catións mostran un patrón evolutivo simétrico.

De modo xeral, é posible identificar o momento a partir do cal prodúcese a chegada do fluído saturado en CO_2 dado que se produce unha marcada diminución no pH e un aumento na condutividade; devanditos parámetros foron analizados en continuo á saída da liña de presión intersticial. Doutra banda, V_P aumenta notoriamente (coincidindo coa etapa de inxección de auga carbonatada) mentres que o contrario sucede con V_{S1} e V_{S2}. É interesante tamén o observar que a magnitude de V_P non se mantén constante ao longo da etapa de inxección de auga saturada en CO_2, experimentando descensos e ascensos.

Se observamos de forma detallada a evolución das concentracións de sílice e potasio poderemos verificar unha pauta de evolución xeoquímica complexa. Na primeira fase do ensaio, cando só circulou auga destilada, a concentración de ambos compoñentes tende a diminuír de forma acusada, aínda que, no caso do K, iníciase unha recuperación ao cabo de tres a catro días desde o inicio do ensaio. A chegada da solución carbonatada na etapa 2 marca un comportamento variado no que, nunha primeira fase, as concentracións de ambos compoñentes mantense estable (5-6 mg/L). Esa etapa coincide, aproximadamente, cun moi leve aumento da permeabilidade da probeta, a cal asociamos coa disolución de carbonatos (probablemente calcita magnesiana). No momento no que parecen haberse esgotado os carbonatos, ten lugar un abrupto descenso na concentración axustada de SiO_2 e K, apuntando os datos dispoñibles cara a un incremento posterior, relacionado co aumento de permeabilidade.

Ensaio de inxección en Carniolas

Este capítulo céntrase nun ensaio reactivo de carniola, o reservorio obxectivo do programa de almacenamento da Fundación Ciuden. A mostra na que se realizou no ensaio presentaba unha porosidade do 9.6% e unha densidade aparente de 2.45gr/cm^3. Trátase dunha mostra cun contido en calcita de aproximadamente 86%.

As etapas de inxección foron 1) auga desionizada 2) salmuera sintética de formación e 3) salmuera sintética de formación saturada en CO_2.

Do mesmo xeito que no ensaio do capítulo 4 é un experimento de inxección continua (25 días) no que os fluídos utilizados foron auga desionizada, salmuera de formación e dita salmuera saturada con CO_2. A temperatura de ensaio foi de 40 °C, a presión axial de 30 MPa, unha presión de confinamento de 10 MPa e unha presión de poro de 4 MPa, o que nos leva a realizar o ensaio nunhas condicións subcríticas desde o punto de vista do CO_2.

A etapa de inxección de salmuera saturada en CO_2 dá lugar a cambios notables na evolución da mostra:

-A velocidade da deformación é practicamente constante ata a aparición da etapa de CO_2 (figura R.4), nesta última obsérvase unha fase reactiva elevada en comparación coas anteriores e obsérvanse os maiores cambios desde o punto de vista químico, hidrodinámico e mecánico.

-A condutividade hidráulica aumenta abruptamente nesta etapa mentres que ao longo dos primeiros 20 días permanece constante.

-Ao analizar en dominio de frecuencias as ondas P, S_1 e S_2 tamén se observan certas variacións ao longo do ensaio. No caso da onda P obsérvase perfectamente o efecto da sustitución de fluídos mentres

que no caso da onda S_1 e S_2 obsérvanse fenómenos que se achacan a procesos de disolución.

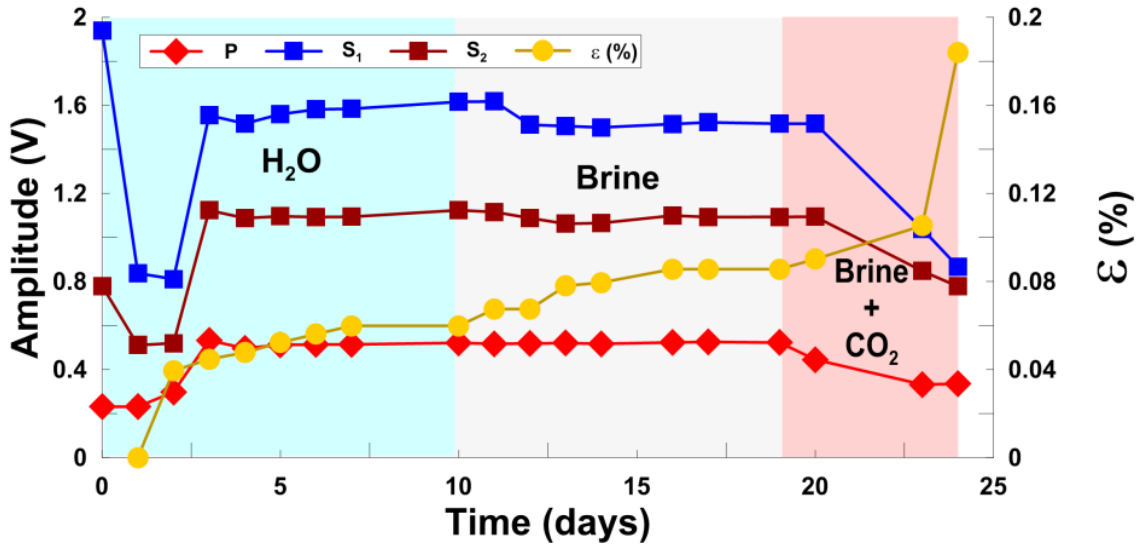

Figura R.4. Evolución da deformación axial xunto ca amplitude de las ondas P, S_1 y S_2.

Caracterización xeomecánica e anisotrópica de arenisca de Corvio

Os experimentos realizados poñen en evidencia as complexas interaccións que teñen lugar cando un fluído carbonatado acedo interactúa cunha roca e como, a raíz diso, desenvólvense importantes acoplamentos hidrodinámicos, mecánicos e químicos. Con obxecto de realizar ensaios sobre unha roca onde a parte reactiva sexa menor e en busca de caracterizar a súa parte mecánica en profundidade, nace o capítulo 6. Devandito capítulo céntrase nunha arenisca comercial da Formación Corvio. Nel preséntase unha caracterización completa da física, mineraloxía, propiedades xeomecánicas, xeofísicas e

hidrodinámicas da Arenisca de Corvio. Esta información, xunto cunha avaliación detallada da súa anisotropía, é necesaria para establecer este material como un estándar de referencia para ensaios de laboratorio enfocados cara aos fenómenos termo-hidro-mecánico-xeoquímicos axustados de interese para o almacenamiento geológico de CO_2 e outros estudos xeológicos en xeral. Máis de 200 mostras de arenisca de Corvio (diámetro 38.1 e 50 mm, 2:1 de lonxitude a diámetro) utilizáronse neste estudo de caracterización, cunha roca porosidade de 21,7 ± 1,2%, densidade en seco 2036 ± 32 kg m^{-3}, e resistencia a compresión simple e resistencia á tracción de 41 ± 3,28 e 2,3 ± 0,14 MPa, respectivamente. Os ensaios geomecánicos mostran que a roca compórtase elasticamente entre 10 e 18 MPa baixo condicións de confinamento (figura R.5) cun módulo de Young e coeficiente de Poisson asociados de 11,8 ± 2,8 GPa e 0,34 ± 0,01, respectivamente. A permeabilidade diminúe abruptamente con presión de confinamento ata 10 MPa e logo se estabiliza en 1 MD. Velocidades Ultrasónica P e S varían desde ao redor de 2.8 ata 3.8 km s^{-1} e de 1,5 a 2,4 km s^{-1}, respectivamente, ao longo de confinamento e presións diferenciais entre 0,1-35 MPa, permitindo derivar destes os parámetros elásticos dinámicos asociados. A anisotropía investigouse o usando testemuñas orientadas en diversas direccións para a resistividade eléctrica, velocidade da onda elástica e a atenuación, a permeabilidade e ensaios de inxección de trazadores. A Arenisca de

Corvio mostra débil anisotropía transversal (simetría eixe normal á estratificación) de <10% da velocidade e <20% da atenuación.

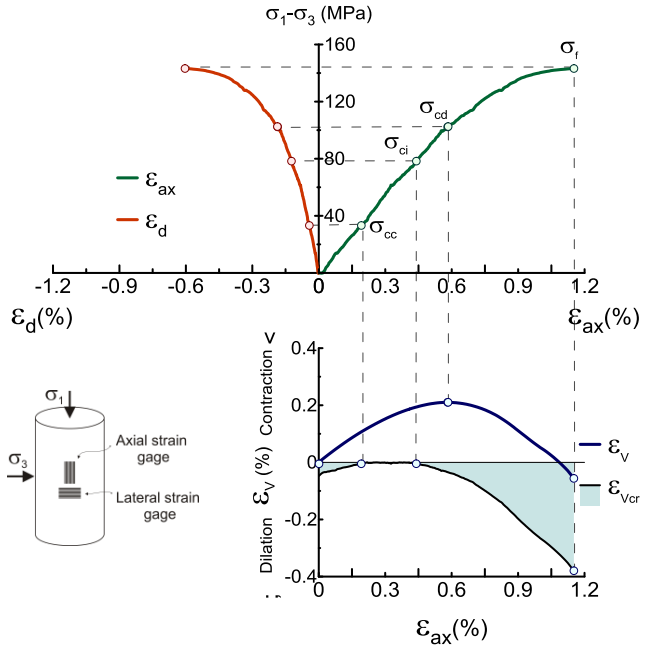

Figura R.5. Ensaio triaxial da Arenisca de Corvio (σ_3=38MPa) usando galgas extensométricas para la medida de deformación. σ_{cc}, peche de fisuras; σ_{ci}, inicio de fisuración; σ_d, dano en las fisuras; σ_f, colapso.

Ensaio de inxección en la Arenisca de Corvio

No capítulo 7 preséntase un ensaio de inyección continúa (35 días) e multietapa desta arenisca realízase a unha temperatura de 40 °C, a unha presión de confinamiento de 10 MPa, unha presión axial de 15 MPa e unha presión de poro de 8 MPa. Este ensaio realízase en caudal imposto de 0.04 mL/min e con dúas etapas diferenciadas, a primeira de auga desionizada e unha segunda de auga desionizada

saturada en CO_2. Estas condicións garanten un réxime supercrítico no CO_2.

A cuarzo arenisca ensaiada neste test tiña un diámetro de 37.4 mm, unha lonxitude de 70.2 mm, porosidade 12.1% e unha densidade aparente de 2.094 gcm^{-3}.

No experimento analízanse os fenómenos axustados e apréciase pequena disolución no material cementante intergranular. Dita disolución ten cambios na permeabilidade, deformación axial (figura R.6), cambios de amplitude na frecuencias das ondas P, S_1 e S_2 como consecuencia dun peor contacto entre os grans.

Como resultados resinables obsérvase que o cambio das amplitudes das ondas P e S é un indicador dun aumento da deformación da mostra, producíndose unha reordenación e re-compactación dos grans. Os procesos que desencadean os fenómenos axustados son de orixe químicos e estes, á súa vez, dan lugar a cambios hidro-mecánicos. A resposta entre ambos presenta un certo desfase, dado que o colapso do material non se produce no inicio do proceso de disolución.

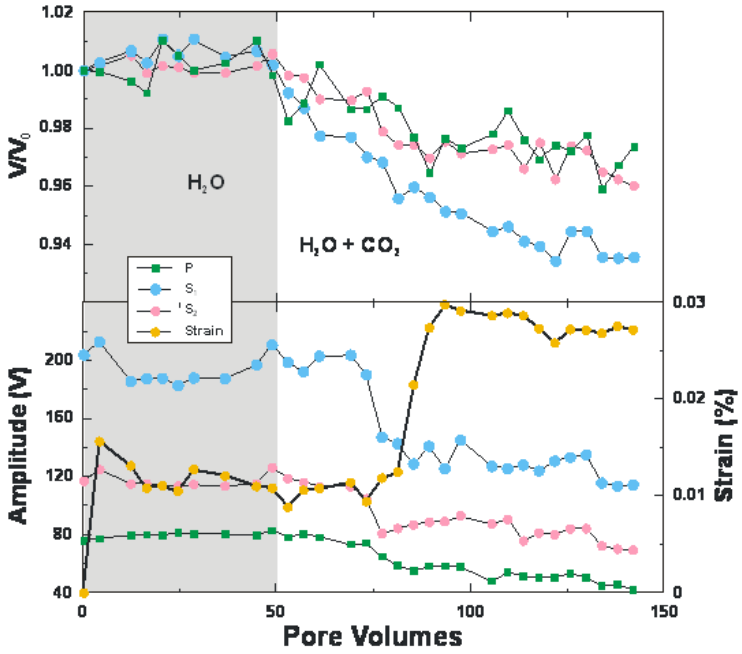

Figura R.6. Evolución da deformación axial xunto ca amplitude de las ondas P, S_1 y S_2.

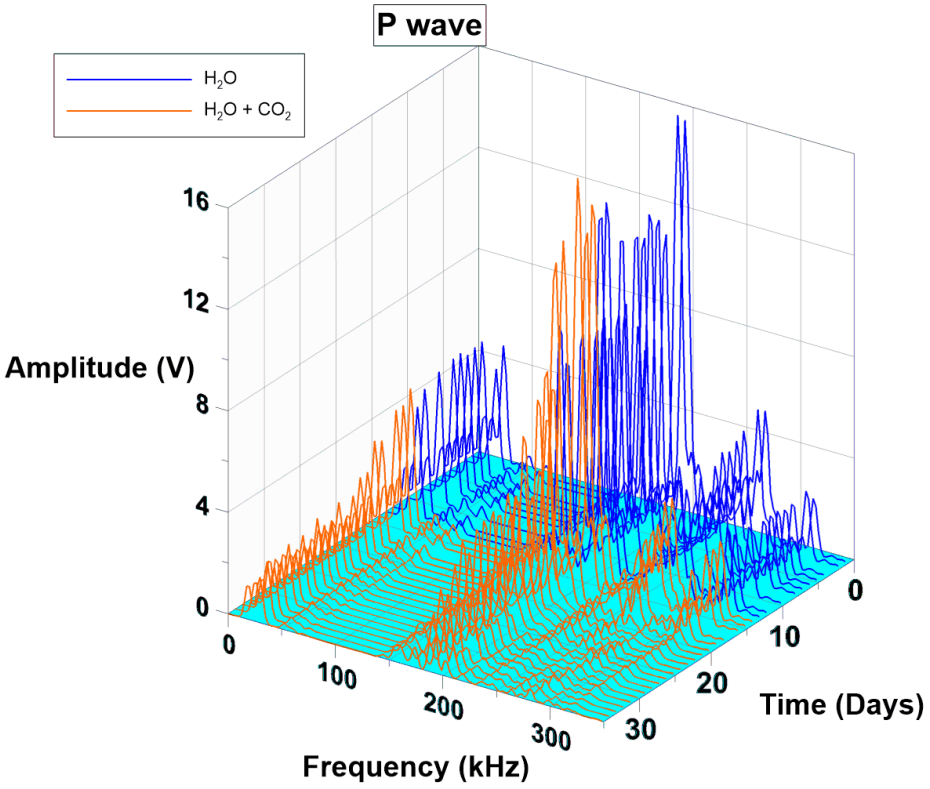

Figura R.7. Evolución das frecuencias de ondas P o longo dos 35 días de duración do experimento de inxección con la Arenisca de Corvio.

Conclusións

Como conclusións xerais do traballo establécense as seguintes:

-Deseñamos, construído e probado unha plataforma experimental versátil que permite desenvolver ensaios axustados (termo-hidro-quimio-mecánicos), con especial atención ao campo da investigación de CCS.

-O Sistema experimental desenvolvido é modular, escalable. O sistema demostrou ser á vez simple e fiable para levar a cabo experimentos axustados de longa duración.

-As condicións impostas de baixo fluxo e un fluído saturado con CO2 pretenden reproducir unhas condicións de ensaio representativas das circunstancias imperantes no almacén, a certa distancia do punto de inxección de CO_2.

-O cociente de velocidades de onda V_p/V_s non é un bo indicador para a detección de cambios no espazo poroso.

-A análise en dominio da frecuencia da ondas V_p/V_s (amplitude) é un bo indicador para os cambios de propiedades derivadas da interacción fluído/roca.

-Os experimentos ilustrados nos Capítulos 5 e 7 mostran un comportamento sensiblemente diferente na análise de frecuencias: A atenuación nas frecuencias da carniola ocorre para todo o rango de frecuencias; Na Arenisca de Corvio a atenuación maior prodúcese para

as frecuencias correspondentes ás lonxitudes de onda máis pequenas. Isto parece estar relacionado co tipo de dano interno na mostra. Nun caso este sería de tipo xeral (arenisca) mentres que no outro, o dano estaría máis focalizado (carniola) a tenor dos fenómenos de disolución localizada que, de forma preferente, teñen lugar na carniola.

-Nunha roca con contactos entre grans de gran tamaño (carniola) pódese observar a sustitución de fluídos (onda P) ao contrario que na arenisca.

O proceso químico é o detonante de todos os demais cambios nas propiedades da roca e polo tanto o que goberna a reacción en cadea.

ANNEX 2. PAPERS

macla nº 15. septiembre 2011
revista de la sociedad española de mineralogía

Inyección de Agua con CO_2 en Condiciones Triaxiales en Rocas Detríticas de la Formación Arcera

/ JACOBO CANAL (1), JORDI DELGADO (2), VICTOR BARRIENTOS (2), RICARDO JUNCOSA (2).

(1) Fundación Ciudad de la Energía. // Avenida de Compostilla nº2 · 24400 Ponferrada (España).
(2) E.T.S. Ingenieros de Caminos, Canales y Puertos. Campus de Elviña s/n. Universidade da Coruña. 15192, A Coruña (España)

INTRODUCCIÓN.

Uno de los objetivos a los que se enfrenta la sociedad actual es reducir la contaminación y producir energías limpias a través de procesos sostenibles tanto en lo ambiental como en lo económico. Para ello, desde hace varios años, se desarrolla una intensa actividad científica en el ámbito del almacenamiento geológico de CO_2. En este contexto, en España, la Fundación Ciudad de la Energía (CIUDEN) es responsable de uno de los programas de investigación más ambiciosos, incluyendo el diseño y construcción de una planta experimental de captura, un laboratorio de inyección profundo así como una variada serie de ensayos de laboratorio. En este último contexto se inscribe el presente trabajo.

MATERIALES Y MÉTODOS.

El experimento realizado se desarrolló en el laboratorio de Ingeniería del Terreno de la E.T.S. de Ingenieros de Caminos, Canales y Puertos de la Universidad de Coruña. De modo resumido, consistió en la circulación forzada de una solución acuosa saturada en CO_2 a través de una probeta sometida ésta a condiciones triaxiales, es decir, con confinamiento simultáneo a la aplicación de una carga axial. Para la aplicación de la carga axial se empleó un bastidor de reacción de 30 toneladas de capacidad, dotado de un actuador acoplado a una bomba manual ENERPAC capaz de entregar hasta 70 MPa. Para transferir a la muestra la presión de confinamiento establecida, empleamos una celda porta-testigos de tipo Hoek-Franklin (Hoek y Franklin, 1968), capaz de resistir presiones de hasta 70 MPa y acoplada a otra bomba hidráulica similar a la anteriormente descrita.

La probeta de roca ensayada fue insertada en la celda triaxial enfundada en una camisa de material plástico elástico de alta resistencia (poliolefina), la cual garantiza la separación física de la roca respecto del fluido hidráulico empleado como medio de transmisión de la presión de confinamiento.

Con el fin de realizar ensayos en los que distintos fluidos acuosos pudieran ser saturados en CO_2 bajo distintas condiciones de temperatura T y presión P, se diseñó *ex profeso* un depósito de carbonatación susceptible de soportar presiones de hasta 15 MPa. Este valor corresponde al de la tara de una válvula de seguridad.

Para la inyección de fluido en los poros de la probeta, los platos de aplicación de carga de la celda triaxial fueron modificados para permitir la conexión de un entramado de tubos, válvulas, manómetros y reguladores de alta presión, todo ello conectado a un sistema de bombas ISCO DX100, capaz de proporcionar un caudal (de 10^{-5} - 50 mL/min) bajo presión de inyección constante (hasta 69 MPa) y libre de pulsos. Asimismo empleamos unos platos de compresión dotados de transductores (emisor y receptor) para medir las velocidades de propagación de ondas P, S_1 y S_2 (V_P, V_{S1}, V_{S2}).

Las condiciones de ensayo prescritas fueron constantes durante la duración del ensayo: 10 MPa de presión de confinamiento; 15 MPa de presión axial; 4 MPa de presión de poro y temperatura ambiente. Respecto del campo de estabilidad del CO_2, estas condiciones son subcríticas, presumiéndose un flujo de tipo monofásico (H_2O+CO_2 disuelto)

La muestra ensayada corresponde a una cuarzoarenita procedente de la Formación Arcera (Purbeck Inf.), muestreada en las proximidades de esa misma localidad. Su mineralogía está dominada por el cuarzo, minerales de la arcilla y pequeñas cantidades de feldespatos y calcita. La probeta se talló en forma de cilindro de 38.3 mm de diámetro y 74.55 mm de altura, con un volumen de 85.89 cm^3. Su densidad seca, antes del ensayo era de 2.428 g/cm^3. Suponiendo una densidad media de los sólidos que componen la roca de ~2.6 g/cm^3, el volumen de huecos de la probeta sería del orden de 6.3 cm^3 por lo que su porosidad inicial sería de, aproximadamente, 7.3 %.

El fluido circulado a través de la probeta (agua desionizada) fue analizado con carácter previo a su carbonatación. Su saturación con CO_2 se produjo a una a presión de 4 MPa (igual a la presión de poro objetivo) y temperatura ambiente (~22 ºC). Bajo esas condiciones, el contenido teórico de CO_2 en el fluido es del 2 % (molar). Empleando la ecuación de estado de Duan y Sun (2003), simplificada por Duan *et al.* (2006), estas condiciones se corresponderían con una concentración de CO_2 disuelto de 1.39 mol/kg H_2O o unos 61.1 g CO_2por cada kg de H_2O. En la misma línea, el cálculo teórico del pH de la solución de infiltración es netamente ácido (3.12).

El experimento se desarrolló en dos etapas, con una duración conjunta de más de dos meses. En la primera etapa se inyectó sólo agua desionizada (~7 días) mientras que en la segunda se inyectó la solución saturada en CO_2. A lo largo de ese tiempo se midió cuidadosamente el volumen de fluido circulado, su composición química (analizada mediante cromatografía iónica e ICP-MS) así como las velocidades de propagación de ondas. Dichos datos permitieron evaluar el valor de la permeabilidad de la roca y cómo ésta cambia en función de la inyección, así como los procesos reactivos que en el seno de la misma

palabras clave: secuestro geológico de CO_2, ensayo triaxial

key words: geological sequestering of CO_2, triaxial

* corresponding author: jcanal@udc.es

macla nº 15. septiembre 2011
revista de la sociedad española de mineralogía

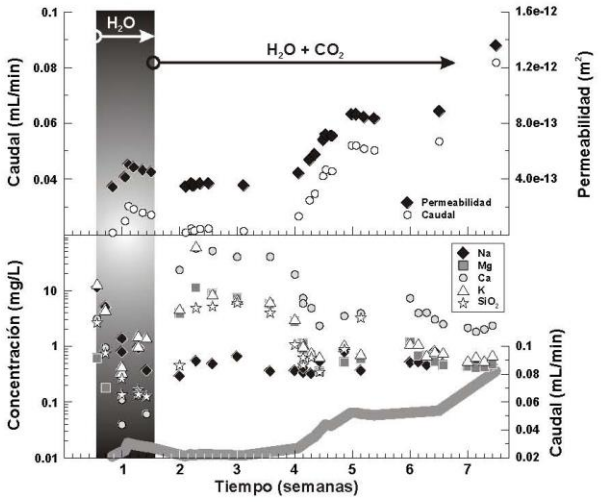

fig 1. Arriba, permeabilidad calculada a partir del caudal drenado de la probeta en función del tiempo de ensayo. Abajo, evolución de la concentración de diversos constituyentes químicos, comparada con el caudal drenado.

tuvieron lugar. La medida de velocidades de ondas permitió, asimismo, tener una primera aproximación al conocimiento de procesos de carácter químico-mecánico.

RESULTADOS Y DISCUSIÓN.

La figura 1 muestra la evolución de la permeabilidad (y el caudal drenado) de la muestra en función del tiempo así como la concentración de ciertos componentes. En la misma se ha indicado el momento que separa la inyección del agua desionizada respecto del de la inyección del agua carbonatada. Es interesante observar que, en la primera etapa, la permeabilidad aumenta ligeramente, para disminuir y estabilizarse cuando se inicia la inyección del fluido carbonatado. Transcurridas unas 2.5 semanas desde el inicio de la segunda etapa, tuvo lugar un notable incremento del valor de la permeabilidad, el cual se estabilizó al cabo de otra semana. Tras ~1.5 semanas adicionales, se produjo un nuevo aumento del valor de la permeabilidad. Conjeturamos que ese comportamiento obedece al acoplamiento entre distintos procesos siendo el más destacable el desarrollo de reacciones químicas que propician la disolución de elementos de la probeta.

De forma simultánea al incremento de la concentración de Ca y Mg, se produce un ligero aumento en la permeabilidad de la probeta (Fig. 1, abajo), lo cual sugiere que el aumento de la porosidad y de la permeabilidad están ligados.

De modo general, es posible identificar el momento a partir del cual se produce la llegada del fluido saturado en CO_2 dado que se produce una marcada disminución en el pH y un aumento en la conductividad; dichos parámetros fueron analizados en continuo a la salida de la línea de presión intersticial. Por otro lado, V_P aumenta notoriamente (coincidiendo con la etapa de inyección de agua carbonatada) mientras que lo contrario sucede con V_{S1} y V_{S2}. Es interesante también el observar que la magnitud de V_P no se mantiene constante a lo largo de la etapa de inyección de agua saturada en CO_2, experimentando descensos y ascensos.

Si observamos de forma detallada la evolución de las concentraciones de sílice y potasio podremos verificar una pauta de evolución geoquímica compleja. En la primera fase del ensayo, cuando sólo circuló agua destilada, la concentración de ambos componentes tiende a disminuir de forma acusada, aunque, en el caso del K, se inicia una recuperación al cabo de tres a cuatro días desde el inicio del ensayo. La llegada de la solución carbonatada en la etapa 2 marca un comportamiento variado en el que, en una primera fase, las concentraciones de ambos componentes se mantiene estable (~5-6 mg/L). Esa etapa coincide, aproximadamente, con un muy leve aumento de la permeabilidad de la probeta, la cual asociamos con la disolución de carbonatos (probablemente calcita magnesiana). En el momento en el que parecen haberse agotado los carbonatos, tiene lugar un abrupto descenso en la concentración acoplada de SiO_2 y K, apuntando los datos disponibles hacia un incremento posterior, relacionado con el aumento de permeabilidad.

CONCLUSIONES.

El experimento realizado pone en evidencia las complejas interacciones que tienen lugar cuando un fluido carbonatado ácido interactúa con una roca silicatada detrítica y como, a raíz de ello, se desarrollan importantes acoplamientos hidrodinámicos y mecánicos.

AGRADECIMIENTOS.

Este trabajo ha sido financiado por la Fundación CIUDEN, así como por la Xunta de Galicia (10REM003CT). Parte de los equipos empleados en este trabajo fue adquirido con cargo a los Fondos FEDER 2007/2013. La determinación de aniones y cationes fue realizada por A. Vázquez, S. Fernández y los SXAIN de la UDC.

REFERENCIAS.

Duan, Z. y Sun (R. (2004) An improved model calculating CO_2 solubility in pure water and aqueous NaCl solutions from 273 to 533 K and from 0 to 2000 bar. Chemical Geology 193, 257-271.

Duan, Z.; Sun, R.; Zhu, C. y Chou, I.M. (2006) An improved model for the calculation of CO_2 solubility in aqueous solutions containing Na^+,K^+,Ca^{+2},Mg^{+2},Cl^- and SO_4^{-2}. Marine Chemistry 98, 131-139.

Hoek, E. y Franklin, J.A. (1968) A simple triaxial cell for field and laboratory testing of rock. Transactions of the Institution of Mining and Metallurgy 77, A22- 26.

Klinkenberg, L.J. (1941) The permeability of porous media to liquids and gases. American Petroleum Institute. Drilling and Productions Practices, 210-213.

Tiab, D. y Donaldson, E.C. (2003) Petrophysics: Theory and Practice of Measuring Reservoir Rock and Fluid Transport Properties. 2ª edición. Gulf Professional Publishing; 800 pp.

Environmental Science & Technology

Article

pubs.acs.org/est

Injection of CO_2-Saturated Water through a Siliceous Sandstone Plug from the Hontomin Test Site (Spain): Experiment and Modeling

J. Canal,[†] J. Delgado,*[,‡] I. Falcón,[‡] Q. Yang,[‡] R. Juncosa,[‡] and V. Barrientos[‡]

[†]Fundación Ciudad de la Energía, Avenida Compostilla II no. 2, 24404 Ponferrada, Spain

[‡]Civil Engineering School, University of A Coruña, Campus de Elviña s/n, 15192, A Coruña, Spain

Supporting Information

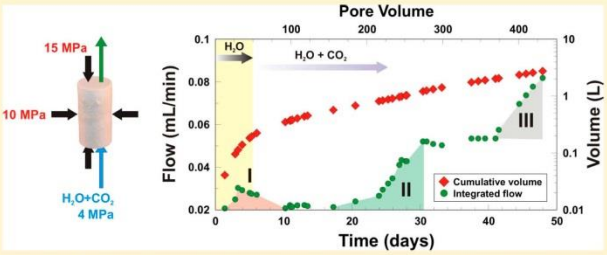

ABSTRACT: Massive chemical reactions are not expected when injecting CO_2 in siliceous sandstone reservoirs, but their performance can be challenged by small-scale reactions and other processes affecting their transport properties. We have conducted a core flooding test with a quartzarenite plug of Lower Cretaceous age representative of the secondary reservoir of the Hontomín test site. The sample, confined at high pressure, was successively injected with DIW and CO_2-saturated DIW for 49 days while monitoring geophysical, chemical, and hydrodynamic parameters. The plug experienced little change, without evidence of secondary carbonation. However, permeability increased by a factor of 4 (0.022−0.085 mD), and the V_P/V_S ratio, whose change is related with microcracking, rose from ∼1.68 to ∼1.8. Porosity also increased (7.33−8.1%) from the beginning to the end of the experiment. Fluid/rock reactions were modeled with PHREEQC-2, and they are dominated by the dissolution of Mg-calcite. Mass balances show that ∼4% of the initial carbonate was consumed. The results suggest that mineral dissolution and microcracking may have acted in a synergistic way at the beginning of the acidic flooding. However, dissolution processes concentrated in pore throats can better explain the permeability enhancement observed over longer periods of time.

1. INTRODUCTION

R&D activities concerning technologies for carbon capture and storage (CCS) in the countries of the European Union have been fostered by the adoption of the European Directive 2009/31/EC.[1] This establishes a legal framework for the environmentally safe geological storage of CO_2 in the EU. The fourth article states that the suitability of a geological formation for use as a storage site shall be determined through its characterization and assessment pursuant to a number of criteria, including their behavior when submitted to the injection of $scCO_2$ or CO_2-saturated solutions.[2]

In June, 2008, the European Council called on the Commission to bring forward a mechanism to incentivize investments to ensure the construction and operation by 2015 of up to 12 CCS demonstration plants. By the end of 2009 the European Commission granted financial assistance to six CCS demonstration projects which are expected to lead future works. The OXYCFB300 Compostilla project, funded by the European Energy Program for Recovery and partnered by ENDESA (the largest Spanish electric utility), CIUDEN (on behalf of the Government of Spain), and Foster Wheeler Energia Oy (a global leader in energy generation technology), is one of them. It aims to demonstrate the full CCS chain[3] and, within its framework, a research facility for the deep injection of CO_2 is being commissioned in Hontomín (Burgos, Spain).

The nature and extent of $scCO_2$ or CO_2-bearing fluid/rock interactions is an important concern when considering injectivity, containment, and long-term safety of geological storage systems.[4] Siliceous detritic formations are not expected to react massively with the injectate, but the presence of lesser amounts of reactive minerals may play a significant role in their performance as geological storage. In fact, there is a wide body of evidence showing that coupled chemo-mechanical processes associated to CO_2 injection in sandstone reservoirs can trigger

Special Issue: Carbon Sequestration

Received: March 30, 2012
Revised: July 3, 2012
Accepted: July 6, 2012
Published: July 6, 2012

dx.doi.org/10.1021/es3012222 | Environ. Sci. Technol. 2013, 47, 159−167

Table 1. Summary of Physical, Chemical, and Mineralogical Properties of the Sample Used in the Experiment

physical properties		chemical composition (wt %)[a]		mineralogy (vol %)[b]	
diameter	38.30 mm	SiO_2	94.87	quartz	92.1
length	74.55 mm	Al_2O_3	2.13	kaolinite	5.0
volume	8.59×10^{-2} L	Fe_2O_3	0.92	Mg-calcite	0.3
initial porosity[c]	7.33%	MgO	0.06	K-feldspar	0.5
dry density	2428 kg/m^3	CaO	0.12	muscovite	0.1
solid density	2620 kg/m^3	Na_2O	0.05	goethite	0.9
pore volume	6.31×10^{-3} L	K_2O	0.1	apatite	0.03
specific surface[d]	0.5 m^2/g	TiO_2	0.08	rutile	0.1
mean pore diameter[e]	0.5 μm	P_2O_5	0.03	barite[f]	3.5×10^{-5}
mean intrinsic permeability	10^{-167} m^2	LOI	1.2	halite[f]	2.6×10^{-6}
				sylvite[f]	1.5×10^{-6}

[a]XRF. [b]Normative calculation based on XRF data. [c]Based on the weight difference between the dry and the fluid-saturated sample. [d]BET isotherm performed on a rock chip. [e]Hg intrusion porosimetry. [f]Minerals used to constrain the geochemical model.

deleterious effects in their transport properties.[5−9] Worth mentioning are the compaction of the rock grain skeleton induced by the dissolution/collapse of cement phases, the migration of fines, or mineral scaling.[10]

The overall objective of this work was to evaluate processes leading to permeability changes in a sandstone plug when flooded with CO_2-saturated water at high pressure and subcritical conditions. We present the results of an experiment performed with a sandstone rock representative of the secondary reservoir of Hontomín in which we monitored hydrodynamic, geophysical and hydrochemical parameters so that it is possible to examine the extent chemo-hydro-mechanical couplings and their role in the evolution of permeability. The experiment is further analyzed from the realm of reactive transport modeling.

2. MATERIALS AND METHODS

The geological setting beneath the Hontomín test site (~25 km north Burgos) is a small, dome-shaped structure (3 × 4 km) developed in a thick series of carbonate and siliciclastic formations. CIUDEN has identified two targets for CO_2 storage: Main and secondary reservoirs. The main reservoir (1376−1502 m b.s.) corresponds to vuggy limestones of Lower Jurassic age while the secondary (837−964 m b.s.) is constituted by siliceous sandstones and conglomerates included in the red mudstones of the Purbeck facies (Upper Jurassic/Lower Cretaceous).[11] For this secondary reservoir, the expected in situ conditions are ~42 °C and 18 MPa for overburden and 9 MPa for pore pressure.

The experiment consisted in the successive injection of deionized water (DIW) and CO_2-saturated DIW through a cylindrical quartzarenite plug obtained from a core sampled from an outcrop of the Arcera Formation (lower Purbeck), near Hontomín (UTM-X: 414003; UTM-Y: 4747617). The plug was carefully trimmed to fulfill standard geometric constrains.[12] A summary of relevant data of the specimen is given in Table 1. The chemical composition of the rock was analyzed by XRF while its mineralogy was identified by the combination of powder-XRD and SEM. Mineral abundances were computed from the XRF data using the MINSQ spreadsheet.[13] The mineralogy is dominated by quartz (~92%) with subordinated quantities of kaolinite (~5%). Scarce crystals of K-feldspar, muscovite, goethite, barite, ilmenite, and rutile are also present in the rock (Figure 1B−D). The average inorganic carbon content of the rock is small (0.18 wt %), and SEM images show that carbonates have a small grain size and are always associated with the pore space of the rock, often in pore throats (Figure 1A). Quartz grains are cemented by microcrystalline silica, and kaolinite fills a portion of the pore space (Figure 1B).

The experiment lasted for 49 days (DIW: 7 days; CO_2-saturated DIW: 42 days), and a total of 2.7 L of fluid was forced to circulate through the sample. Taking into account that the initial porosity of the plug was 7.33%, its pore volume (PV) was flushed ~430 times at an average flow rate of 0.04 mL/min.

2.1. Experimental Rig. The sample, initially dry, was submitted to axi-symmetric stress conditions by vertically inserting it into a modified Hoek-Franklin-type cell.[14] The cell transmits the stresses to the sample through two stainless-steel platens (axial stress; σ_1) and hydraulic oil (confining stress; $\sigma_2 = \sigma_3$). To avoid contact between the confining fluid and the sample, this is jacketed with a polyurethane sleeve. The test was performed at room temperature (22.0 ± 1.6 °C; 2σ) and constant stress conditions (σ_1 = 15 MPa; σ_3 = 10 MPa). These conditions represent a first step toward evaluating permeability changes under more representative in situ conditions. Pressures were supplied by two independent hydraulic pumps equipped with check valves (to maintain pressure) and analogic gauges (for monitoring). Loading of the sample was performed stepwise: First, the axial and confining pressures rose simultaneously at a constant rate to the target σ_3 value. From hereafter, σ_1 was increased while keeping σ_3 constant.

Each of the platens incorporates two fluid ports connected to a thru-hole. For a better fluid distribution, the surfaces in contact with the sample are grooved. During the loading process, in order to avoid an undesired increase of the pore pressure, the sample was kept drained (i.e., inlet and outlet ports open). The bottom fluid port was connected to a dual Teledyne Isco DX100 pump which was used to inject at constant pressure (4 MPa) the flooding fluids. The pressure drop between the inlet and the outlet ports was monitored with two high-resolution (±0.1%) absolute pressure transducers. The top fluid port was connected to a tube line whose purpose was to collect the outlet fluid. This line was equipped with a low-volume flow-thru, temperature-compensated, microelectrode (Microelectrodes Inc.) array. Because these devices cannot attain pressures > 100 kPa, the fluid was decompressed prior to the measurements. However, in the second phase of the experiment decompression triggered the outgassing of CO_2 and the growth and transient accumulation of small gas bubbles in the dead volume of the microelectrodes. This turned out to increase the internal pressure and, as a result, small external leaks from the 3 M KCl reference electrode happened. That

dx.doi.org/10.1021/es3012222 | Environ. Sci. Technol. 2013, 47, 159−167

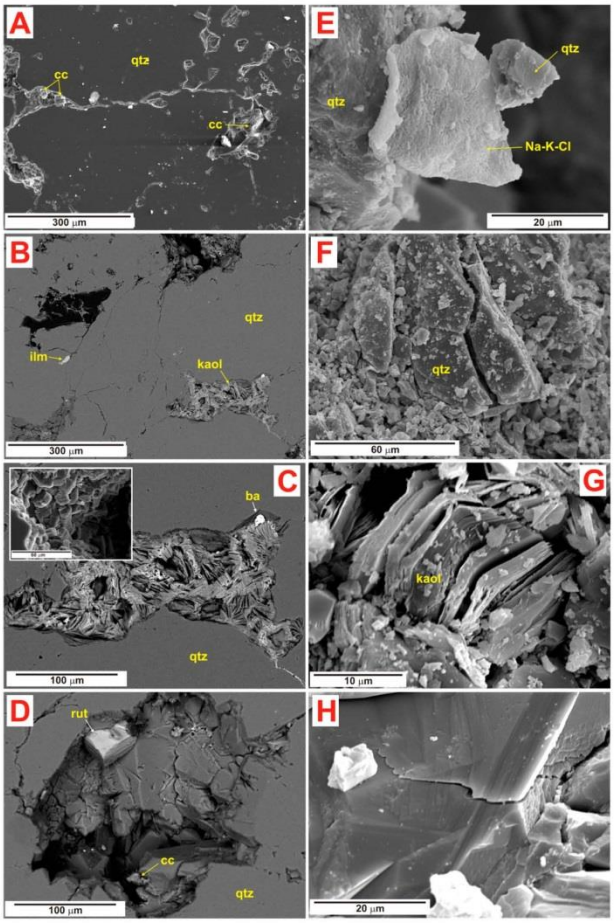

Figure 1. Secondary (A, E, F, G, H) and backscattered electron (B, C, D) SEM images of the Arcera sandstone. Images A–E correspond to the sample before flooding while F–H were taken after the experiment. Cc: calcite; qtz: quartz; ilm: ilmenite; kaol: kaolinite; ba: barite; rut: rutile; Na–K–Cl: salt precipitate. See text for explanation.

originated data loss and the continuous need for maintenance and calibration.

The top and bottom platens are instrumented each with a stack of 1.3 MHz resonant frequency piezoelectric transducers for the measurement of direct (V_P) and shear (V_{S1}, V_{S2}) ultrasonic wave velocities. Squared-pulse waves were generated with a transducer–pulser unit and monitored with a digital oscilloscope. Velocities were determined applying the time-of-flight technique, according to published recommendations.[15]

The saturation of water with CO_2 was accomplished in a 2.7 L carbonation vessel which was first filled with DIW. To accelerate water saturation, CO_2 was micronized at low pressure (~0.5 MPa). CO_2 was delivered in excess to develop a gaseous headspace. The compression to the target pressure of 4 MPa was performed with a pressure generator. The system was left to equilibrate for a week. This time is believed to be sufficient to guarantee the satisfactory saturation of water.[16,17] The transfer of fluid from the carbonation vessel to the injection pump was performed by setting the latter in constant pressure mode and a back-pressure regulator, both set to 4 MPa. Thermodynamic calculations[18,19] show that the theoretical concentration of CO_2 in the carbonated fluid is 1.39 mol/kg H_2O and pH 3.12.

dx.doi.org/10.1021/es3012222 | Environ. Sci. Technol. 2013, 47, 159–167

2.2. Analytical Procedures. Injection flow rates and pore pressure were directly monitored with the control software and the transducers of the injection pumps. From this data we evaluated permeability using Darcy's Law for steady flow.[20] In short, the ratio of volumetric flow rate, Q (m^3/s), to the pressure drop, ΔP (Pa), between the inlet and the outlet of a sample of cross-sectional area, A (m^2), and length, L (m), is related with its intrinsic permeability, k (m^2) through the following expression:

$$k = \frac{\mu L Q}{A \Delta P}$$

where μ represents the dynamic viscosity of the fluid (Pa·s). The fluid leaving the sample through the outlet port was collected and analyzed for its anionic (Cl, F, SO_4), cationic (Na, K, Ca, Mg, Al, Ba), and silica concentrations. Anions were determined by ion chromatography while cations and silica by HR ICP-MS.

Analytical concentrations have been represented against PV in Figures 2−4. Because each sample was collected after a variable period of time, their volumes represent different PV values. This uncertainty has been incorporated into the plots as the PV error bar.

2.3. Reactive Transport Modeling. The PHREEQC-2 code[21] (version 2.18.3-5570) and the wateq4f.dat database were used to model the results of the experiment. We defined a one-dimensional domain made of 20 cells, each one having a length equal to 1/20th of the total length of the sample. Relevant information of the model and associated parameters is provided Table S1 as Supporting Information. The experiment was segmented into five consecutive modeling stages (I to V) based on the visual inspection of the evolution of Ca, Mg, SiO_2, and Al. These components display a sawtooth pattern (Figures 3 and 4) whose boundaries, in terms of PV (I = 0−35; II = 35−150; II I =150−200; IV = 200−280; V = 280−440), were used to constrain the model. Stage I considers only the injection of DIW while for stages II−V the model accounts for the flooding with CO_2-saturated water.

PHREEQC-2 does not allow the direct input of hydraulic conductivity (K) or pressure gradients ($\Delta h/\Delta L$). These parameters have to be implicitly considered in the space and time discretization by relating the cell length, Δx (m), with the time step, Δt (s), through the pore flow or Darcy's velocity, v (m/s): $v = -K\Delta h/\Delta L$. Consequently, $v = \Delta x/\Delta t$. Pore flow velocity was not constant throughout the experiment, and we constructed the model using different values consistent with the observations: 5×10^{-6} m/s for stages I and II; 10^{-5} m/s for stages III and IV ($2 \times K_I$) and 1.25×10^{-5} m/s for stage V ($2.5 \times K_I$).

PHREEQC-2 can simulate diffusive/dispersive transport by defining the hydrodynamic dispersion coefficient, D_L (m^2/s), that relates the effective diffusion coefficient, D_e (m^2/s), the velocity of the fluid, v (m/s), and the dispersivity of the porous media, α_L (m): $D_L = D_e + v\alpha_L$.[22] In the absence of sample-specific data, we assumed that dispersivity approaches 1/10th of the travel distance ($\alpha_L = 7.5 \times 10^{-3}$ m). Similarly, D_e is related to the molecular diffusion coefficient in free water, D_β by the relationship $D_e = D_f \varepsilon^m$, where ε represents porosity and m the Archie's law cementation exponent. Assuming m equal to 1.64[23] and for an average value of D_f of 10^{-9} m^2/s,[22] D_e becomes equal to 1.4×10^{-11} m^2/s. The value of the diffusion coefficient and dispersivity were kept constant for all the modeling stages.

The chemical composition of the boundary injectates were determined from chemical analysis and the theoretical considerations outlined before. The model considered the presence of certain minerals: Mg-calcite, halite, sylvite, barite, amorphous silica, and kaolinite. These solids were assumed to be present in the rock at the beginning of the experiment, and they were modeled considering far from equilibrium kinetic rate laws, R_k. According to published overall kinetic rates,[21,22,24] R_k can be modeled using the transition-state theory derived expression:

$$R_i = \pm r_i \frac{A_0}{V}\left(\frac{m_i}{m_{0i}}\right)^n \left[1 - \left(\frac{\mathrm{IAP}}{K_{\mathrm{sp},i}}\right)^\sigma\right]$$

where r_i represents the specific rate (positive for dissolution and negative for precipitation) of solid i (mol m^{-2} s^{-1}), A_0 its initial surface area (m^2), V the pore volume (m^3), m_{0i} the initial mass of solid i (mol), m_i the mass of solid i present at a given time (mol), n a shape factor (0.67 for spherical particles), and σ the stoichiometric factor of the kinetic reaction. $\mathrm{IAP}/K_{\mathrm{sp},i}$ accounts for the saturation ratio of the solid i.

PHREEQC-2 incorporates a flexible scheme to help the inclusion of different formulations for the specific rates of minerals and other substances. In the case of halite, sylvite (assumed equal to halite), barite, amorphous silica, and kaolinite we used the parameters and sources reported in the literature,[25] which are applicable to the following expression:

$$r_i = k_{25}^{\mathrm{nu}} \exp\left[\frac{-E_a^{\mathrm{nu}}}{R}\left(\frac{1}{T} - \frac{1}{298.15}\right)\right] + k_{25}^{\mathrm{ac}} \exp\left[\frac{-E_a^{\mathrm{ac}}}{R}\left(\frac{1}{T} - \frac{1}{298.15}\right)\right] a_{H^+}^{n_{\mathrm{ac}}} + k_{25}^{\mathrm{ba}} \exp\left[\frac{-E_a^{\mathrm{ba}}}{R}\left(\frac{1}{T} - \frac{1}{298.15}\right)\right] a_{H^+}^{n_{\mathrm{ba}}}$$

R represents the universal gas constant (8.314 J mol^{-1} K^{-1}), T the absolute temperature (K), k_{25} the rate constant of the substance at 25 °C (mol m^{-2} s^{-1}), E_a the activation energy (kJ mol^{-1}), a_{H^+} the activity of the hydrogen ion, and n an exponential factor. The acronyms nu, ac, and ba account for the eventual acid, neutral, and base dissolution/precipitation mechanisms. Because no information was available on the reactive surface area of the minerals in the sample, their values were calibrated in the model.

The model included ion exchange processes to evaluate competitive proton exchange in clay minerals triggered by the flooding with the acidic fluid.[26]

3. RESULTS AND DISCUSSION

The low-flow conditions reproduced in the experiment (~0.4 m/day) can be representative of the circumstances prevailing in the bulk sandstone reservoir, at some distance of the injection point.

No significant physical or mineralogical differences were found in the sample before and after the experiment. However, a noticeable change in the hydrodynamic and acoustic properties took place as well as discernible patterns in the evolution of the outlet fluid. Figure 2A illustrates the evolution of permeability. We see that from 0 to 20 PV, permeability first rises (0.022 to 0.032 mD) and, after ~60 PV (~10 days), drops again to the initial value. From hereafter permeability displays a

dx.doi.org/10.1021/es3012222 | Environ. Sci. Technol. 2013, 47, 159−167

SEM images illustrate that microcracks are mainly open structures, with lengths shorter than ~100 μm, many of them not fully crossing grains (Figure 1G) and with orientations roughly parallel to σ_1. From the inversion of our velocity data, assuming a simplified crack model (isotropically distributed penny-shaped, noninterfering cracks), it is possible to compute the theoretical dimensionless crack density number.[31,32] At the end of the experiment this number had a value of about 0.07, which, considering the sample volume (85.89 cm^3) and a hypothetical maximum crack length of 100 μm, would correspond to ~5 × 10^4 cracks (<1 crack/mm^3).

Figure 2B,C shows the evolution of pH and specific conductance (SC) of the outlet solution. Due to the microelectrode problems described earlier, it was not possible to obtain a continuous record and, when the measurements were possible, the data displayed a significant dispersion. In order to gain clarity in the presentation, data was smoothed to mean daily values while the 5−95th percentile rank of the corresponding period was set as a description of dispersion.

pH corresponding to the DIW flooding is not available. For the CO_2-saturated flooding, pH first decreased and later stabilized to a value slightly above 5. This value is significantly higher than the theoretically expected ~3.1. Moreover, model results indicate that, after a certain time, the pH of the outlet fluid is expected to be acidic. The apparent inconsistency between the model and observations can be reconciled if we take into account that the pH measured corresponds to a previously degassed fluid, a phenomenon which is known to raise pH. On the basis of widely accepted EOS[18,19] and the protolysis constants of relevant species for the aqueous carbon system[33−35] and water,[36,37] we can compute that the pH change when dropping from 4 MPa to atmospheric pressure is ~1.8 units. Once this correction is performed, model and observations, within the range of uncertainty, become consistent. CO_2 degassing may also trigger the precipitation of carbonates. Although mineral precipitates were not observed in the water collecting reservoir, it is hard to confirm whether carbonate scaling occurred or not in the tubes following fluid decompression. Model results show that the highest saturation index attained by calcite during the flooding was slightly higher than −4 and its correction to account for the P_{CO2} drop still results in water undersaturated with respect to calcite so that its precipitation is not to be expected.

SC values clearly identify phases I and II of the experiment. Provided that relevant data is included in the working database, PHREEQC-2 is able to compute the SC of polyelectrolyte aqueous solutions based on the concentration, activity coefficient, and diffusion coefficient of the species present. Figure 2C shows that model results are reasonably consistent during the first and beginning of the second flooding phases and that a much better agreement can be obtained when taking into account CO_2 degassing by stripping the relevant carbon species from the SC calculation. However, the SC measured after ~100 PV is not consistent with the model either, considering or not degassing. In fact, the experimental conductance values are exceedingly low to what is expected from the analytical concentrations. Consequently, we suspect that the electrode did not work properly, probably due to the persistence of gas bubbles inside it.

Figures 3 and 4 illustrate the evolution of some chemical constituents in the outlet water, and we observe that their concentrations are higher than in the flooding water, suggesting that dissolution is a key geochemical process. Model results

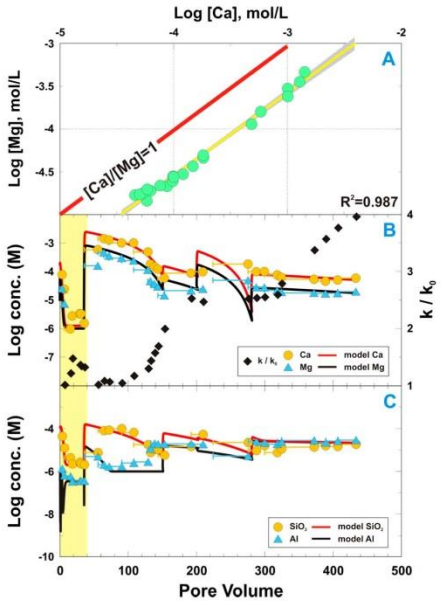

Figure 4. Ca/Mg relationship (A) and experimental data (symbols) corresponding to the concentrations of Ca and Mg (B) and Al and SiO_2 (C) compared with model results (lines). Horizontal error bars correspond to the PV range associated with each discrete analysis. The light yellow rectangle identifies phase I of the experiment (injection of DIW).

indicate that all the mineral phases considered (either present or potentially precipitating) remained undersaturated throughout the entire experiment. In agreement with what has been observed elsewhere,[5,9,38] the acidic flooding promotes the mobilization of certain minor and trace elements (F, P, and Ba among the ones analyzed).

Figure 3A illustrates the evolution of Na and Cl. At the beginning of the experiment, water attained its highest concentration, dropping fast then in less than 10 PV. This is the likely result of the washout of a tiny amount of Na−K−Cl salt precipitates (confirmed with SEM; Figure 1E) initially present in the sample. The origin of these salts may not be geological but related with the oven-drying of the sample prior to the test. Taking halite and sylvite as model minerals and assuming that the measured concentrations result from their dissolution, it is possible to perform a mass balance based on the model or the experimental results (Table S2; Supporting Information) . In either case, the mass required is ~0.78 and ~0.75 mg of halite and sylvite, respectively. After this initial washout period, the concentrations of Na and Cl become steady and consistent with the chemical composition of the flooding water.

Figure 3B shows the evolution of potassium and, in contrast to what happens with Na and Cl, there is a noticeable rise in its concentration when the CO_2-saturated water is injected. Potassium attains its peak concentration after ~60 PV,

dx.doi.org/10.1021/es3012222 | Environ. Sci. Technol. 2013, 47, 159−167

dropping to a nearly steady concentration after ~150 PV. According to the mineralogy present in the rock, K-bearing phases are scarce, and their contribution is not sufficient to explain the observed trend. It is well-known that kaolinite has a moderate cation exchange capacity (CEC). It is also known that, under acidic conditions, protons may compete with the monovalent cations of the exchange complex in a process described in the literature as hydrolytic exchange.[39] There is no available information on the CEC of the Arcera sandstone or its corresponding selectivity coefficients. These values were calibrated in the model from the experimental data. In a preliminary approach, we chose a simple one-site model to simulate the exchange reactions taking place in a hypothetical surface representing kaolinite between K and H^+. According to the PHREEQC-2 formalism,[21] exchange half-reactions were added to the definition of the problem. An acceptable match to the experimental data can be obtained when considering 0.05 equiv of exchange sites per liter of PV and a selectivity constant for the H^+/K^+ exchange equal to 0.5. According to the characteristics of the sample (~5 vol % kaolinite; ~7.3% porosity; 79.58 cm^3 solid volume), this value equates to a CEC of ~0.03 equiv/kg, which is consistent with the typical range attributed to kaolinite: 0.02−0.15 equiv/kg.[40] Therefore, H^+/K^+ exchange is a plausible candidate to explain the evolution of potassium in the experiment. Although other cations could be involved in the ion exchange process (Ca, Mg, Na, ...), attempts made to reproduce the experimental trends considering a variety of selectivity coefficients were unsuccessful. In turn, it has been possible to model reasonably well the behavior of these cations without the concourse of ion exchange.

Figure 3C displays the experimental concentrations of SO_4 and Ba in the outlet water. Following the initial washout, the concentrations of both components steeply rise (in the case of SO_4 from below the detection limit) when the sample is flooded with the CO_2-saturated water. The similarity in the evolution of both components suggests a common mineral source, which is conjectured to be barite. Mass balances based on the measured concentrations of SO_4 and Ba are in excellent agreement with the model, and both indicate that ~0.22 mg of barite would have been dissolved.

There is a good correlation between the concentrations of Ca and Mg in the outlet fluid (Figure 4A), suggesting a common mineral source (Mg-calcite) and a codissolution process. Assuming that the dissolution is congruent, the theoretical stoichiometry of the carbonate would be $Ca_{0.78}Mg_{0.22}CO_3$. Following the washout stage, the evolution of these two components describes a distinct sawtooth pattern (Figure 4B) which is different to what has been described so far. In a first step there is a sharp increase in the concentrations which is attributed to the arrival of the acidic fluid. After a short steady period, they go slowly down up to ~150 PV. Visual inspection of the remaining part of the experiment allows us to identify two to three additional steps, although the relative change in concentration is small compared with that previously described. The origin of the stepped pattern is not clear, although we speculate that it could be related to the access of fluid to the new reactive surface in connection with (a) microcracking, (b) the dissolution of material containing carbonates, or (c) changes in the flow path induced by the evolving pore connectivities.

In order to model the dissolution of Mg-calcite, we applied the stoichiometric saturation concept[24] while the solubility product and the kinetic dissolution rate were obtained from published data[21,41,42] (see Table S3; Supporting Information). The experimental mass balance indicates that the amount of carbonate dissolved was ~0.10 g while the model points toward a slightly higher, but still consistent, value of ~0.14 g. Assuming that all the inorganic carbon present in the rock (0.18 wt %) is in the form of carbonates, the mass initially available (scaled to the plug size) was ~3 g. Therefore, only ~4% of the total carbonate would have reacted. That would mean that only those carbonate grains more easily accessible to the flooding fluid (i.e., the ones located in pores within the main flow paths) would have been dissolved, while those isolated (inside less soluble phases) or located in dead ends would not have.

Figure 4C presents the concentration of aqueous SiO_2 and Al. We observe the same general sawtooth features described for Ca and Mg, and we speculate similar origins. The reactive transport model provides a reasonably good match to the observations using amorphous silica and kaolinite as constraining minerals. The model predicts the cumulative dissolution of ~3.8 mg of amorphous silica and ~5.5 mg of kaolinite.

If we add all the volumes associated with the minerals dissolved, we see that the porosity change is very small (~0.77%). This value becomes slightly larger (~0.85%) when we include the extra PV associated to cracks (5×10^{-4} to 5×10^{-3} cm^3, computed for a total of 5×10^4 penny-shaped cracks, 50 μm radius, 1−10 μm aperture). It is worth remarking that a small porosity change connects with a large hydrodynamic impact. To this respect, other authors[43] have observed similar effects in the siliceous Fontainebleau sandstone when flooded with a reactive alkaline fluid: Samples with porosities similar to ours (5.1−8.9%) but with higher permeability (0.27−0.57 mD) increase it by a factor of two to three while porosity only changes by 1.2−1.4%. According to them, this phenomenon would be linked to the concentrated dissolution of minerals in pore throat locations, where a minimum modification of the pore space will lead to a major impact over transport properties.

With the exception of certain trace minerals, the relatively simple mineralogy of the Arcera sandstone makes it possible for the model to be relatively successful in reproducing the experimental trends. For the investigated conditions, the sandstone from Hontomín does not experience significant damage, although this needs to be contrasted with new experiments under true reservoir conditions using the brackish fluid expected in situ.

■ ASSOCIATED CONTENT

Supporting Information

Location map (Figure S1), stratigraphic column (Figure S2), pore size distribution (Figures S3 and S4), experimental rig (Figure S5), timeline and flow evolution (Figure S6), model parameters (Table S1), experimental results (Table S2), and kinetic constants (Table S3). Workbook for calculation of activity coefficient and related properties of CO_2. This material is available free of charge via the Internet at http://pubs.acs.org

■ AUTHOR INFORMATION

Corresponding Author

*E-mail: jdelgado@udc.es. Phone: +34(0) 981167000. Fax: +34(0)981167170.

Notes

The authors declare no competing financial interest.

■ ACKNOWLEDGMENTS

This project has been partly funded by the Spanish Ministry of Industry, Tourism and Trade, through a CIUDEN-GEAMA contract, Xunta de Galicia (10REM003CT), and the European Regional Development Funds 2007/2013. OXYCFB300 is cofinanced by the EU Energy Programme for Recovery. The sole responsibility of this publication lies with the authors. The EU is not responsible for any use that may be made of the information contained therein. Special thanks are also given to A. Vázquez, S. Fernández, SAI-UDC, and three anonymous reviewers.

■ REFERENCES

(1) Official Journal of the European Union Directive 2009/31/EC of the European Parliament and the Council of 23 April 2009 on the geological storage of carbon dioxide and amending Council Directive 85/337/EEC, European Parliament and Council Directives 2000/60/EC, 2001/80/EC, 2004/35/EC, 2006/12/EC, 2008/1/EC and Regulation (EC) No 1013/2006. June 5, 2009. http://eur-lex.europa.eu/LexUriServ/LexUriServ.do?uri=OJ:L:2009:140:0114:0135:EN:PDF (accessed July, 2012).

(2) Implementation of Directive 2009/31/EC on the Geological Storage of Carbon Dioxide; Guidance Document 2; Characterisation of the Storage Complex, CO_2 Stream Composition, Monitoring and Corrective Measures. European Commission: Brussels, Belgium, 2011. http://ec.europa.eu/clima/policies/lowcarbon/ccs/implementation/docs/gd2_en.pdf (accessed July, 2012).

(3) Lupión, M.; Navarrete, B.; Otero, P.; Cortés, V. J. Experimental programme in CIUDEN's CO_2 capture technology development plant for power generation. *Chem. Eng. Res. Des.* **2011**, *89*, 1494−1500, DOI: 10.1016/j.cherd.2010.10.017.

(4) Gaus, I. Role and impact of CO_2−rock interactions during CO_2 storage in sedimentary rocks. *Int. J. Greenhouse Gas Control* **2010**, *4*, 73−89, DOI: 10.1016/j.ijggc.2009.09.015.

(5) Bowker, K.; Shuler, P. J. Carbon dioxide injection and resultant alteration of the Weber sandstone, Rangely Field, Colorado. *AAPG Bull.* **1991**, *75*, 1489−1499.

(6) Luquot, L.; Andreani, M.; Gouze, P.; Camps, P. CO_2 percolation experiment through chlorite/zeolite-rich sandstone (Pretty Hill Formation − Otway Basin − Australia). *Chem. Geol.* **2012**, *294*−*295*, 75−88, DOI: 10.1016/j.chemgeo.2011.11.018.

(7) Hangx, S. J. T.; Spiers, C. J.; Peach, C. J. Creep of simulated reservoir sands and coupled chemical-mechanical effects of CO_2 injection. *J. Geophys. Res.* **2010**, *115*, B09205 DOI: 10.1029/2009JB006939.

(8) Le Guen, Y.; Hellmann, R.; Collombet, M.; Gratier, J. P. Enhanced deformation of limestone and sandstone in the presence of high PCO_2 fluids. *J. Geophys. Res.* **2007**, *112*, B05421 DOI: 10.1029/2006JB004637.

(9) Wigand, M.; Carey, J. W.; Schütt, H.; Spangenberg, E.; Erzinger, J. Geochemical effects of CO_2 sequestration in sandstones under simulated in situ conditions of deep saline aquifers. *Appl. Geochem.* **2008**, 2735−2745, DOI: 10.1016/j.apgeochem.2008.06.006.

(10) Zemke, K.; Liebscher, A.; Wandrey, M. CO_2SINKGroup. Petrophysical analysis to investigate the effects of carbon dioxide storage in a subsurface saline aquifer at Ketzin, Germany (CO_2SINK). *Int. J. Greenhouse Gas Control* **2010**, *4*, 990−999, DOI: 10.1016/j.ijggc.2010.04.008.

(11) Beroiz, C.; Permanyer, A. Hydrocarbon habitat of the Sedano trough, Basque-Cantabrian Basin, Spain. *J. Pet. Geol.* **2011**, *34*, 387−410, DOI: 10.1111/j.1747-5457.2011.00511.x.

(12) Franklin, J. A. Suggested methods for determining the strength of rock materials in triaxial compression. *Int. J. Rock Mech. Min. Sci.* **1983**, *20*, 285−290.

(13) Herrmann, W.; Berry, R. F. MINSQ − a least squares spreadsheet method for calculating mineral proportions from whole rock major element analyses. *Geochem.: Explor., Environ., Anal.* **2002**, 2, 361−368, DOI: 10.1144/1467-787302-010.

(14) Hoek, E.; Franklin, J. A. A simple triaxial cell for field and laboratory testing of rock. *Trans. - Inst. Min. Metall.* **1968**, *77*, A22−26.

(15) Rummel, F.; Van Heerden, W. L. Suggested methods for determining sound velocity. *Int. J. Rock Mech. Min. Sci.* **1978**, *15*, 53−58.

(16) Diamond, L.; Akinfiev, N. A. Solubility of CO_2 in water from −1.5 to 100 °C and from 0.1 to 100 MPa: evaluation of literature data and thermodynamic modelling. *Fluid Phase Equilibr.* **2003**, *208*, 265−290, DOI: 10.1016/S0378-3812(03)00041-4.

(17) Farajzadeh, R.; Zitha, P. L. J.; Bruining, J. Enhanced mass transfer of CO_2 into water: Experiment and modeling. *Ind. Eng. Chem. Res.* **2009**, *48*, 6423−6431, DOI: 10.1021/ie801521u.

(18) Duan, Z. Y.; Sun, R. An improved model calculating CO_2 solubility in pure water and aqueous NaCl solutions from 273 to 533 K and from 0 to 2000 bar. *Chem. Geol.* **2004**, *193*, 257−271, DOI: 10.1016/S0009-2541(02)00263-2.

(19) Duan, Z.; Sun, R.; Zhu, C.; Chou, I. M. An improved model for the calculation of CO_2 solubility in aqueous solutions containing Na^+,K^+,Ca^{+2},Mg^{+2},Cl^- and SO_4^{-2}. *Mar. Chem.* **2006**, *98*, 131−139, DOI: 10.1016/j.marchem.2005.09.001.

(20) Luquot, L.; Gouze, P. Experimental determination of porosity and permeability changes induced by injection of CO_2 into carbonate rocks. *Chem. Geol.* **2009**, *265*, 148−159, DOI: 10.1016/j.chemgeo.2009.03.028.

(21) Parkhurst, D. L.; Appelo, C. A. J. *User's guide to PHREEQC*, Version 2; U.S. Geological Survey Water Resources Investigation Report 99-4259; U.S. Department of Interior: Denver, USA, 1999; p 312.

(22) Appelo, C. A. J.; Postma, D. *Geochemistry, Groundwater and Pollution*, 2nd ed.; A.A. Balkema Publishers: Amsterdam, The Netherlands, 2005; p 649.

(23) Adler, P. M.; Jacquin, C. G.; Thovert, J. F. The formation factor of reconstructed porous media. *Water Resour. Res.* **1992**, *28*, 1571−1576, DOI: 10.1029/92WR00059.

(24) Appelo, C. A. J.; Verweij, E.; Schäfer, H. A hydrogeochemical transport model for an oxidation experiment with pyrite/calcite/exchangers/organic matter containing sand. *Appl. Geochem.* **1998**, *13*, 257−268, DOI: 10.1016/S0883-2927(97)00070-X.

(25) Palandri, J. L.; Kharaka, Y. *A compilation of rate parameters of water-mineral interaction kinetics for application to geochemical modeling*; U.S. Geological Survey Open-File Report 2004-1068; U.S. Department of Interior: Menlo Park, USA, 2004; p 64.

(26) Heidmann, I.; Christl, I.; Leu, C.; Kretzschmar, R. Competitive sorption of protons and metal cations onto kaolinite: experiments and modeling. *J. Colloid Interface Sci.* **2005**, *282*, 270−282, DOI: 10.1016/j.jcis.2004.08.019.

(27) Guéguen, Y.; Fortin, J.; Schubnel, A. Cracks in porous rocks: Tiny defects strong effects. *The Leading Edge* **2009**, *28*, 40−47, DOI: 10.1190/1.3064145.

(28) Fortin, J.; Guéguen, Y.; Schubnel, A. Effects of pore collapse and grain crushing on ultrasonic velocities and V_p/V_s. *J. Geophys. Res.* **2007**, *112*, B08207 DOI: 10.1029/2005JB004005.

(29) Zoback, M. D.; Byerlee, J. D. The effect of microcrack dilatancy on the permeability of Westerly granite. *J. Geophys. Res.* **1975**, *80*, 752−755, DOI: 10.1029/JB080i005p00752.

(30) Hangx, S. J. T.; Spiers, C. J.; Peach, C. J. Creep of simulated reservoir sands and coupled chemical-mechanical effects of CO_2 injection. *J. Geophys. Res.* **2010**, *115*, B09205 DOI: 10.1029/2009JB006939.

(31) Ougier-Simonin, A.; Fortin, J.; Guéguen, Y.; Schubnel, A. Cracks in glass under triaxial conditions. *Int. J. Eng. Sci.* **2010**, *49*, 105−121, DOI: 10.1016/j.ijengsci.2010.06.026.

(32) Stanchits, S.; Vinciguerra, S.; Dresen, G. Ultrasonic velocities, acoustic emission characteristics and crack damage of basalt and granite. *Pure Appl. Geophys.* **2006**, *163*, 974−993, DOI: 10.1007/s00024-006-0059-5.

(33) Harned, H.; Davis, R. The ionization constant of carbonic acid in water and the solubility of carbon dioxide in water and aqueous salt solutions from 0 to 50°. *J. Am. Chem. Soc.* **1943**, *65*, 2030−2037, DOI: 10.1021/ja01250a059.
(34) Harned, H.; Scholes, S. The ionization constant of HCO_3^- from 0 to 50°. *J. Am. Chem. Soc. J.* **1941**, *63*, 1706−1709.
(35) Li, D.; Duan, Z. The speciation equilibrium coupling with phase equilibrium in the H_2O-CO_2-NaCl system from 0 to 250 °C, from 0 to 1000 bar and from 0 to 5 molality of NaCl. *Chem. Geol.* **2007**, *244*, 730−751, DOI: 10.1016/j.chemgeo.2007.07.023.
(36) Dickson, A. G.; Riley, J. P. The estimation of acid dissociation constants in seawater media from potentiometric titrations with strong base. I. The ionic product of water - K_w. *Mar. Chem* **1979**, *7*, 89−99, DOI: 10.1016/0304-4203(79)90001-X.
(37) Marshall, W. L.; Franck, E. U. Ion product of water substance, 0−10,000 °C, 1−10,000 bar new international formulation and its background. *J. Phys. Chem. Ref. Data* **1981**, *10*, 295−304, DOI: 10.1063/1.555643.
(38) Kharaka, Y. K.; Cole, D. R.; Hovorka, S. D.; Gunter, W. D.; Knauss, K. G.; Freifeld, B. M. Gas-water-rock interactions in Frio Formation following CO_2 injection: Implications for the storage of greenhouse gases in sedimentary basins. *Geology* **2006**, *34*, 577−580, DOI: 10.1130/G22357.1.
(39) McBride, M. B. *Environmental Chemistry of Soils*; Oxford University Press: New York, USA, 1994; p 416.
(40) Sposito, G. *The Surface Chemistry of Soils*; Oxford University Press: New York, USA, 1984; p 234.
(41) Morse, J. W.; MacKenzie, F. T. *Geochemistry of Sedimentary Carbonates*; Elsevier: Amsterdam, The Netherlands, 1990; p 707.
(42) Plummer, L. N.; Wigley, T. M. L.; Parkhurst, D. L. The kinetics of calcite dissolution in CO_2-water systems at 5 to 60 °C and 0.0 to 1.0 atm CO_2. *Am. J. Sci.* **1978**, *278*, 179−216(43).
(43) Jové-Colón, C. F.; Oelkers, E. H.; Schott, J. Experimental investigation of the effect of dissolution on sandstone permeability, porosity, and reactive surface area. *Geochim. Cosmochim. Acta* **2004**, 805−817, DOI: 10.1016/j.gca.2003.06.002.

macla nº 17. junio '13
revista de la sociedad española de mineralogía

Mineralogy, Geochemistry, Petrophysics and Rock Mechanics of the Corvio Sandstone

/ JACOBO CANAL VILA (1), ISMAEL FALCÓN SUÁREZ (2), VICTOR BARRIENTOS RODRÍGUEZ (2), JORDI DELGADO MARTÍN (2,*)

(1) Fundación Ciudad de la Energía. Avenida Presidente Rodríguez Zapatero s/n. 24492, Cubillos de Sil, León (Spain)
(2) Civil Engineering School. Campus de Elviña s/n. University of a Coruña. 15192, A Coruña (Spain)

INTRODUCTION.

It is well known that the injection of reactive fluids, like CO_2, into geological formations trigger a series of interlinked phenomena (thermo- hydro- chemo-mechanical or THCM) that affect the properties of the reservoir, its seal or even the cementitious materials used in wellbores. Because water is always present in the porous space of these systems, the forced injection of CO_2 (either as gas, liquid or supercritical fluid) induces a significant acidification and the onset of reactive processes which are especially notorious when carbonate or carbonate-bearing rocks are present. The co-injection of subordinated gasses accompanying CO_2 (O_2, SO_2...) might exacerbate this reactivity due to the oxidation of reduced mineral phases already present in the rocks or by promoting an enhanced acidity associated to S-bearing gasses.

Petrophysics and rock mechanics provide with invaluable toolbox with which to assess key rock properties and to elaborate integrated reservoir models. However, in their classical use they do not acknowledge the crucial importance of the THCM couplings which are inherent, however, to reactive systems.

Core-flooding experiments performed at P-T conditions akin to those *in situ* have a great potential in helping us to unravel complex THCM processes provided that it is feasible the separation of each of their corresponding contributions. To this respect, in the present study we focus on the comprehensive characterization of a reference rock material with a dual purpose: First, as a necessary first step before proceeding with more complex experimental protocols like reactive fluid injection; second, to evaluate the adequacy of this material as laboratory standard for petrophysical and rock mechanics studies.

MATERIALS AND METHODS.

The studied material has the trade name of Corvio Sandstone®. Geologically speaking, this material defines the Corvio Mb which appears as a 20 m thick lithosome at the top section of the Frontada Fm (Campoó Gr; Lower Cretaceous). It is made of siliceous sandstones and conglomerates associated with braided fluvial channels showing dm to m trough-type cross bedding (Hernández el al., 1999).

Four blocks of the Corvio Sandstone (0.3x0.2x0.5 m each; Fig. 1) were used to obtain a total of 228 cylindrical plugs of 38.1 and 50 mm diameter. Additional irregular samples were selected in order to apply a number of physico-chemical characterization techniques: FRX (Bruker-AXS S4 Pionner), ATD-TG-FTIR (TA Inst. SDT 2690 coupled to Bruker Vector 22), DRX (Siemens D5000), CHNS (ThermoFinnigan FlashEA1112), BET (Micromeritics Gemini VII 2390a), SEM-EDS (JEOL JSM-6400), petrography, He pycnometry (Quantachrome Ultrapyc 1200e), Hg porosimetry (Quantachrome Poremaster-60). With respect the mechanical, petrophysical and hydrodynamic properties our assessment included the measurement of the indirect tensile (Brazilian), unconfined and confined (triaxial) strengths (MTS 815), P- and S- wave velocities, water and gas (N_2) permeability, immersion porosity and dry density. Based on the previous data the static and dynamic elastic moduli, as well as the critical stress states (Hakala et al., 2007) where computed. The characterization of the Corvio Sandstone was complemented with an X-Ray μCT-scan (XRadia MicroXCT-300).

On a general basis, 10 samples were used to assess the statistical significance of the properties determined.

fig 1. Rock blocks of the Corvio Sandstone after core plug extraction.

RESULTS.

Corvio Sandstone can be classified as a grain-supported quartzarenite with microcrystalline silica cement. The main mineral constituents are quartz (~94 wt. %) with subordinated kaolinite (~3.5 wt. %) and K-feldspar (~1.7 wt. %). Trace amounts of ilmenite (~0.2 wt. %) have been observed in the μCT scans while ~0.5 wt. % of carbonates is inferred from the ATD-TG-FTIR. Quartz grains are typically sub-rounded, well sorted and their average grain size hovers around 0.15-0.3 mm. In the studied samples fossils are reduced to scarce cm-size spots with remnants of tree debris (*cf.* Hernández *et al.*, 2009). Based on ATD-TG-FTIR, the weight % of hydrated minerals is ~0.5 while C, N and S-compounds are below 0.05 wt. %. The average BET specific surface is 1.09±0.07 m^2/g (n=12) while porosity and dry density are 14.45% (n=224) and 2037 kg/m^3 (n=227). Hg porosimetry shows that pore size spans from 2.5 to

palabras clave: Arenisca de Corvio, permeabilidad, resistencia, petrofísica, velocidad de ondas P y S

key words: Corvio sandstone, permeability, strength, petrophysics, P- and S- wave velocities

* corresponding author: jdelgado@udc.es

macla nº 17. junio '13
revista de la sociedad española de mineralogía

100 μm while the median is ~20 μm. μCT-scan data shows that although pores tend to have an equant-shape some of them may be compliant upon load. This observation is supported by the stress-strain curves obtained.

Strength and Stress-Strain Behavior.

Geomechanical tests were performed on 50 mm diameter cylindrical plugs prepared to meet the recommendations of the International Society for Rock Mechanics. In the case of the unconfined compression strength (UCS) and triaxial tests, the axial strain was recorded with a dual-averaging, knife-edge type, extensometer while the lateral strain was measured with the aid of a circumferential, chain-type, gage.

The mean tensile strength of the Corvio Sandstone is 2.3±0.14 MPa (n=11) while UCS is 41.3±1.0 MPa (n=10). These data were combined with the results obtained in additional drained triaxial tests performed at 5, 10, 30 and 50 MPa which were needed to obtain the full strength envelope (Fig. 2). This was computed following the intact rock Hoek and Brown (1980) criterion (HB), as updated by Hoek *et al.* (2002). Assuming that the parameters s and a of the HB model are equal to 1 and 0.5, respectively, m_b is 15.0. Similarly, application of the linear Mohr-Coulomb criterion provides with an apparent cohesion (c) of ~20 MPa and a friction angle (ϕ) of 28.5º.

Taking into account the stress-strain behavior observed in the UCS tests, the static Young modulus (E) and Poisson ratio (ν) of the Corvio Sandstone are 11.41±0.35 GPa and 0.38±0.01, respectively. In addition, based on the computed volumetric strain and the method discussed by Nicksiar and Martin (2012), the crack initiation and crack damage stresses occur at 6.2±0.2 and 26.0±0.8 MPa, respectively.

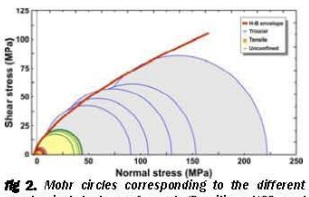

fig 2. *Mohr circles corresponding to the different mechanical tests performed (Brazilian, UCS and triaxial) with the Corvio Sandstone. The computed Hoek-Brown strength envelope computed from these tests is also shown.*

Ultrasonic P- and S- Wave Velocities.

P- and S- wave velocities were measured by applying the time-of-flight technique to cylindrical, 38.1 mm diameter plugs submitted to unconfined conditions and a small load (3 MPa) to improve the sample/transducer contact. A pair of stacked P-S_1-S_2 1.3 MHz transducers (ErgoTech) was located at the bottom (emitter) and top (receiver) of the plug. In order to check the anisotropy of the rock, 3 plugs cored in orthogonal directions were also extracted: one normal to bedding (Z) and two parallel to bedding (X and Y). Each one of these plugs was stepwise rotated (20º increment).

The average P- and S- velocity in the Y-Z directions are 3.32 and 1.72 km/s, respectively. However the velocities obtained in the X direction are smaller (2.99 and 1.53 km/s). These low values suggest that porosity is not equally distributed (larger in the X-direction) , what could obey to local changes in the cross bedding sets sampled by the X and Y plugs. The dynamic Young modulus and Poisson ratio computed from the previous velocities are 15.90±0.06 GPa and 0.316±0.001 (Y-Z directions) and 12.55±0.11 GPa and 0.323±0.002 (X direction). Static moduli, as expected, are lower than the dynamic ones because the latter only captures the elastic response of the rock under low stress conditions.

Hydraulic Conductivity.

The hydraulic conductivity of the Corvio Sandstone was tested in three 38.1 mm plugs sampled in the previously described orthogonal directions. The tests were conducted in a Hassler-type core holder (Temco THC) at different confining pressures (up to 30 MPa; fig. 3) and room T. In the tests, deaireated tap water was injected (Quizix SP-5400 syringe pump) at a constant P while flow was measured at the outlet of the plug at 0.1 MPa. P and flow was carefully recorded with the Quizix system. Attainment of the steady flow condition while keeping injection P constant makes possible the computation of hydraulic conductivity based on Darcy's Law. Results show that the plug sampled in the X-direction shows higher conductivity han in the other directions, which give similar results. This is consistent with the observations made with P- and S- wave velocities. Significant hysteresis is observed when

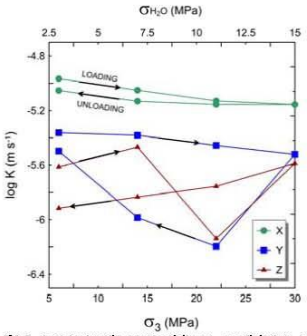

fig 3. *Log hydraulic conductivity vs. confining (σ_3) and pore (σ_{H2O}) pressures of three Corvio Sandstone plugs sampled in orthogonal directions: X and Y parallel to bedding and Z at right angle.*

considering loading/unloading stress paths, with lower conductivities in the unloading branch. Hysteresis is higher in the Y and Z directions. This behavior can be explained by the irreversible compaction of the samples.

ACKNOWLEDGEMENTS.

Some of the determinations were performed at the esCO_2-CIUDEN facilities and the Colorado School of Mines. Assistance and advice of Drs. T. Kovacs and M. Batzle are kindly acknowledged. Funds for this work have been provided by the XUGA Project 10REM003CT and the European Regional Development Funds 2007/2013

REFERENCES.

Hakala, M., Kuula, H., Hudson, J.A. (2007): Estimating the transversely isotropic elastic intact rock properties for in situ stress measurement data reduction: A case study of the Olkilouto mica gneiss, Finland. Int. J. Rock. Mech. Min. Sci., ***44****, 14-46.*

Hernández, J.M., Pujalte, V., Robles, S., Martín-Closas, C. (1999): División estratigráfica genética del Grupo Campóo (Malm-Cretácico Inferior, SW Cuenca Vascocantábrica). Rev. Soc. Geol. España, ***12****, 377-396.*

Hoek, E., Brown, E.T. (1980): Underground Excavations in Rock. The Institute of Mining and Metallurgy. London, 527 p.

Hoek, E., Carranza-Torres, C., Corkum, B. (2002): Hoek-Brown criterion–2002 edition. Proc. NARMS-TAC Conference, Toronto, 267-273.

Nicksiar, M., Martin, C.D. (2012): Evaluation of methods for determining crack initiation in compression tests of low porosity rocks. Rock Mech. Rock. Eng., ***45****, 607-617*

Rock Engineering and Rock Mechanics: Structures in and on Rock Masses – Alejano, Perucho, Olalla & Jiménez (Eds)
© 2014 Taylor & Francis Group, London, 978-1-138-00149-7

Laboratory simulation of CO_2 injection in sandstones and sands for improved seismic monitoring of CO_2 reservoirs

I. Falcón-Suarez, L. North, A. Best & J. Sothcott
National Oceanography Centre, University of Southampton Waterfront Campus, Southampton, UK

J. Canal-Vila & J. Delgado-Martín
Civil Engineering School, University of A Coruña, A Coruña, Spain

ABSTRACT: The primary focus of this research is toward determining seismic rock properties (i.e., wave velocities and attenuation) of real and artificial brine-CO_2-bearing sandstone and sand samples that are representative of real CCS scenarios. The measurements require experimental rigs for conducting flooding tests that simulate real Carbon Capture and Store (CCS) conditions. The control of pore fluid, confining pressure, temperature and flow and integrated monitoring tools is essential. Thus we present a protocol for the design and assembly of high pressure experimental rigs for simulating supercritical CO_2 injection, equipped with tools to simultaneously measure seismic, electrical and mechanical properties of the testing samples.

1 INTRODUCTION

Carbon Capture and Storage (CCS) is a worldwide large scale greenhouse gas mitigation technology based on injecting supercritical CO_2 into deep geological formations through boreholes. Monitoring of reservoir rock stability during injection is typically achieved with time-lapse (4D) seismic surveying tools, used to discriminate between fluid pressure and fluid saturation changes. However, the seismic technique is a non-intrusive tool that needs to be calibrated for a given medium to properly interpret results and predict and diagnose reservoir behavior.

The calibration deals with measuring rock properties of CCS scenarios by simulating real reservoir conditions in the laboratory. Typically, triaxial cells hosting small plugs of reservoir rock were pressurized to reach target conditions of confining and pore pressure. The seismic response of the rock can be determined using integrated ultrasonic transducers in pulse-echo mode (Best et al., 2007). Seismic properties depend on the confining and pore pressure but also on the saturation and chemical composition of the pore fluid. The rock is originally gas-, oil- or brine-saturated, so the injection of CO_2 leads to a diverse range of pore fluid compositions between CO_2 and the original fluid. Moreover, mineralogy reactions may occur in the rock as a result of CO_2-brine-rock interactions (CO_2 is a reactive fluid), which would trigger changes in the pore network (Canal et al., 2013) and, consequently, the mechanical and physical properties of the rock would also vary (i.e., Thermo-Hydro-Mechano-Chemical coupled processes).

We intend to perform experiments where we simultaneously control CO_2 saturation of the supercritical pore fluid and rock deformation while monitoring the physical properties. The design of experimental rigs for conducting flooding tests with supercritical CO_2 is far from trivial; accurate control of pore fluid, confining pressure, temperature and flow and integrated monitoring tools are essential. Thus, we present a helpful protocol regarding the design and assembly of high pressure experimental rigs to supercritical CO_2 injection tests, based on existing instrumentation at the University of La Coruña and the National Oceanography Center (NOC), Southampton.

1.1 *Experimental rig*

A schematic diagram of our experimental rig is shown in Figure 1. The core plugs are housed in a triaxial cell that axially and laterally confines them (up to 69 MPa) using a high pressure pumping controller (ISCO). Inside the triaxial cell, the rubber sleeve that isolates the core plug from the confining fluid (ideally mineral oil) is equipped with electrodes for electrical resistivity tomography measurements (ERT). Before being inserted into the core holder strain gauges (350 Ohm) are applied to the sample to accurately measure axial and lateral strains during loading. The ultrasonic pulse-echo instrumentation is able to measure the ultrasonic velocity to a precision of $\pm 0.3\%$ and the ultrasonic attenuation to a precision of ± 0.1 dB/cm. The core plug is isolated from the rest of the rig and the ultrasonic transducer by two acrylic buffer roads. These buffer rods have well defined acoustic impedance and

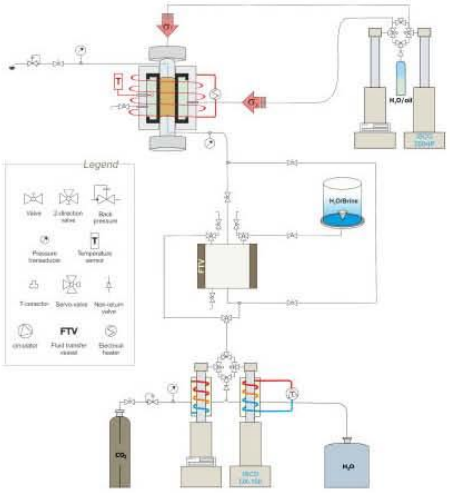

Figure 1. Experimental rig for CCS research.

low loss and provide a delay path to enable the identification of top/base sample reflections for calculating velocity and attenuation. The buffer rods allow pathways (in- and out-let ports) to conduct pore fluid through the sample.

Pore fluid is injected from a fluid transfer vessel (FTV), which acts as an intermediate flow transmitter that isolates the corrosive fluids (brine, brine + CO_2) from the pumping controller, preventing potential damages to the controller. Up- and downstream, two piezoresistivity pressure transducers (0–70 MPa Keller-Druck pressure transmitter) continuously monitor the pore pressure. A pressure regulator closes the hydraulic circuit downstream, guaranteeing to drain the pressurized system when required without drops in the pore pressure.

The system target temperature is maintained using a digitally controlled electrical heating system wrapped around the hydraulic circuit, including the triaxial cell and the FTV.

2 MATERIALS AND METHODS

2.1 *Design of the experimental rig*

Experimental rigs for CCS flooding tests are typically composed of three groups of elements: controllers, data loggers and hydraulic accessories. (1) Controllers provide the means to impose target conditions of temperature, pressure or flow. In our experimental rig (Figure 1), pressure is controlled by an ISCO Teledyne model 100DX pumping pressure controller, while the temperature is imposed by the digital electric heating system and regulated from the information reported by a thermocouple inserted in the triaxial cell. (2) Loggers continuously record data during testing to extract the maximum information from the experiment. We integrate three types of loggers in our rig to simultaneously obtain seismic responses (ultrasonic pulse-echo), stress-strains evolutions (electrical gauges) and electrical resistivity distribution (ERT). Additionally, data from the various pressure transducers used to control the system may also be used to determine hydrodynamic properties of the sample (e.g. permeability). (3) High pressure tubes, valves and other accessories (pressure regulators) complete the hydraulic network that, besides, includes the FTV and triaxial cell core holder.

Before constructing the experimental rig, the hydraulic circuit layout should be carefully planned in order to minimize tube lengths and the use of hydraulic accessories. Hydraulic valves split the hydraulic circuit into sub-reservoirs. We recommend designing the rig as a network of linked reservoirs limited by valves, clustered around a central sub-reservoir (i.e., the triaxial cell).

Our experimental rig presents a central sub-reservoir that isolates the core holder and two pressure transmitters to pore pressure control both up- and down-stream of the sample (upper-left side of Figure 1). This is the central section of the sub-reservoir that connects the FTV with the sample and ends, on the other side (down-stream), with a pressure regulator that allows draining the system at high pressure. The FTV is a sub-reservoir itself where the solution is pressurized before being injected. It is connected to the main source reservoirs (pressure controller; water/brine deposit) by other sub-sections.

2.2 *Experimental setup: The protocol*

The primary focus of the research at the NOC is toward determining seismic rock properties (i.e., elastic wave velocities and attenuation) and electrical resistivity of real and artificial brine-CO_2-bearing sandstone and sand samples, representative of three real CCS scenarios: Sleipner, In-Salah and Snohvit. Samples are 50 mm diameter core plugs while lengths vary from 20 to 30 cm. Once cored, cut and surface ground either from the intact original or artificial samples, the plugs are oven-dried and the electrical gauges pasted on the lateral sides. Then, the plugs are saturated in the original solution of the studied reservoir (brine).

The brine-bearing sample is located in the triaxial cell. Using vacuum pumps, the air within the tubes is extracted and the valves closed to isolate sub-reservoirs. From hereafter, we set a stepwise protocol up to achieve target conditions (i.e., CCS reservoir conditions):

1. Set the target confining pressure by a constant loading ratio (0.5 MPa s^{-1}, ISRM) while recording the stress-strain evolution (gauges) and, besides, seismic and electrical data where possible.
2. Fill the main source reservoirs with CO_2 and water; brine remains within an external reservoir, continuously removing to avoid salt precipitation (i.e.,

compositional changes). Note that we suggest to fill with water the cylinder pressurizing the FTV because it can be also used to clean the circuit after concluding the experiment (see the bypass in the Figure 1); mineral oil is also suitable.

3. Fill the FTV with brine. Set constant flow through the sample to achieve a differential pressure downstream (i.e., tuning the pressure regulator) equal to the target pore pressure of the experiment (e.g. 8 MPa). Keep controlled the volume of drained brine to calculate the remaining FTV by volume difference. When considered appropriate, close the system downstream (we recommend to keep the system draining between 10–20 times the pore volume).
4. Pressurize with CO_2: close the central sub-reservoir and pressurize the FTV from the sub-reservoir of CO_2 (i.e., the ISCO cylinder filled with CO_2, closed at down-stream since the beginning of the test). Notice that the pressure of CO_2 must be higher than that of the original FTV (e.g. 8,5 MPa) to drive the flow in.
5. Open the FTV access and let saturate the initial solution up to the desired level. Keep bearing in mind that the volume of CO_2 dissolved in the brine can be calculated from the back-displacement of the floating cylinder within the FTV (i.e, the received volume in the ISCO cylinder filled with water).
6. Set a flow of CO_2-brine solution through the sample imposing a differential pressure of 0.5 MPa to drive the flow in the direction of the sample (i.e. FTV pressure, 8,5 MPa, minus the pore pressure previously set in the central sub-reservoir, 8 MPa). Let the system drain at down-stream, keeping constant the pressure difference up-stream (fix the regulator position after step 3 to ensure the stability). Once the CO_2-brine solution replaces the original brine in the sample (i.e., brine drainage becomes CO_2-brine), close the system downstream and set the experimental target conditions.

It is worth noting that when working with supercritical CO_2, experimental conditions must be above 7.3 MPa and 31°C. We suggest working above 8 MPa and 38°C to avoid random peaks in the laboratory conditions.

3 CONSIDERATIONS AND EXPECTED RESULTS

3.1 *Stress-strain*

Changes in sample volume associated with the compression lead to variations in the original porosity. Besides, shortness must be corrected to accurately interpret ultrasonic and electrical data (i.e., correction to sample length).

The deformation of the rock can be inferred from Young's modulus and Poisson's coefficient, based on linear approaches of the stress-strain curves. However, far from being linear, stress-strain diagrams commonly show four progressive strain-stages (Lau and Chandler, 2004) according to the inferred damage (Figure 2): initial crack closure (σ_{cc}), linear elastic (σ_{ci}), crack growth (σ_{cd}), and unstable crack growth (σ_{UCS}).

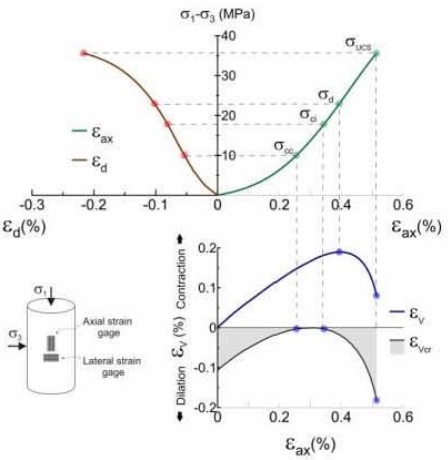

Figure 2. Typical stress-strain diagram of a sandstone sample (Corvio sandstone) under a load rate of 0,5 MPa s^{-1}.

Figure 2 shows the stress-strain evolution of a Corvio sandstone (Canal-Vila et al., 2013) when submitted to a constant load rate of 0.5 MPa. It is worth noting that Young's modulus and Poisson's coefficient are parameters representative of the linear elastic stage (i.e., σ_{cc} to σ_{ci}), insofar as they are calculated from this stage. But, the linear stage explains only partially the strain evolution.

It is expected that from one stage to another, the mechanical response of the rock varies significantly. Neglecting the initial state of stress may lead to incorrect data interpretation. Therefore, the first step of the experimental protocol aims to associate target conditions with strain stages for a given rock type.

3.2 *Electrical resistivity*

Saturating the sample with CO_2 + brine solution at high pressure, to ensure CO_2 remains supercritical, implies replacing the original pore solution (brine). This affects the electrical resistivity of the sample. From changes in resistivity we will be able to investigate the electrochemical reaction of the rock as a result of the CO_2 injections.

To monitor the solution replacement process in the core plug, the rubber sleeve of our triaxial cell is fitted with 16 electrodes for measuring ERT (North et al., 2013). Figure 3 illustrates the laboratory measurement "stack" showing the array of 16 electrodes, in red, around the sample. On the right, an example of three cross-sections through the sample shows heterogeneities in the distribution of the electrical resistivity of the core plug.

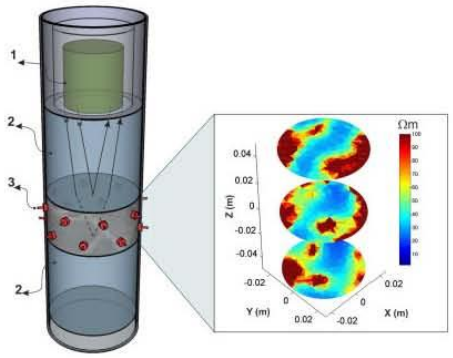

Figure 3. Inner butyl sleeve of the triaxial core holder: 1, Ultrasonic transducer; 2, Perspex buffers; 3, Electrodes. Zoom box shows three slides of electrical resistivity at different sample heights.

Furthermore, monitoring ERT we recognize progressive stages of partial saturation that can be converted into relative permeability, measuring changes in the flow rate while keeping constant both up- and down-stream pressures, according to Darcy's law. Relative permeability are indispensable to feed the numerical simulation of the evolution of CO_2 plumes in the subsurface (Busch and Müller, 2011).

3.3 *Ultrasonic (elastic) data*

The aim of the present experimental rig is to determine seismic (elastic wave) properties of rocks at reservoir conditions, before and after CO_2 injection. However, it is also interesting to apply the procedure described above to measure elastic properties while the pore solution replacement occurs in the sample. This provides data useful for determining irregularities in the front of CO_2 plume advance as well as heterogeneities in the reservoir.

Figure 3 shows the ultrasonic measurement transducer, highlighted in green, positioned on top of the stack and used in pulse-echo mode.

ACKNOWLEDGMENTS

This work is part of the UK EPSRC DiSECCS project. Funds from Xunta de Galicia (10REM003CT) and the European Regional Development Funds 2007/2013 are also acknowledged.

REFERENCES

Best, A.I., Sothcott, J. and McCann, C. 2007. A laboratory study of seismic velocity and attenuation anisotropy in near-surface sedimentary rocks. *Geophysical Prospecting* 55(5): 609–625.

Busch, A. and Müller, N. 2011. Determining CO2 /brine relative permeability and capillary threshold pressures for reservoir rocks and caprocks: Recommendations for development of standard laboratory protocols. *Energy Procedia* 4(0): 6053–6060.

Canal-Vila, J., Falcon-Suarez, I., Barrientos-Rodriguez, V. and Delgado-Martin, J. 2013. Mineralogy, geochemistry, petrophysics and rock mechanics of the Corvio sandstone. In: F. Guillen-Mondejar, M.A. Alias-Linares and A. Sanchez-Navarro (Editors), *XXXIII Reunion Cientifica de la Sociedad Espanola de Mineralogia, Murcia.*

Canal, J., Delgado, J., Falcón, I., Yang, Q., Juncosa, R. and Barrientos, V. 2013. Injection of CO2-Saturated Water through a Siliceous Sandstone Plug from the Hontomin Test Site (Spain): Experiment and Modeling. *Environmental Science & Technology* 47(1): 159–167.

Lau, J.S.O. and Chandler, N.A. 2004. Innovative laboratory testing. International *Journal of Rock Mechanics and Mining Sciences* 41(8): 1427–1445.

North, L., Best, A.I., Sothcott, J. and MacGregor, L., 2013. Laboratory determination of the full electrical resistivity tensor of heterogeneous carbonate rocks at elevated pressures. *Geophysical Prospecting* 61(2): 458–470.

Rock Engineering and Rock Mechanics: Structures in and on Rock Masses – Alejano, Perucho, Olalla & Jiménez (Eds)
© 2014 Taylor & Francis Group, London, 978-1-138-00149-7

Effect of supercritical CO_2 on the Corvio sandstone in a flow-thru triaxial experiment

J. Canal, J. Delgado-Martín, V. Barrientos, R. Juncosa & B. Rodríguez-Cedrún
Civil Engineering School, University of A Coruña, A Coruña, Spain

I. Falcón-Suarez
National Oceanography Centre, Southampton, UK

ABSTRACT: The effect of the injection of CO_2-saturated deionized water (DIW) at supercritical state was investigated in the siliceous Corvio Sandstone while recording stress, strain, wave propagation and fluid chemical composition during a flow-through experiment. Our investigation correlated simultaneously chemical and rock physics parameters in a unique flow through experiment. The experiment illustrates interlinked hydro-mechanical processes with a minor contribution of reactive phenomena. This is a relevant approach when considering the extent of the relative contribution of isolated hydro-chemo-mechanical processes.

1 INTRODUCTION

Over the past 250 years, the concentration of greenhouse gases has increased in the atmosphere and this has been connected by many researchers with the enhancement of heat trapping. CO_2 is the main anthropogenic greenhouse gas and its sources are the burning of fossil fuels, solid waste, trees and wood products, etc. It is generally accepted now that some limits need to be placed on the atmospheric emissions.

Carbon Capture and Storage (CCS) is widely used approach aimed at reducing CO_2 emissions or, at least, laminating them while seeking for a new paradigm of energy production and consumption. It's importance stems from the fact that, currently, about 85% of the world's commercial energy needs are supplied by fossil fuels. A rapid change to non-fossil energy sources, even if possible, would result in large disruption in terms of energy supply, what would have dramatic consequences for the global economy. Thus, CCS techniques would allow an interim period in which it would be possible to take advantage of fossil fuels for energy production while reducing substantially the emissions of CO_2.

Deep saline aquifers represent, by far, the most typical scenario for CO_2 geosequestration. They also have the largest volumetric storage capacity. In the case of Spain, where conventional gas and oil fields are virtually non-existent, they represent the most realistic option for CCS. The EU GeoCapacity (2009) project assessed that Spain had the highest onshore storage capacity of all European countries, with a conservative estimate of 14,000 Mt in combined onshore and offshore deep saline reservoirs. In December 2010 Spain also became the first European country to transpose the CCS Directive 2009/31/EC. Most of the storage capacity is associated to deep saline aquifers of the major sedimentary basins (Douro, Ebro, Guadalquivir and Tagus). The Douro basin, in particular, is of interest as it has an extension of approximately 50,000 km^2 and is the largest Cenozoic basin on the Iberian Peninsula.

It is well known that the injection of reactive fluids, like CO_2, into geological formations trigger a series of interlinked phenomena (thermo-hydro-chemo-mechanical or THCM) that affects the properties of the reservoir, its seal or even the cementitious materials used in wellbores. Because water is always present in the porous space of these systems, the forced injection of CO_2 (either as gas, liquid or supercritical fluid) induces a significant acidification and the onset of reactive processes which are especially notorious when carbonate or carbonate-bearing rocks are present. The co-injection of subordinated gasses accompanying CO_2 (O_2, SO_2,…) might exacerbate this reactivity due to the oxidation of reduced mineral phases already present in the rocks or by promoting an enhanced acidity associated to S-bearing gasses.

Petrophysics and rock mechanics provide with invaluable toolbox with which to assess key rock properties and to elaborate integrated reservoir models. However, in their classical use they do not consider the crucial importance of the THCM couplings which are inherent, however, to reactive systems. Routinely, laboratory data is used to correlate model logs or the seismic response to study the feasibility of monitoring a dynamic reservoir with geophysical methods (e.g. production, enhanced oil recovery, CO_2 sequestration). During injection or extraction, fluids in the reservoir change what induces changes in the elastic and visco-elastic rock moduli. In seismic data or

full-waveform sonic logs the preferential loss of amplitude with frequency is referred to as apparent (or effective) attenuation. This attenuation is the combination of intrinsic and scattering loss.

Core-flooding experiments performed at P-T conditions similar to those in situ have a great potential in helping us to unravel complex THCM processes, provided that it is feasible the separation of each of their corresponding contributions. To this respect, based on previous experiences (Canal et al. 2013a), in this study we focus on the evolution of different properties of a reference rock material (Corvio Sandstone) during a core-flooding test in which we sequentially inject deionized water (DIW) and CO_2-saturated DIW. The studied rock was selected among several candidates in order to minimize, as much as possible, chemical couplings so that the observed phenomena could be mostly related with non-reactive processes.

2 MATERIALS AND METHODS

The tested material has the trade name of Corvio Sandstone®. Geologically speaking, this material defines the Corvio Mb, in northern Spain, which appears as a 20 m thick lithosome at the top section of the Frontada Fm (Campoó Gr; Lower Cretaceous). It is made of siliceous sandstones and conglomerates associated with braided fluvial channels showing dm to m cross bedding lamination (Hernández et al., 1999). This sandstone was selected as a testing material for its good porosity and compliance, homogeneity as well as for having a relatively small content of reactive minerals different to quartz.

The Corvio Sandstone can be classified as a grain-supported quartzarenite with microcrystalline silica cement. Relevant chemical, mineralogical and physical properties are presented in Tables 1, 2, and 3 (Canal et al. 2013b).

Table 1. Chemical composition of the Corvio sandstone as determined from XRF analysis.

Component	wt.%	Component	wt.%
Na_2O	0.037	P_2O_5	0.023
K_2O	0.299	TiO_2	0.241
MgO	0.048	Fe_2O_3	0.003
CaO	0.125	SO_3	0.012
Al_2O_3	1.802	LOI	0.597
SiO_2	96.867		

Table 2. Mineralogy of the Corvio sandstone as determined by DRX analysis.

Mineral	wt.%	Mineral	wt.%
Quartz	94	Kaolinite*	2.9
K-Feldspar	1.7	Ilmenite	0.2
Carbonates*	0.05		

*Inferred from ATD-TG-FTIR and CHNS analysis.

The petrographical survey shows that quartz crystals are mostly monocrystalline and they typically exhibit uniform extinction and, less often, wavy extinction. Microcrystalline quartz crystals with sub rounded shapes can also be recognized. Rock fragments of up to 250 microns are formed by quartz and mica minerals. Isolated mica platens have 70–250 microns while K-feldspar has ~250 microns. Opaque phases range in size from 60 to 300 microns and some of them are oxidized (Fig. 1). Grains are cemented by microcrystalline quartz cement.

The average BET specific surface (method based on the physical adsorption of gas molecules on a solid surface) is $1.09 \pm 0.07\ m^2/g$ ($n = 12$) while porosity and dry density are 23.15% and $2037\ kg/m^3$ ($n = 227$).

Table 3. Physical and mechanical properties of the Corvio sandstone.

Property	Value	Units	Property	Value	Units
BET	1.09	m^2/g	T*	2.3	MPa
Porosity	0.145	m^3/m^3	UCS	41.3	MPa
Dry density	2037	kg/m^3	E	11.4	GPa
log k**	$\sim 10^{-5.7}$	m/s	ν	0.38	–

*Tensile strength. **Hydraulic conductivity.

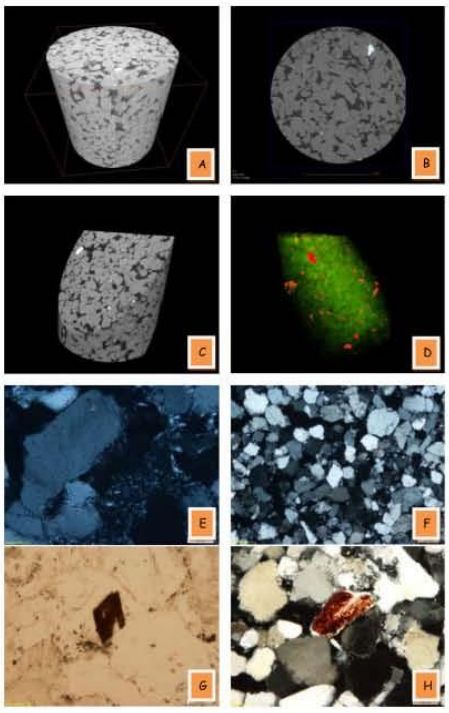

Figure 1. Micro-CT scans (A-D) and microphotographs (E-H) of the Corvio Sandstone.

Hg porosimetry shows that pore size spans from 2.5 to 100 μm while the median is ~20 μm.

The mechanical properties of the Corvio Sandstone were also assessed as part of the basic characterization of this material. The mean tensile strength of the Corvio Sandstone is 2.3 ± 0.14 MPa (n = 11) while UCS is 41.3 ± 1.0 MPa (n = 10). These data were combined with the results obtained in additional drained triaxial tests performed at 5, 10, 30 and 50 MPa which were needed to obtain the full strength envelope. This was computed following the intact rock Hoek & Brown (1980) criterion (HB), as updated by Hoek et al. (2002). Assuming that the parameters s and a of the HB model are equal to 1 and 0.5, respectively, m_b is 15.0. Similarly, application of the linear Mohr-Coulomb criterion provides with an apparent cohesion (c) of ~20 MPa and a friction angle (ϕ) of 28.5°.

Taking into account the stress-strain behavior observed in the UCS tests, the static Young modulus (E) and Poisson ratio (ν) of the Corvio Sandstone are 11.41 ± 0.35 GPa and 0.38 ± 0.01, respectively. In addition, based on the computed volumetric strain and the method discussed by Nicksiar & Martin (2012), the crack initiation and crack damage stresses occur at 6.2 ± 0.2 and 26.0 ± 0.8 MPa, respectively.

The average P- and S-velocity of the rock are 3.32 and 1.72 km/s, respectively, while the dynamic Young modulus and Poisson ratio computed from the previous velocities are 15.90 ± 0.06 GPa and 0.316 ± 0.001. Static moduli, as expected, are lower than the dynamic ones because the latter only captures the elastic response of the rock under low stress conditions.

The tested sample plug was carefully trimmed to fulfill standard geometric constrains in rock mechanics experiments (flatness, slenderness and cilindricity; Franklin, 1983). The core flooding experiment was performed under an axisymmetric confining stress conditions by inserting the polyolefin-sleeved rock plug (37.4 mm diameter; 70.2 mm length; $\phi = 12.1\%$; $\rho_d = 2094$ kg/m^3) into a modified Hoek-Franklin-type cell (Hoek & Franklin 1968). The axial force is applied with a hydraulic jack supported by a loading frame equipped with a 30 ton load cell. The jack was connected to a servo-controlled GDS-ADVDPC screw pump. The axial pressure is transmitted to the sample by drilled load platens allowing (via circular and radial grooves) a homogeneous access of the pore fluid to the edges of the plug. The confining pressure is applied to the core holder with the aid of a high pressure, servo-controlled syringe pump cell (Teledyne Isco 260D) by pressurizing the confining fluid using a servo controlled pump. The cell is equipped with an aluminum heating jacket which is connected to a temperature controller that receives the feedback of a PT1000 temperature sensor installed through the external wall of the cell.

The test was performed at 40°C and under hydrostatic stress conditions ($\sigma_1 = \sigma_2 = \sigma_3 = 15$ MPa) and a pore pressure ~8 MPa ($P_F = 8.2 - 9.4$ MPa). Loading of the sample was performed stepwise: In the first step the axial and confining pressures were increased simultaneously (Q = 0), at a constant rate and under drained conditions to the target stress value. Then, following a short period to allow the mechanical re-conditioning of the plug, DIW (deionized water) was injected at a constant flow rate (0.04 mL/min) through the bottom platen in order to saturate the sample. For the injection, a high pressure syringe pump (Teledyne Isco DX-100) was used. The pressure drop between the inlet and outlet ports was monitored with two high resolution ($\pm 0.1\%$) absolute pressure transducers (Keller-Drück LEO Record Ei).

In order to ensure that the experimental conditions inside the plug were compatible with CO_2 supercritical conditions (>7.38 MPa; >31.1°C) the outlet port was equipped with a back pressure valve (BPV) rated to a maximum fluid pressure of 7.6 MPa at the sample side. The small pore pressure gradient inside the sample made it difficult to obtain accurate information about the evolution of permeability. After the BPV the pipeline was allowed to drop to ambient pressure in order to collect the water circulated through the sample. This section of the pipeline was equipped with a low volume flow-thru, temperature compensated, microelectrode array (Micro-electrodes Inc.) allowing the inline (although depressurized) measurement of pH and electrical conductance (EC_{25}). The electrodes were connected to an ELIT 9705b Aqualyser (Nico2000 Ltd.) data conditioning and acquisition system. The calibration of these electrodes was done periodically (2–3 days) due to the harsh working conditions. In addition, the cumulative effluent water was collected on a daily basis for analysis (Na, K, Ca, Mg, SiO_2, Fe, Mn, Al, F, Cl, SO_4) and its pH and EC_{25} also recorded.

The top and bottom compression platens are instrumented each with a stack of 1.3 MHz resonant frequency piezoelectric transducers (PZT) for the measurement of direct (V_P) and shear (V_{S1}, V_{S2}) ultrasonic wave velocities. Squared-pulse waves were generated with a transducer-pulser unit (PT100-1000; ErgoTech Ltd.) and monitored with a digital oscilloscope (PicoScope 3204A; Pico Technologies Ltd.). Velocities were determined once a day by applying the time of flight technique, according to the recommendations given in Rummel et al. 1978.

Only axial strains were recorded in this experiment with the aid of two-averaged Linear Displacement Sensors (Vishay LDS HS50). To separate the true sample strain from system deflection, a series of sample-less calibration tests were performed in the load frame (plus the corresponding accessories: load cell, spacers, platens, etc.). Therefore, strains reported in this work are frame-corrected values.

The saturation of DIW with CO_2 was accomplished in a 2.7 L carbonation vessel for several days (different sources in the literature report that equilibrium can be reached in 24 to 48 h; Diamond et al. 2003). To speed-up the equilibration process, CO_2 was micronized inside the vessel at low pressure (~0.5 MPa). CO_2 was supplied in excess, what allowed the development of a gaseous headspace. The vessel was then driven at room

temperature to the target condition of 8 MPa with the aid of a manual pressure generator (HiP mod. 62-6-10). The transfer of fluid from the carbonation vessel to the ISCO pump was performed by setting the later in constant pressure mode and a back-pressure regulator. According to the EOS described in Duan et al. 2004; Duan et al. 2006, the theoretical concentration of CO_2 in the injected fluid is ~1.2 m and the corresponding pH ~3.1.

3 RESULTS AND DISCUSSION

The experiment lasted for 35 days and during that time ~140 pore volumes of fluid (~2.02 L) circulated through the porous space of the plug. Figure 2 illustrates the evolution of selected parameters and concentrations as a function of the number of pore volumes (PV) circulated. The gray-shadowed area represents the DIW injection stage (~50 PV), which is followed by the CO_2-saturated DIW injection period (from ~50 to ~140 PV). Circulated fluid shows evidences of chemical reactivity, although this is limited. Nonetheless, the time-evolution of recorded parameters provided with interesting information. The evolution of pH and EC_{25e} (electrical Conductivity) is illustrated in Figure 2A. With respect pH, the DIW stage shows a slight tendency of acidification, which is a typical situation during the injection of weakly buffered fluid into siliciclastic rocks. In the second stage, there is a significant pH increase that can be related with the dissolution of carbonates that can be inferred from the sharp increase in Ca and Mg concentrations observed in figure 2B. EC_{25} shows virtually no changes during the first stage and a sharp rise (although to a moderate value of ~110 µS/cm) immediately after the beginning of the injection of the carbonated fluid. This is interpreted as being the result of mineral dissolution reactions. Then, EC_{25} drops steadily for the remaining of the test. That suggests that the mineral phases available for reaction are being exhausted and that chemical processes have a very limited impact in this experiment.

The evolution of Ca and Mg follows a parallel trend what points towards co-dissolution phenomena. In the case of Ca, the appearance of a two-peak pattern suggests that dissolution occurred in two main steps: The first one upon CO_2-saturated DIW injection and the second slightly later on. Following the conjectures of Canal et al. (2013a) and the strain evidences observed in this experiment (Fig. 2B), we conclude that the second step is connected with the late access to new carbonate surfaces following cracking or micro-cracking of the plug.

The evolution of other parameters is also illustrated in Figure 2 (Na and K, plot C; SiO_2 in plot D, Fe and Mn in plot E and major anions in plot F). Following the previous considerations, we observe that no major elemental mobilization occurred during the test and that the major constituent of the rock (SiO_2, present in quartz and other silicates) experiences a slight increase

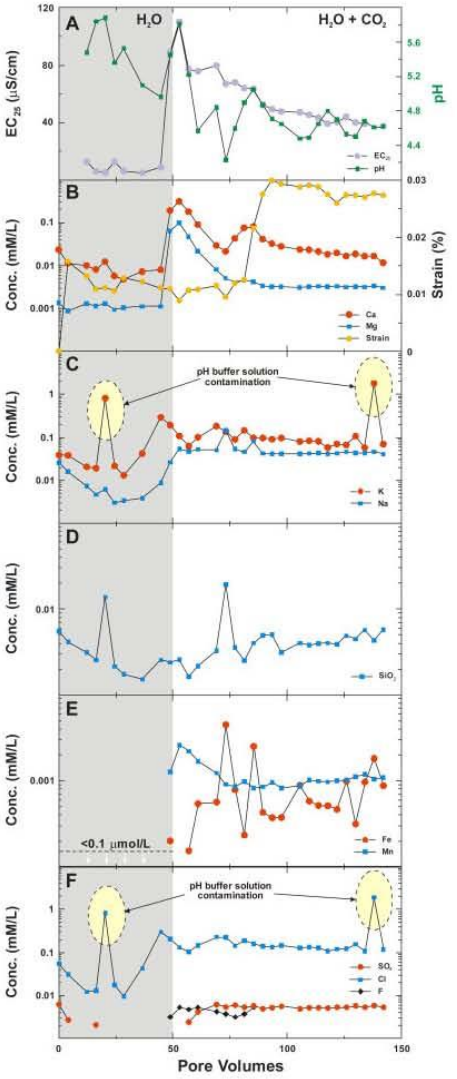

Figure 2. Chemical evolution of selected parameters and concentrations during the experiment. The ellipses highlight water samples affected by electrode leakage.

in concentration trend which is to be expected as the result of the undersaturation of silica of the injected fluids. Other features include the mobilization of Fe, Mn and F upon arrival of the carbonated fluid and virtual absence of contributions from the rock to the measured concentration of SO_4 and Cl. Na and K show also a very small washout from the rock, probably associated with the re-equilibration of the exchange complex linked to the presence of kaolinite in the rock.

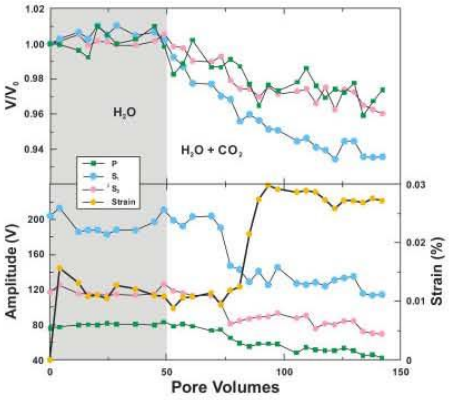

Figure 3. Evolution of compressional (P) and shear (S_1 and S_2) relative wave velocities (top) and their corresponding change in amplitude. Amplitude data is compared with strain evolution during the experiment.

Two peaks have been identified in Figure 2 (plots C for K, and F, for Cl) in which we identify the existence of perturbations in the concentrations measured in the water samples. This is likely due to a contamination accident associated to the entrance into the sample beaker of some drops of the calibration fluid of the EC_{25} electrode (a KCl solution).

Figure 3, top, shows the evolution of P and S wave velocities (expressed as relative velocities computed from the velocity at time t, V, with respect velocity at time 0 of the experiment, V_0) during the experiment. We observe that both, compressional and shear velocities remain constant (even slightly increase) during the DIW injection stage but they significantly decrease (~100 m/s) during the injection of the carbonated fluid. Attenuation has been recognized as a significant seismic indicator, which is not only useful for amplitude analysis and improving resolution, but also to obtain information on lithology, saturation (fluid type), permeability and pore pressure (Carcione et al., 2000). Figure 3, bottom, illustrates the P and S wave amplitude evolution during the test and compare it with the observed axial plug strain. It is interesting to pay attention to the fact that wave amplitudes remain virtually constant at the beginning of the injection of CO_2-saturated DIW and that they drop coinciding with the sudden strain increase developed at ~75 PV. The decrease-in-amplitude effect is visualized also in Figure 4, where three P-waveforms illustrate the two stages of the experiment and the post-experiment condition. We have recognized this effect earlier in previous experiments and it has been already described in recent literature by Hangx et al. (2013). However, it is worth noting that while wave velocity reduction occurs at the beginning of the injection of the carbonated fluid (fluid substitution effect) the largest change in amplitude shows a significant delay with respect this event. The good time-correspondence between

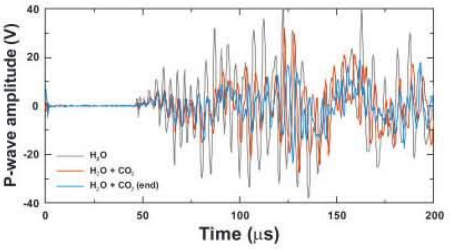

Figure 4. Comparison of experimental P-waveforms associated to the two stages of the experiment and at the end.

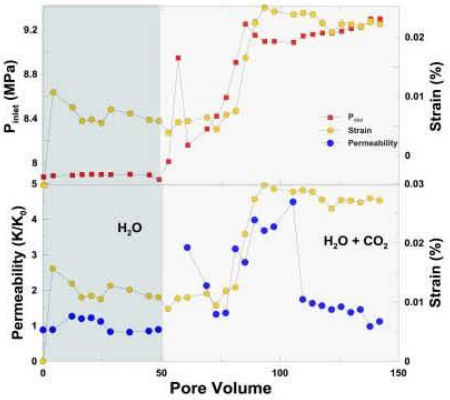

Figure 5. Evolution of strain and pore pressure at the inlet port of the plug during the experiment (top) and computed permeability (bottom) referred to the permeability measured the first day (K_0).

amplitude drop and axial strain rise suggests that wave attenuation is more likely associated to mechanical rather than to fluid-substitution effects.

The evolution of axial strain illustrates some interesting features. Figure 5 illustrates the relationship between strains, pore pressure at the inlet of the plug and computed permeability. Following an initial dilatation likely associated with the pass from ambient pressure to the constant flow condition (P_F ~8.2 MPa), the average strain rise to a value of ~0.015% and then steadily drops up to ~50 PV. This drop is likely associated with the compaction of the sample. From 50 to 75 PV, strain remains more or less constant, although this is the period in which reactive processes (due to the injection of the carbonated fluid) have the largest impact (see Fig. 2B). As it was mentioned earlier, the experiment was conducted under constant flow condition. That means that the pore pressure at the inlet was not constant. In Figure 5, top, we observe that, while the inlet pressure was nearly constant (~8.2 MPa) during the DIW injection stage, it was appreciably higher in the CO_2-saturated DIW injection phase (~9.4 MPa). Thus, the strain increase

from 75 to to ~90 PV is likely due to a supplementary dilation of the plug due to the pore pressure increase. From ~90 PV to the end of the experiment strain experiences again a steady drop that we interpret as being the result of plug compaction.

The evolution of permeability is depicted in Figure 5, bottom. We observe that there is a small (and transient) permeability increase between 10 and 30 PV. Following the considerations made in Canal et al. (2013a), we conjecture that this could obey to small-scale fines-migration processes (blocking/unblocking of flow paths associated with the release of clayey particles). This process could be connected also with the inlet pressure peak observed at ~60 PV. We observe also that there is a significant permeability increase following the sharp rise in strain between 75–90 PV. This effect requires the enhancement of flow paths, probably associated with the onset of microcracking in the plug. After ~110 PV, permeability suddenly drops, decreasing from hereafter steadily and, probably, as a consequence of the observed sample compaction. Overall, in this experiment, reactive processes have a minor effect on the evolution of permeability.

This experiment illustrates interlinked hydro-mechanical processes with a minor influence of reactive (chemical) phenomena. This is a relevant approach when trying to quantify the relative contribution of mixed hydro-chemo-mechanical processes.

ACKNOWLEDGEMENTS

This project has been partly funded by the Spanish Ministry of Industry, Tourism and Trade, through a CIUDEN-GEAMA contract, Xunta de Galicia (10REM003CT), and the European Regional Development Funds 2007/2013. OXYCFB300 is co-financed by the EU Energy Programme for Recovery. The sole responsibility of this publication lies with the authors. The EU is not responsible for any use that may be made of the information contained therein. Special thanks are also given to A. Vázquez, S. Fernández, T. Kovacs, M. Santín, M. Batzle, SAI-UDC, ESCO and Center for Rock Abuse (MINES).

REFERENCES

Canal, J., Delgado, J., Falcoìn, I., Yang, Q., Juncosa, R. & Ba-rrientos, V. 2013a. Injection of CO_2-saturated water through a siliceous sandstone plug from the Hontomin test site (Spain): Experiment and modeling. Environmental Science and Technology 47(1):159–167.

Canal, J., Falcón, I., Barrientos, V., Delgado, J. 2013b. Mineralogy, geochemistry, petrophysics and rock mechanics of the Corvio Sandstone. Macla 17:31–32.

Carcione, J.M. & Gangi, A.F. 2000. Non-equilibrium compaction and abnormal pore-fluid pressures: effects on rock properties. Geophysical Prospecting 48:521–537.

Diamond, L. & Akinfiev, N.A. 2003. Solubility of CO_2 in water from −1.5 to 100°C and from 0.1 to 100 MPa: evaluation of literature data and thermodynamic modelling. Fluid Phase. Equilbria 208:265–290.

Duan, Z. & Sun, R. 2004. An improved model calculating CO_2 solubility in pure water and aqueous NaCl solutions from 273 to 533 K and from 0 to 2000 bar. Chemical Geology 193:257–271.

Duan, Z., Sun, R., Zhu, C. & Chou, I.M. 2006. An improved model for the calculation of CO_2 solubility in aqueous solutions containing Na^+, K^+, Ca^{+2}, Mg^{+2}, Cl^- and SO_4^{-2}. Marine Chemistry 98:131-139.

Franklin, J.A. 1983. Suggested methods for determining the strength of rock materials in triaxial compression. International Journal of Rock Mechanics and Mining Sciences 20:285–290.

GeoCapacity. 2009. EU GeoCapacity. Assessing European Capacity for Geological Storage of Carbon Dioxide. Final Activity Report, 37 pp.

Hangx, S., van der Linden, A., Marcelis, F. & Bauer, A. 2013. The effect of CO_2 on the mechanical properties of the Captain Sandstone: Geological storage of CO_2 at the Goldeneye field (UK). International Journal of Greenhouse Gas Control 19:609–619.

Hernández, J.M., Pujalte, V., Robles, S. & Martín-Closas, C. 1999. División estratigráfica genética del Grupo Campóo (Malm-Cretácico Inferior, SW CuencaVascocantábrica). Revista de la Sociedad Geológica de España 12:377–396.

Hoek, E., Brown, E.T. 1980. *Underground Excavations in Rock*. The Institute of Mining and Metallurgy.

Hoek, E. & Franklin, J.A. 1968. A simple triaxial cell for field and laboratory testing of rock. Transactions of the Institution of Mining and Metallurgy 77:A22–26.

Hoek, E., Carranza-Torres, C., Corkum, B. 2002. Hoek-Brown criterion–2002 edition. Proceedings NARMS-TAC Conference, Toronto, 267–273.

Nicksiar, M., Martin, C.D. 2012. Evaluation of methods for determining crack initiation in compression tests of low porosity rocks. Rock Mechanics and Rock Engineering 45:607–617.

Rummel, F. & Van Heerden, W.L. 1978. Suggested methods for determining sound velocity. International Journal of Rock Mechanics and Mining Science 15:53–58.

Geophysical Prospecting

Characterization and Multifaceted Anisotropy Assessment of Corvio Sandstone for Geological CO_2 Storage Studies

Journal:	*Geophysical Prospecting*
Manuscript ID	GP-2015-0064.R2
Manuscript Type:	Special Issue
Date Submitted by the Author:	n/a
Complete List of Authors:	Falcon-Suarez, Ismael; National Oceanography Centre, Marine Geophysics research group Canal, Jacobo; Repsol, Centro de Tecnología de Repsol; Universidade da Coruna, Civil Engineering School Delgado-Martin, Jordi; Universidade da Coruna, Civil Engineering School North, Laurence; National Oceanography Centre, Marine Geoscience Best, Angus; National Oceanography Centre, Southampton, Marine Geoscience Research Group
Keyword:	Wave velocities, Permeability, Anisotropy

EAGE Publications B.V., PO Box 59, 3990 DB, Houten, The Netherlands

Characterization and Multifaceted Anisotropy Assessment of Corvio Sandstone for Geological CO_2 Storage Studies

by

Ismael Falcon-Suarez[2]

Jacobo Canal-Vila[1,3]

Jordi Delgado-Martin[1]

Laurence North[2]

&

Angus Best[2]

(1) Civil Engineering School. University of A Coruña. Campus de Elviña s/n 15071 A Coruña. Spain

(2) National Oceanography Centre, University of Southampton Waterfront Campus, European Way, Southampton, SO14 3ZH, UK

(3) Centro de Tecnología de Repsol Ctra. Extremadura, N-V Km 18, 28935 Móstoles. Spain

Manuscript submitted to:

Geophysical Prospecting

Special Issue "Advances in Rock Physics"

Date: August, 2015

EAGE Publications B.V., PO Box 59, 3990 DB, Houten, The Netherlands

Abstract

We present a comprehensive characterization of the physical, mineralogical, geomechanical, geophysical and hydrodynamic properties of Corvio sandstone. This information, together with a detailed assessment of anisotropy, is needed to establish Corvio sandstone as a useful laboratory rock-testing standard for well-constrained studies of thermo-hydro-mechanical-geochemical coupled phenomena associated with CO_2 storage practices and for geological reservoir studies in general. More than 200 core plugs of Corvio sandstone (38.1 and 50 mm diameter, 2:1 length to diameter ratio) were used in this characterization study, with a rock porosity of 21.7 ± 1.2%, dry density 2036 ± 32 kg m^{-3}, and unconfined compressive and tensile strengths of 41 ± 3.28 and 2.3 ± 0.14 MPa, respectively. Geomechanical tests show that the rock behaves elastically between ~10 and ~18 MPa under unconfined conditions with associated Young's modulus and Poisson's ratio of 11.8 ± 2.8 GPa and 0.34 ± 0.01, respectively. Permeability decreases abruptly with confining pressure up to ~10 MPa and then stabilizes at ~1 mD. Ultrasonic P- and S-wave velocities vary from about 2.8 to 3.8 km s^{-1} and 1.5 to 2.4 km s^{-1}, respectively, over confining and differential pressures between 0.1 - 35 MPa, allowing derivation of associated dynamic elastic moduli. Anisotropy was investigated using oriented core plugs for electrical resistivity, elastic wave velocity and attenuation, permeability and tracer injection tests. Corvio sandstone shows weak transverse isotropy (symmetry axis normal to bedding) of <10% for velocity and <20% for attenuation.

Key words: Corvio sandstone, weak anisotropy, wave velocities, strength, permeability, CO_2 storage, EOR.

1 Introduction

The injection of reactive fluids like CO_2 into geological formations for enhanced oil recovery (EOR) or carbon capture and storage (CCS) has been widely studied in the recent past. Before implementing CO_2 injection on large scale sites, it is crucial to assess the viability of the host geological strata. The main concern is that CO_2 injection could trigger a series of interlinked phenomena that affect the physical (or mechanical) and hydraulic properties of the reservoir, its seal, and even the cementing materials used in wellbores (Hangx *et al.* 2010; Kutchko *et al.* 2008; Liu *et al.* 2012; Rutqvist 2012; Song and Zhang 2012). Because water (brine) is always present in the rock pore space, the forced injection of CO_2 (whether in gas, liquid or supercritical state) induces significant acidification that leads to the onset of reactive processes, especially in the presence of carbonate or carbonate-bearing rocks (Le Guen et al. 2007; Gaus 2010; Vialle and Vanorio 2011). Siliciclastic formations are not expected to react significantly following the injection of CO_2–rich fluids, although the presence of lesser amounts of reactive minerals may play a significant role in their geological storage performance (Canal *et al.* 2013; Sim and Adam 2015). Hence, brine saturated sandstone reservoirs are the preferred targets for CO_2 storage because of their low reactive potential and high storage capacities.

The successful assessment of suitable reservoir formations relies heavily on an adequate understanding of the thermal, hydrodynamic, mechanical and geochemical (THMG) coupled processes that occur during injection and the resulting fluid-rock interactions. Typically, laboratory studies of reservoir and seal formation rocks are a major input to the assessment process. The limited availability (or even absence) of *in situ* samples is commonly solved by using rock analogues to the ones found in the target reservoir. A significant amount of literature can be found on the use of rocks

with well-known properties for conducting a range of laboratory tests (strength, permeability, etc.), to understand the behaviour of reservoir core flooding or to check instrument performance (Churcher *et al.* 1991). Also, in recent years, digital rock physics has evolved rapidly through the increasing resolution of X-ray computed tomography (CT) imaging , and has become a valuable tool for quick, non-destructive assessment of many rock properties (Andrä *et al.* 2013). However, these digital imaging techniques still require standard rock samples for calibration purposes and complementary destructive/non-destructive tests.

The specialist literature includes a wide number of reference rock materials used in many research works so that they now constitute *de facto* standard materials within the discipline of rock mechanics/rock physics. Among many other rocks, Berea sandstone (Krevor *et al.* 2012; Pini *et al.* 2012; Akbarabadi and Piri 2013; Nakagawa *et al.* 2013; Oh *et al.* 2013;), Tako sandstone (Xue and Ohsumi 2004; Xue and Lei 2006; Lei and Xue 2009; Nakatsuka *et al.* 2010) Bentheim sandstone (Klein *et al.* 2001), Bleurswiller sandstone (Fortin *et al.* 2005), Fontainebleau sandstone (Fredrich *et al.* 1993; Song and Renner 2008), Donnybrook sandstone (Mikhaltsevitch *et al.* 2014) and Navajo sandstone (Lu *et al.* 2011) have been used to investigate CO_2 injection in sandstone reservoirs, as well as for general reference materials in the petroleum industry. However, despite their widespread use and availability, none of them can be considered to be truly traceable standard materials because they display significant heterogeneity and anisotropy (although these are in themselves valid properties). Indeed, most sedimentary rocks of interest in exploration geophysics are considered to be weakly anisotropic, *i.e.*, with less than 20% anisotropy (Thomsen 1986). Sample heterogeneity is the greater problem because of what constitutes a representative laboratory sample volume for valid

upscaling of measured properties to large geological formations. The key point is that both heterogeneity and anisotropy must be accurately quantified for a valid standard material, not always achieved in the above mentioned works.

Sample anisotropy can be assessed from the contrast in P- and S- wave velocities propagating in directions orthogonal and parallel to bedding planes (Thomsen 1986; Wang 2002; Schubnel *et al.* 2006; Martínez and Schmitt 2013), and similarly for P- and S-wave attenuation (Q^{-1}, the reciprocal of the quality factor Q; Zhu and Tsvankin 2006; Best *et al.* 2007; Zhu *et al.* 2007; Chichinina *et al.* 2009). Electrical resistivity (Ellis *et al.* 2010) and magnetic susceptibility (*e.g.* Louis *et al.* 2004) have also been employed for this purpose. Although weak anisotropy can lead to negligible effects in some instances (Thomsen 1986), especially at the laboratory scale, it can be significant for the accurate calibration of geophysical techniques, fluid transport phenomena (*e.g.*, fingering) and when studying THMG coupled processes.

Corvio sandstone was chosen as a local reference material during the commissioning a CO_2 injection pilot plant in Northern Spain (Alcalde et al. 2014). In this paper, we present a comprehensive laboratory characterization of the properties of Corvio sandstone including anisotropy. The aims of this work is to summarize the most relevant physical, chemical, geomechanical and hydrodynamic properties of Corvio sandstone to provide a baseline database for subsequent studies, and to identify the extent and magnitude of anisotropy to inform studies of its possible impact on THMG coupled processes associated with CO_2 storage in siliceous sandstone reservoirs.

EAGE Publications B.V., PO Box 59, 3990 DB, Houten, The Netherlands

2 Materials and Methods

2.1 Corvio Sandstone

Corvio sandstone (CS) forms a c. 20 m thick unit (Corvio Formation) that appears in the top section of the Frontada Formation (Campoó Group; Lower Cretaceous) located in Northern Spain in the southern margin of the Basque-Cantabrian Basin. It is composed of siliceous sandstones and conglomerates. It displays decimetric to metric trough-type cross bedding associated with braided fluvial channels (Hernández *et al.* 1999). A total of 228 cylindrical plugs of diameter 38.1 and 50 mm, with an approximately length to diameter ratio of 2.0, were cored from four blocks (dimensions 0.3 x 0.2 x 0.5 m) of Corvio sandstone, orthogonally to the three independent surfaces of the sample block (arbitrarily denoted as X, Y, Z). Onwards, we denote samples as X-, Y- and Z-plugs to refer to the corresponding coring direction. The core plugs were carefully trimmed to meet geometric standards for rock mechanics studies (ISRM 1983).

2.2 Physical and chemical characterization

Knowledge of the physical and chemical properties of Corvio sandstone is important for CO_2 injection studies, since CO_2 is a reactive fluid whether in a liquid, gaseous or supercritical state. Hence, core chips were employed to determine mineralogy, density, porosity and pore size distribution.

The following techniques were used: X-ray diffraction and fluorescence (XRD and XRF; Siemens D5000 and Bruker-AXS S4 Pioneer, respectively); thermogravimetric analysis; differential thermal analysis and outgas analyses via Fourier transform infrared spectroscopy (TGA-DTA-FTIR; TA Inst. SDT 2960 coupled to Bruker Vector 22), which also provide information on water evaporation

mechanisms under controlled heating (Barrientos et al. 2010); Brunauer-Emmett-Teller (BET, Micromeritics Gemini VII 2390a) specific surface area; scanning electron microscopy coupled to energy dispersive microanalysis (SEM-EDS, JEOL JSM-6400); petrography (Olympus BX51); He pycnometry (Quantachrome Ultrapyc 1200e); Hg porosimetry (Quantachrome Poremaster-60); and X-Ray μCT-scans (XRadia MicroXCT-300). A total of 10 samples were used to assess the statistical significance of the measured properties.

2.3 Mechanical characterization

The long-term integrity of CO_2 repositories is linked to the potential mechanical deformation induced during the injection process. The mechanical stability of reservoirs is addressed through geomechanical modelling. The accuracy of these models depends on the available information about stresses and rock mechanical properties, based on geomechanical studies. This is crucial to identify the linear elasticity field from which static elastic moduli of the rock are calculated; but also to quantify deviations from perfect linear behaviour associated with compliant fractures and pores (Angus et al. 2010).

Geomechanical tests were performed on a total of 28 cylindrical plugs (diameter 50 mm; length to diameter ratio ~2) of Corvio sandstone, which were prepared to meet the recommendations of the International Society for Rock Mechanics (ISRM 1978; ISRM 1983): 11 for tensile strength (Brazilian test), 10 for unconfined compressive strength (UCS) and 6 for confined compressive strength (CCS).The tests were carried out using a MTS 815 testing system located at the facilities of the Rock Mechanics Laboratory (LaMEROC) of the University of A Coruña (Figure 1). During compressive strength tests, the axial strains were recorded with a dual-averaging knife-edge type extensometer, while the lateral strain

was measured using a circumferential chain-type extensometer. Some plugs were equipped additionally with four 350 Ω strain gages (two axial and two radial). Tensile strength was calculated indirectly (Brazilian test) by applying radial compression to induce tensile stresses in a thin discs of rocks (Bednárik and Kohút, 2012; Cai, 2010; Hakala et al., 2007).

Based on the measured stress-strain information, we computed the static elastic moduli according to ASTM (2007), and the critical stress states as presented in Hakala *et al.* (2007). Tangent Young's modulus (E) and Poisson's ratio (ν) were calculated at the strength level equal to 50% of UCS. The slope of the stress-strain curves was determined as the first derivative at a stress value equivalent to 50% of the peak strength, using a 3rd degree polynomial approximation. We also determined the characteristic stress levels describing the brittle behaviour of the rock, based on the work presented by Martin and Chandler (1994), further developed by Lau and Chandler (2004), Cai (2010) and Nicksiar and Martin (2012). These stress levels are known as crack closure stress (σ_{cc}), crack initiation stress (σ_{ci}), crack damage stress (σ_d) and failure (or peak) stress (σ_f). The crack closure stress corresponds to the load level up to which the strain occurs as a result of pore compaction and compliant crack closing.

2.4 Elastic waves

There is widespread use of seismic methods to monitor CO_2 movement and distribution in reservoir formations. Seismic properties of rocks are pressure-dependent, and so elastic wave velocities were measured on dry and water-saturated Corvio sandstone samples over a wide range of confining pressures, both under hydrostatic and non-hydrostatic conditions. These velocities were also

employed to compute the corresponding dynamic moduli (E_{dyn}, ν_{dyn}, K_{dyn} and μ_{dyn}) assuming isotropic homogeneous materials and standard relationships (*e.g.* Batzle *et al.* 2006; Rae *et al.* 2007).

Ultrasonic wave velocities (V_P, V_{S1} and V_{S2}: *P-wave, fast S-wave and slow S-wave, respectively*) were measured on 38.1 mm diameter core plugs with the aid of a pair of ErgoTech compression platens both equipped with one P-wave, and two orthogonally polarized S-wave, 1.3 MHz PZT transducers in pulse-transmission mode; time-of-flight was determined by picking first breaks (LaMEROC). The ultrasonic pulse-echo technique was used at the National Oceanography Centre, Southampton (NOC) on 50 mm diameter plugs, as presented in McCann and Sothcott (1992).

2.5 Permeability

Permeability is pressure-dependent and controls the rate of fluid advance through the reservoir formation. When mixed phase fluids (*e.g.*, brine and CO_2) are injected into a porous medium, the permeability to water (absolute permeability or hydraulic conductivity) is needed to calculate the relative permeability curves of the corresponding fluids. Hence, we measured the absolute permeability to water for different pairs of hydrostatic confining and pore fluid pressures. Permeability was determined by the steady state flow method (*i.e.*, Darcy's law) using water. We assumed a homogenous contribution to the flow of the full core cross-sectional area, and the absence of hydro-mechanical end-effects (Nguyen *et al.* 2013). In short, the ratio of volumetric flow rate, Q ($m^3\ s^{-1}$), to the pressure drop, ΔP (Pa), between the inlet and outlet of a sample of cross sectional area, A (m^2), and length, L (m), for a fluid dynamic viscosity, μ (Pa s), is related to absolute permeability, k (m^2), through the expression:

$$k = \frac{\mu L Q}{\Delta P A} \quad (1)$$

The equipment used to conduct these tests combines a high pressure Hassler (LaMEROC) or Hoek-Franklin-type (NOC) core holders together with a number of high-pressure, high-resolution syringe pumps (ISCO 100DX, Quizix SP-5400, GDS ADVDPC) for maintaining confining pressure and fluid injection rates. Confining and pore pressure were continuously monitored with several pressure transducers (Keller-Drück series 33X). The system was configured to set a constant pore pressure gradient, while recording the flow rate upstream and downstream of the sample. For permeability calculations, only the steady flow condition was considered within a single step.

2.6 Anisotropy assessment

Assessing the potential of Corvio sandstone as a reference material requires an evaluation of how the main properties of the rock vary with orientation. Hence, we used a multicore approach similar to that described by Louis *et al.* (2004). We cored additional 38.1 and 50 mm diameter plugs orthogonal to the three independent surfaces of the sample block (arbitrarily denoted as X, Y, Z), trimmed to a length-to-diameter ratio of 2 and 0.4, respectively. Dry ultrasonic measurements were conducted at LaMEROC (pulse-transmission method) on long core plugs, including a set of measurements on three orthogonal plugs whereby the samples were rotated 20° stepwise around the longitudinal axial under minimum loading (~1 MPa) to ensure good coupling between the platen and sample. This results in 9 measurements per core plug and a total of 27 for the three X-, Y-, and Z-plugs. Long plugs were also used for permeability assessment and tracer injection tests.

Dry and fluid saturated short plugs were used for the pulse-echo technique at NOC for different combinations of confining and pore pressure. Short plugs were also employed to assess the dynamic coefficients, permeability and bulk electrical resistivity.

As a preliminary step, unconfined dry ultrasonic velocity was measured to assess weak anisotropy in the samples of interest. Based on these results, we designed two main sets of experiments to better characterize the observed anisotropy: (i) combined electrical resistivity, ultrasonic velocity and permeability on brine-saturated plugs under nearly hydrostatic confining conditions at NOC; (ii) tracer injection tests at LaMEROC.

P-wave velocity and attenuation, electrical resistivity and permeability were together analysed on three short orthogonal brine saturated samples using the experimental rig at NOC described in Falcon-Suarez *et al.* (2014). This rig employs a triaxial cell with a specially adapted rubber sleeve with a 16-electrode array, and bespoke data acquisition systems and software developed at the NOC. This enabled the determination of the full 9-component resistivity anisotropy tensor without bias from measurements on a single core sample (North *et al.* 2013; North and Best 2014). Because we employed a set of orthogonal plugs, we can also compare the equivalent isotropic resistivity by fitting a homogeneous, isotropic model to the resistivity data. This yields a crude estimate of the overall resistivity of the sample, although it must be acknowledged that this is biased by the geometry of the electrode array and the measurement protocol.

The combined electrical resistivity, ultrasonic P-wave velocity and attenuation, and permeability experiments (referred as RuVAK tests) were performed at room temperature on three 50 mm diameter, 20 mm length plugs (X-plug porosity ϕ= 0.23;

Y-plug $\phi = 0.21$; Z-plug $\phi = 0.22$). The test procedure consisted of a drainage steady state flow test, setting a constant upstream flow of 0.5 cm^3 min^{-1} and a constant downstream pressure of 5 MPa. The pore fluid was 35 g L^{-1} NaCl brine solution. The test was repeatedly conducted for a loading/unloading path of differential pressure ($P_{diff} = \sigma_c - P_p$), by increasing the confining pressure 5 MPa stepwise from 10 to 25 MPa and back to 10 MPa, while keeping the *Pp* constant at 5 MPa. Furthermore, confining conditions were quasi-hydrostatic ($\sigma_1 - \sigma_3 = 0.5$ MPa) to emphasize the effect of the anisotropy along the longitudinal axis of each plug. For each loading/unloading step, a fluid volume of no less than 10 mL was circulated through the sample, corresponding to approximately one pore volume. Permeability was continuously monitored based on the final change in pore pressure gradient and corresponding flow.

The tracer tests performed were pulse-type (Shackelford *et al.* 1999; Ptak *et al.* 2004) and are referred to here as TPT tests. The tests used a brackish NaCl solution of 1000 μS cm^{-1} as injectate for the three 38.1 mm diameter X-, Y- and Z-plugs confined at 10 MPa under hydrostatic conditions. This confining pressure makes possible the closing of compliant cracks in order to better assess the relevance of small-scale porosity heterogeneities over fluid and solute transport. Rather than monitoring a chemical constituent, we continuously monitored the electrical conductivity of the effluent using a low-volume, flow-through, temperature-compensated conductivity sensor (MicroElectrodes Inc. mod. 8-900) coupled to a data acquisition system (ELIT 9705c Aqualyser) set to 1 Hz.

EAGE Publications B.V., PO Box 59, 3990 DB, Houten, The Netherlands

3 Results

3.1 Rock characterization

Corvio sandstone is light grey with occasional purple veins and has a medium grain size. It can be classified as a grain-supported quartzarenite with microcrystalline silica cement. The mineralogy of the Corvio sandstone is summarized in Table 1. Based on X-ray diffraction, the main mineral constituents are quartz (~94 wt. %) with subordinated kaolinite (~3.5 wt. %) and K-feldspar (~1.7 wt. %). Trace amounts of ilmenite (~0.2 wt. %) were observed in the μCT scans, while ~0.5 wt. % of carbonates, ~0.5 wt. % of hydrated minerals and <0.05 wt. % of C, N and S-compounds are inferred from the TGA-DTA-FTIR (Figure 2; weight loss sensitivity 0.1 μg or 0.0002%). The rock typically comprises sub-rounded quartz grains, is well sorted with an average grain size around 0.15 - 0.3 mm. In the studied samples, fossils comprised scarce cm-sized spots with remnants of tree debris (Hernández *et al.* 1999).

The average BET specific surface is 1.09 ± 0.07 $m^2 g^{-1}$ (n = 12) while porosity and dry density are 21.7 ±1.2 % (n = 224) and 2036 ±32 kg m^{-3} (n = 227) on average (Figure 3a - b). Available BET sorption/desorption isotherms show low hysteresis and correspond to the IUPAC's Type III (Rouquerol et al. 1994). This is typical of macroporous absorbents with weak surface affinity. The values obtained are comparable with that reported for the Berea (Zhan *et al.* 2010) and other sandstones.

From mercury porosimetry, we observed pore sizes from 0.1 to 1000 μm with a median pore size of ~20 μm (Figure 4a). Additionally, 3D and 2D-sections from the μCT-scanner (Figure 4b) revealed that, although pores tend to show an equant

shape, some larger open areas can be distinguished. These may lead to a compliant behaviour upon loading as confirmed by the stress-strain results presented below.

3.2 Rock strength and stress-strain behaviour

The mean tensile strength of Corvio sandstone is 2.3 ± 0.14 MPa, while UCS is 41.15 ± 3.28 MPa. Drained CCS values vary according with confining pressure (see Table 2). Figure 5 illustrates the corresponding strength envelope based on the Hoek-Brown model (Hoek and Brown 1980; Hoek *et al.* 2002) according to equation 2, which results in a m_b value of 13.2 by setting the *s* and *a* constants to 1 and 0.5, respectively (m_b, *s* and *a* are the Hoek-Brown material constants):

$$\sigma_1 = \sigma_3 + \sigma_c \left(m_b \frac{\sigma_3}{\sigma_c} + s \right)^a \qquad (2)$$

Static moduli were computed from the stress-strain curves from the UCS tests. For such conditions, the static Young's modulus (E) and Poisson's ratio (ν) are 11.8 ± 2.8 GPa and 0.34 ± 0.01, respectively; however, under confined conditions, E increases slightly (15.2 ± 2.8 GPa), while ν remains unchanged.

A further study of the stress levels presented by Corvio sandstone, shown in Figure 6, reveals that crack closure occurs up to a stress level, σ_{cc}, of 9.7 ± 1 MPa. With increasing stress, the rock shows elastic behaviour to a maximum value of 17.7 ± 2.3 MPa, which corresponds to the crack initiation stress, σ_{ci}; the crack damage onset stress, σ_d, initiates at 26.0 ± 2.4 MPa up to failure (*i.e.*, peak strength, σ_f). The peak strength of Corvio sandstone is consistently attained during the UCS tests at 41.15 ± 3.28 MPa under uniaxial conditions, although it rises to 222 MPa at 50 MPa confining pressure under dry conditions.

3.3 P- and S- wave velocities

V_P and V_S velocities were axially measured on 50 mm diameter X-plugs following a loading/unloading path from 0.5 to 35 MPa; the pressure steps were 2.5 and 5 MPa for non-hydrostatic and hydrostatic conditions, respectively. Figures 7a - b show wiggle-trace plots corresponding to the change in V_P and V_S of Corvio sandstone for 5 MPa steps, following the display used by Njiekak et al. (2013). We observe that, when increasing confining pressure, both velocities increase from 2.92 to 3.69 km s^{-1} and 1.51 to 2.09 km s^{-1}, respectively. Below 10 MPa, the loading effect follows an exponential curve consistent with the previously described crack closure stress stage, an effect that has been reported or inferred from experimental data in a number of works (Asef and Najibi 2013; King 1983; Mikhaltsevitch et al. 2014; Xu et al. 2006). The unloading path is slightly different from the loading one, with higher average velocities. This hysteresis is associated with irreversible damage suffered by the rock above the ~18 MPa limit associated with the crack initiation stress (Fortin et al. 2007; Xu et al. 2006).

Figures 8a - b illustrate the V_P and V_S curves obtained under non-hydrostatic conditions by increasing the axial load while keeping constant the radial confining pressure (*i.e.*, increasing the deviatoric stress). We observe that for low load (<10 MPa) and low confining pressure (0.1 MPa) there is a significant dependence of velocity with stress. This effect becomes less pronounced above 10 MPa loading, or at higher confining pressures. That means that closing of compliant cracks and pore compaction must be kept in mind when considering the ultrasonic characterization of plugs in the laboratory (Asef and Najibi 2013; King 1983).

Based on the previous elastic wave velocities and the dry density of the samples, we calculated the dynamic moduli of the rock: Young's modulus and

Poisson's ratio (E_{dyn} and ν_{dyn}; Figure 9a - b), and the bulk modulus and shear modulus (K_{dyn} and G_{dyn}; Figure 10a - b). Furthermore, comparing dynamic to static moduli we observe Edyn is higher than Est while vdyn is lower than vst, which has been largely identified in the past (Asef and Najibi 2013; Eissa and Kazi 1988; King 1983; Fjær 2009). The differences are related with deformation amplitudes between static and dynamic methods (at ultrasonic frequencies), and also with the heterogeneities between the different components of porous rocks, which lead to local non-elastic behaviours - stress-induced anisotropy - when subjected to external stress changes (Blake and Faulkner 2016; Fjær et al. 2013). In our case, the static moduli are determined at the strength level equal to 50% of UCS, laying above the elastic limit of the rock in all the cases. Hence, to correlate static and dynamic moduli, a further analysis of the sensitivity of static moduli to the stress level (measure point along the failure envelope) is needed (Fjær 2009), using damage controlled tests (Lau and Chandler 2004).

3.4 Permeability

The permeability of 38.1 mm diameter X-type plugs was evaluated with a series of 4 consecutive steady state flow tests performed along step wise loading/unloading cycles (between 5 and 30 MPa of hydrostatic confining pressure, *i.e.*, $\sigma_c = \sigma_1 = \sigma_2 = \sigma_3$). Each one has a constant pore pressure (P_p, from 1 to 16 MPa), which is increased from one to the next to repeat the differential stress sequence ($P_{diff} = \sigma_c - P_P$). Figure 11 shows that permeability progressively varies from 4 to 0.8 mD (~$8 \cdot 10^{-16}$ to ~$4 \cdot 10^{-15}$ m^2) while increasing confining pressure. There is a significant drop in permeability once the first loading/unloading cycle is completed, thought to be associated with pore closing and crack compliance. The permeability change after the 2nd, 3rd and 4th loading/unloading cycles is much smaller, although the P_{diff} is

kept constant along the sequence, which provides further evidence of the permanent deformation of the sample during initial loading due to pore closure. Hysteresis upon unloading is relatively small, below 15%. Overall, the observed permeability evolution can be attributed to compaction of pore space and favourably oriented cracks, already documented in other sandstones (Bernabé 1991; Zhu and Wong 1996; Ojala *et al.* 2004).

4 Anisotropy assessment

4.1 Exploratory approach

None of the 4 Corvio sandstone blocks, from which core plugs were taken, displayed any clear evidence of heterogeneity (especially cross bedding), and that was also the case for the small scale μCT X-ray scans. To further investigate the existence of anisotropy, we performed an exploratory survey with the plugs sampled orthogonally to the three independent surfaces (denoted as X, Y and Z) of the parallelepiped sandstone block. Figure 12 shows the vector-distribution of V_P, V_{S1} and V_{S2} (transverse to V_{S1}) resulting from the non-saturated unconfined test in which three X-, Y- and Z-plugs were revolved in steps of 20º around their longitudinal axes. Calculations show that V_p and V_s (average of V_{s1} and V_{s2}) are 2986 ±18 and 1515 ± 32 m s^{-1} for the X-plug; 3289 ± 48 and 1716 ± 21 m s^{-1}, for the Y-plug; and 3360 ± 32 and 1729 ± 20 m s^{-1}, for the Z-plug. Hence, V_p in the longitudinal direction of the X-plug is ~10% slower than in the Z-plug, and ~8% slower than in the Y-plug. Similarly, V_s is about 12% slower in both the Y- and Z-plugs. Further observation of the same figure lets us conclude that the rock is transversely isotropic in the longitudinal direction of Z-plugs, since the P and S-wave velocities are relatively insensitive to rotation, while the X- and Y-plugs are slightly orthotropic. It is worth noting that the X-plug shows 90º crossed symmetric values, indicating some sort of

EAGE Publications B.V., PO Box 59, 3990 DB, Houten, The Netherlands

preferential void alignment perpendicular to the axis. Besides, the difference between Vs1 and Vs2 is a proof of anisotropy, since different velocities along different wave paths may imply heterogeneity. The case of the Y-plug is more difficult to explain since V_p should be unaffected by axial rotation, but the results show the contrary (V_p is higher at 45º).

4.2 RuVAK tests analysis

Figure 13a - b show the P- and S wave velocities and corresponding attenuation coefficients for the three plugs and how they change with differential pressure (P_{diff}). As observed in the first exploratory assessment, the X-plug displays the lowest V_P and V_S while the smaller attenuations (Q_P^{-1} and Q_S^{-1}) correspond to the Z-plug. Attenuations for X- and Y-plugs show, however, similar values. In all the RuVAK tests, the three samples display consistent trends and similar slight hysteresis upon unloading, which suggests a *quasi*-isotropic mechanical behaviour. This behaviour is inferred from V_P and Q_P^{-1} against bulk electrical resistivity (*ER;* Figure 14), where the three plugs display parabolic trends with parallel symmetry axes (*i.e.*, constant V_P:*ER* and Q_P^{-1}:*ER* ratios). Likewise, *ER* seems to be relatively unaffected by stress-strain (<10% for an increment of 15 MP in P_{diff}) when compared to wave velocities, possibly because of the relatively high porosity of the rock (*i.e.*, most ionic flow is through large open pores, and relatively insensitive to pressure-dependent crack-related flow); *ER* is expected to be more sensitive to pore fluid electrical conductivity changes. This observation is highly relevant when considering reactive transport phenomena which imply changes in the electrical conductivity of the fluid or the replacement of the resident fluid by some other, for instance CO_2 (*e.g.* Alemu *et al.* 2013).

Figure 15 shows the change in resistivity and permeability during the RuVAK tests performed with the oriented plugs. We observe that both parameters slightly vary with P_{diff} (<10%) and, as expected, they show opposite trends, *i.e.*, pore compliance results in an increase in ER but a decrease in permeability. However, the relative difference among the three directions reaches ~18% for *ER* and up to 80% for permeability, with the plane defined by the X- and Z-plugs showing the greatest degree of anisotropy. The permeability values obtained during the RuVAK tests coincides with the previous assessments when P_{diff} and σ_c are above 5 and 10 MPa, respectively (Figure 11). The X-and Z-plugs have the highest and lowest permeability values, respectively, although the difference between them is of the order of 1 mD. Following the transverse isotropy (TI) model, permeability is lower in the direction perpendicular to the bedding surface (*i.e.*, X-plug). The minimum permeability in this direction is related to a more variable grain size distribution, compaction and pore collapse during burial (Farrell *et al.* 2014). Similarly, the lowest *ER* is also orthogonal to bedding, which is in agreement with the data reported by North and Best (2014) for other sedimentary rocks. The same authors have also reported that *ER* anisotropy in sandstones may reach up to 25%, emphasizing the possible importance of anisotropy on the assessment of CO_2 storage reservoirs.

The *ER* anisotropy has been further analysed by using the approach described in North and Best (2014). The process to extract anisotropy from the raw data is based on an algorithm that tries to fit a uniformly anisotropic forward model to the ER observations, unbiased by preconceptions of the symmetry of anisotropy or the orientation of the sample. Figure 16 illustrates the 3D anisotropy tensor ellipsoid (*i.e.*, the full 9-component resistivity tensor) associated with the measurements performed on each orthogonal plug. In the ideally isotropic case, observations made on

reciprocal pairs should coincide (*e.g.*, $Z_x = X_z$). However, because we induced a small deviatoric stress of 0.5 MPa to emphasize anisotropy evidences, the results are slightly biased along the axial component of each plug. Nonetheless, the high degree of sphericity and the small variation of resistivity in absolute terms show that the rock is only very slightly anisotropic.

Based on sedimentary fabric models presented by North *et al.* (2013), we interpret the presence of the following sedimentary structures in Corvio sandstone: (i) the X-plugs have bedding orthogonal to the axis of the plug; (ii) the Y-plugs have tubular micro-structure slightly oblique to the axis of the plug; and (iii) the Z-plugs have laminated micro-structure along the axis of the plug. Based on all the previous information, we infer the presence of a weak cross-bedding structure that would somehow reflect the macroscale cross bedding previously reported for the Corvio sandstone by Hernández *et al.* (1999).

The tracer TPT tests also provide an alternative mean to test the anisotropy of Corvio sandstone. These tests are significant as they directly emphasize the transport properties of the rock, providing information about actual flow-paths and fluid-flow through. Hence, it is possible to obtain information on the pore space (and transport properties) of the rock from the shape of the breakthrough curve (Ptak *et al.* 2004). It is far from the scope of this contribution to provide a detailed assessment of TPT tests although some general ideas can be presented. Assuming that the movement of the tracer conforms to piston-type flow, the injection of a discrete stepped pulse at the inlet of the sample translates into a tailed bell-shape breakthrough curve at its outlet (Fetter 1993). The change from a squared to a, more or less pronounced, tailed bell-shape curve depends on the relative importance of diffusive/dispersive effects while the tracer is crossing the pore space of the sample.

The tracer injection tests were repeated up to five times for the X-, Y- and Z-plugs, obtaining comparable results in each case. Representative breakthrough curves are illustrated in Figure 17. From a merely descriptive point of view, we see in our experiments that the faster travel time occurs for the Y-plug and is followed by the Z- and X-plugs. The relative height of the peak conductivity has the opposite order (highest for the X-plug and lowest for the Y-plug). Because electrical conductivity is a conservative tracer in our test (were chemical reactions are negligible according to the mineralogy of the rock, at the time-scale of the test) the surface area covered by each breakthrough curve is nearly identical.

Permeability results show that the plug showing the lowest value was the X-plug. This is consistent with the slowest arrival time of the same orientation in the TPT tests. However, the Y-plug has lower k than the Z-plug which is in apparent contradiction with the TPT results from the same plugs. Furthermore, if we focus on the shape of the Y-plug breakthrough curve, the recession curve shows a protuberance (*i.e.*, the trailing limb after the peak value) which points towards a double-porosity system. One porosity, well connected, would contribute providing fast trackways for tracer transport (also responsible for the early breakthrough) and a second one, less well connected, providing a delayed arrival of tracer with a peak value (the first inflexion point in the recession curve) located between the peak times for the X- and Z-plugs. The double porosity effect on permeability is imperceptible since the measurements are conducted in a constant flow mode, so dominated by preferential path flows (primary porosity), instead of a single pulse (TDT tests). Nonetheless, such a feature is consistent with our previous interpretation of weak cross-bedding.

EAGE Publications B.V., PO Box 59, 3990 DB, Houten, The Netherlands

4.3 Weak anisotropy assessment: detailed approach

The previous results encouraged the development of a more detailed anisotropy investigation. Based on these, we assumed that Corvio sandstone is transversely isotropic (TI), allowing the application of weak anisotropy formulae (Thomsen 1986). Accordingly, since V_p is normally lower in the direction perpendicular to bedding (King 2009; Martínez and Schmitt 2013; Thomsen 1986; Wang 2002), the direction along the X-plug (or vector V) would correspond to the symmetry axis, while the isotropic plane containing the Y- and Z-plugs axial directions (with velocities about 10% higher) defines the bedding plane (*i.e.*, two perpendicular directions to the anisotropy symmetry axis H_1 and H_2). Then, taking the Thomsen's (1986) notation and equations, it is possible to evaluate the anisotropy for P-wave velocity (ε) and *S-wave velocity* (γ) from four of the five elastic constants of the material (C_{11}, C_{33}, C_{44} and C_{66}) as follows:

$$\varepsilon = \frac{C_{11} - C_{33}}{2C_{33}} \quad (3)$$

$$\gamma = \frac{C_{66} - C_{44}}{2C_{44}} \quad (4)$$

where $C_{11} = \rho V_{p(H1,2)}{}^2$; $C_{33} = \rho V_{p(V)}{}^2$; $C_{66} = \rho V_{s(H1,2)}{}^2$; and $C_{44} = \rho V_{p(V)}{}^2$. A more detailed explanation of the notation and equations is given in Thomsen (1986), Wang (2002) and Louis *et al.* (2004). It is worth noting that we independently compute ε and γ for H_1 and H_2 (*i.e.*, Y- and Z-plugs) since both directions are orthogonal to the symmetry axis. In this study we lack a sample cored at 45º, hence the third Thomsen's anisotropy parameter δ (Thomsen 1986) cannot be calculated. Likewise, to analyse the anisotropy of the rock in terms of P- and S-wave attenuations (Q_p^{-1}

and Q_s^{-1}), we use the Thomsen-style parameters proposed by Zhu and Tsvankin (2006), as presented in Best *et al.* (2007):

$$\varepsilon_Q = \frac{Q_P^{-1}(H_{1,2}) - Q_P^{-1}(V)}{Q_P^{-1}(V)} \quad (5)$$

$$\gamma_Q = \frac{Q_S^{-1}(H_{1,2}) - Q_S^{-1}(V)}{Q_S^{-1}(V)} \quad (6)$$

The computed velocity and attenuation anisotropies are represented in Figure 18a - b, as ε, γ, ε_Q, γ_Q percentages versus differential stress. The P- and S- wave velocity anisotropy parameters ε and γ display similar evolution versus P_{diff}, decreasing from 12 to 8% and 8 to 4%, respectively, when P_{diff} increases 15 MPa. Furthermore, the changes of ε and γ in the plane defined by the X- and Y-plugs (ε_{xy} and γ_{xy}) are less pronounced (*i.e.,* less anisotropic) than those observed for the plane defined by the X- and Z-plugs (ε_{xz} and γ_{xz}); this suggests that pore compaction is more significant along the former plane. Additionally, the low hysteresis observed at the end of the unloading path (~2%) would suggest that the reduction of anisotropy due to compression is largely controlled by the compliance of equant pores. In this regard, the non-linear trends are likely indicating that microcrack-closing is also playing a role (Martínez and Schmitt 2013). Nevertheless, our data suggest that all core plugs evolve to a more isotropic state when confining pressure is increased as ε and γ tend to decrease.

The attenuation parameters (ε_Q and γ_Q) show similar trends to those described previously for velocities, although ε_Q is positive (<12%) and γ_Q negative (20 – 25%). The parameter γ_Q ranges between -5 to 5% for the plane defined by the X- and Y-

plugs, and stays around -10% for that defined by the X- and Z-plugs, without showing a clear dependence on P_{diff}. As noted by Best *et al.* (2007), for P_{diff} increments greater than those used in this study, attenuation anisotropy in sandstones is more sensitive to pressure changes than velocity anisotropy. So that P- and S-wave attenuation parameters provide more information about the magnitude of the anisotropy. Nonetheless, whether the velocity or attenuation anisotropy is considered, Corvio sandstone seems to be weakly anisotropic according to Martinez and Schmitt (2013).

5 Summary and conclusions

We have reported a comprehensive characterization for Corvio sandstone and paid special attention to the assessment of weak anisotropy from a multifaceted perspective. The average mineralogy is dominated by quartz (~94%), kaolinite (~3.5%) and k-feldspar (~1.7%), which suggests low chemical reactivity when submitted to the injection of CO_2 or CO_2-saturated fluids, at least on short time scales. This is useful when trying to focus on thermo-hydro-mechanical processes associated to CO_2 injection with minimum impact of chemical processes.

The standard geomechanical characterization also provides relevant information. The crack closing stress (which refers to pore compaction and compliant crack closing) occurs at 10 MPa while the onset of crack initiation occurs at ~18 MPa. These values have been indirectly verified by different techniques. Direct application of these results implies better assessment of experimental conditions in order to reduce undesired effects like enhanced permeability due to non-closed cracks at low stress levels, or associated with rock damage induced by high stresses.

The average permeability of Corvio sandstone varies from 4 to 0.8 mD, decreasing with confining pressure. It is worth noting that, within the studied testing range, the main process inducing hysteresis in the rock (reflected in the hydrodynamic and velocity responses) is related to pore compaction and compliant crack closure below 10 MPa.

Although no sedimentary structures were detected at block-scale or through the X-ray μCT-scans, we have developed a multifaceted anisotropic analysis (multicore analysis), concluding that Corvio sandstone is weakly anisotropic: ultrasonic P-wave velocity anisotropy is <12% (<8% for the S-wave), attenuation anisotropy is < 20%, electrical resistivity varies <18% with plug orientation and permeability slightly oscillates (±1 mD) depending on the direction considered. Nonetheless, the anisotropy is again more significant within the crack closure domain, emphasising the importance of considering this mechanical limit when interpreting rock behaviour during hydromechanical studies. In addition, the bulk electrical resistivity analysis and the tracer injection tests both infer the presence of weak cross-bedding.

These characterization results constitute a useful baseline for CO_2 injection studies using this sedimentary rock. Our results are of direct application when working with this rock in the laboratory, as they help us: (i) to understand non-obvious processes such as thresholds for pore compaction, compliant crack closure, and physicochemical coupling; (ii) to better calibrate geophysical techniques by reducing uncertainty and providing a well-constrained fabric model; (iii) to improve experimental design parameters such as stress ranges, plug orientation, and vector properties, among others. Furthermore, we want to highlight the importance of weak anisotropy when considering naturally homogeneous materials (at least in

appearance). These observations can be scaled up to field scenarios in order to improve reservoir models.

This comprehensive characterization of Corvio sandstone covers geomechanical, geochemical, geophysical and hydrodynamic properties. Together with the detailed assessment of anisotropy presented here, the results indicate that Corvio sandstone could be used as a particularly interesting rock-standard to improve the understanding of reservoirs subjected to complex thermo-hydro-mechano-geochemical coupled phenomena, typically associated with CO_2 storage practices.

Acknowledgments

Some of the measurements reported here were performed at the esCO_2–CIUDEN facilities (OXY CFB 300 Compostilla Project) and the Colorado School of Mines. Assistance and advice of Drs. T. Kovacs, M. Batzle, V. Barrientos, B. Rodriguez, K. Amalokwu and Gaye Bayrkci are kindly acknowledged. Funds for this work have been provided by the XUGA Project 10REM003CT and the European Regional Development Funds 2007/2013. Additional support was provided by UK EPSRC grant EP/K035878/1 and the UK Natural Environment Research Council. This work is dedicated to the memory of Dr. Mike Batzle.

EAGE Publications B.V., PO Box 59, 3990 DB, Houten, The Netherlands

References

Alcalde J., Marzán I., Saura E., Martí D., Ayarza P., Juhlin C., Pérez-Estaún A., Carbonell R. 2014. 3D geological characterization of the Hontomín CO_2 storage site, Spain: Multidisciplinary approach from seismic, well-log and regional data. Tectonophysics 627, 6-25.

Akbarabadi M. and Piri M. 2013. Relative permeability hysteresis and capillary trapping characteristics of supercritical CO_2/brine systems: An experimental study at reservoir conditions. Advances in Water Resources, 52, 190-206.

Alemu B.L., Aker E., Soldal M., Johnsen Ø. and Aagaard P. 2013. Effect of sub-core scale heterogeneities on acoustic and electrical properties of a reservoir rock: a CO_2 flooding experiment of brine saturated sandstone in a computed tomography scanner. Geophysical Prospecting, 61, 235-250.

Andrä H., Combaret N., Dvorkin J., Glatt E., Han J., Kabel M., Keehm Y., Krzikalla F., Lee M., Madonna C., Marsh M., Mukerji T., Saenger E.H., Sain R., Saxena N., Ricker S., Wiegmann A. and Zhan X. 2013. Digital rock physics benchmarks—Part I: Imaging and segmentation. Computers & Geosciences, 50, 25-32.

Angus D.A., Kendall J.M., Fisher Q.J., Segura J.M., Skachkov S., Crook A.J.L. and Dutko M. 2010. Modelling microseismicity of a producing reservoir from coupled fluid-flow and geomechanical simulation. Geophysical Prospecting, 58, 901-914.

Asef, M.R. and Najibi, A.R. 2013. The effect of confining pressure on elastic wave velocities and dynamic to static Young's modulus ratio. Geophysics, 78, D135-D142.

ASTM 2007. Standard Test Method for Compressive Strength and Elastic Moduli of Intact Rock Core Specimens under Varying States of Stress and Temperatures; D7012:2007 Annual Book of ASTM Standards, Section 4: Construction, Volume 04.09: Soil and Rock (II), ASTM International, West Conshohocken (PA), pp. 1429-1436.

Batzle M.L., Han D.H. and Hofmann R. 2006. Fluid mobility and frequency-dependent seismic velocity-Direct measurements. Geophysics, 71, N1-N9.

Barrientos V., Delgado J., Navarro V., Juncosa R., Falcón I. and Vázquez A. 2010. Characterization and geochemical-geotechnical properties of granite sawdust produced by the dimension stone industry of O Porrino (Pontevedra, Spain). Quarterly Journal of Engineering Geology and Hydrogeology, 43, 141-155.

Bednárik, M. and Kohút, I. 2012. Three-dimensional colour functions for stress state visualisation. Computers & Geosciences, 48, 117-125.

Bernabé, Y. 1991. Pore geometry and pressure dependence of the transport properties in sandstones. Geophysics, 56, 436-446.

Best A.I., Sothcott J. and McCann C. 2007. A laboratory study of seismic velocity and attenuation anisotropy in near-surface sedimentary rocks. Geophysical Prospecting, 55, 609-625.

Blake, O.O. and Faulkner, D.R. 2016. The effect of fracture density and stress state on the static and dynamic bulk moduli of Westerly granite. Journal of Geophysical Research: Solid Earth, 121, 2382–2399.

Cai M. 2010. Practical estimates of tensile strength and Hoek–Brown strength parameter m_i of brittle rocks. Rock Mechanics and Rock Engineering, 43, 167-184.

EAGE Publications B.V., PO Box 59, 3990 DB, Houten, The Netherlands

Canal J., Delgado J., Falcón I., Yang Q., Juncosa R. and Barrientos V. 2013. Injection of CO_2-Saturated Water through a Siliceous Sandstone Plug from the Hontomin Test Site (Spain): Experiment and modeling. Environmental Science & Technology, 47, 159-167.

Chichinina T., Obolentseva I., Gik L., Bobrov B. and Ronquillo-Jarillo G. 2009. Attenuation anisotropy in the linear-slip model: Interpretation of physical modeling data. Geophysics, 74, WB165-WB176.

Churcher P.L., French P.R., Shaw J.C. and Schramm L.L. 1991. Rock properties of Berea sandstone, Baker dolomite and Indiana limestone, SPE International Symposium on Oilfield Chemistry Anaheim, CA, 20-22 February, SPE 21044.

Eissa, E.A. and Kazi, A. 1988. Relation between static and dynamic Young's moduli of rocks. International Journal of Rock Mechanics and Mining Sciences & Geomechanics Abstracts 25, 479-482.

Ellis M.H., Sinha M.C., Minshull T.A., Sothcott J. and Best A.I. 2010. An anisotropic model for the electrical resistivity of two-phase geologic materials. Geophysics, 75, E161–E170.

Falcon-Suarez I., North L. and Best A. 2014. Experimental rig to improve the geophysical and geomechanical understanding of CO_2 reservoirs. Energy Procedia, 59, 75-81.

Farrell N.J.C., Healy D. and Taylor C.W. 2014. Anisotropy of permeability in faulted porous sandstones. Journal of Structural Geology, 63, 50-67.

Fetter C.W. 1993. Contaminant Hydrogeology. 2nd edition. Macmillan Publishing Company, New York.

Fjær, E. 2009. Static and dynamic moduli of a weak sandstone. Geophysics, 74, WA103-WA112.

Fjær, E., Stroisz, A.M. and Holt, R.M. 2013. Elastic Dispersion Derived from a Combination of Static and Dynamic Measurements. Rock Mechanics and Rock Engineering, 46, 611-618.

Fortin, J., Guéguen, Y. and Schubnel, A. 2007. Effects of pore collapse and grain crushing on ultrasonic velocities and Vp/Vs. Journal of Geophysical Research, 112, B08207.

Fortin J., Schubnel A. and Guéguen Y. 2005. Elastic wave velocities and permeability evolution during compaction of Bleurswiller sandstone. International Journal of Rock Mechanics & Mining Sciences, 42, 873–889.

Fredrich J.T., Greaves K.H. and Martin J.W. 1993. Pore geometry and transport properties of Fontainebleau sandstone. International Journal of Rock Mechanics and Mining Sciences & Geomechanics Abstracts, 30, 691-697.

Gaus I. 2010. Role and impact of CO_2-rock interactions during CO_2 storage in sedimentary rocks. International Journal of Greenhouse Gas Control, 4, 73-89.

Hakala M., Kuula H. and Hudson J.A. 2007. Estimating the transversely isotropic elastic intact rock properties for in situ stress measurement data reduction: A case study of the Olkiluoto mica gneiss, Finland. International Journal of Rock Mechanics and Mining Sciences, 44, 14-46.

Hangx S.J.T., Spiers C.J. and Peach C.J. 2010. Creep of simulated reservoir sands and coupled chemical-mechanical effects of CO_2 injection. Journal of Geophysical Research: Solid Earth, 115, B09205.

Hernández J.M., Pujalte V., Robles S. and Martín-Closas C. 1999. División estratigráfica genética del Grupo Campóo (Malm-Cretácico Inferior, SW Cuenca Vascocantábrica). Revista de la Sociedad Geológica de España, 12, 377-396.

Hoek E. and Brown E.T. 1980. Underground Excavations in Rock. The Institute of Mining and Metallurgy, London.

Hoek E., Carranza-Torres C. and Corkum B. 2002. Hoek-Brown criterion–2002 edition, Proc. NARMS-TAC Conference, Toronto, Extended Abstracts, 267-273.

ISRM 1978. Suggested methods for determining the strength of rock materials in triaxial compression. International Journal of Rock Mechanics and Mining Sciences & Geomechanics Abstracts, 15, 99-103.

ISRM 1983. Suggested methods for determining the strength of rock materials in triaxial compression: Revised version. International Journal of Rock Mechanics and Mining Sciences & Geomechanics Abstracts, 20, 285-290.

King, M.S. 1983. Static and dynamic elastic properties of rocks from the Canadian shield. International Journal of Rock Mechanics and Mining Sciences & Geomechanics Abstracts, 20, 237-241.

King M.S. 2009. Recent developments in seismic rock physics. International Journal of Rock Mechanics and Mining Sciences, 46, 1341-1348.

Klein E., Baud P., Reuschlé T. and Wong T.F. 2001. Mechanical behaviour and failure mode of Bentheim sandstone under triaxial compression. Physics and Chemistry of the Earth, Part A: Solid Earth and Geodesy, 26, 21-25.

Krevor S.C., Pini R., Zuo L. and Benson S.M. 2012. Relative permeability and trapping of CO_2 and water in sandstone rocks at reservoir conditions. Water Resources Research, 48, W02532.

Kutchko B.G., Strazisar B.R., Lowry G.V., Dzombak D.A. and Thaulow N. 2008. Rate of CO_2 attack on hydrated class-H well cement under geologic sequestration conditions. Environmental Science & Technology, 42, 6237-6242.

Lau J.S. and Chandler N.A. 2004. Innovative laboratory testing. International Journal of Rock Mechanics and Mining Sciences, 41, 1427-1445.

Le Guen, Y., Renard, F., Hellmann, R., Brosse, E., Collombet, M., Tisserand, D. and Gratier, J.P. 2007. Enhanced deformation of limestone and sandstone in the presence of high fluids. Journal of Geophysical Research: Solid Earth 112, B05421.

Lei X. and Xue Z. 2009. Ultrasonic velocity and attenuation during CO_2 injection into water-saturated porous sandstone: Measurements using difference seismic tomography. Physics of the Earth and Planetary Interiors, 176, 224-234.

Liu F., Lu P., Griffith C., Hedges S.W., Soong Y., Hellevang H. and Zhu C. 2012. CO_2–brine–caprock interaction: Reactivity experiments on Eau Claire shale and a review of relevant literature. International Journal of Greenhouse Gas Control, 7, 153-167.

Louis, L., Robion, P. and David, C. 2004. A single method for the inversion of anisotropic data sets with application to structural studies. Journal of Structural Geology 26, 2065–2072.

Lu P., Fu Q., Seyfried Jr. W.E., Hereford A. and Zhu C. 2011. Navajo sandstone-brine-CO_2 interaction: implications for geological carbon sequestration. Environmental Earth Sciences, 62, 101-118.

Martin C.D. and Chandler N.A. 1994. The progressive fracture of Lac du Bonnet granite. International Journal of Rock Mechanics and Mining Sciences & Geomechanics Abstracts, 31, 643-659.

EAGE Publications B.V., PO Box 59, 3990 DB, Houten, The Netherlands

Martínez J.M. and Schmitt D.R. 2013. Anisotropic elastic moduli of carbonates and evaporites from the Weyburn-Midale reservoir and seal rocks. Geophysical Prospecting, 61, 363-379.

McCann C. and Sothcott J. 1992. Laboratory measurements of the seismic properties of sedimentary rocks. Geological Society, London, Special Publications, 65, 285-297.

Mikhaltsevitch V., Lebedev M. and Gurevich B. 2014. Measurements of the elastic and anelastic properties of sandstone flooded with supercritical CO_2. Geophysical Prospecting, 62, 1266-1277.

Nakagawa S., Kneafsey T.J., Daley T.M., Freifeld B.M. and Rees E.V. 2013. Laboratory seismic monitoring of supercritical CO_2 flooding in sandstone cores using the Split Hopkinson resonant bar technique with concurrent X-ray computed tomography imaging. Geophysical Prospecting, 61, 254-269.

Nakatsuka Y., Xue Z., Garcia H. and Matsuoka T. 2010. Experimental study on CO_2 monitoring and quantification of stored CO_2 in saline formations using resistivity measurements. International Journal of Greenhouse Gas Control, 4, 209-216

Nguyen V.H., Gland N., Dautriat J., David C., Wassermann J. and Guélard J. 2013. Compaction, permeability evolution and stress path effects in unconsolidated sand and weakly consolidated sandstone. International Journal of Rock Mechanics and Mining Sciences, 67, 226 - 239.

Nicksiar M. and Martin C.D. 2012. Evaluation of Methods for Determining Crack Initiation in Compression Tests on Low-Porosity Rocks. Rock Mechanics and Rock Engineering, 45, 607-617.

EAGE Publications B.V., PO Box 59, 3990 DB, Houten, The Netherlands

Njiekak, G., Schmitt, D.R., Yam, H., Kofman, R.S., 2013. CO2 rock physics as part of the Weyburn-Midale geological storage project. International Journal of Greenhouse Gas Control, 16, S118-S133.

North L., Best A.I., Sothcott J. and MacGregor L. 2013. Laboratory determination of the full electrical resistivity tensor of heterogeneous carbonate rocks at elevated pressures. Geophysical Prospecting, 61, 458-470.

North L.J. and Best A.I. 2014. Anomalous electrical resistivity anisotropy in clean reservoir sandstones. Geophysical Prospecting, 62, 1315-1326.

Oh J., Kim K.-Y., Han W.S., Kim T., Kim J.-C. and Park E. 2013. Experimental and numerical study on supercritical CO_2/brine transport in a fractured rock: Implications of mass transfer, capillary pressure and storage capacity. Advances in Water Resources, 62, 442-453.

Ojala I.O., Ngwenya B.T. and Main I.G. 2004. Loading rate dependence of permeability evolution in porouos Aeolian sandstones. Journal of Geophysical Research, 109, B01204.

Pini R., Krevor S.C.M. and Benson S.M. 2012. Capillary pressure and heterogeneity for the CO_2/water system in sandstone rocks at reservoir conditions. Advances in Water Resources, 38, 48-59.

Ptak T., Piepenbrink M. and Martac E. 2004. Tracer tests for the investigation of heterogeneous porous media and stochastic modelling of flow and transport - a review of some recent developments. Journal of Hydrology, 294, 122-163.

Rae P.J., Brown E.N. and Orler E.B. 2007. The mechanical properties of poly(ether-ether-ketone) (PEEK) with emphasis on the large compressive strain response. Polymer, 48, 598-615.

Rouquerol J., Avnir D., Fairbridge C.W., Everett D.H., Haynes J.M., Pernicone N., Ramsay J.D.F., Sing K.S.W. and Unger K.K. 1994. Recommendations for the characterization of porous solids. Pure and Applied Chemistry 66, 1739-1758

Rutqvist J. 2012. The geomechanics of CO_2 storage in deep sedimentary formations. Geotechnical and Geological Engineering, 30, 525-551.

Shackelford C.D., Malusis M.A., Majeski M.J. and Stern R.T. 1999. Electrical conductivity breakthrough curves. Journal of Geotechnical and Geoenvironmental Engineering, 125, 260-270.

Schubnel A., Benson P., Thompson B., Hazzard J. and Young R. 2006. Quantifying damage, saturation and anisotropy in cracked rocks by inverting elastic wave velocities. Pure and Applied Geophysics, 163, 947-973.

Sim C.Y. and Adam L. 2015. Are seismic velocity time-lapse changes due to fluid substitution or matrix dissolution? A CO_2 sequestration study at Pohokura Field, New Zealand. SEG Technical Program Expanded Abstracts, 3123-3128.

Song, I. and Renner, J. 2008. Hydromechanical properties of Fontainebleau sandstone: Experimental determination and micromechanical modelling. Journal of Geophysical Research 113, B09211

Song J. and Zhang D. 2012. Comprehensive review of caprock-sealing mechanisms for geologic carbon sequestration. Environmental Science & Technology, 47, 9-22.

Thomsen L. 1986. Weak elastic anisotropy. Geophysics, 51, 1954-1966.

Vialle S. and Vanorio T. 2011. Laboratory measurements of elastic properties of carbonate rocks during injection of reactive CO_2-saturated water. Geophysical Research Letters, 38, L01302.

Wang Z. 2002. Seismic anisotropy in sedimentary rocks, part 1: A single-plug laboratory method. Geophysics, 67, 1415-1422.

Xu X., Hofmann R., Batzle M. and Tshering T. 2006. Influence of pore pressure on velocity in low-porosity sandstone: Implications for time-lapse feasibility and pore-pressure study. Geophysical Prospecting, 54, 565-573.

Xue Z. and Lei X. 2006. Laboratory study of CO_2 migration in water-saturated anisotropic sandstone, based on P-wave velocity imaging. Exploration Geophysics, 37, 10-18.

Xue Z. and Ohsumi T. 2004. Seismic wave monitoring of CO_2 migration in water-saturated porous sandstone. Exploration Geophysics, 35, 25-32.

Zhan X., Schwartz L.M., Nafi-Toksoz M., Smith W.C. and Dale-Morgan F. (2010). Pore-scale modeling of electrical and fluid transport in Berea sandstone.Geophysics 75, F135F142

Zhu W. and Wong T.F. 1996. Permeability evolution in a dilatating rock: Network modelling of damage and tortuosity. Geophysical Research Letters 23, 3099-3102.

Zhu Y. and Tsvankin I. 2006. Plane-wave propagation in attenuative transversely isotropic media. Geophysics, 71, T17-T30.

Zhu Y., Tsvankin I., Dewangan P. and Wijk K.V. 2007. Physical modeling and analysis of P-wave attenuation anisotropy in transversely isotropic media. Geophysics, 72, D1-D7.

EAGE Publications B.V., PO Box 59, 3990 DB, Houten, The Netherlands

Table 1. Chemical composition of the Corvio Sandstone as resulting from XRF analysis

Constituent	wt.%	Constituent	ppm
Na_2O	0.04	Zr	332
K_2O	0.65	Mn	63
CaO	0.07	Ba	65
MgO	0.09	Sr	31
SiO_2	93.36	Rb	13
TiO_2	0.32	Ni	3
Al_2O_3	4.41	Zn	4
Fe_2O_3	0.10	Cu	2
SO_3	0.01	Pb	3

Table 2. Geomechanical characterization of Corvio sandstone.

Sample	ρ_d (kg m^{-3})	ϕ (%)	σ_3 (MPa)	σ_1 (MPa)	E (GPa)	ν	G (GPa)	K (GPa)
Confined compressive strength				*(CoCS)*				
C91	2026.2	22.1	5	90.6	-	-	-	-
C78	2030.2	21.9	10	107.3	14.71	0.34	5.48	15.44
C87	1998.7	23.2	15	129.9	-	-	-	-
C74	2023.4	22.2	30	153.1	14.62	0.34	5.47	14.99
T115	2122.5	18.4	38	181.4	17.54	0.34	6.57	17.72
C64	2052.7	21.1	50	221.9	13.99	0.34	5.23	14.41
Unconfined compressive strength				*(UCS)*				
C1	2008.8	22.7	0.1	36.0	9.33	0.35	3.47	10.08
C4	2022.7	22.2	0.1	41.1	11.11	0.35	4.11	12.39
C8	2032.0	21.9	0.1	43.7	12.04	0.35	4.47	13.12
C11	2021.4	22.3	0.1	43.3	11.09	0.35	4.10	12.65
C12	2030.9	21.9	0.1	44.4	11.38	0.34	4.25	11.63
C15	2025.3	22.1	0.1	35.4	19.72	0.34	7.34	20.90
C21	2035.3	21.8	0.1	41.4	10.81	0.33	4.08	10.36
C25	2037.5	21.7	0.1	43.7	10.99	0.35	4.08	11.94
C26	1990.9	23.5	0.1	39.4	9.47	0.34	3.53	10.01
C32	2032.3	21.9	0.1	42.9	12.03	0.35	4.46	13.29
Tensile strength (Brazilian)			*(TS)**					
C68-1	2043.5	21.4	3.0	-	-	-	-	-
C68-3	2043.5	21.4	1.8	-	-	-	-	-
C75-1	2020.8	22.3	1.9	-	-	-	-	-
C75-2	2020.8	22.3	2.1	-	-	-	-	-
C75-3	2020.8	22.3	2.7	-	-	-	-	-
C76-1	2016.2	22.5	2.3	-	-	-	-	-
C76-2	2016.2	22.5	1.9	-	-	-	-	-
C76-3	2016.2	22.5	2.4	-	-	-	-	-
C77-1	2035.7	21.7	2.2	-	-	-	-	-
C77-2	2035.7	21.7	2.2	-	-	-	-	-
C77-3	2035.7	21.7	3.1	-	-	-	-	-

* TS = -σ_3; Tensile strength is obtained from indirectly from radial compression (Brazilian test)

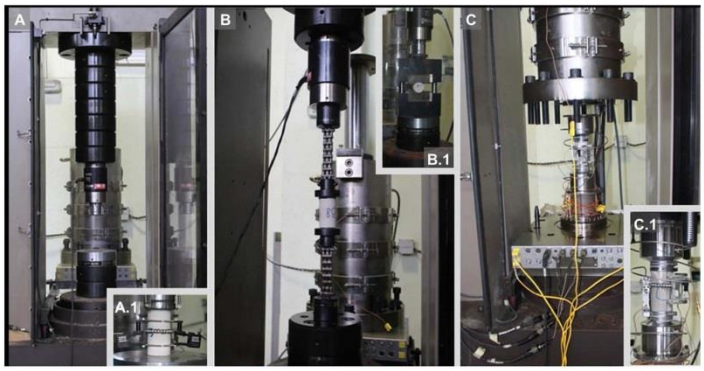

Figure 1. MTS 815 Rock Mechanics Testing System. A, uniaxial configuration and sample (A.1) equipped with extensometers dual-averaging knife-edge type (longitudinal deformation) and chain-type (circumferential deformation); B and B.1, direct and indirect (Brazilian) tensile configurations; C, open-chamber vision of the triaxial configuration and sample (C.1) ready for testing (same type of extensometers as the uniaxial configuration).
293x152mm (150 x 150 DPI)

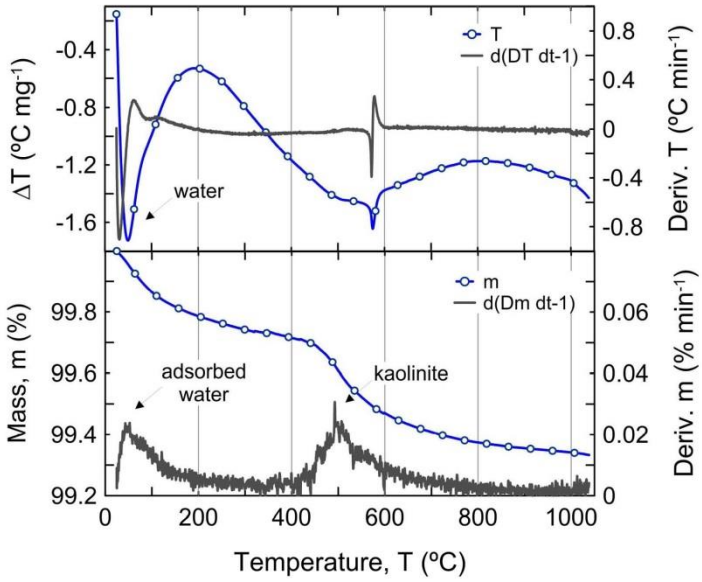

Figure 2. Typical TGA-DTA of Corvio sandstone. The prescribed heating rate was 5 ºK min^{-1} from room temperature 20 ºC to 1050 ºC.
177x145mm (300 x 300 DPI)

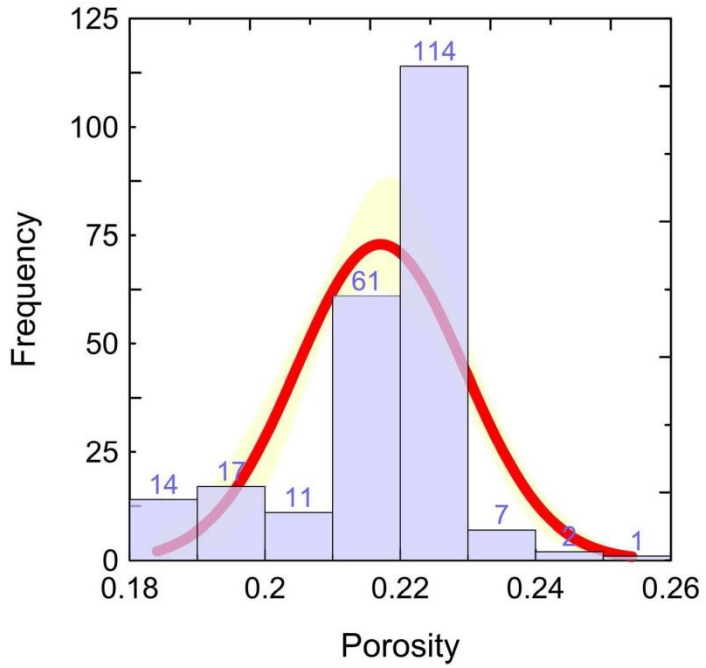

Figure 3a. Measured porosity of Corvio sandstone for 227 samples. The line corresponds to a normal distribution function; the shadow represents the associated 95% confidence band.
155x147mm (300 x 300 DPI)

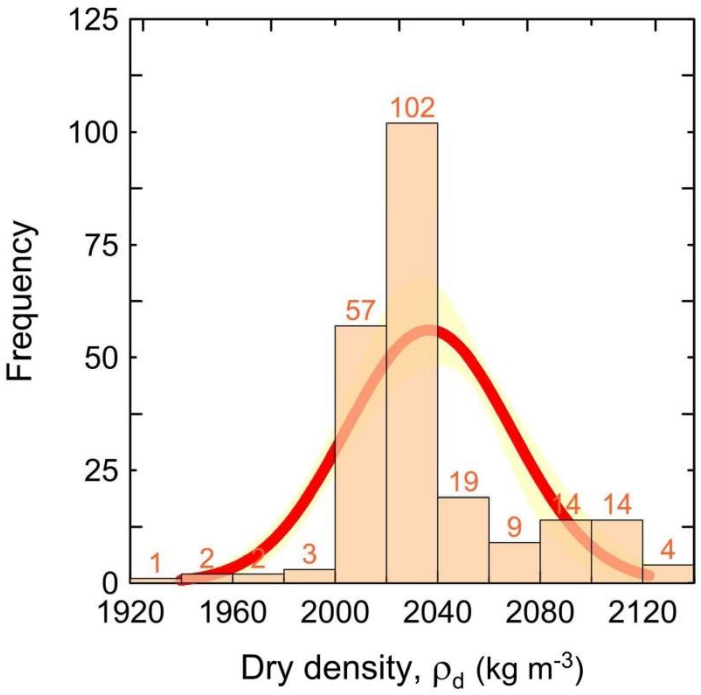

Figure 3b. Measured dry density of Corvio sandstone for 227 samples. The line corresponds to a normal distribution function; the shadow represents the associated 95% confidence band.
155x154mm (300 x 300 DPI)

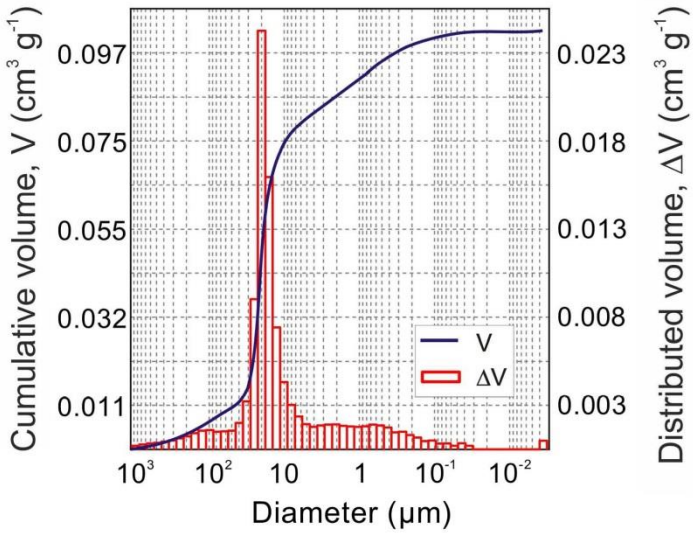

Figure 4a. Typical pore size distribution of the Corvio sandstone
164x126mm (300 x 300 DPI)

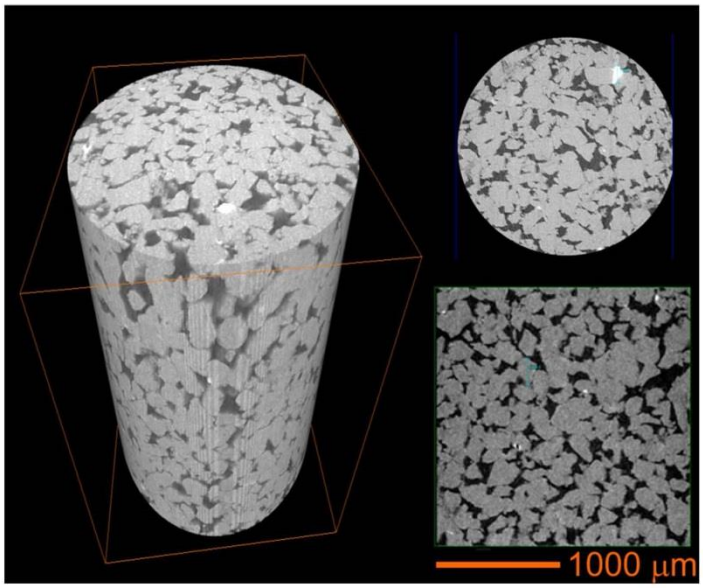

Figure 4b. X-Ray µCT-scan (full plug, radial and transversal sections; right) of the Corvio sandstone.
299x249mm (72 x 72 DPI)

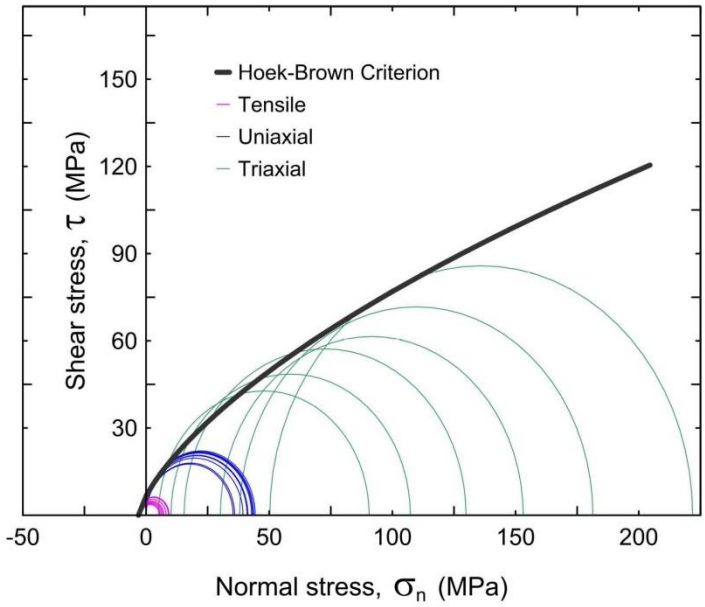

Figure 5. Mohr circles corresponding to the different mechanical tests performed: Tensile (Brazilian tests), Uniaxial (UCS) and Triaxial (CCS) with the Corvio sandstone. The computed strength envelope, computed from the Hoek-Brown model is also shown.
179x154mm (300 x 300 DPI)

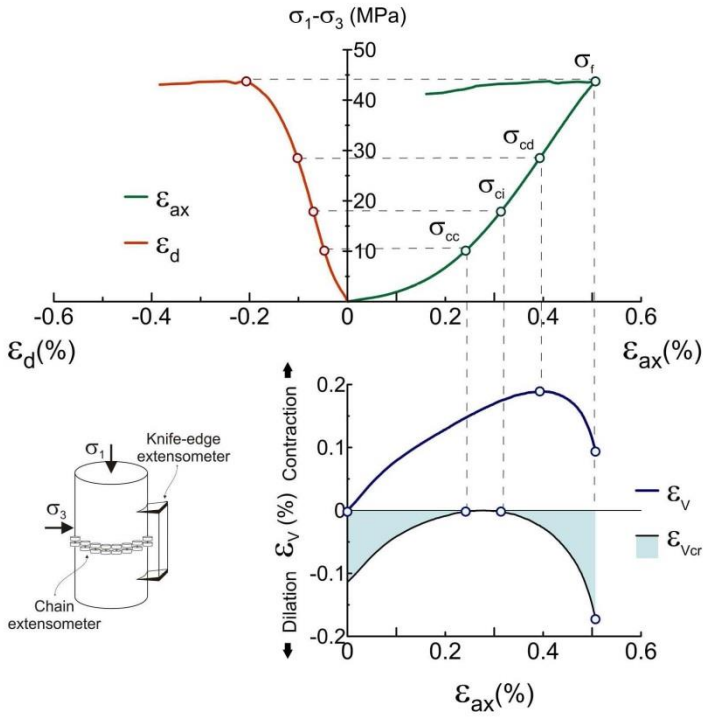

Figure 6. Typical UCS strain-stress curves of the Corvio sandstone and identification of the critical stress states.
217x225mm (300 x 300 DPI)

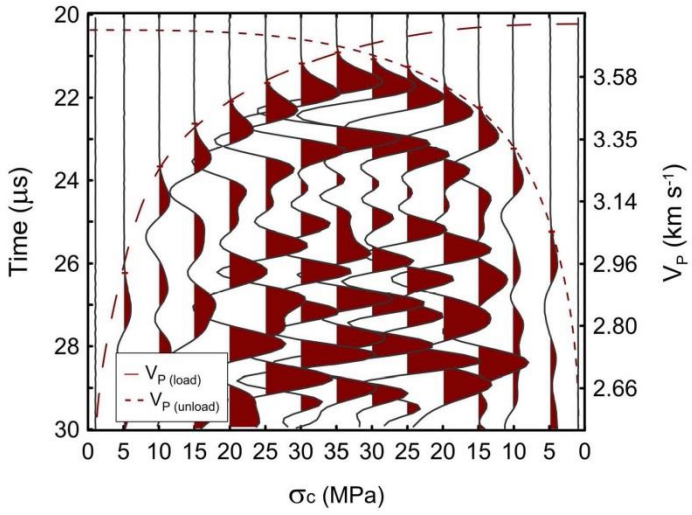

Figure 7a. Wiggle-trace plot corresponding to the change in P-wave propagation in Corvio sandstone. Loading/unloading test performed under hydrostatic conditions ($\sigma_1=\sigma_2=\sigma_3$). Discontinuous and dotted lines indicate the first pulse arrival during the loading and unloading sequence, respectively.
155x113mm (300 x 300 DPI)

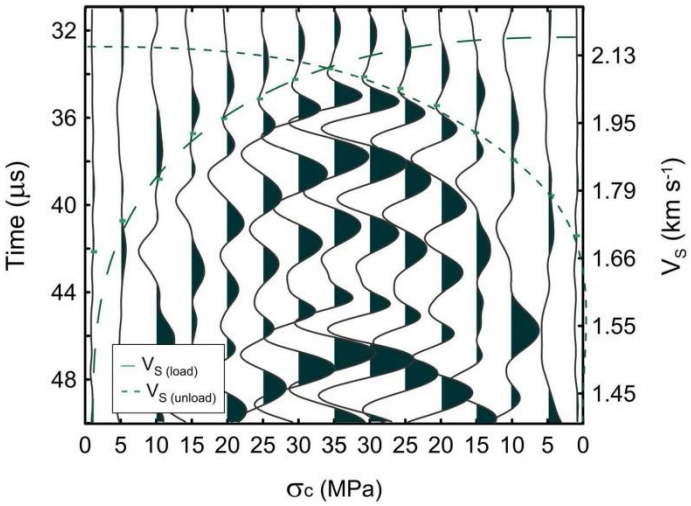

Figure 7b. Wiggle-trace plot corresponding to the change in S-wave propagation in Corvio sandstone. Loading/unloading test performed under hydrostatic conditions ($\sigma_1=\sigma_2=\sigma_3$). Discontinuous and dotted lines indicate the first pulse arrival during the loading and unloading sequence, respectively.
152x109mm (300 x 300 DPI)

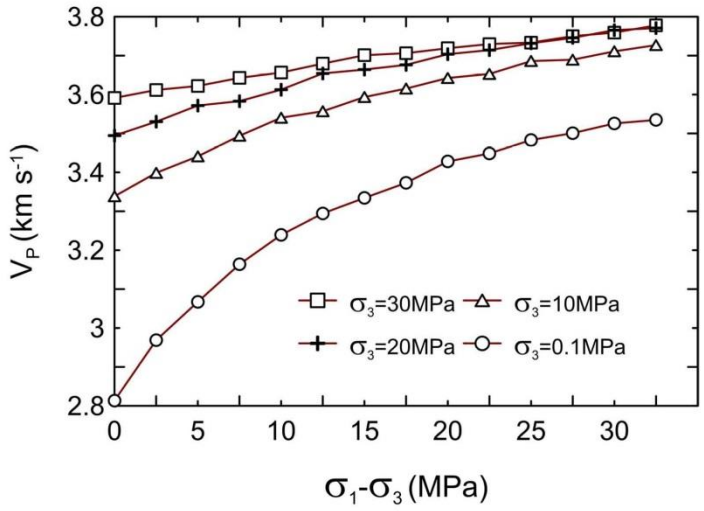

Figure 8a. V_p versus deviatoric stress ($\sigma_1 \neq \sigma_2 = \sigma_3$) for different confining conditions for Corvio sandstone.
132x96mm (300 x 300 DPI)

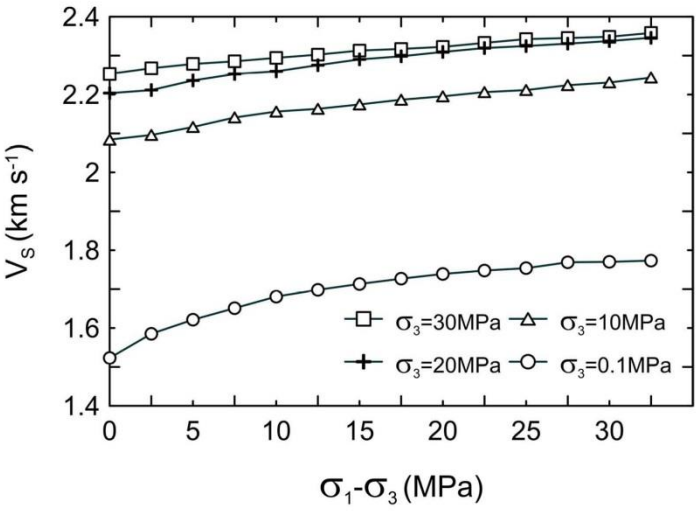

Figure 8b. V_s versus deviatoric stress ($\sigma_1 \neq \sigma_2 = \sigma_3$) for different confining conditions for Corvio sandstone.
132x96mm (300 x 300 DPI)

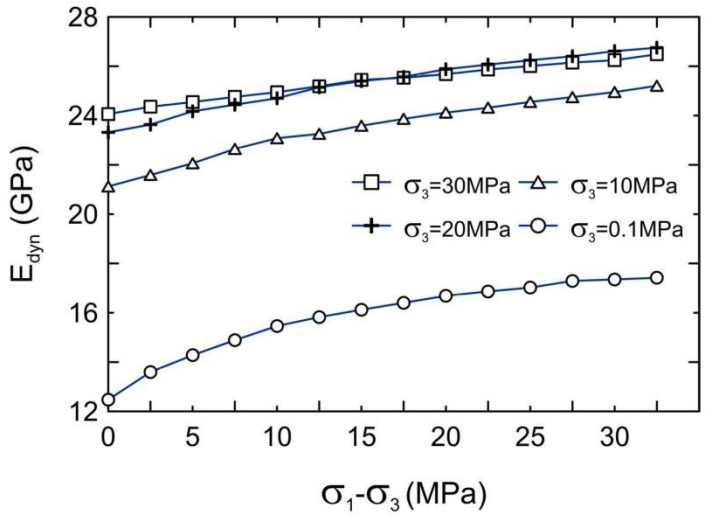

Figure 9a. Dynamic Young's modulus (E_{dyn}) versus deviatoric stress for different confining conditions ($\sigma_1 \neq \sigma_2 = \sigma_3$), for Corvio sandstone.
132x97mm (300 x 300 DPI)

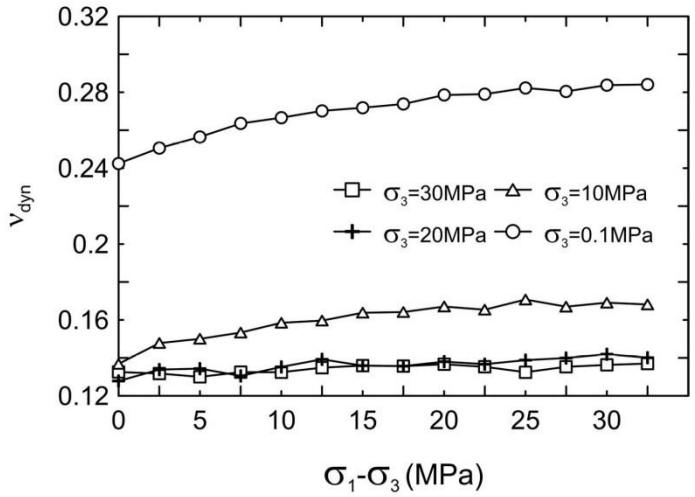

Figure 9b. Dynamic Poisson's ratio (v_{dyn}) versus deviatoric stress for different confining conditions ($\sigma_1 \neq \sigma_2 = \sigma_3$), for Corvio sandstone.
132x93mm (300 x 300 DPI)

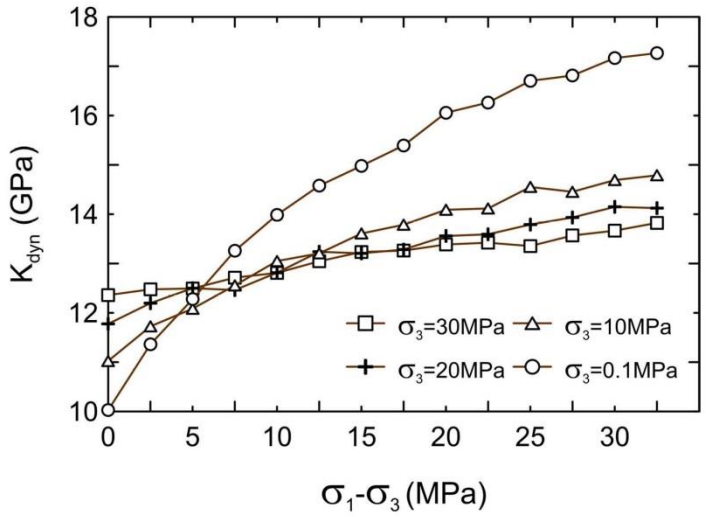

Figure 10a. Dynamic bulk modulus (K_{dyn}) versus deviatoric stress for different confining conditions ($\sigma_1 \neq \sigma_2 = \sigma_3$), for Corvio sandstone.
132x97mm (300 x 300 DPI)

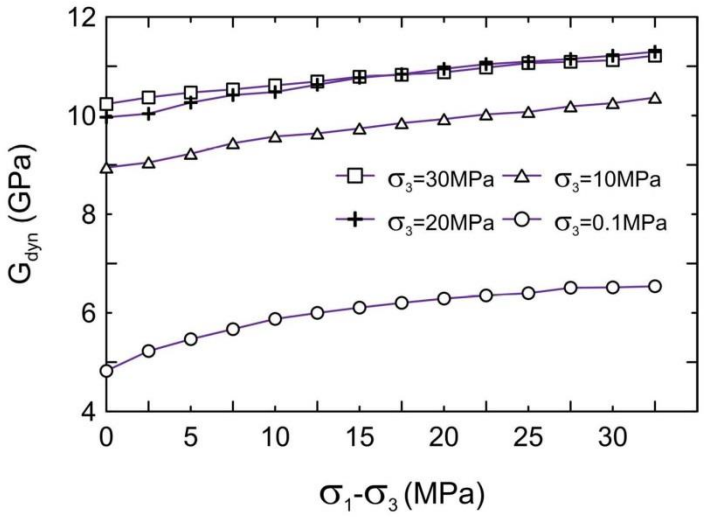

Figure 10b. Dynamic shear modulus (G_{dyn}) versus deviatoric stress for different confining conditions ($\sigma_1 \neq \sigma_2 = \sigma_3$), for Corvio sandstone.
132x97mm (300 x 300 DPI)

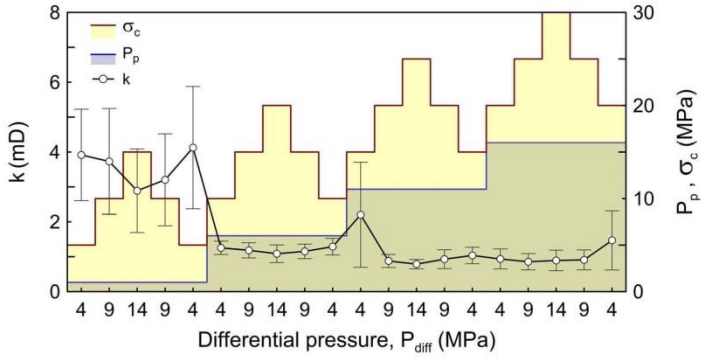

Figure 11. Permeability of Corvio sandstone as resulting from 4 consecutive loading/unloading each one of them performed at constant pore pressure.
128x65mm (300 x 300 DPI)

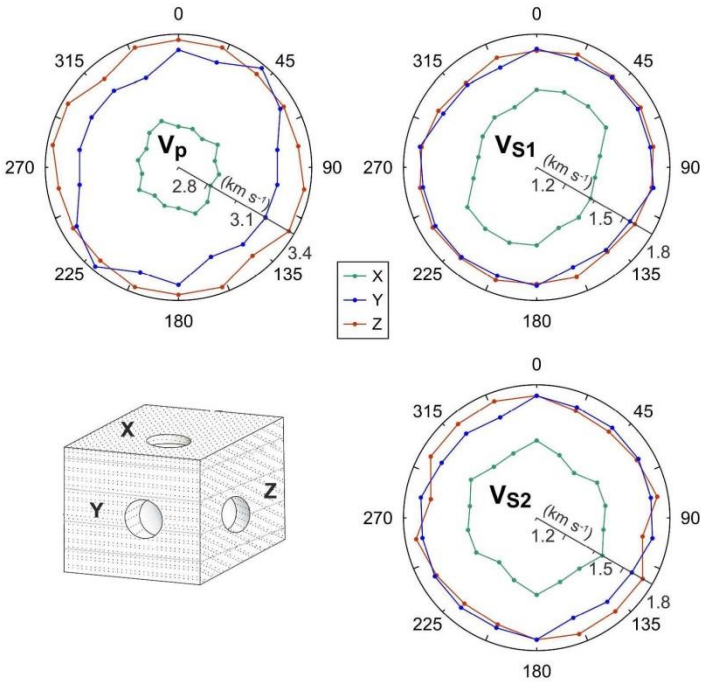

Figure 12. Acoustic wave velocities for the three main orthogonal directions (X-, Y- and Z-plugs) of Corvio sandstone, measured at 20º axially-rotating-steps. The measurements were carried out under unconfined conditions and a load of 1 MPa. The block-diagram illustrates the orientation of each plug.
323x315mm (300 x 300 DPI)

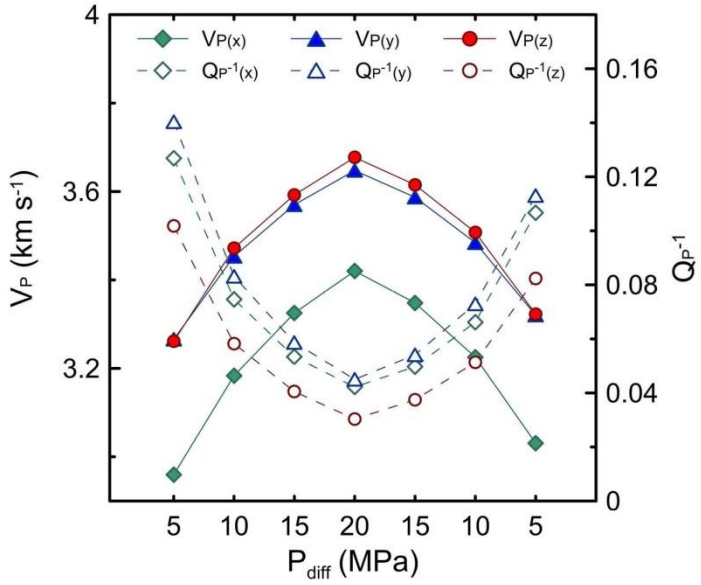

Figure 13a. P-wave velocity and attenuation for the three main orthogonal directions (X-, Y- and Z-plugs) of Corvio sandstone of Corvio sandstone.
152x127mm (300 x 300 DPI)

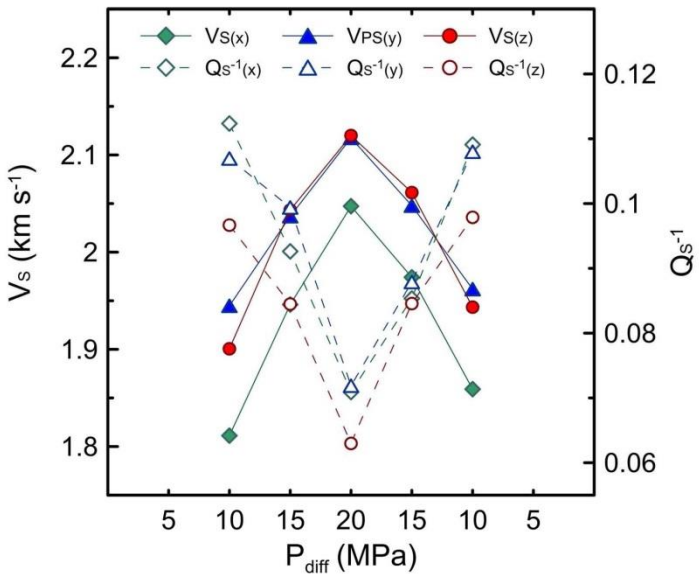

Figure 13b. S-wave velocity and attenuation for the three main orthogonal directions (X-, Y- and Z-plugs) of Corvio sandstone of Corvio sandstone.
148x121mm (300 x 300 DPI)

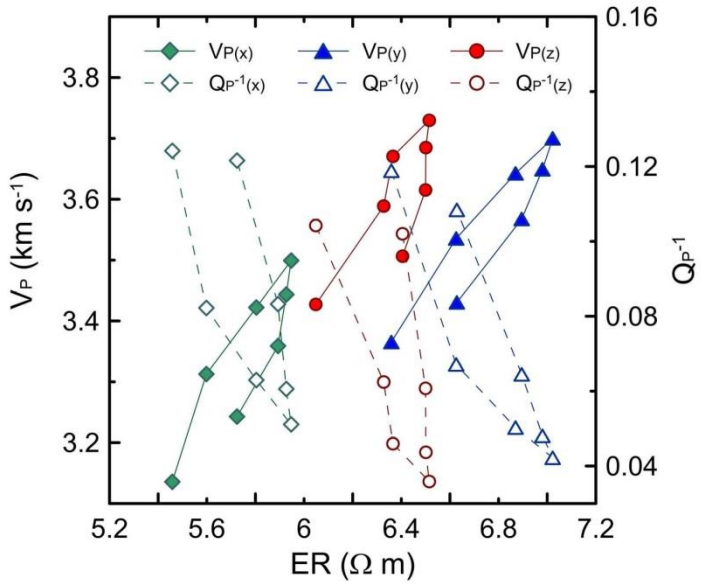

Figure 14. Figure 12. P-wave velocity and attenuation versus bulk electrical resistivity for the three main orthogonal directions (X-, Y- and Z-plugs) of Corvio sandstone.
150x125mm (300 x 300 DPI)

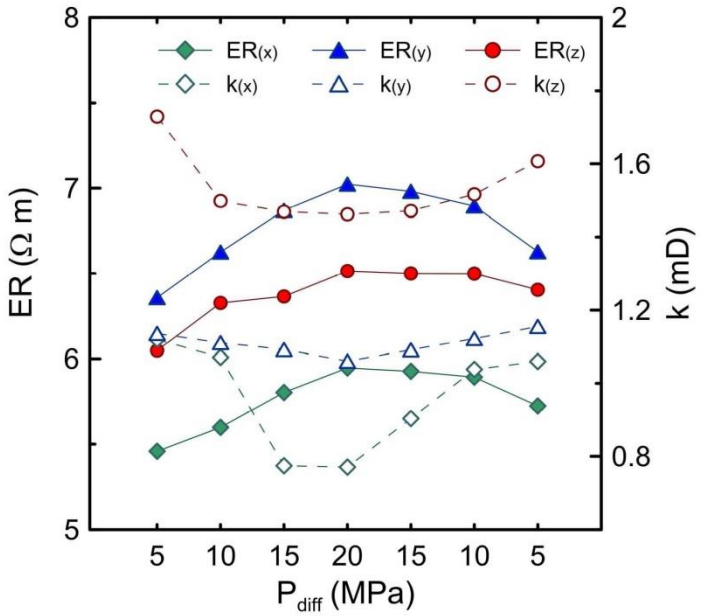

Figure 15. Electrical resistivity (ER) and permeability (k) versus effective pressure for the three main orthogonal directions (X-, Y- and Z-plugs) of Corvio sandstone.
152x134mm (300 x 300 DPI)

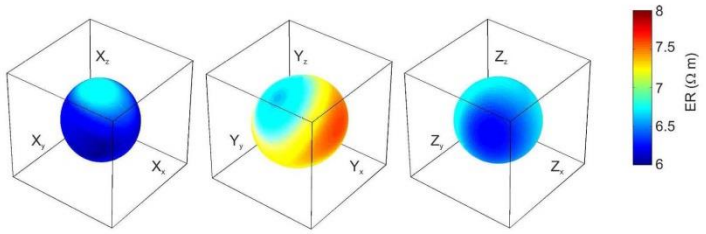

Figure 16. ER anisotropy ellipsoids for the three orthogonal samples of Corvio sandstone (X-, Y- and Z-plugs). The radius of each ellipsoid and colour are scaled according to the resistivity values observed along the axial direction of each plug (subscripts x,y and z refer to the three main directions of each sample).
521x168mm (300 x 300 DPI)

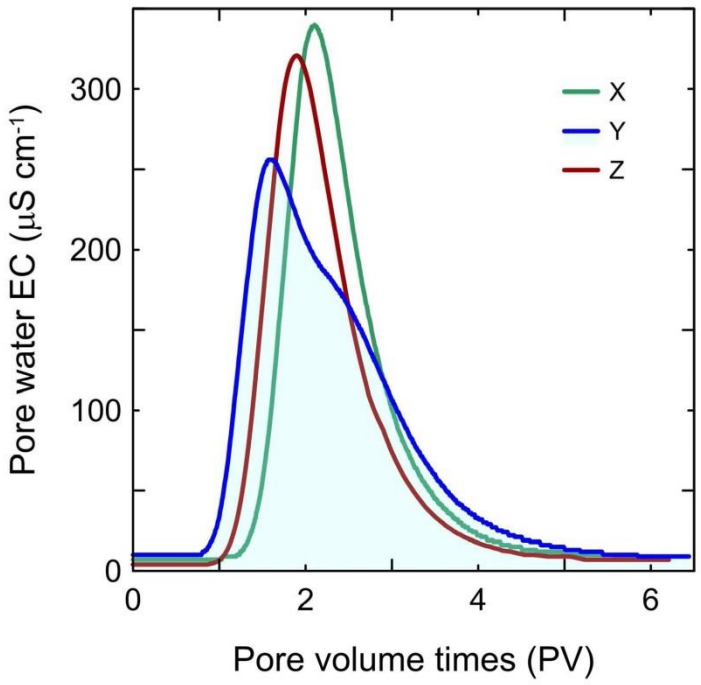

Figure 17. Breakthrough electrical conductivity curves corresponding to pulse-injection tracer tests performed along the three main orthogonal directions (X-, Y- and Z-plugs) of Corvio sandstone.
151x145mm (300 x 300 DPI)

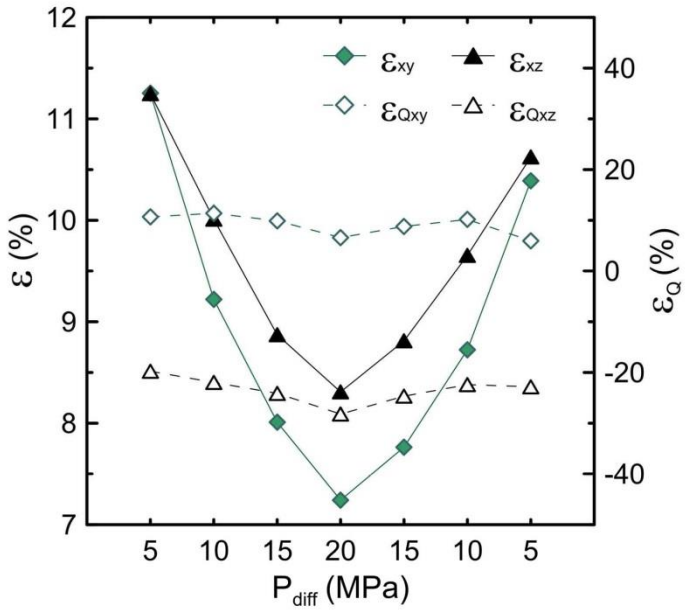

Figure 18a. P-wave velocity and attenuation anisotropy (ε and ε_Q) of the Corvio sandstone.
152x133mm (300 x 300 DPI)

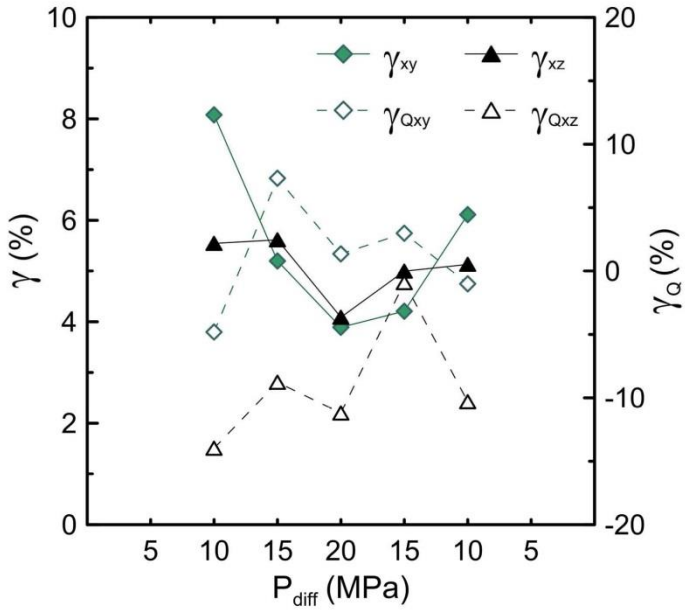

Figure 18b. S-wave velocity and attenuation anisotropy (γ and γ_Q) of the Corvio sandstone.
152x133mm (300 x 300 DPI)